Development of formable metal batteries (Mettery)

By

Xiangnan Yu

A thesis submitted to Imperial College London for the degree of Doctor of Philosophy

Department of Mechanical Engineering

South Kensington Campus

Imperial College London

London SW7 2AZ
U. K.

2023

Declaration of originality

This thesis hereby presented is based on the research by the author at the Department of Mechanical Engineering of Imperial College London. I declare the work contained in this thesis is the result of my independent research, except where appropriately referenced or acknowledged. Not any part of the present work has been submitted for a degree or diploma at any other university or institution.

Xiangnan Yu

Aug 2023

Declaration of copyright

The copyright of this thesis rests with the author. Unless otherwise indicated, its contents are licensed under a Creative Commons Attribution-Non Commercial 4.0 International Licence (CC BY-NC).

Under this licence, you may copy and redistribute the material in any medium or format. You may also create and distribute modified versions of the work. This is on the condition that: you credit the author and do not use it, or any derivative works, for a commercial purpose.

When reusing or sharing this work, ensure you make the licence terms clear to others by naming the licence and linking to the licence test. Where a work has been adapted, you should indicate that the work has been changed and describe those changes.

Please seek permission from the copyright holder for uses of this work that are not included in this licence or permitted under UK Copyright Law.

Abstract

As global energy demand grows exponentially, the heavy use of fossil fuels has contributed significantly to climate change and environmental pollution. The implementation of renewable energy combined with energy storage technologies has become a priority to alleviate oil shortages and solve environmental pollution. Driven by this, an innovative metal battery, called 'mettery', manufactured by metal forming technologies was developed. The proposed mettery will enable electrical energy storage in conventional metal components while maintaining the load-bearing capability of the material.

A formable solid-state polyvinylidene fluoride (PVDF)-polymethylhydrosiloxane (PMHS)-$Li_{6.4}La_3Zr_{1.4}Ta_{0.6}O_{12}$ (LLZTO) electrolyte, named PPL electrolyte, was developed as a candidate used in mettery. The PMHS could not only work as a bridge between the PVDF matrix and LLZTO to enhance the mechanical strength but also reduce the desolvation energy of Li-ions from the Li-DMF complex to activate the Li-ion transport pathways through LLZTO. As a result, the PPL electrolyte delivered a high tensile strength of 3.63 MPa and ionic conductivity of 7.5×10^{-4} S cm^{-1} at 25 °C, enabling the solid-state NCM811|PPL|Li coin cell to exhibit ultrahigh long-term cycling stability (initial specific capacity of 125.5 mAh g^{-1} with 81.9% capacity retention after 2200 cycles at 2C).

NCM811|PPL|Li mettery (referred to as PPL-mettery) was manufactured and the effect of plastic deformations on electrochemical performance was studied. The detrimental effect of pure bending deformation on the electrochemical performance was slight when the bending radius-thickness ratio (R/t) was more than 1.77. However, the micro-cracks in tensile deformed PPL electrolyte (tensile strain>10%) hindered the Li-ion transport and caused uneven lithium deposition, leading to an evident negative effect on electrochemical performance. Compared to PPL-mettery (tensile strain of 0.5%), PPL-mettery (tensile strain>10%) showed a capacity decrease of more than 21.7% at 1C and 28.9% at 2C after 100 cycles.

To improve the electrochemical performance of tensile deformed mettery, a small amount of fluoroethylene carbonate (FEC, 5 μL/cm^2) was introduced into the PPL electrolyte to form a quasi-solid-state electrolyte (QSE), referred to as PPL+FEC electrolytes. Attributing to the fast ion-conductive network constructed by mobile FEC liquid, the PPL+FEC electrolytes exhibited a high ionic conductivity of 1.5×10^{-3} S/cm and still maintained 1.3×10^{-3} S/cm after tensile deformation with a tensile strain of 15% at 25 °C. Moreover, the introduction of FEC helped to construct a stable interface between the electrolyte and lithium metal anode, enhancing the electrochemical performance and limiting the overgrowth of lithium dendrites. The tensile deformed NCM811|PPL+FEC|Li mettery (referred to as PPL+FEC-mettery) delivered a significantly increased capacity (more than 33.2% at 1C, more than 23.6% at 2C and more than 44.8% at 5C) compared to tensile deformed PPL-mettery.

Acknowledgements

First and foremost, I would like to express my gratefulness to my supervisor Dr Liliang Wang, who has provided careful guidance and kind support to me throughout my PhD study. I am very pleased to be his student and I very much enjoyed my 4 year's research journey with him. He always comes up with innovative ideas which inspire me to conduct interesting and challenging work. Also, he gave me enough freedom to independently complete my research. From his patient guidance, I am developing a more scientific way of thinking and studying. He encouraged me when I encountered challenges and continuously inspired me after I made progress in my research work. He not only gives me enough support in my PhD research but also gives me valuable suggestions for my future academic career. More importantly, his enthusiastic and motivated attitude toward academic research will inspire me in my future research work. In addition, I would like to thank my co-supervisor, Professor Jianguo Lin, for his ongoing support of my PhD research. I really appreciate the guidance and motivation my supervisors have given me.

Then, I wish to thank my research collaborators in Mechanic of Material Group, Yuhai Jin, Heli Liu, Dr Denis J. Politis, Dr Dhawan Saksham, Dr Xi Luan, Dr Zhaoheng Cai and Dr Xiao Yang. Especially for Yuhai Jin, who always shares ideas and knowledge with me in every weekly meeting. He also helped to conduct novel designs and modelling for my research project. I would also like to say warm thanks to my MSc and ME4 students, in particular, Arnav Rai, Sicheng Dong, Paul Bernheim, Luke Henry Walters, Michelle Kostin and de Noronha Agostinho, for the excellent work they have conducted to support my research from different aspects.

In addition, I would like to thank Professor Yanbing He from Tsinghua Shenzhen International Graduate School, who has been supportive and provided a great experimental platform for my research. And also, I wish to thank the members from Professor He's group.

Finally but most importantly, I intend to offer my sincere appreciation to my parents, who unconditionally love and care for me all the time. Thank you for being so encouraging and always backing up for me. Thanks for you are always there for me.

Content

Declaration of originality I
Declaration of copyright II
Abstract 1
Acknowledgements 2
Content 3
List of Figures 6
List of Tables 12
List of publications 13
List of symbols and acronyms 14
Chapter 1. Introduction 17
1.1 Background 17
1.2 Aims and objectives 18
Chapter 2. Literature review 19
2.1 Introduction 19
2.2 Overview of renewable energy 20
2.2.1 Hydroelectric energy 21
2.2.2 Wind energy 23
2.2.3 Solar energy 25
2.2.4 Development and applications 27
2.2.5 Raw material demand for renewable energy sources 29
2.3 Centralized energy storage technologies realized by rechargeable batteries 30
2.3.1 Lead acid batteries 31
2.3.2 Nickel-metal hydride batteries 31
2.3.3 Lithium-ion batteries 31
2.3.4 Solid-state lithium batteries 35
2.4 Centralized energy storage technologies realized by hydrogen fuel cells 37
2.5 Distributed energy storage realized by embodied energy storage technologies 38
2.6 Summary 42
Chapter 3. Development of solid-state PPL electrolyte 44
3.1 Introduction 44
3.2 Background 44
3.3 Experimental details 46
3.3.1 Preparation of PVDF-based SSEs 46
3.3.2 Material characterisation 46
3.3.3 Density functional theory (DFT) calculation 47
3.3.4 Electrochemical measurements of PVDF-based SSEs by coin cells 47

3.4 Reaction mechanism in the PPL electrolyte....48
3.5 Desolvation mechanism of solvated Li-ions in PPL electrolyte....51
3.6 Physicochemical characterisations of PVDF-based SSEs....54
3.7 Electrochemical properties of PPL electrolytes with different PMHS weight ratios....59
3.8 Electrochemical characterisations of PVDF-based SSEs....61
3.9 Electrochemical performances of NCM811|SSE|Li coin cells....66
3.10 Structural evolution and interfacial chemistry of SSEs and electrodes....73
3.11 Summary....84
Chapter 4. Effect of plastic deformation on electrochemical performance of PPL-metteries....86
4.1 Introduction....86
4.2 Background....86
4.3 Experimental details....87
4.3.1 Preparation of raw material of mettery....87
4.3.2 Preparation of bending deformed PPL-metteries....87
4.3.3 Preparation of tensile deformed PPL-metteries....87
4.3.4 Electrochemical characterization of plastic deformed PPL-metteries....88
4.4 Architecture of the raw material of mettery....88
4.5 PPL-metteries manufactured by metal forming technologies....89
4.6 Effect of bending deformation on the electrochemical performance of PPL-mettery....91
4.6.1 EIS of bending deformed PPL-metteries....92
4.6.2 Cycling performance of bending deformed PPL-metteries....92
4.6.3 Rate performance of bending deformed PPL-metteries....95
4.7 Effect of uniaxial tensile deformation on the electrochemical performance of PPL-mettery 96
4.7.1 EIS of tensile deformed PPL-metteries....97
4.7.2 Cycling performance of tensile deformed PPL-metteries....98
4.7.3 Rate performance of tensile deformed PPL-metteries....101
4.8 Electrochemical-damage mechanics in tensile deformed PPL-metteries....103
4.8.1 Microstructures of tensile deformed electrodes and PPL electrolytes....103
4.8.2 Mechanism of Li-ion transport in tensile deformed PPL electrolyte....105
4.9 Summary....106
Chapter 5. Development of a quasi-solid-state PPL+FEC electrolyte to enhance the electrochemical performance of tensile deformed mettery....108
5.1 Introduction....108
5.2 Background....108
5.3 Experimental details....109
5.3.1 Fabrication of uniaxial tensile deformed PPL+FEC-metteries....109
5.3.2 Material characterisation....109

5.3.3 Electrochemical characterisations of tensile deformed PPL+FEC electrolytes 109
5.3.4 Electrochemical measurements of tensile deformed PPL+FEC-metteries.....109
5.4 Mechanism of Li-ion transport in PPL+FEC electrolyte 110
5.5 Electrochemical properties of PPL+FEC electrolytes with different FEC contents 110
5.6 Physicochemical characterization of PPL and PPL+FEC electrolytes 112
5.7 Electrochemical characterisations of tensile deformed PPL and PPL+FEC electrolytes....113
5.8 Effect of uniaxial tensile deformation on electrochemical performance of PPL+FEC-mettery 117
5.8.1 EIS of tensile deformed PPL+FEC-metteries.....117
5.8.2 Cycling performance of tensile deformed PPL+FEC-metteries.....118
5.8.3 Rate performance of tensile deformed PPL+FEC-metteries 121
5.9 Structural evolution of tensile deformed electrolytes and electrodes.....123
5.10 Summary.....127
Chapter 6. Conclusion and future works 127
6.1 Thesis review and conclusions.....127
6.2 Future work.....129
Appendix A: Developing mettery structural circuits enabling the interaction intelligence in conventional metal formed products 131
Appendix B: Developing mettery structural circuits enabling the logic intelligence in conventional metal formed products 133
Appendix C: Developing mettery structural circuits enabling the learning intelligence in conventional metal formed products 135
Reference 137

List of Figures

Figure 2-1 Renewable energy share of global electricity production (2011, 2016, 2021) [6, 7]. 20

Figure 2-2 Annual capacity additions of renewable energy sources [2]. 21

Figure 2-3 Hydropower energy generation system [9]. 21

Figure 2-4 Hydropower amount and its percentage of renewable electricity from 2016 to 2021 [6, 7]. 22

Figure 2-5 Energy mix for electricity production [2]. 22

Figure 2-6 Direct in-line full variable speed-controlled wind turbine with the generator connected to the electrical grid through a full-scale power converter [22]. 24

Figure 2-7 Comparison of offshore and onshore wind turbines. 25

Figure 2-8 Diagram of photovoltaic cell [32]. 26

Figure 2-9 Solar power installed capacity projections [34]. 27

Figure 2-10 2030 Renewable electricity share prediction. 28

Figure 2-11 2019 Renewable energy usage in buildings, industry & agriculture and transportation. .. 28

Figure 2-12 Share of renewable energy in transport from 2009 to 2019 [37]. 29

Figure 2-13 Raw materials breakdown for building 1 MW solar PV plant, 50 MW onshore wind plant, and 500 MW offshore wind plant [40]. 30

Figure 2-14 (a) Global EV sales and growth in the past decade and (b) EV sales and growth in Europe, China, Northern America, and other worldwide areas in 2020 and 2021 [41]. 31

Figure 2-15 Comparison of different rechargeable batteries. 32

Figure 2-16 Schematic of the charging process in LIBs. 33

Figure 2-17 Comparison of NCM and LFP LIBs. 33

Figure 2-18 Three typical formats of LIBs: pouch cell, cylindrical cell and prismatic cell. 34

Figure 2-19 The Comparison between the mass share of energy sources in an EV of TESLA MODEL S and a petrol car of HONDA CIVIC. 34

Figure 2-20 The comparison of the Celgard, PEO-based and PVDF-based electrolytes. 37

Figure 2-21 Schematic of hydrogen fuel cell. 38

Figure 2-22 Structural battery used in an EV [100]. 38

Figure 2-23 The first-generation DARPA Wasp micro-air vehicle showing custom structure-battery cells [105]. 39

Figure 2-24 Sandwich structural battery (a) Sandwich structure of a battery core bonded with two face skins and (b) assembled sandwich structural battery [106]. 40

Figure 2-25 (a) 3D schematic of MESC and (b) as-fabricated MESC coupon [104]. 40

Figure 2-26 (a) Flat laminate structural supercapacitor, (b) model car body, and (c) trunk lid with lit LED lights for Volvo S80 [114]. 41

Figure 2-27 Modelling schematic of an EV by using an original steel roof, an updated roof made from epoxy and carbon fibres and a multifunctional roof made from the structural battery [115]. 42

Figure 3-1 Reaction mechanism of the PPL electrolyte. 49

Figure 3-2 (a) FTIR spectra and (b) Raman spectra of LLZTO particles. 49

Figure 3-3 FTIR spectra of (a) PMHS, PVDF, PL, PPL electrolytes and (b) LLZTO nanoparticles, PMHS and the mixing suspension of LLZTO and PMHS. 50

Figure 3-4 Raman spectra of PVDF, PL and PPL electrolytes. 51

Figure 3-5 The colour difference in the precursor dispersions of PVDF, PL and PPL electrolytes. 51

Figure 3-6 Schematic Li-ion transport pathways and Li-ion desolvation mechanism in PL and PPL electrolytes. 52

Figure 3-7 MAS ^{6}Li solid-state NMR spectra of PVDF, PL and PPL electrolytes. 53

Figure 3-8 Calculated desolvation energy of Li-ions in (a) PVDF, (b) d-PVDF and (c) PVDF-PMHS by the DFT method. 54

Figure 3-9 Top-view SEM images of the (a) PVDF, (b) PL and (c) PPL electrolytes. 55

Figure 3-10 Cross-sectional SEM images of the (a) PVDF, (b) PL and (c) PPL electrolytes. 56

Figure 3-11 Inner structures of (a) PL and (b) PPL electrolytes characterised by the FIB-SEM technique. 56

Figure 3-12 EDS mapping of F, La and Si elements in the PPL electrolyte. 57

Figure 3-13 AFM images of the surface of (a) PVDF electrolyte, (b) PL electrolyte and (c) PPL electrolyte. 58

Figure 3-14 (a) Stress-strain curves of PVDF, PL and PPL electrolytes, (b) TGA curves of PVDF, PL and PPL electrolytes. 59

Figure 3-15 EIS plots of SS|SSE|SS coin cells by using (a) PPL (8:0.5:1), (b) PPL (8:1:1) and (c) PPL (8:2:1) electrolytes at different temperatures, (d) calculated ionic conductivities of PPL (8:0.5:1), PPL (8:1:1) and PPL (8:2:1) electrolytes at 25 °C. 60

Figure 3-16 (a) Arrhenius plots of the ionic conductivities and (b) calculated activation energy of PPL electrolytes with different PMHS weight ratios. 60

Figure 3-17 Electrochemical performance of PPL electrolytes with different PMHS weight ratios. (a) EIS plots, (b) rate performances, cycling performance and coulombic efficiency of NCM811|PPL|Li cells at (c) 0.5C and (d) 1C at 25 °C. 61

Figure 3-18 EIS plots of SS|SSE|SS coin cells by using (a) PVDF and (b) PL electrolytes at different temperatures, (c) calculated ionic conductivities of PVDF, PL and PPL electrolytes at 25 °C. 62

Figure 3-19 (a) Arrhenius plots of the ionic conductivities and (b) calculated activation energy of PVDF, PL and PPL electrolytes. 63

Figure 3-20 Li-ion transference number of PVDF, PL and PPL electrolytes. Chronoamperometry curves and corresponding EIS plots before and after the DC polarization of Li|SSE|Li symmetric cells by using (a) PVDF, (b) PL and (c) PPL electrolytes, (d) calculated Li-ion transference number of PVDF, PL and PPL electrolytes. 64

Figure 3-21 (a) LSV curves and (b) oxidation voltages of PVDF, PL and PPL electrolytes..... 64

Figure 3-22 Galvanostatic voltage profiles of the Li|SSE|Li symmetric cells at a current density of (a) 0.1 mA cm^{-2} and (b) 1 mA cm^{-2}, (c) CCD test of the Li|SSE|Li symmetric cells with PVDF, PL and PPL electrolytes at 25 °C. 66

Figure 3-23 CV profiles of NCM811|SSE|Li cells with (a) PVDF, (b) PL and (c) PPL as electrolytes. 67

Figure 3-24 (a) EIS plots and (b) rate performances of NCM811|SSE|Li cells with PVDF, PL and PPL electrolytes at 25 °C. 68

Figure 3-25 Charge-discharge profiles of NCM811|SSE|Li cells with (a) PVDF, (b) PL and (c) PPL electrolytes at different current densities at 25 °C. 68

Figure 3-26 Cycling performance and coulombic efficiency of NCM811|SSE|Li cells with PVDF, PL and PPL electrolytes at (a) 0.5C and (b) 2C at 25 °C. 69

Figure 3-27 Galvanostatic charge-discharge profiles of NCM811|SSE|Li cells with (a) PVDF, (b) PL and (c) PPL electrolytes at the current density of 1C..... 70

Figure 3-28 Cycling performance and coulombic efficiency of NCM811|SSE|Li cells with higher cathodic areal capacities of 1.6 mAh cm^{-2} by using PVDF, PL and PPL electrolytes at 0.2C at 25 °C. 71

Figure 3-29 Cycling performance and coulombic efficiency of NCM811|PPL|Li cell with high cathodic areal capacities of 3.1 mAh cm^{-2} at 0.1 at 25 °C. 71

Figure 3-30 Cycling performance and coulombic efficiency of NCM811|SSE|Li pouch cells with PVDF, PL and PPL electrolytes at 0.5 C at 25 °C. 72

Figure 3-31 Optical pictures of NCM811|PPL|Li solid-state pouch cells powering an LED under (a) normal, (b) folding and (c) cutting states. 72

Figure 3-32 Cycling performance of NCM811|PPL|Li cell at 0.1C at -20 °C. 73

Figure 3-33 SEM images of (a) PVDF, (b) PL and (c) PPL electrolytes after 100 cycles at 1C. 74

Figure 3-34 TEM images of CEI of cycled NCM cathodes by using (a) PVDF, (c) PL and (e) PPL electrolytes, TEM and FFT images of cycled NCM cathodes by using (b) PVDF, (d) PL and (f) PPL electrolytes after 100 cycles at 1C. 75

Figure 3-35 SEM images of cycled NCM811 cathodes by using (a) PVDF, (b) PL and (c) PPL electrolytes after 100 cycles at 1C. 76

Figure 3-36 SEM images of cycled Li anodes by using (a) PVDF, (b) PL and (c) PPL electrolytes after 100 cycles at 1C. 77

Figure 3-37 EIS plots of (a) NCM811|PVDF|Li, (b) NCM811|PL|Li and (c) NCM811|PPL|Li cells after 1st, 50th and 100th cycles. 78

Figure 3-38 EIS plots of (a) Li|PVDF|Li, (b) Li|PL|Li and (c) Li|PPL|Li cells before cycle and after 50th and 100th cycles. 79

Figure 3-39 XPS spectra for (a) C 1s, (b) F 1s, (c) N 1s, (d) S 2p and (e) Si 2p signals of NCM811 cathodes using PVDF, PL and PPL electrolytes after 100 cycles. 81

Figure 3-40 XPS spectra for (a) C 1s, (b) Si 2p, (c) S 2P and (d) N 1s signals of Li anodes using PVDF, PL and PPL electrolytes after 100 cycles. 82

Figure 3-41 ToF-SIMS depth profiling and the 3D reconstructed images of representative negative secondary ions of (a) NCO^-, (b) SO_2^-, (c) SiO_2^- and (d) CH_3SiO^- at the vicinity of Li anode surface. 84

Figure 4-1 Galvanostatic charge and discharge tests of plastic deformed PPL-metteries on the LAND system. 88

Figure 4-2 The sandwich architecture of the raw material of mettery. 89

Figure 4-3 (a, b) Optical photography of formable PPL electrolyte and (c) the raw material of PPL-mettery. 89

Figure 4-4 LED lighted by plastic deformed metteries. 90

Figure 4-5 LED lighted by (a) serial SC, (b) parallel SC and (c) hybrid SC assembled by V-shape metteries. 90

Figure 4-6 Metteries with various geometries manufactured by metal forming technologies. 91

Figure 4-7 (a) Bending deformed PPL-mettery formed by using three-point bending tool and (b) optical photography of bending deformed PPL-metteries with bend radius to mettery thickness ratio (R/t) of 4.30 (bend radius: 9.2 mm), 2.33 (bend radius: 5.0 mm), 1.77 (bend radius: 3.8 mm) and 1.00 (bending radius: 2.15 mm). 91

Figure 4-8 (a) EIS plots of bending deformed PPL-metteries with the equivalent circuit inside and (b) the effect of bending deformation on the impedance of PPL-metteries. 92

Figure 4-9 Cycling performance and coulombic efficiency of bending deformed PPL-metteries at a current density of (a) 1C and (b) 2C at 25°C. 93

Figure 4-10 Effect of bending deformation on the specific capacity of PPL-metteries at different cycles at the current densities of (a) 1C and (b) 2C at 25 °C. 94

Figure 4-11 Galvanostatic charge-discharge profiles of bending deformed PPL-metteries with R/t of (a) 4.3, (b) 2.33, (c) 1.77 and (d) 1 at the current density of 1C at 25 °C. 95

Figure 4-12 Rate performance of bending deformed PPL-metteries at 25 °C. 95

Figure 4-13 Experimental and modelling results for the effect of rate on the specific capacity of bending deformed PPL-metteries at 25 °C. 96

Figure 4-14 (a) Mettery formed by applying uniaxial tensile test and (b) the tensile deformed PPL-metteries with tensile strains of 0.5%, 5%, 10% and 15%. 97

Figure 4-15 Uniaxial tensile strain-stress curve of PPL-mettery. 97

Figure 4-16 (a) EIS plots of PPL-metteries formed by applying uniaxial tensile deformation with the equivalent circuit inside and (b) the effect of uniaxial tensile deformation on the impedance of PPL-metteries. 98

Figure 4-17 Cycling performance and coulombic efficiency of tensile deformed PPL-metteries at a current density of (a) 1C and (b) 2C at 25°C. 99

Figure 4-18 Effect of uniaxial tensile deformation on the specific capacity of PPL-metteries at 5th, 10th, 50th and 100th at a current density of (a) 1C and (b) 2C at 25 °C 100

Figure 4-19 Galvanostatic charge-discharge profiles of PPL-metteries formed by applying uniaxial tensile deformation with the tensile strains of (a) 0.5%, (b) 5%, (c) 10% and (d) 15% at 1C at 25 °C. 101

Figure 4-20 Rate performance of uniaxial tensile deformed PPL-metteries at 25 °C 102

Figure 4-21 Experimental and modelling results for the effect of current rate on the specific capacity of tensile deformed PPL-metteries. 102

Figure 4-22 SEM images of NCM811 cathodes with the tensile strains of 0.5%, 5%, 10% and 15%. 103

Figure 4-23 SEM images of Li-metal anodes with tensile strains of 0.5%, 5%, 10% and 15%. 104

Figure 4-24 SEM images of PPL solid-state electrolytes with tensile strains of 0.5%, 5%, 10% and 15%. 105

Figure 4-25 Li-ion transport mechanism in (a) intact PPL electrolyte and (b) PPL electrolyte with micro-cracks caused by uniaxial tensile deformation. 106

Figure 5-1 (a) EIS plots of SS|PPL+FEC(tensile strain of 0.5%)|SS metteries, (b) calculated ionic conductivities of PPL+FEC electrolytes (tensile strain of 0.5%) with FEC contents of 0.2, 0.5, 0.7 and 1 μL/cm^2 at 25°C 111

Figure 5-2 (a) EIS plots with the equivalent circuit inside and (b) impedance of PPL+FEC-metteries (tensile strain of 0.5%), (c) cycling performance of PPL+FEC-metteries (tensile strain of 0.5%) with FEC contents of 0.2, 0.5, 0.7 and 1 μL/cm^2 at 1C at 25°C. 112

Figure 5-3 FTIR spectra of the FEC, PPL and PPL+FEC electrolytes. 113

Figure 5-4 LSV curves of the PPL electrolyte and PPL+FEC electrolyte. 113

Figure 5-5 EIS plots of SS|SS metteries by using (a) PPL electrolytes and (b) PPL+FEC electrolytes with tensile strains of 0.5% and 15% at 25°C. 114

Figure 5-6 Arrhenius plots of the ionic conductivities of (a) PPL electrolytes and (b) PPL+FEC electrolytes with tensile strains of 0.5% and 15% 115

Figure 5-7 Li-ion transference number of PPL and PPL+FEC electrolytes (tensile strains of 0.5% and 15%). Chronoamperometry curves and corresponding EIS plots before and after the DC polarisation of Li|PPL|Li symmetric metteries with tensile strains of (a) 0.5% and (b) 15%, Li|PPL+FEC|Li symmetric metteries with tensile strains of (c) 0.5% and (d) 15%. 116

Figure 5-8 Voltage curves of (a) Li|PPL|Li and (b) Li|PPL+FEC|Li symmetric metteries with tensile strains of 0.5% and 15% at a current density of 0.1 mA cm^{-2} at 25 °C 117

Figure 5-9 (a) EIS plots with the equivalent circuit inside and (b) the effect of tensile deformation on the impedance of PPL+FEC-metteries with tensile strains of 0.5%, 5%, 10% and 15% formed by uniaxial tensile deformation. 118

Figure 5-10 Cycling performance and coulombic efficiency of tensile deformed PPL+FEC-metteries at a current density of (a) 1C and (b) 2C at 25°C. 119

Figure 5-11 Effect of uniaxial tensile deformation on the specific capacity of PPL+FEC-metteries at different cycles at a current density of (a) 1C and (b) 2C at 25°C. 120

Figure 5-12 Galvanostatic charge-discharge profiles of tensile deformed PPL+FEC-metteries with tensile strains of (a) 0.5%, (b) 5%, (c) 10% and (d) 15% at 1C at 25°C. 121

Figure 5-13 Rate performance of tensile deformed PPL+FEC-metteries at 25°C. 122

Figure 5-14 Experimental and modelling results for the effect of rate on the specific capacity of tensile deformed PPL+FEC-metteries at 25°C. 122

Figure 5-15 SEM images of cycled (a) PPL electrolytes and (b) PPL+FEC electrolytes in tensile deformed metteries with tensile strains of 0.5%, 10% and 15% after 100 cycles at 1C. 124

Figure 5-16 TEM images of CEI of cycled NCM cathodes in tensile deformed (a) PPL-metteries and (b) PPL+FEC-metteries with tensile strains of 0.5%, 10% and 15% after 100 cycles at 1C. 125

Figure 5-17 SEM images of cycled NCM cathodes in tensile deformed (a) PPL-metteries and (b) PPL+FEC-metteries with tensile strains of 0.5%, 10% and 15% after 100 cycles at 1C. 126

Figure 5-18 SEM images of cycled Li-metal anodes in tensile deformed (a) PPL-metteries and (b) PPL+FEC-metteries with tensile strains of 0.5%, 10% and 15% after 100 cycles at 1C. 127

Figure A-1 Open-circuit voltage of (a) A single mettery and (b) Serial SC and parallel SC..... 131

Figure A-2 Interaction intelligence realsed by built by a SC composed of two U-shape metteries. .. 132

Figure B-1 Logic gates characteristics enabled by three U-shape metteries..... 133

Figure B-2 Combination of multiple mettery logic gates (two OR Gates and one AND Gate). 134

Figure C-1 Meta-learning machinery assembled by four U-shape metteries..... 136

List of Tables

Table 2-1 Summary of different types of active inorganic fillers. 36
Table 4-1 Values of constants in equation (4). 96
Table 4-2 Values of constants in equation (5). 103
Table 5-1 Values of constants in equation (6). 123

List of publications

Peer-reviewed journal publications

1. **Xiangnan Yu**, Yuhai Jin, Heli Liu, Denis J. Politis, and Li-Liang Wang. Adding Value to Metal Components by Advancing Metal Forming Technology. To be submitted.

2. **Xiangnan Yu**, Liang Zhao, Yuhai Jin, Denis J. Politis, Yan-Bing He, Ming Liu, and Li-Liang Wang. Decoupling Ionic Conductivity and Ion-Solvent Complex Migration by Facilitating Desolvation Process in Composite Solid Electrolytes. To be submitted.

3. Liang Zhao, **Xiangnan Yu (Equal contribution)**, Junyu Jiao, Xin Song, Xing Cheng, Ming Liu, Li-liang Wang, Jiaxin Zheng, Wei Lv, Guiming Zhong, Yan-Bing He, and Feiyu Kang. (2023). Building cross-phase ion transport channels between ceramic and polymer for highly conductive composite solid-state electrolyte. *Cell Reports Physical Science*, *4*(5).

4. **Xiangnan Yu**, Yuhai Jin, Heli Liu, Arnav Rai, Michelle Kostin, Dimitrios Chantzis, Denis J. Politis, and Liliang Wang. (2022). A Review of Renewable Energy and Storage Technologies for Automotive Applications. *International Journal of Automotive Manufacturing and Materials,* 10-10.

5. **Xiangnan Yu**, Yang Jiang, Xiao Yang, Zhaoheng Cai, Yang Hua, Shichun Yang, Huizhi Wang, Xinhua Liu, and Liliang Wang. (2021). Dodecanethiol coated multi-walled carbon nanotube films as flexible current collector for lithium-ion batteries. *Materials Letters*, *291*, 129508.

6. Xiaochuan Liu, Bozhou Di, **Xiangnan Yu**, Heli Liu, Saksham Dhawan, Denis J Politis, Mateusz Kopec, and Liliang Wang. (2022). Development of a formability prediction model for aluminium sandwich panels with polymer core. *Materials*, *15*(12), 4140.

Patent

1. **Xiangnan Yu**, Yuhai Jin, Heli Liu, Zhaoheng Cai, Saksham Dhawan, Gang Wu, Mingqing Zhu, Jianguo Lin, and Liliang Wang, Mettery: a metal battery manufactured by metal forming technologies. Under review.

List of symbols and acronyms

AFM	Atomic force microscope
AMS	Anodic metal sheet
CAE	Computer-aided engineering
CAG	Carbon aerogel
CCD	Critical current density
CEI	Cathode electrolyte interphase
CF	Carbon fibre
CMS	Cathodic metal sheet
CSE	Composite solid electrolyte
CV	Cyclic voltammetry
DFT	Density functional theory
DMC	Dimethyl carbonate
DMF	N, N-dimethylformamide
d-PVDF	Dehydrofluorination of PVDF
E_a	Activation energy
EDS	X-ray energy dispersive spectrometer
EIS	Electrochemical impedance spectroscopy
EV	Electric vehicle
FEA	Finite element analysis
FEC	Fluoroethylene carbonate
FFT	Fast Fourier transform
FIB	Focused ion beam

FTIR	Fourier transform infrared spectroscopy
IEA	International Energy Agency
IRENA	International Renewable Energy Agency
LED	Light-emitting diode
LFP	Lithium iron phosphate
Li-ion	Lithium-ion
LIB	Lithium-ion batteries
LiFSI	Lithium bis(fluorosulfonyl)imide
$LiPF_6$	Lithium hexafluorophosphate
LLZTO	$Li_{6.4}La_3Zr_{1.4}Ta_{0.6}O_{12}$
LSV	Linear sweep voltammetry
MAS	Magic angle spinning (MAS)
MESC	Multifunctional energy storage composite
MoT	Mettery of Things
NCM811	$LiNi_{0.8}Co_{0.1}Mn_{0.1}O_2$
NMP	N-methyl-2-pyrrolidone
NMR	Nuclear magnetic resonance
OCV	Open circuit voltage
PAN	Polyacrylonitrile
PDMS	Polydimethylsiloxane
PEO	Poly(ethylene oxide)
PMHS	Polymethylhydrosiloxane
PVDF-PMHS	PMHS-grafted PVDF

PMMA	Polymethyl methacrylate
PL	PVDF-LLZTO composite solid electrolyte
PPL	PVDF-PMHS-LLZTO composite solid electrolyte
PPL+FEC-metteries	NCM811|PPL+FEC|Li metteries
PPL-metteries	NCM811|PPL|Li metteries
PV	Photovoltaic
PVDF	Poly(vinylidene fluoride)
QSE	Quasi-solid-state electrolyte
SC	Structural circuit
SEI	Solid electrolyte interphase
SEM	Scanning electron microscope
SPE	Solid polymer electrolyte
SS	Stainless steel
SSE	Solid-state electrolyte
SSLBs	Solid-state lithium batteries
TEGDME	Tetraethylene glycol dimethyl ether
TEM	Transmission electron microscopy
TGA	Thermogravimetry analysis
ToF-SIMS	Time-of-flight secondary ion mass spectrum
UTS	Ultimate tensile strength
XPS	X-ray photoelectron spectroscopy

Chapter 1. Introduction

1.1 Background

Inspired by the requirements of alleviating environmental contamination, exploring renewable energy integrated environmentally friendly and cost-effective energy storage technology with easily obtained materials that are able to be manufactured by a simple process is urgently demanded. Global society currently consumes 238 kg of steel and 8.2 kg of aluminium per person per year by transforming them into vehicles, equipment, buildings, and a variety of other goods, over 90% of which are produced, at the lowest cost, through plastic deformation of metals. Plastically deformed metals have supported the development and growth of society as the foundation of various industrial sectors. Driven by this, a new innovative 'mettery', which is a metal battery manufactured by metal forming technologies, has been proposed and developed. It combines the intrinsic mechanical property of the metal with the electrochemical property of the battery. The proposed mettery technology will, for the first time, enable electrical energy storage in metal components to provide a low-cost and large-scale electrical energy storage solution. In addition, the mettery can rely on renewable sources as supply sources, increasing drastically the duration and facilitating zero-pollution society.

With additional intrinsic intelligence characteristics, the mettery technology will potentially bring transformative and disruptive impacts on various industrial sectors supporting the transition to a zero-pollution society, through the proposed Mettery of Things (MoT). (1) MoT-transportation enables energy storage in the body panels and structural components of vehicles, trains, bikes, ships and aircraft/satellites, in combination with renewable energy, to achieve zero pollution MoT-transportation. This will fundamentally shift the existing knowledge of 'stand-alone centralized' storage to 'integrated distributed' storage. With the expectation of widespread adoption of future electric vehicles, electrical energy storage in the metal panels of the chassis will enable additional range extension and reduced battery pack size which have been limitations thus far. These mettery body panels will be formed by advanced metal forming technologies, performing structural and electrochemical energy storage tasks simultaneously. (2) MoT-industrial equipment enables metteries to be implemented into industrial facilities. For example, electrical motors could be powered by mettery structures without the need for traditional external power sources. Moreover, by utilising the feature of mettery-embodied sensing, the motor output can be simply controlled through the components' own structures, whilst enabling more advanced computer processing to be activated only for more complicated requirements. (3) MoT-construction enables distributed home energy storage (harvested from renewable energy) in the metal components in buildings, furniture and white goods etc. The inability to store and send power when required is regarded as one of the primary drawbacks of renewable energy. With metteries used in

multiple sectors of construction, the storage of renewable energy can reach an extensive scale. (4) MoT: Towards zero-emission society. New personal eco-systems towards the Zero-emission utopia will be realised through the low-cost decentralized energy storage in the MoTed personal utilities found in transportation, equipment and construction. MoT empowered 'Zero-emission utopia' will be scaled up leading to an accelerated and cost-effective transition to zero-pollution society.

1.2 Aims and objectives

Integrating appropriate energy storage into the power system plays an important role in reducing the variability and improving the reliability of renewable energy generation, which facilitates to relieve the greenhouse gas emissions and climate change. A formable metal battery (mettery), enabling electrical energy storage in conventional metal components, has been developed. The main aim of this research is to design and fabricate formable solid-state electrolytes (SSEs) used in mettery that can sustain plastic deformation and perform electrical energy storage function. In order to realise the aim, the research objectives were set as follows:

- Conduct a literature review of various means of production for renewable energy and energy storage technologies.
- Develop a formable solid polymer electrolyte (SPE) with high mechanical strength and ionic conductivity. Investigate the reaction mechanism, physicochemical characteristics, electrochemical characteristics and electrochemical performances of SPE by applying experimental characterisation techniques, including electrochemical testing (e.g., charge-discharge test, impedance test), diffraction, spectroscopic and microscopic methods. It is expected that fomed mettery by using dedicated SPE is able to stably charge-discharge cycle at room temperature.
- Study the effect of plastic deformation on the electrochemical performance of metteries. Apply electrochemical measurements to investigate the electrochemical performances of metteries with pure bending and uniaxial tension deformations, providing a basic foundation for the design of mettery in the future.
- Investigate the electrochemical-damage mechanics in plastic deformed mettery. Improve the electrochemical performance (including specific capacity, cycling stability and cycle life) of plastic deformed mettery by developing a formable quasi-solid-state electrolyte (QSE) with higher ionic conductivity and lithium-ion transference number.

Chapter 2. Literature review

2.1 Introduction

[1] The issue of climate change corresponding with rising greenhouse gas emissions is one of the most significant challenges faced by the world today. Global warming caused by human-related emissions has already seen catastrophic consequences through rising sea levels, extreme weather events, and more frequent wildfires and floods. Reducing greenhouse gas emissions to prevent further climate instability requires a rapid transition away from carbon-based fuels. Therefore, there is an incentive to explore renewable energy and energy storage technologies which can mitigate the rise in future greenhouse gas emissions.

As part of the present review, the renewable energy generation methods included were solar, wind, and hydroelectric power. These low-carbon resources were deemed as the most influential based on their significant contribution to the global energy mix [1] and their greater annual power capacity compared to other renewables [2].

Although energy generation is essential, the ability to store this energy is critical to the success of a renewable economy. At present, efficient energy storage presents numerous challenges and effective energy storage solutions are critical to further penetration of renewable assets such as solar and wind [3]. It is anticipated that increasing flexibility and stability of supply through storage will increase the utilisation of renewable power. This would facilitate a cost-effective transition away from fossil fuels.

In the present study, centralized energy storage technologies-specifically lithium-ion batteries (LIBs) are discussed since they are the most widely used battery storage technology. Moreover, demand for LIBs is expected to increase exponentially as the electric vehicle (EV) market expands, with projections suggesting a rise from 580 GWh in 2021 up to 9300 GWh in 2030 [4]. As an ideal alternative, distributed energy storage realised by embodied energy storage technology is also discussed. Although distributed energy storage technologies remain mostly in the research phase, they offer great potential to enable volume and mass savings, thus enhancing the efficiency of energy storage system in the future.

[1] This chapter is reproduced from the paper of the author: 'X. Yu *et al.*, A Review of Renewable Energy and Storage Technologies for Automotive Applications. *International Journal of Automotive Manufacturing and Materials*, 10-10 (2022).'

2.2 Overview of renewable energy

To address the impact of climate change, there has been substantial development and investment in technologies aimed at clean and renewable energy, including solar photovoltaic, geothermal, solar thermal, hydroelectric, biofuels and ocean power.

Among renewable technologies, hydropower accounts for the largest renewable energy source of electricity, generating more than all other renewable technologies combined [5]. Solar and wind sources have also been major contenders in the market due to commercial acceptance and technological maturity. As shown in Figure 2-1, the percentage of renewable energy in global electricity generation is growing from 20.3% in 2011 to 28.5% in 2021 [6, 7]. Hydroelectric, wind and solar energy are three major sources of renewable electricity generation.

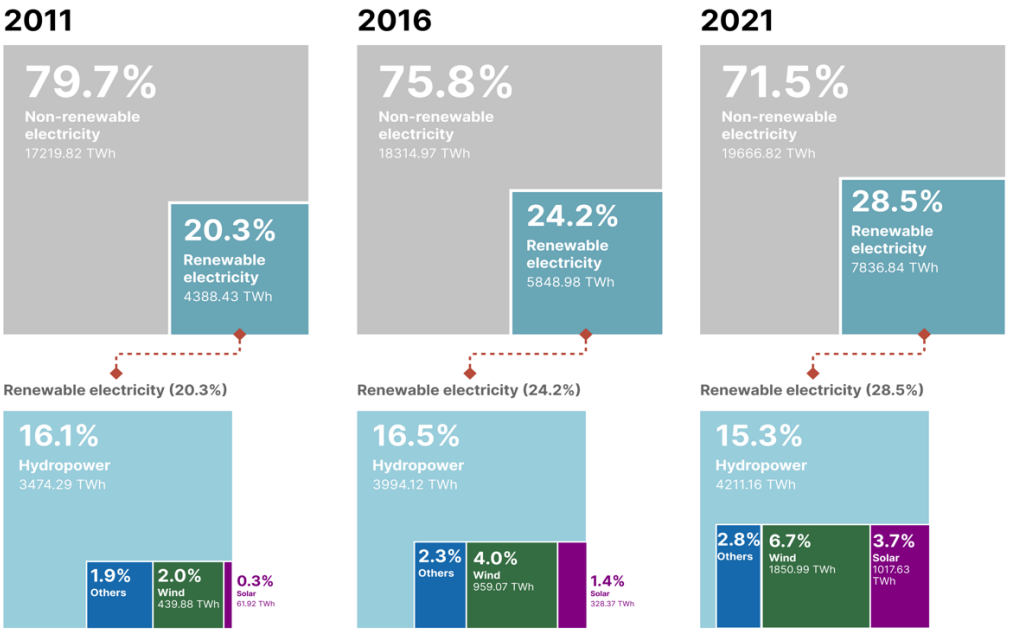


Figure 2-1 Renewable energy share of global electricity production (2011, 2016, 2021) [6, 7].

Besides, the capacity of these sources is growing at an ever-increasing rate as shown in Figure 2-2. In 2020, the total addition of renewable energy capacity was more than 256 GW, including 139 GW of solar power, 93 GW of wind power, and 20 GW of hydropower [2].

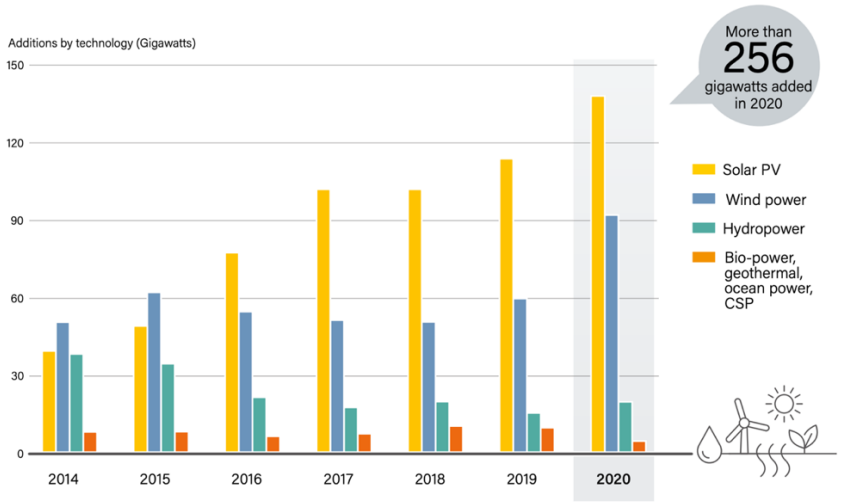


Figure 2-2 Annual capacity additions of renewable energy sources [2].

2.2.1 Hydroelectric energy

Hydroelectric generation is one of the most widely used and reliable renewable energy sources. It is generated by transferring water between two reservoirs at different heights through a turbine, as shown in Figure 2-3. The fast-flowing or falling water drives turbines at the end of its passage which is coupled to the rotor of an electrical generator [8]. A set of three-phase voltages are then induced in the stator of the electrical generator. Step up transformers are then used to increase the alternating voltage, making it more suitable for long-distance transmission.

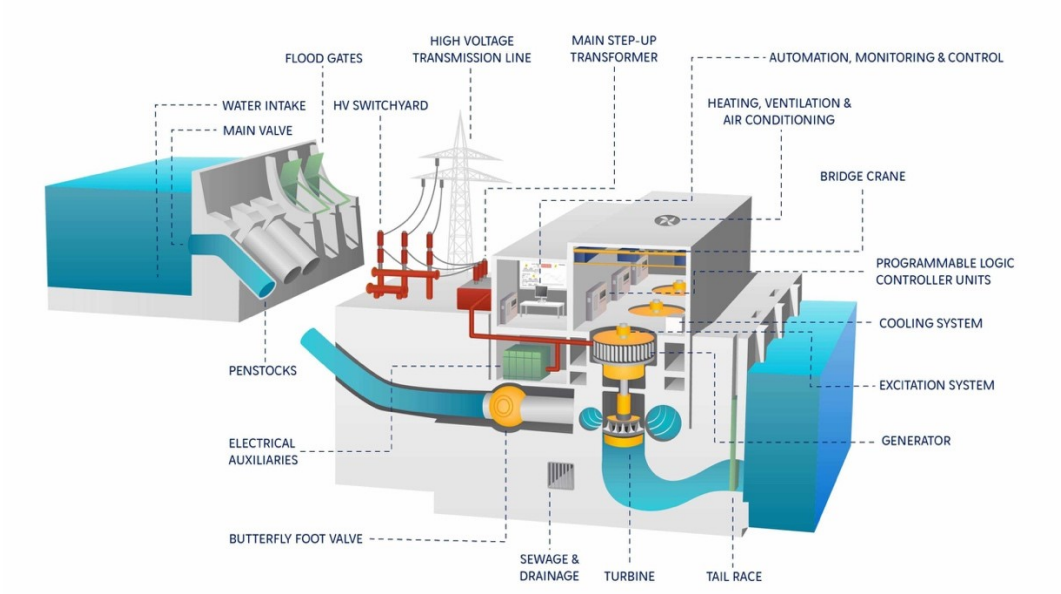


Figure 2-3 Hydropower energy generation system [9].

In 2020, the total installed capacity of hydroelectric power reached its greatest level, at an overall capacity of 4425.43 TWh [6, 7], which is approximately 60% of all renewable electricity generated [10].

As shown in Figure 2-4, from 2016 to 2021, hydroelectric power remained the largest renewable and still exceeded the energy from all other renewable electricity combined. However, solar and wind energy capacity has grown at a tremendous rate, where the percentage of hydropower in renewable electricity generation falling from 68.29% in 2016 to 53.74% in 2021.

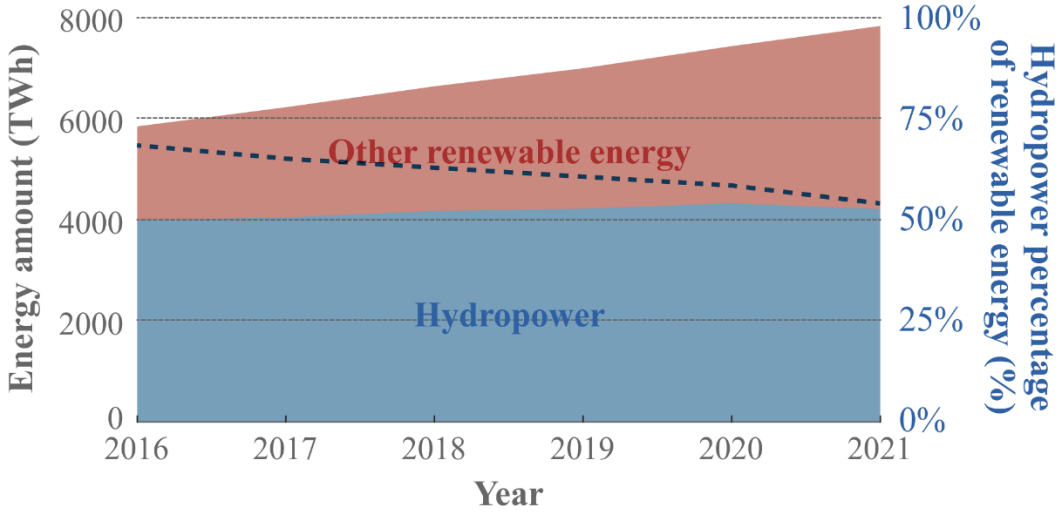


Figure 2-4 Hydropower amount and its percentage of renewable electricity from 2016 to 2021 [6, 7].

As also shown in Figure 2-5, the additional annual installed capacity for hydropower is considerably smaller than non-hydro renewables, specifically solar and wind energy. However, hydropower is still an important and vast renewable source. In 2020, electricity generated by using renewable energy was approximately 28% of the total electricity production, with hydropower being 16.8% of the world's total electricity generation.

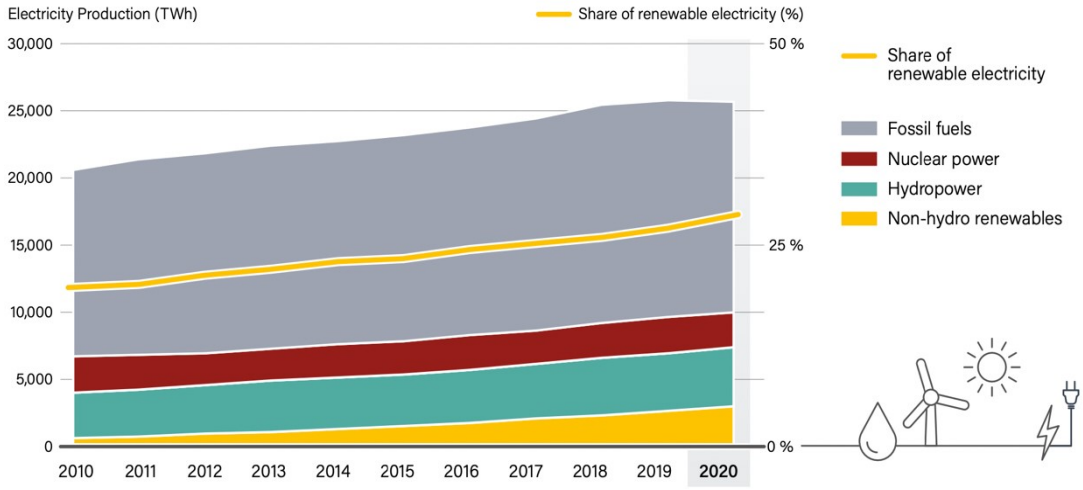


Figure 2-5 Energy mix for electricity production [2].

Unlike solar and wind energy, hydropower is not an intermittent resource and provides a constant power output. This leads to several advantages including the ability to provide ancillary services to the grid such as frequency regulation, which is vital for balancing energy supply and demand [11]. This will become increasingly important when managing future power networks with greater flexibility and more distributed electricity generation.

Many large-scale hydroelectric plants are currently in operation, such as the Three Gorges dam in China with a capacity of 22.5 GW, and Itaipu on the border between Brazil and Paraguay with a capacity of 14 GW. Possible reasons for the slower annual capacity addition of hydroelectric power compared to wind and solar could include its large capital cost and long lead times for construction. Furthermore, the construction of large-scale dams can have huge environmental and social impacts such as destroying wildlife habitats and displacing communities [12]. Creating artificial reservoirs traps vegetation under water, which decays and releases methane into the atmosphere. This counteracts the reduction in emissions associated with renewable resources since methane is a much more potent greenhouse gas than carbon dioxide, with a global warming potential 25 times larger [13].

Therefore, the future outlook of hydroelectric power is likely to include smaller-scale 'micro-hydropower' plants as discussed by Somani et al. [14], which have less of an environmental impact. Furthermore, pumped-hydro storage is a promising option to exploit the high conversion efficiency of hydroelectric power while minimising environmental impact. These plants make use of excess power generated during periods of low demand, to pump water to an upper reservoir. This can then be released to generate extra renewable electricity during high-demand periods. With a very high round-trip efficiency of 70-80%, it provides an effective form of energy storage, which could be used to provide regulation services to the grid.

2.2.2 Wind energy

In the last decade, the cost of producing wind energy has dropped by 56% [15]. In 2021, the current total capacity of wind energy has reached 743 GW globally, helping to reduce over 1.1 billion tonnes of CO_2 generation annually [16]. The growth is also reflected in the annual wind energy generation in 2020 of 1591 TWh-an increase of 360% compared to 2010 levels [17]. Projections indicate that this growth will continue, with 116 GW of installed capacity to be added to the existing 236 GW from 2022-2026 in Europe [18]. The fact that 93 GW of installed capacity was implemented globally in 2020 despite the COVID-19 pandemic demonstrates the incentive to pursue this option [2].

The distribution of wind energy varies with altitude. The generic height of wind turbines is 80 m where wind speeds are greater than 6.5 m/s [19]. High speeds are crucial as power is proportional to the cube of the velocity. From Betz Law, the theoretical maximum efficiency of a turbine is approximately 59%

with most turbines being able to extract only 50% that passes through the rotor [20]. The mechanical energy of the wind turbine is fed to the generator through a gear box that helps maintain the same speed for the synchronous generator. The output can then be fed into a Matrix or Z-source power converter. Most modern wind turbines have a horizontal axis with three rotors placed up wind of the nacelle, the main body that contains the gearbox, mechanical brake, control systems, yaw drive and generator.

Wind turbines can either be designed to operate at variable or fixed speeds. More effective power capture, up to 8-15%, is produced with variable speed generators as well as being more cost-effective noise-reduced and lighter designs [21]. As shown in Figure 2-6, a synchronous generator produces variable frequency AC power that is transformed into fixed frequency AC, ensuring a smooth grid connection.

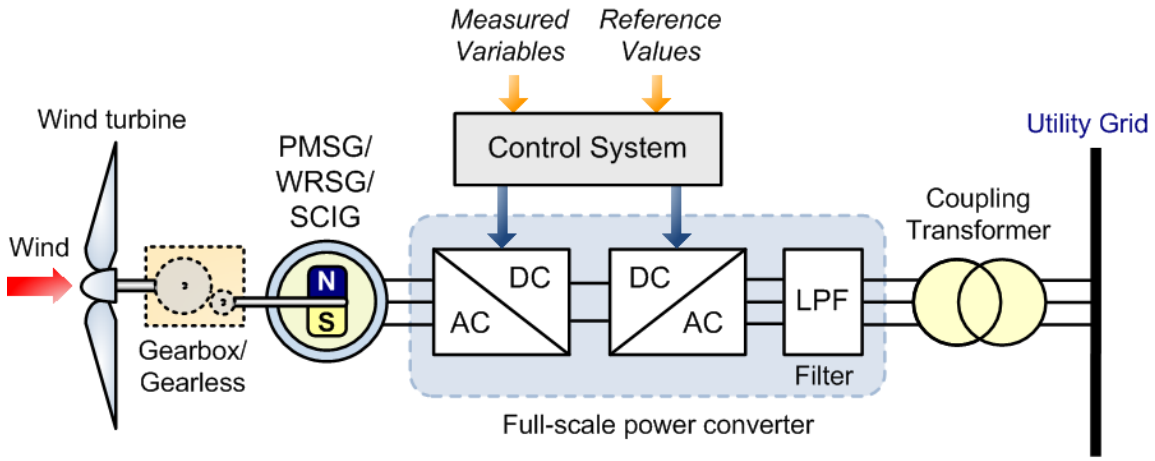


Figure 2-6 Direct in-line full variable speed-controlled wind turbine with the generator connected to the electrical grid through a full-scale power converter [22].

The two main categories for wind power in electricity generation are offshore and onshore. Onshore wind is the more established approach, holding a 95% share of the current global installed capacity of wind. However, European energy policies have driven uptake in offshore projects, with 26 offshore wind farms currently under construction [23]. Greater average wind speeds and a more regular supply are two significant advantages of offshore wind, as these lead to higher capacity factors and hence greater utilisation of the available wind energy. The capacity factor is a measure of the reliability of an energy resource, describing how much its output can be trusted. While the capital and operating costs for offshore wind are currently higher than onshore alternatives, the offshore potential energy generation is much greater [24], as shown in Figure 2-7.

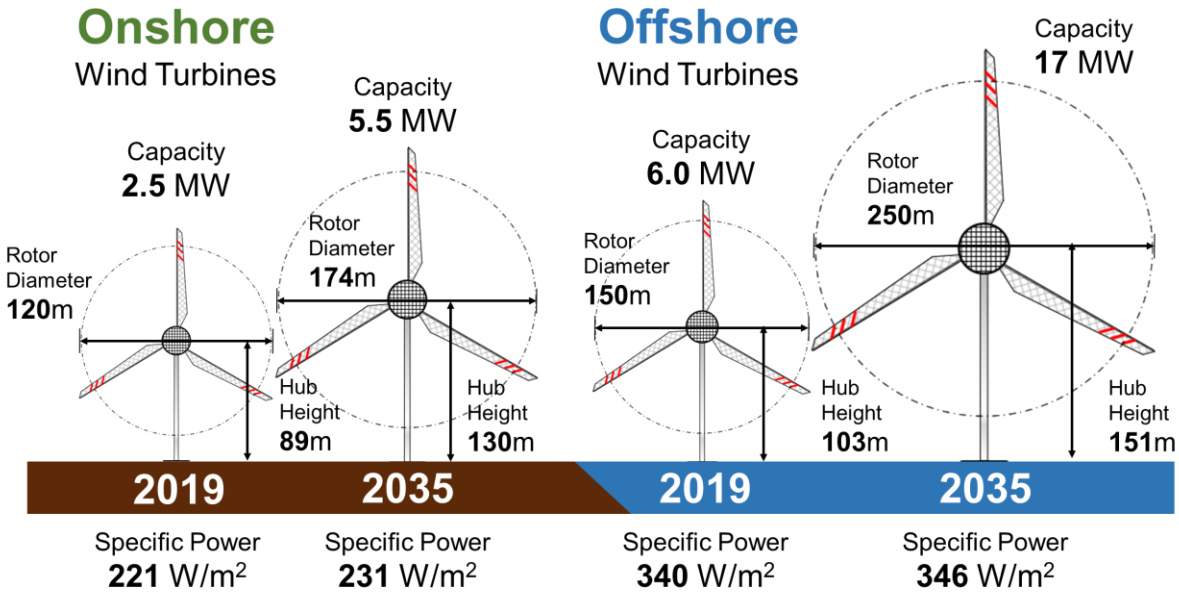


Figure 2-7 Comparison of offshore and onshore wind turbines.

In 2019, predictions indicate that offshore wind could provide 420,000 TWh annually-18 times greater than current global electricity demand [25]. Offshore farms allow for higher capacity wind turbines to be built, as there is no space constraint. This enables a larger rotor diameter for each turbine, increasing the swept area and therefore capturing more wind through which electricity can be generated as shown in Figure 2-7 [26]. The huge offshore potential could be further exploited through the recent development of floating wind farms. These remove the constraint of having to build farms close to shore where the seabed is shallow, allowing higher and steadier windspeeds at greater ocean depths to be accessed. It is estimated that 80% of the offshore wind potential could lie at ocean depths greater than 60 m, which would only be accessible through floating farms [27]. This concept has been explored further by Lathigara et al. [28].

The UK is the current world leader in offshore wind power generation, with the most installed capacity of any country and ambitious plans to power every home through offshore wind by 2030 [29]. As well as powering one million UK homes, the electricity produced is being used to generate renewable hydrogen through the Gigastack project. As part of this project, water is decomposed into hydrogen and oxygen through electrolysis, enabling carbon-free hydrogen to be collected [30]. This forms a key part of the UK energy strategy going forward as hydrogen can be used to target hard-to-abate sectors such as transport and industry, as explored further by Chapman et al [31].

2.2.3 Solar energy

Much like wind energy generation, the deployment of solar energy generation is rapidly increasing, driven by policy incentives and the pursuit of decarbonisation. Favourable economics and subsides have

increased interest in public investment into rooftop solar Photo-Voltaic systems, effectively eliminating demands for electricity from the grid.

The solar panels comprise many smaller photovoltaic cells, arranged in series, that are made of two semi-conductive layers, typically silicon or germanium, as shown in Figure 2-8. Each individual solar cell acts as a PN junction. The oppositely charged layers create an electric field and as photon particles hit the surface, the cell becomes energised causing freed electrons to shuttle in the circuit, creating an electrical current. For power appliances, an inverter is used for the conversion from DC to AC with any surplus AC going back to the grid.

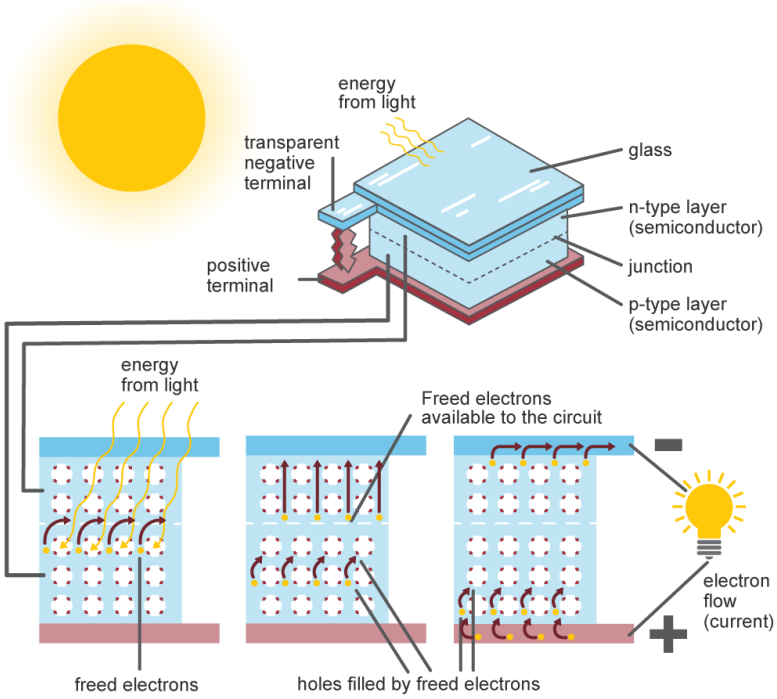


Figure 2-8 Diagram of photovoltaic cell [32].

The two main types of solar energy technologies are photovoltaic (PV) and solar-thermal. PV technology is used to directly convert solar irradiation into electricity. PV cells are made from semiconductor materials, and each individual cell with a standard size of 156 mm by 156 mm can produce 1-2 W of power. Therefore, individual cells are connected in series and parallel to form solar modules with greater overall power output. Modules can then be connected to form solar arrays which are used to supply electricity to the grid, or for distributed generation purposes. Solar-thermal technologies capture heat energy directly from solar irradiation, which can then be used to meet consumer heat demand through space and water heating appliances. The increased use of solar thermal as a low-carbon substitute for gas heating could therefore significantly reduce gas consumption and accelerate decarbonisation [33].

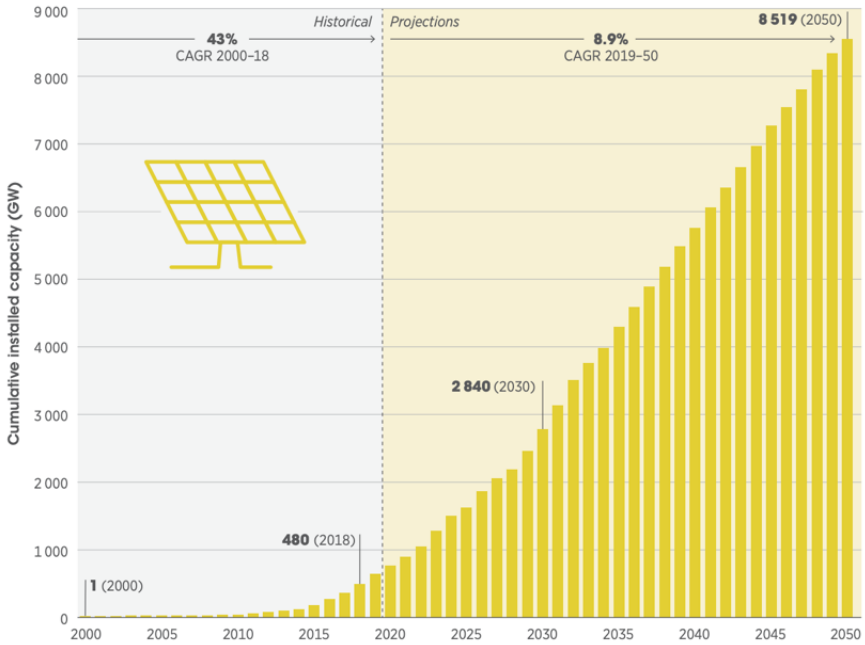


Figure 2-9 Solar power installed capacity projections [34].

From 2010 to 2020, the cost of producing solar energy using utility-scale solar photovoltaics (PV) has dropped by 85% [35]. The global installed capacity of solar photovoltaic (PV) power in 2021 was 760 GW, with an additional 139 GW being installed in 2020. This surpassed the growth of wind power in 2020 which saw only a 93 GW increase in installed capacity [2]. With the significant growth of installed solar energy capacity, the International Energy Agency (IEA) predicted an installed capacity of 1830 GW by 2026 [36], which is 2.4 times of that in 2021. According to the International Renewable Energy Agency (IRENA), the solar energy capacity has the potential to increase to 8519 GW (11.2 times that in 2021) by 2050 to meet the targets set out in the Paris Climate Agreement of 2015. The current installed capacity is shown in Figure 2-9 alongside the future projections.

2.2.4 Development and applications

Due to the significant growth rate of renewable energy generation, the proportion of renewable electricity in global electricity increased from 20.3% in 2011 to 28.5% in 2021, and it is predicted to achieve 60% in 2030, as shown in Figure 2-10 [7]. Following the IEA 1.5 degree pathway until 2030, total renewable electricity will increase by about 3 times, with solar energy increasing by 6.8 times and wind energy by 4.3 times [7].

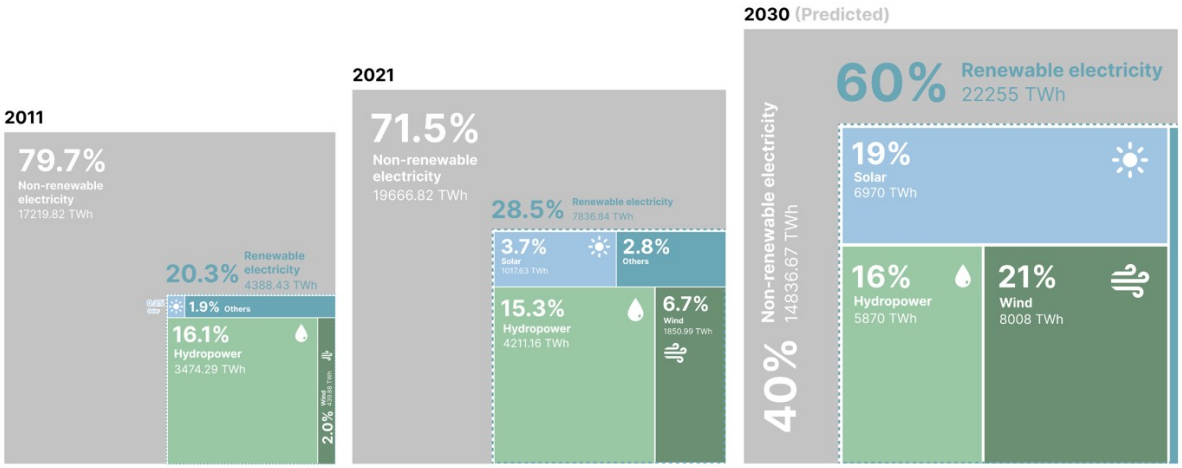


Figure 2-10 2030 Renewable electricity share prediction.

Although renewable energy is developing at a tremendous speed, the amount of usage is significantly lower than its availability. There are three main application sectors where renewable energy can make a substantial difference: buildings, industry & agriculture, and transport. Based on data in 2019, the proportion of renewable energy usage is 14.7% in buildings, 16.1% in industry & agriculture, and only 3.7% in transport [37]. The proportion of renewable electricity was 26.63% in 2019, but renewable energy usage was only 19.32%, as shown in Figure 2-11. One of the reasons behind the limited amount of renewable energy usage is its limitation in storage. Renewable energy could be wasted if there is no effective storage, and the energy stored will also be discounted due to storage efficiency. The inability to store and send power when required is regarded as one of the primary drawbacks of renewable energy [38].

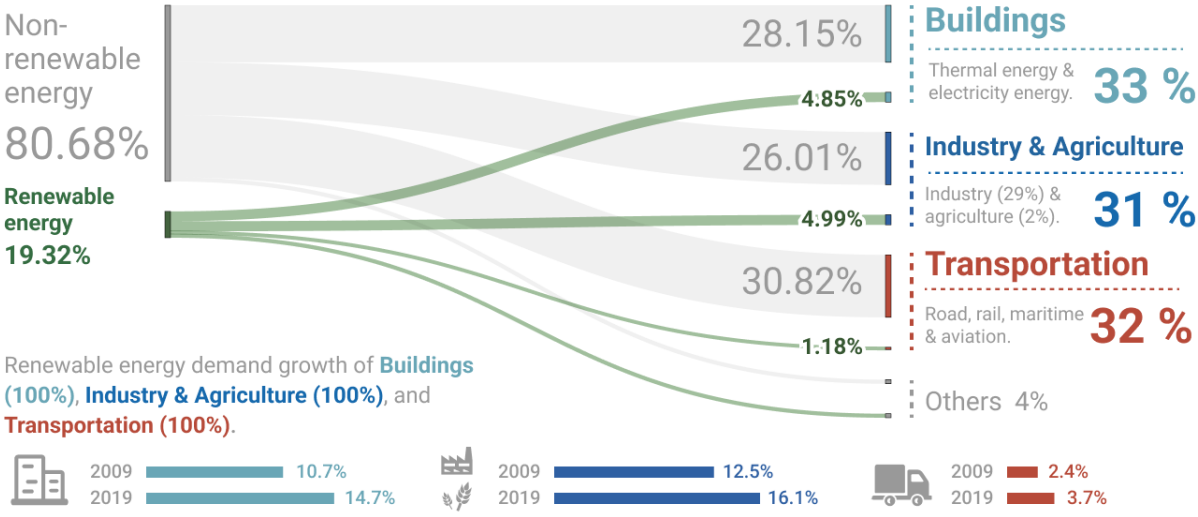


Figure 2-11 2019 Renewable energy usage in buildings, industry & agriculture and transportation.

Figure 2-12 shows a more detailed composition of energy usage in transport. From 2009 to 2019, the share of renewables used in transport increased from 2.4% to 3.7%, but the usage of renewable electricity increased from 0.2% to only 0.4%. By the end of 2019, 99.6% of transports are still using internal combustion engines [37]. With the encouragement of government policies and customer preferences, the EVs sales tripled between 2019 and 2021 [39]. However, fuels still have higher power densities than that of batteries, so a more effective energy storage technology needs to be developed to replace conventional internal combustion engines for more extensive renewable electricity usage in the transport sector.

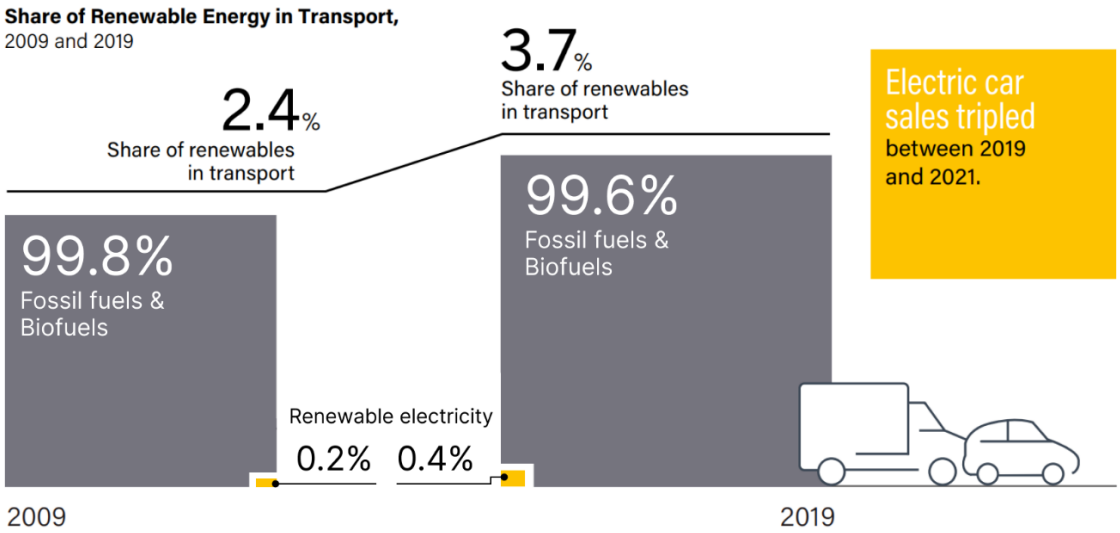


Figure 2-12 Share of renewable energy in transport from 2009 to 2019 [37].

2.2.5 Raw material demand for renewable energy sources

The development of renewable energy is also accompanied with raw material cost for building individual operating systems. Figure 2-13 shows the raw materials requirements for building a 1 MW solar PV plant, 50 MW onshore wind plant, and 500 MW offshore wind plant.

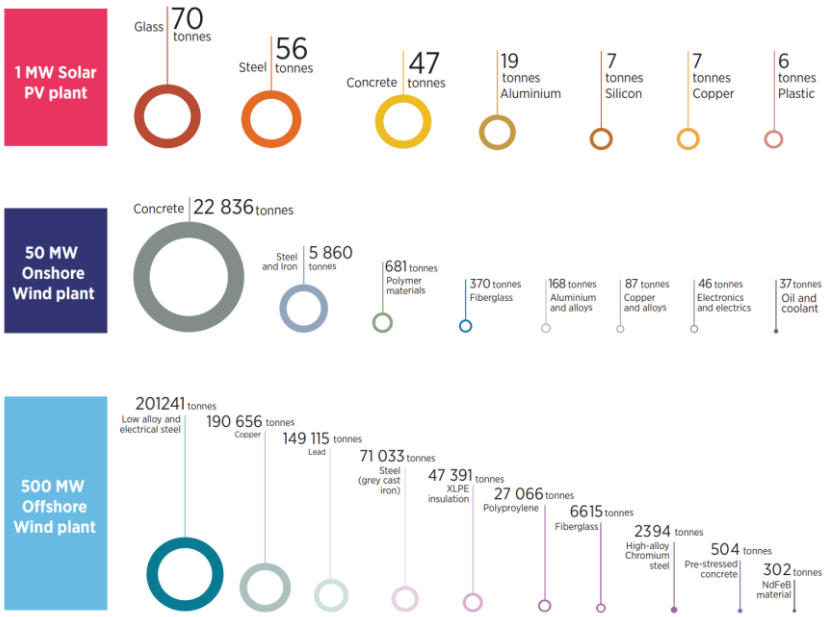
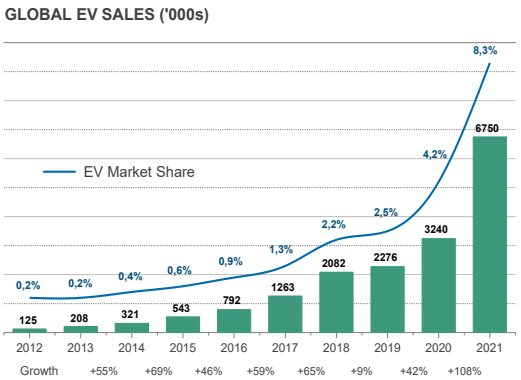


Figure 2-13 Raw materials breakdown for building 1 MW solar PV plant, 50 MW onshore wind plant, and 500 MW offshore wind plant [40].

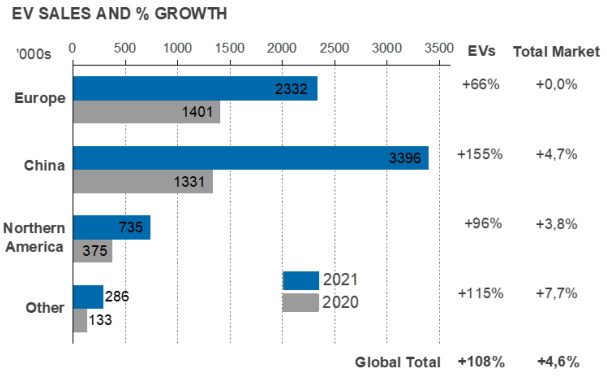
Although the renewable energy was developed for environmental-friendly purposes, the number and variety of raw material used in building power plants are larger than expected.

2.3 Centralized energy storage technologies realized by rechargeable batteries

With global EV sales dramatically growing in the past years (Figure 2-14) [41], environmentally friendly rechargeable batteries have attracted tremendous attention around the world. They convert chemical energy stored in their active materials into electrical energy, through reduction and oxidation reactions occurring at the interfaces between the electrode and the electrolyte.



(a)



(b)

Figure 2-14 (a) Global EV sales and growth in the past decade and (b) EV sales and growth in Europe, China, Northern America, and other worldwide areas in 2020 and 2021 [41].

2.3.1 Lead acid batteries

The Lead acid (Pb-acid) battery composes of lead oxide as a cathode, lead as an anode, and sulphuric acid as an electrolyte [42]. It was introduced in 1859 and has become the most used and cost-effective rechargeable battery around the world. Moreover, it shows high inherent safety [43], high electrochemical activity, long cycle life [44], low-temperature operation [45], and low self-discharge rates. However, the low energy density (30-50 Wh/kg) owing to the high weight of lead impedes the further development of Pb-batteries.

2.3.2 Nickel-metal hydride batteries

The nickel-metal hydride (Ni-MH) battery is the main contender in the group of alkaline batteries, in which the alkaline solution serves as an electrolyte. Nickel-cadmium (Ni-Cd) battery has been eliminated by the EV market because of the environmental issues caused by the toxic metal cadmium, lower energy density (~50 Wh/kg) and high cost. Nickel-zinc (Ni-Zn) battery also exhibits severe problems such as the fast growth of dendrites, leading to battery failure. In comparison, Ni-MH battery with higher energy density (60-120 Wh/kg) and lower cost has become a substitute for other alkaline batteries and has been applied in hybrid vehicle propulsion systems, since it was commercialized in 1989 [46].

A Ni-MH battery composes of metal hydride (MH) as a negative electrode, nickel hydroxide as a positive electrode and KOH as an alkaline electrolyte, allowing hydroxide ions to shuttle between the MH negative electrode and nickel hydroxide positive electrode [47]. In the Ni-MH battery, the alkaline electrolyte and lower-reactivity metals enable safety in operation at high voltage [48, 49]. Moreover, the Ni-MH battery has high power density, environmental compatibility, tolerance to overcharge and overdischarge, long cycle life and better low-temperature performance which enables EVs in cold climates [50, 51]. However, there still exist several problems such as high self-discharge and relatively low capacity compared to LIBs, hampering the development of Ni-MH batteries.

2.3.3 Lithium-ion batteries

Compared with other rechargeable batteries (Figure 2-15), lightweight lithium-ion batteries (LIBs) with high energy density (100-265 Wh/kg), stable cycling performance and long cycle life [52, 53] are currently considered one of the most ideal rechargeable batteries. The LIBs have been used in a wide range of applications, such as aircraft, electric vehicles, portable electronics (e.g. cell phones and laptops) and medical instruments etc.

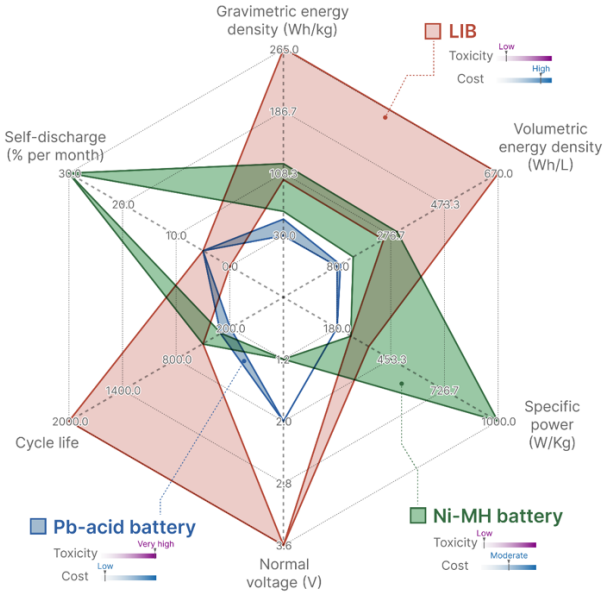


Figure 2-15 Comparison of different rechargeable batteries.

The primary components for a LIB involve electrodes (cathode and anode), electrolyte, separator, and packaging. For most LIBs, the cathode is composed of a positive current collector (aluminium foil) with lithium-oxide active material coated on it while the anode is composed of a negative current collector (copper foil) with graphite-based active material coated on it. To keep the cathode and anode in close proximity while fully separated to prevent short-circuiting, there is usually a separator soaked in a lithium-ion (Li-ion) conductive liquid electrolyte in between. Aluminium alloy, stainless steel or aluminium plastic seal are usually used as packaging. These components should be rationally assembled into a whole battery according to the basic principle of battery structural design. The structure of a LIB in a schematic diagram is shown in Figure 2-16. During the charging process, Li-ion de-intercalating from the cathode material transfers through the electrolyte to reach and intercalate into the anode material, while the electrons transfer from the cathode to the anode via an external circuit. When discharging, the movements of Li-ions and electrons are reversed. Cathode materials for conventional LIBs used are usually lithium nickel-rich oxide (NCM) and lithium iron phosphate (LFP), which can be charged to higher voltage when Li-ions are removed [54, 55]. Anode materials used in commercial LIBs involve graphite material and graphite incorporating silicon-based materials.

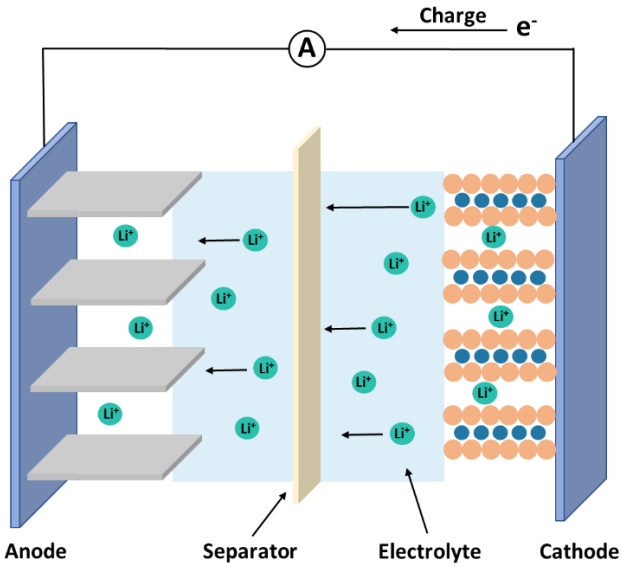


Figure 2-16 Schematic of the charging process in LIBs.

Figure 2-17 shows the comparison between NCM and LFP LIBs in terms of specific energy, specific power, cycle life, safety, cost and voltage. The NCM LIBs with high energy density due to high voltage and high cost due to the scare of cobalt and nickel, are expected to be used in high-end performance EVs. While LFP LIBs with lower cost and specific energy are expected to be used in buses and delivery trucks.

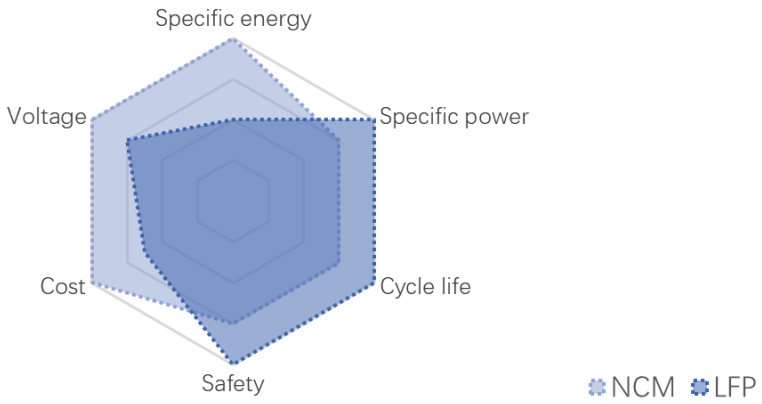


Figure 2-17 Comparison of NCM and LFP LIBs.

Regarding physical implementation, conventional LIBs are generally categorized into three typical formats, including pouch cells, cylindrical cells, and prismatic cells, as shown in Figure 2-18. Pouch cells with a relatively high specific energy, cycling performance, and safety have been growing in popularity in recent years. But they are costly and cannot be mass-produced on a large scale. Cylindrical cell with high capacity, long cycle life, and low cost is the most commonly used LIB format. However, the cylindrical cells cannot be densely stacked owing to space cavities, thus occupying more space in

devices. Prismatic cells possess a thinner size but are heavy, bulky, and concentrated, which delivers negative impacts on the driving range, storage space and dynamic handling. All these conventional LIBs remain with lots of accessories, increasing the inactive weight.



Figure 2-18 Three typical formats of LIBs: pouch cell, cylindrical cell and prismatic cell.

Moreover, LIBs as centralized monofunctional energy supplies remain isolated from the system. The LIB pack takes up nearly 30% of the total weight of a typical EV of TESLA MODEL S, while the fuel only takes up approximately 3% in a petrol-run car of HONDA CIVIC, as shown in Figure 2-19 [56, 57]. Therefore, exploring lightweight and efficient battery energy storage systems is urgently demanded.

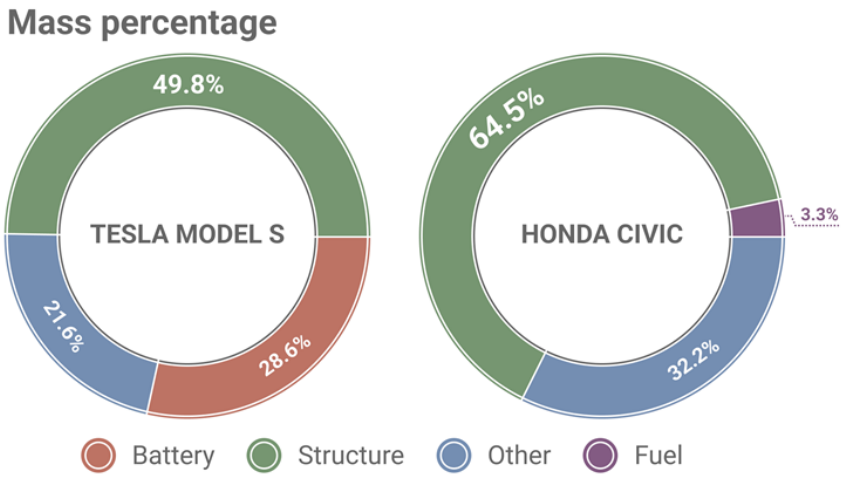


Figure 2-19 The Comparison between the mass share of energy sources in an EV of TESLA MODEL S and a petrol car of HONDA CIVIC.

Although extensive work has been performed on LIBs to minimize inactive weight [58], simplify fabrication procedures by using a full-automatic assembly line, including coating, stacking, welding and enclosing processes [59, 60] and optimize packaging by using the metal case with higher mechanical properties [61, 62], there have been only very few improvements over the past decade.

2.3.4 Solid-state lithium batteries

Solid-state lithium batteries (SSLBs) are considered the next generation high energy density LIBs due to the high specific capacity (3680 mAh/g) and low electrochemical potential of Li-metal anode [63]. However, the overgrowth of Li dendrites on the Li-metal anode easily penetrates the separator and thus leads to short circuits. To solve the safety issues caused by using the Li-metal anode and conventional liquid organic electrolyte with low thermal stability and low flame point [64-66], solid-state electrolytes with high mechanical and non-flammable properties are expected to be applied in EVs in the future. The SSLBs would significantly improve the energy density and at the same time, reduce fire accident explosions.

Solid-state electrolytes (SSEs) serve as the ion transport medium allowing efficient shuttling of Li-ions between cathode and anode while preventing short circuit between two electrodes during charge-discharge cycling. So far, a wide range of SSEs, including solid oxide electrolytes (e.g. NASICON-type [67, 68], garnet-type [69, 70] and perovskite-type [71, 72] et al.), solid sulfide electrolytes, solid polymer electrolytes (SPEs) such as poly(ethylene oxide) (PEO)-based electrolytes and poly(vinylidene fluoride) (PVDF)-based electrolytes, are being intensively studied [73-76].

SPEs exhibit outstanding flexibility, low cost and easier processability, which has received growing broad attention over the past decade. However, the low room temperature ionic conductivity fails to meet the practical utilization requirement. To improve their conductivity, tremendous works have been performed, including cross-linking [77], adding plasticizers [78-80], block copolymerizing [81, 82], exploring gel composite electrolytes [83, 84] and incorporating inorganic ceramic fillers. Among these efforts, introducing inorganic ceramic fillers into a polymer matrix to construct a composite solid electrolyte (CSE) has been demonstrated as an effective strategy for improving both the physicochemical and electrochemical performance of electrolytes. Inorganic ceramic fillers can be generally classified into active fillers and passive fillers. The active fillers possessing high ionic conductivity include various types of inorganic solid ceramic electrolytes (LISICON-type [85], NASICON-type [86], garnet-type [87, 88] and perovskite-type electrolytes [89]) and sulfide electrolytes [90]. The passive fillers without ionic conductivity themselves, such as metal oxide ceramics (Al_2O_3, SiO_2 and TiO_2 etc.) [91, 92], ferroelectric ceramics ($BaTiO_3$, $PbTiO_3$, $LiNbO_3$, etc.) [93], and natural clays, can enhance the ionic conductivity of polymer matrices. Comparatively, active fillers are able to provide efficient Li-ion transportation pathways and improve the both thermal stability and mechanical strength of the resulting CSE. The summary of different types of active fillers with respect to ionic conductivity, advantages and limits is shown in Table 2-1. In particular, garnet-type LLZTO as active inorganic fillers holds great potential to incorporate into polymer matrix for constructing desirable

performance CSE due to high mechanical strength, ionic conductivity and electrochemical oxidation voltage.

Table 2-1 Summary of different types of active inorganic fillers.

Type	Example	Conductivity, S cm^{-1}	Advantages	Limits
LISICON	$Li_{14}Zn(GeO_4)_4$	$10^{-5} \sim 10^{-3}$	High chemical stability, high mechanical strength and high oxidation potential	Costly for mass production
NASICON	LATP, LAGP	$10^{-5} \sim 10^{-3}$	High mechanical strength and high oxidation potential	Costly for mass production and incompatible with Li metal
Garnet	LLZO, LLZTO	$10^{-4} \sim 10^{-3}$	Higher ionic conductivity, high mechanical strength, compatibility with lithium metal, high oxidation potential and simple preparation condition	Poor stability in humidity
Perovskite	LLTO	$10^{-5} \sim 10^{-3}$	High mechanical strength and high oxidation potential	Costly for mass production, incompatible with Li-metal anode and high grain boundary resistance
Sulfide	$Li_3P_7S_{11}$, Li_6PS_5Cl, $Li_{10}GeP_2S_{12}$, Na_3PS_4	$10^{-7} \sim 10^{-2}$	High mechanical strength, high ionic conductivity and low grain boundary resistance	Low oxidation stability, unstable in air, unstable with lithium metal and costly for production

In terms of the polymer matrix, PEO has been extensively investigated to construct the SPEs and CSEs, own to high compatibility with Li-metal anode. However, PEO-based electrolytes with low ionic conductivity due to the high crystallinity of PEO chains at room temperature, high viscosity, and narrow voltage window hinder them from real application. Afterwards, many other types of polymer matrix, including polyvinylidene fluoride (PVDF), polyacrylonitrile (PAN), polymethyl methacrylate (PMMA) and polydimethylsiloxane (PDMS), have been explored to construct the SPEs and CSEs. Comparatively, as shown in Figure 2-20, PVDF-based electrolytes with the following advantages have attracted tremendous attention: (1) excellent mechanical strength; (2) high chemical stability, compatibility with cathode and anode materials; (3) high thermal stability with melting temperature up to 171 °C and decomposition temperature up to 400 °C, non-flammable; (4) wide voltage window up to 4.5 V and (5) easy processability.

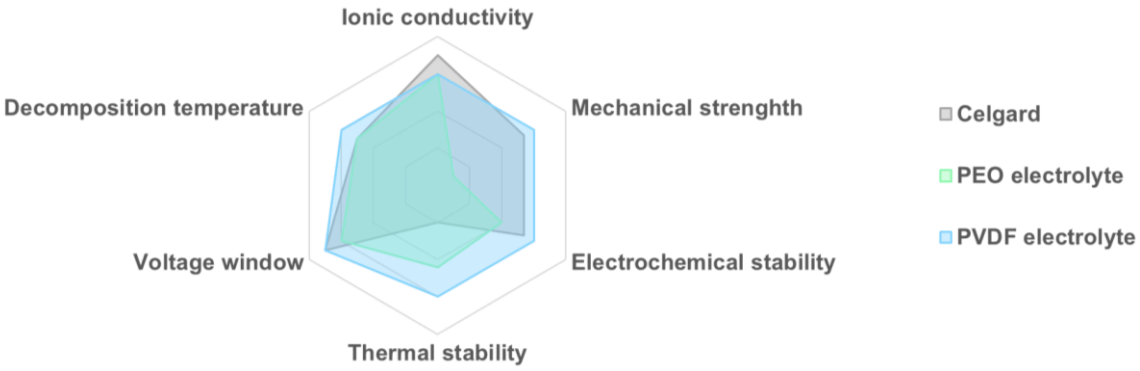


Figure 2-20 The comparison of the Celgard, PEO-based and PVDF-based electrolytes.

In summary, SSLBs, especially for SSLB with CSE, show great improvements in safety, mechanical properties and energy density compared to traditional liquid LIBs, which is promising to be used in real applications in the Future. However, the low ionic conductivity at room temperature (10^{-7}-10^{-4} S/cm) of it fails to meet the practical utilization requirement.

2.4 Centralized energy storage technologies realized by hydrogen fuel cells

The fuel cell is an electrochemical device that efficiently produces electricity from the chemical energy of hydrogens and other fuels by a pair of redox reactions. The schematic of a hydrogen fuel cell was shown in Figure 2-21. Hydrogen fuel cells have great potential for decarbonisation in the automotive industry since hydrogen can be produced from renewable energy sources [94, 95]. And the products in a hydrogen fuel cell are electricity, water, and small amounts of heat, causing negligible environmental impacts. However, the high cost of components in hydrogen fuel cells, including humidifiers, costly platinum catalyst, and heat exchangers, hinders their commercial advancement [96, 97]. Additionally, the challenge of hydrogen storage, transportation, and distribution is another barrier to real application [98]. More research efforts need to be devoted to addressing these challenges in the future.

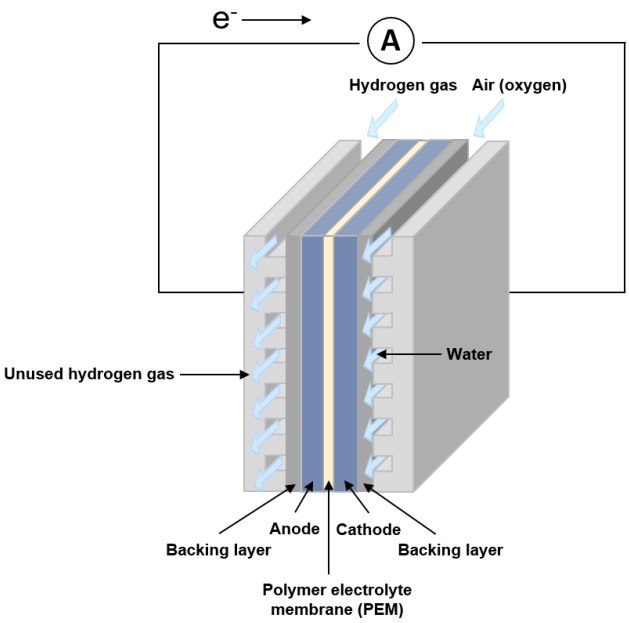


Figure 2-21 Schematic of hydrogen fuel cell.

2.5 Distributed energy storage realized by embodied energy storage technologies

Inspired by the requirement of lightweight production, distributed embodied energy storage technologies are being intensively explored. Embodied energy storage can be achieved by introducing structural power batteries and supercapacitors, which simultaneously enable electrical energy storage function and mechanical function [99]. This would promote the energy storage system toward lightweight and volume-saving development. More specifically, as shown in Figure 2-22, the future EVs are expected to have electrical energy storage function in the body metal panels, e.g. frames, roof, doors, chairs, and floor [100].

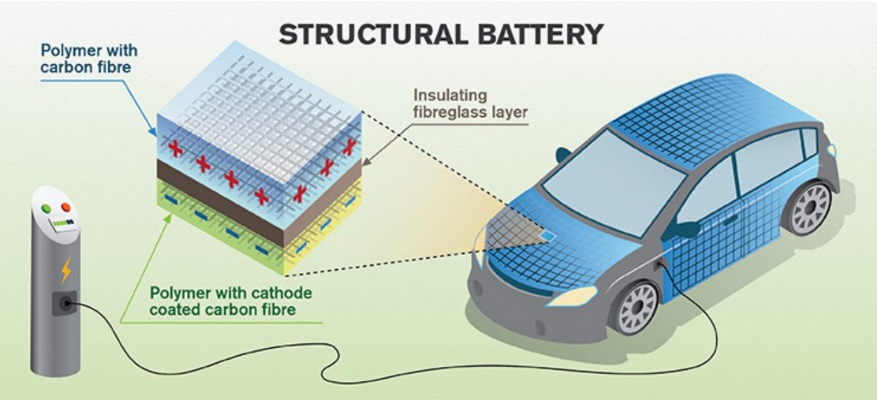


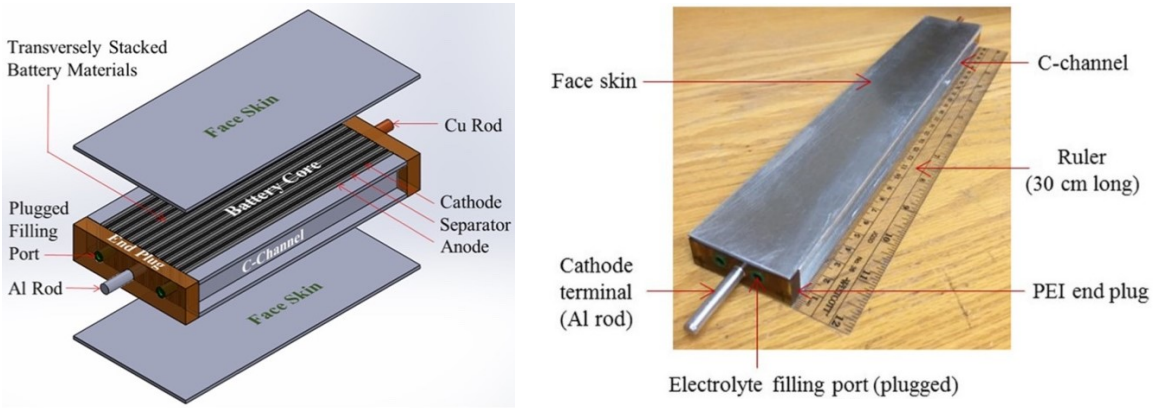
Figure 2-22 Structural battery used in an EV [100].

To date, two strategies have been reported to realize structural power batteries. One strategy is to embed a thin prismatic battery cell core into composite laminate skin panels (e.g. carbon fibre reinforced laminates), assembling a sandwich structure. This strategy enables electrochemical energy storage in a structural component. Numerous structural power batteries have been assembled by following this strategy [101-104]. A Wasp micro-air vehicle was developed by AeroVironment, Inc. [105]. Figure 2-23 shows the original prototype of Wasp. The four embedded structural polymer lithium-ion batteries were fabricated and used in wing skin. A record-setting flight endurance time of 107 minutes was achieved by this micro-air vehicle.



Figure 2-23 The first-generation DARPA Wasp micro-air vehicle showing custom structure-battery cells [105].

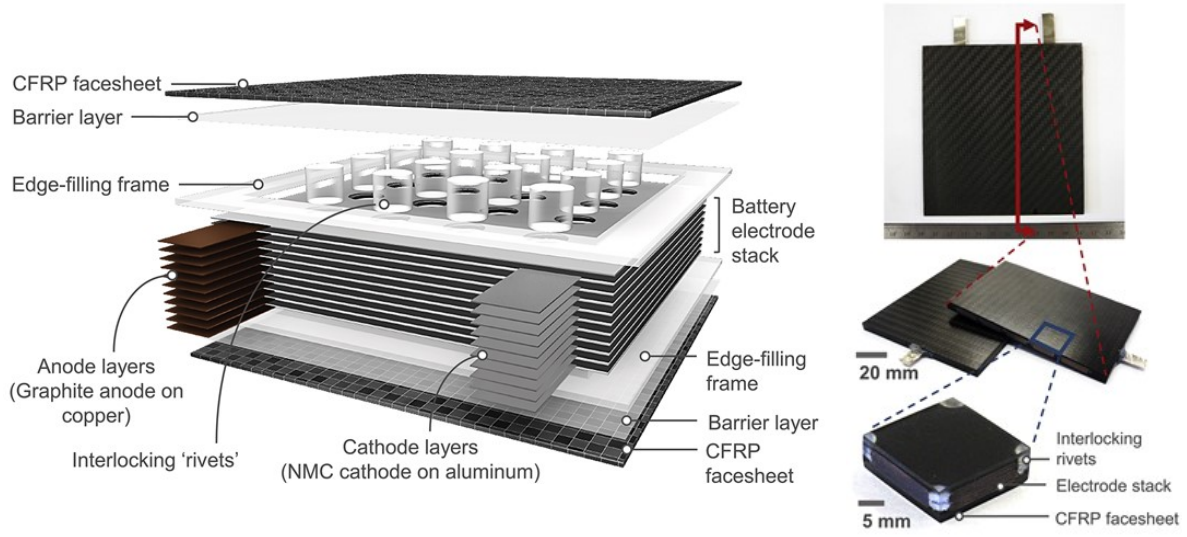
As shown in Figure 2-24, Zhang et al. [106] presented a multifunctional structural lithium-ion battery, using mesocarbon microbeads as the anode, $LiNi_{1/3}Co_{1/3}Mn_{1/3}O_2$ as the cathode and $LiPF_6$ as the electrolyte, in a sandwich panel architecture. It demonstrated an energy density of 248 Wh/L with a capacity retention of 85.9% after 190 cycles at ~C/3 rate and three-point bending tests at a load up to 1060 N.



(a) (b)

Figure 2-24 Sandwich structural battery (a) Sandwich structure of a battery core bonded with two face skins and (b) assembled sandwich structural battery [106].

Ladpli P et at. [104] developed a multifunctional energy storage composite (MESC) structure, in which the LIB was embedded in the carbon fibre composites by polymer rivets without any battery chemistry modifications, shown in Figure 2-25. However, this strategy provides only limited weight and volume reduction for the system. Meanwhile, the mechanical and electrochemical performances of such structural batteries still need to be enhanced. Although structural battery manufactured by this strategy exhibited higher energy density, it provides limited weight and volume reduction for the system, which has inspired the development of multifunctional structural battery composite materials to enhance the potential for weight reduction.



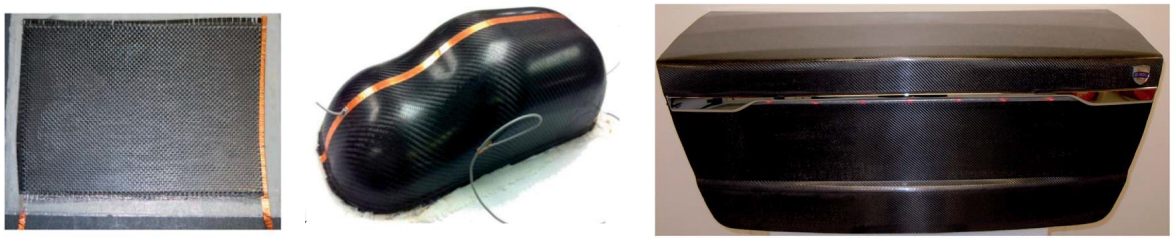
(a) (b)

Figure 2-25 (a) 3D schematic of MESC and (b) as-fabricated MESC coupon [104].

Developing multifunctional structural battery composite materials is an alternative strategy to achieve structural power batteries, in which all constituents concurrently perform multiple roles, including structural electrode composites, structural separator composite and structural electrolyte composite [57, 107-110]. In this case, the reinforcing carbon fibres employ as an electrode and the polymer composites serve as matrix and electrolyte. The first structural battery composite material was designed by Wong et al. [111]. The carbon fibre anode, $LiFePO_4$ deposited on a metal substrate as a cathode, glass fibre separator and a solvent-free structural vinyl ester polymer electrolyte matrix were employed in this design. The structural battery material delivered outstanding mechanical properties, however, fails to be characterised by electrochemical tests as a result of poor electronic insulation. Later, Ekstedt et al. [112] fabricated the structural battery composite materials based on carbon and aluminium fibre weave

electrodes, a glass fibre separator, and a gel electrolyte. This structural battery composed of Li_xC_6 and $LiFePO_4$ has an Open Cell Potential of 3.3 V. But it was not able to provide matching mechanical and electrochemical capacities compared with the conventional polymer composite and solid polymer electrolyte-based LIB respectively. Asp et al. [107] demonstrated a structural battery composite, consisting of a $LiFePO_4$ cathode and a carbon fibre (CF) anode separated by a glass fibre fabric separator in a structural battery electrolyte. It delivered an energy density of 24 Wh/kg at a current density of 0.05C with an elastic modulus of 25 GPa. To improve the electrochemical performance of the multifunctional structural battery, Moyer et al. [113] employed an electroconductive poly acrylonitrile (PAN) coating onto the surface of $LiFePO_4$ cathode and graphite anode with the CF current collectors to assemble a full-cell structural LIB. As-prepared PAN reinforced interfaces enhanced the mechanical adherence and ion transportation between battery active materials and CF current collectors. As a result, this Li-ion structural battery presented capacity retention of 80.5% over 100 charge-discharge cycles at a cycling rate of 0.1 C and achieved an average gravimetric energy density of 52 Wh/kg, which is approximately twice higher than a structural battery without PAN reinforced interface.

For practical application of embodied energy storage, Shaffer et al. [114] manufactured a structural supercapacitor by using carbon aerogel (CAG) modified structural carbon fibre (CF) fabric electrodes, which are separated by structural glass fibre fabric filled with a polymer electrolyte. A component of the car trunk lid was produced for a Volvo S80, in which LEDs were lightened by the structural supercapacitors, as shown in Figure 2-26.



(a) (b) (c)

Figure 2-26 (a) Flat laminate structural supercapacitor, (b) model car body, and (c) trunk lid with lit LED lights for Volvo S80 [114].

W Johannisson et al. [115] modelled and compared three roofs used in an EV made from mild steel, carbon fibre and epoxy composite, and a multifunctional structural battery. As shown in Figure 2-27, the roof made from the structural battery delivered a mass saving of 62% and 20% compared with the original steel roof and updated composite roof, respectively. Complementary, Asp et al. [116] presented three scenarios for Tesla Model S and the BMW i3, where the conventional monofunctional LIBs pack was fully or partially replaced by the structural battery composite. The modelling results illustrate that

a driving distance could increase by approximately 70% for the BMW i3 with maintained original vehicle weight by introducing the structural battery design.

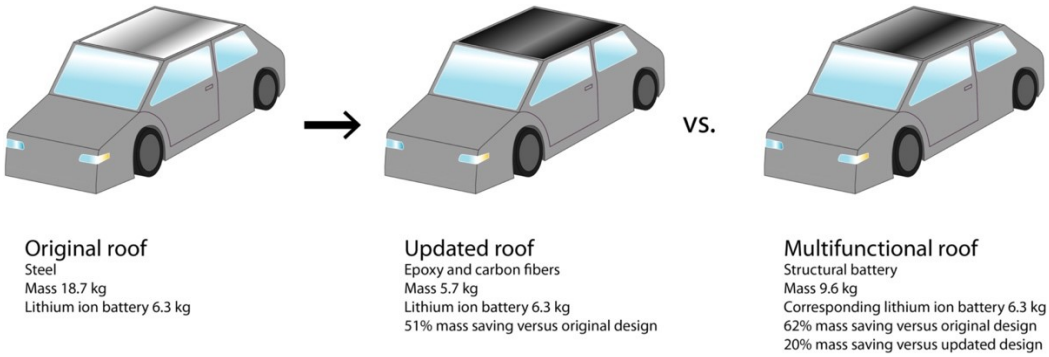


Figure 2-27 Modelling schematic of an EV by using an original steel roof, an updated roof made from epoxy and carbon fibres and a multifunctional roof made from the structural battery [115].

Different from monofunctional centralized energy storage which is independent of the vehicle's body, the distributed embodied energy storage technologies could perform structural component and electrochemical energy storage tasks at the same time, holding significant potential in mass and volume savings. Moreover, it offers more flexibility and convenience in the design and applications. However, despite great efforts that have been devoted to exploring structural power batteries and supercapacitors to date, there are still several existing challenges limiting its practical application. Further research for these embodied energy storage technologies is urgently needed in optimizing the manufacturing procedure to scale up and improve the energy density, specific power and cycle stability.

2.6 Summary

Renewable energy with appropriate energy storage technology is expected to mitigate climate change and environmental pollution around the world. Although conventional fossil fuel still contributes to approximately 70% of electricity and power generation today, with great potential and fast-development, extensive usage of renewable energy will be achieved by combining appropriate energy storage technology in the near future. This has triggered tremendous efforts to explore advanced energy storage technologies. As centralized energy storage, LIBs with high energy density and long cycle life have been growing popular. To further improve energy density and safety, solid-state Li-metal batteries are expected to be used in the future. On the other hand, the embodied energy storage that imultaneously achieves electrical energy storage and mechanical loads carrying functions has become an emerging research area. However, its electrochemical performance is limited which is equivalent to 5%-25% of that of LIBs, and it is difficult to scale up due to the difficult manufacturing process, hindering meeting the application requirement. Moreover, the relation between mechanical deformation and electrochemical performance, which is necessary for designing and optimising the embodied energy storage, is still not clear.

The futher research is needed to further explore energy storage with easily accessed material via an efficient production process. Also, it is important to conduct research on effects of mechanical deformation on electrochemical performance of embodied energy storage.

Chapter 3. Development of solid-state PPL electrolyte

3.1 Introduction

To successfully develop mettery, exploring a formable solid-state electrolyte (SSE) with a high mechanical strength and high ionic conductivity is essentail. Composite solid electrolytes (CSEs) with inherent structural elasticity and plasticity is considered the most promising candidate employed in mettery. However, the current CSEs still fail to meet the requirements for use in mettery. Although most of the CSEs are flexible, it is difficult for them to sustain plastic deformation due to non-formability. Furthermore, the synthesis of CSEs with high ionic conductivity and effective interface with the electrodes are still major challenges that needed to be overcome for the application in mettery.

A novel method to improve the ionic conductivity of PVDF-LLZTO (PL)-based CSE by decoupling the Li-ion transport from the migration of $[Li(DMF)_x]^+$ complex was carried out. Polymethylhydrosiloxane (PMHS) was introduced into the PL CSE, denoted as PPL CSE, by cross-linking with the PVDF matrix to facilitate the desolvation process of Li-ions from tightly bounded $[Li(DMF)_x]^+$ by the intermolecular interaction. This decouples Li-ion conduction from $[Li(DMF)_x]^+$ migration, achieving fast ceramic-involved Li-ion pathways in the CSE and a high ambient ionic conductivity. Moreover, the easy Li-ion desolvation at electrode/electrolyte interfaces could enhance the electrode kinetics and restrict the side reactions between DMF and electrodes. On the other hand, PMHS could work as a bridge to connect the PVDF and LLZTO, hence improving the mechanical strength of the PPL electrolyte. As a result, the as-prepared formable PPL electrolyte holds great potential to be applied in mettery.

3.2 Background

Solid-state lithium batteries (SSLBs) with SSEs as separators prevail over traditional liquid lithium batteries in safety and energy density due to their low flammability, reduced side reaction with Li-metal anode and the hindrance for Li dendrites penetration [117]. Among SSEs, inorganic electrolytes such as oxides (e.g. garnet-type $Li_7La_3Zr_2O_{12}$ [118] and perovskite-type $Li_{3x}La_{2/3-x}TiO_3$ [119]) and sulfides (e.g. argyrodite-type Li_6PS_5Cl [120]) exhibit desirable ambient ionic conductivities (10^{-4}-10^{-2} S cm^{-1}) but prominent interface issues with electrodes either due to their rigid contact or chemical/electrochemical compatibility. Instead, solid polymer electrolytes (SPEs) such as poly(ethylene oxide) (PEO) [121] and polyacrylonitrile (PAN) [122] with soft and ductile nature can form conformal contact with electrodes and are fully compatible with the existing roll-to-roll production process. However, the low ambient ionic conductivity (<10^{-5} S cm^{-1}) seriously limits its application. Incorporating inorganic fillers into SPEs to form CSEs can significantly improve their ionic

conductivity by (1) increasing amorphous regions and enhancing the segmental motion of polymers, (2) facilitating Li salt dissociation through the interaction with anions, and (3) creating additional Li-ion pathways along polymer/inorganic interfaces and through bulk inorganic fillers [123, 124].

The mechanism regarding Li-ion transport and the contributions from different components in CSEs have been investigated [125-131]. It is found that in most cases of CSEs, the improvement in ionic conductivity is mainly attributed to the fast Li-ion conduction along polymer/inorganic interfaces [129, 132]. Although the bulk inorganic fillers can be dominant in ion transport when their contents reach the percolation threshold, the ionic conductivity of CSEs is rather decreased due to the weak Li-ion conduction of loosely junctional inorganic fillers and the blockage of polymer pathways [125]. From this point of view, activating the Li-ion conduction of inorganic fillers in addition to interfaces at low to moderate filler contents may further improve the ion transport efficiency of CSEs. Introducing plasticizers [127, 131] and constructing ion transport channels between polymer and inorganic using coupling agents [133-135] have demonstrated effective strategies in enhancing the ionic conductivity of CSEs by lowering the energy barrier for Li-ion transport across the polymer/inorganic interface.

In recent years, polyvinylidene fluoride (PVDF)-based SSEs have attracted increasing attention due to their higher ionic conductivity (10^{-4} S cm^{-1}) compared with that of PEO or PAN-based SSEs [74, 136-139]. This is because a small amount of dimethylformamide (DMF) is trapped in the electrolytes and totally solvated with Li-ions to form $[Li(DMF)_x]^+$ complex, which enhances ion mobility through the polymer chains [140, 141]. Introducing inorganic fillers into PVDF electrolytes can also improve their ionic conductivity by forming PVDF/filler interfaces or facilitating Li salt dissociation[137, 138]. Nevertheless, the presence of DMF solvent makes it more complex to clarify the Li-ion transport mechanism, especially when it comes to the process regarding the desolvation of Li-DMF complex from the PVDF phase and the migration of naked Li-ions through the inorganic fillers. It was reported that in PVDF-$Li_{6.4}La_3Zr_{1.4}Ta_{0.6}O_{12}$ (LLZTO)-based CSEs, the bulk LLZTO fillers contributed negligibly to Li-ion conduction but solvated lithium ions-polymer was the dominant component [135]. A similar phenomenon was also observed in PEO-$Li_7La_3Zr_2O_{12}$-based CSEs, where the ceramic-dominant Li-ion pathways were converted to Li-solvent-PEO-dominant pathways after introducing tetraethylene glycol dimethyl ether (TEGDME) as a plasticizer [125, 127]. Therefore, it is reasonable to assume that during the Li-ion journey in such CSEs, the desolvation of Li-ions, a necessary process before passing through bulk inorganic fillers, requires a higher activation energy than that for Li-solvent complex transport through the polymer phase. This results in a large difficulty for inorganic fillers participating in Li-ion conduction, which limits the further improvement in the ionic conductivity of CSEs. From this point of view, reducing the Li-ion desolvation energy from $[Li(DMF)_x]^+$ complex in

PVDF-based CSEs to activate the conduction of inorganic fillers is by no means trivial, as it could improve the ionic conductivity of the CSEs by facilitating high-efficiency multipath Li-ion transport.

3.3 Experimental details

3.3.1 Preparation of PVDF-based SSEs

The PPL electrolyte was fabricated by a solution-casting method. Specifically, 50 mg LLZTO (D_{50}=500 nm, Zhejiang FunLithium New Energy Technology Co., Ltd.), 267 mg LiFSI (Tinci Materials Technology Co., Ltd.) were first dissolved in 15 mL DMF solvent and stirred at 45 °C for 30 minutes. After that, 50 mg PMHS (M_w=1900, Alfa) was added to the dispersion and stirred for 1 h, and 400 mg PVDF (M_w=300,000, Arkema, Kynar 761) was then added and stirred for 6 h to obtain a homogeneous dispersion. The as-obtained dispersion was poured into a clean glass mold and further dried at 55 °C oven for 24 h to remove the free DMF solvent. Finally, the obtained PPL electrolyte membrane was stored in an Ar-filled glove box for 24 h before use. Similarly, the PVDF and PL electrolytes were also prepared using the above method.

3.3.2 Material characterisation

The Fourier transform infrared (FTIR) was conducted on VERTEX 70 spectrometer in an attenuated total reflection (ATR) mode and the Raman spectra were collected on Horiba LabRAM HR800 using a 785 nm incident radiation. The morphology and microstructure of the PVDF, PL and PPL electrolytes were characterized by field-emission SEM (HITACHI SU8010) equipped with energy-dispersive spectral (EDS) for elemental analysis. The mechanical properties were tested by a Zwick stretch testing machine at a stretching speed of 1 mm S^{-1}. The thermal properties of SPEs were investigated by thermogravimetry analysis (TGA) that was performed under a nitrogen (N_2) atmosphere at a heating rate of 5 °C min^{-1} with an instrument (TA TGA-Q500). The roughness of the sample surfaces was measured by Atomic Force Microscope (AFM) (Bruker Dimension Ico). The X-ray photoelectron spectroscopy (XPS) was collected on PHI 5000 Versaprobe II using Al Kα 1486.6 eV radiation. TEM (FEI Tecnai F30) was used to characterise the cathode electrolyte interfaces (CEI) and structural phase transition of NCM811 cathodes. The time-of-flight secondary ion mass spectrum (ToF-SIMS) was carried out on a Nano TOF 2 instrument (ULVAC- PHI, Japan) equipped with a 30 keV Bi primary ion beam (data acquisition area 100×100 μm) and 3keV Ar sputter ion beam (sputter area 400×400 μm). The sputtering rate was 0.3 nm s^{-1} for SiO_2 standard sample. The solid-state ^{6}Li nuclear magnetic resonance (NMR) measurement was performed on a Bruker 400 MHz AVANCE III spectrometer with 5.5 μs 90° pulse length and spinning frequency of 12 kHz (1 M LiCl solution as reference).

3.3.3 Density functional theory (DFT) calculation

The stable structure of $Li(DMF)_3^+$, $Li(DMF)_2^+$, DMF, PVDF($(CH2CF2)_8$ chain), d-PVDF, PMHS, and d-PVDF-PMHS molecules were optimized by the quantum chemistry calculation with the GAUSSIAN 16 software package with a basis set of b3lyp/6-311++G(d, p). The desolvation energy of $Li(DMF)_3^+$ to $Li(DMF)_2^+$ and DMF molecule in PVDF, d-PVDF and d-PVDF-PMHS as defined as follows:

$$\mathrm{E}_{desol} = E_{Li(\mathrm{DMF})_2{}^+@\mathrm{PVDF/d-PVDF/d-PVDF-PMHS}} + E_{DMF} - E_{Li(\mathrm{DMF})_3{}^+@\mathrm{PVDF/d-PVDF/d-PVDF-PMHS}}$$

Where $\mathrm{E}_{desol} = E_{Li(\mathrm{DMF})_2{}^+@\mathrm{PVDF/d-PVDF/d-PVDF-PMHS}}$ and $E_{DMF} - E_{Li(\mathrm{DMF})_3{}^+@\mathrm{PVDF/d-PVDF/d-PVDF-PMHS}}$ were the energy of the Li-DMF complex in PVDF, d-PVDF and d-PVDF-PMHS and obtained by the quantum chemistry calculation under the same calculation conditions.

3.3.4 Electrochemical measurements of PVDF-based SSEs by coin cells

Electrochemical impedance spectroscopy (EIS) was recorded at a frequency ranging from 5 MHz to 100 mHz with an electrochemical workstation (Biologic VMP-3) at 25 °C. The ionic conductivity (σ) was characterized by stainless steel (SS)|SSE|SS sandwich coin cells. It was calculated according to the following equation (1):

$$\sigma_{Li^+} = \frac{L}{RS} \tag{1}$$

where $\sigma_{(Li+)}$ (S cm^{-1}) is the ionic conductivity of the SSEs, L (cm) is the thickness of the SSEs, R (Ω) is the bulk resistance and S (cm^2) is the area of the SS.

The activation energy (E_a) of SSEs was calculated according to the Arrhenius formula which describes the relationship between temperature and ionic conductivity (2):

$$\sigma_{Li^+} = A\exp\left(-\frac{E_a}{RT}\right) \tag{2}$$

Where A is a pre-exponential factor, T is the absolute temperature (K) and R is the universal gas constant (J K^{-1} mol^{-1}).

The Li-ion transference number (t_{Li+}) was measured by applying a DC polarized voltage (△V=10 mV) for 5000 s on Li|SSE|Li symmetric cells and testing the impedance before and after the polarization, as illustrated in the following equation (3):

$$t_{Li^+} = \frac{I_S(\triangle V - I_0R_0)}{I_0(\triangle V - I_SR_S)} \tag{3}$$

where I_0 and I_S are the initial and steady-state current response before and after the polarisation, respectively, R_0 and R_S are the initial and steady-state interfacial impedance of symmetrical Li|SSE|Li cell before and after the polarisation, respectively, and $\triangle V$ is the applied polarised potential.

The electrochemical stability window of SSEs was investigated by linear sweep voltammetry (LSV) method using a Li|SSE|SS cell with the electrochemical workstation over a voltage range of 0-6 V at a scan rate of 0.5 mV s^{-1} at 25 °C. The cyclic voltammetry (CV) measurements were conducted between 2.8 and 4.3 V at a scan rate of 0.1 mV s^{-1}.

The cathode was prepared by dispersing single crystal $LiNi_{0.8}Co_{0.1}Mn_{0.1}O_2$ (NCM811), super P and PVDF5130 (weight ratio of 8:1:1) in N-methyl-2-pyrrolidone (NMP) followed by a blade casting process on Al foil and then dried at 80 ℃ for 10 h. The general mass loading of NCM811 electrode was around 1 mg cm^{-2}. The CR2032-type coin cells were assembled with the NCM811 cathode, Li-metal anode, and PVDF-based SSEs in an Ar-filled glove box (O_2 < 0.5 ppm, H_2O < 0.5 ppm). Galvanostatic charge and discharge tests were carried out on the LAND system with a voltage ranging from 2.8 to 4.3 V at 25 °C. For the high mass loading test, the active material loadings of the NCM cathode were approximately 8.5 mg cm^{-2} and 18.1 mg cm^{-2}.

3.4 Reaction mechanism in the PPL electrolyte

In the as-developed PPL electrolyte, PVDF worked as a polymer matrix, LLZTO as the active inorganic ceramic filler and PMHS as an additive cross-linked with the PVDF matrix. Figure 3-1 illustrates the reaction mechanism of the PPL electrolyte. During the preparation of the PL electrolyte, the residual LiOH as Lewis bases on the surface of LLZTO particles could trigger partial dehydrofluorination of PVDF (d-PVDF) chains in the DMF solvent to form C=C double bonds on PVDF chains. Subsequently, C=C double bonds of d-PVDF would react with the Si-H group of PMHS by hydrosilylation reaction, forming PMHS-grafted PVDF (PVDF-PMHS) backbones with a Si-C chemical bonding. In addition, the hydrogen bond is generated between the Si-O of PMHS and O-H of LiOH which is on the surface of LLZTO. In this way, PMHS acts as a bridge to strongly connect the PVDF and LLZTO, thus effectively reducing the interface impedance and facilitating Li-ion transport between the organic PVDF matrix and inorganic LLZTO ceramic filler, further improving mechanical strength and ionic conductivity.

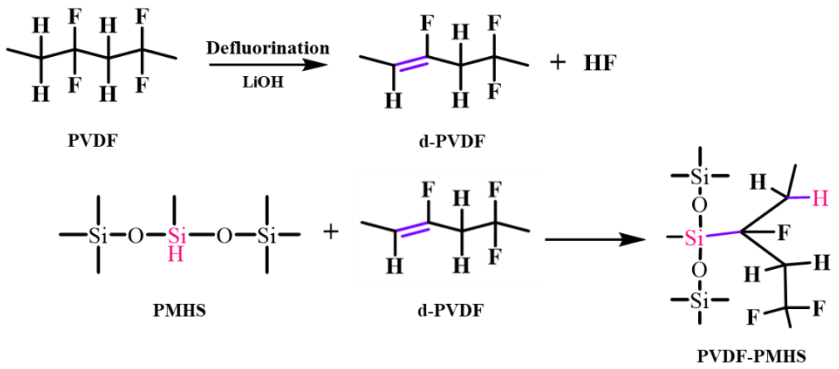


Figure 3-1 Reaction mechanism of the PPL electrolyte.

The LLZTO particles were characterized by FTIR and Raman to confirm the existence of LiOH (Figure 3.2), which is one of the key reactants to trigger the above-mentioned reactions. The peaks at ~3676 cm^{-1} in FTIR (Figure 3-2a) and ~3665 cm^{-1} in Raman spectroscopy (Figure 3-2b) belong to the vibration of LiOH on the surface of LLZTO particles, originating from the inevitable side reactions between LLZTO and H_2O in the air during the synthesis of LLZTO. The LiOH would trigger the partial dehydrofluorination of PVDF in DMF solvent. Besides, the hydrogen bond would be generated between the O-H of LiOH and the Si-O of PMHS.

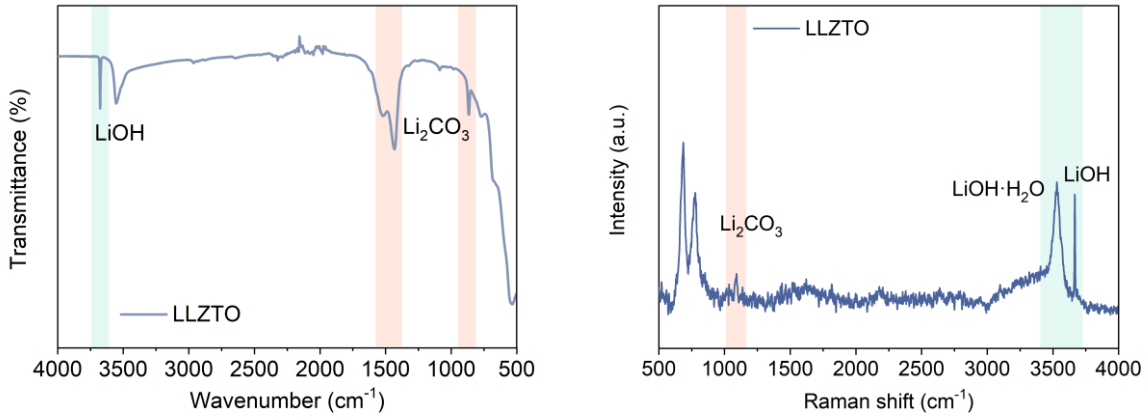
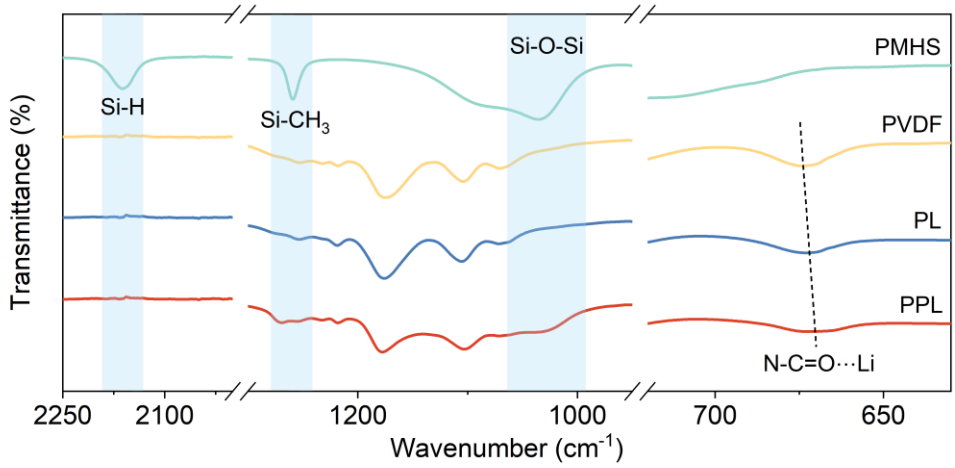


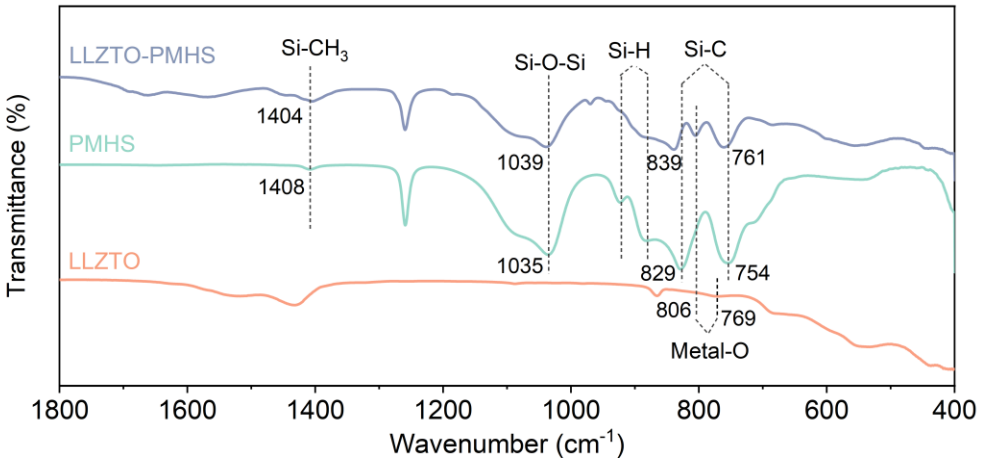
Figure 3-2 (a) FTIR spectra and (b) Raman spectra of LLZTO particles.

To verify the reaction mechanisms in the PPL electrolyte, the FTIR and Raman spectra were performed. Figure 3-3 (a) depicts the FTIR spectra of the PVDF, PL and PPL electrolytes and PMHS. The FTIR characterization band of Si-H vibration at 2163 cm^{-1} from PMHS disappeared in the PPL electrolyte, and the Si-CH_3 and Si-O-Si vibrations were observed in the PPL electrolyte, demonstrating the hydrosilylation reaction between d-PVDF and PMHS [142].

In addition, the interaction between LLZTO and PMHS was evidenced by the FTIR spectra of LLZTO nanoparticles, PMHS and the mixing suspension of LLZTO and PMHS (Figure 3-3b). The vibration peaks of Si-CH_3, Si-O-Si and Si-C from PMHS shifted from 1408, 1035, 829 and 754 cm^{-1} to 1404, 1039, 839 and 761 cm^{-1}, and the vibration peak of transition metal-O from LLZTO shifted from 769 cm^{-1} to 806 cm^{-1}, indicating the strong interaction between PMHS and LLZTO. Moreover, the much-decreased vibration peak of Si-H from PMHS indicated the reaction between PMHS and LLZTO. Hence, the PMHS could react with both PVDF and LLZTO to enhance their compatibility and improve mechanical strength.



(a)



(b)

Figure 3-3 FTIR spectra of (a) PMHS, PVDF, PL, PPL electrolytes and (b) LLZTO nanoparticles, PMHS and the mixing suspension of LLZTO and PMHS.

Figure 3-4 shows Raman spectra of PVDF, PL and PPL electrolytes. Compared with the PVDF electrolyte, the PL electrolyte exhibited additional peaks at 1141 and 1536 cm^{-1}, which were vibration modes of C=C resulting from the dehydrofluorination of PVDF induced by the LLZTO filler.

Nevertheless, after introducing PMHS into the PL electrolytes, these two Raman signals of C=C double bonds vanished in the PPL electrolyte. This was attributed to the hydrosilylation reaction between the Si-H group from PMHS and the C=C double bonds from d-PVDF that consumed the C=C bonds, resulting in PMHS-grafted PVDF backbones. The colour difference in the mixture solution during the preparation of the PPL electrolyte and PL electrolyte also indicated the reaction (Figure 3-5).

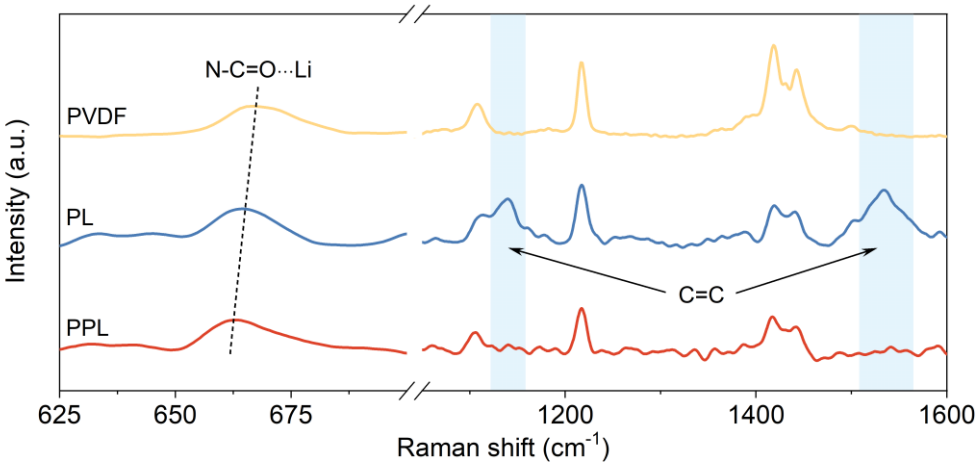


Figure 3-4 Raman spectra of PVDF, PL and PPL electrolytes.

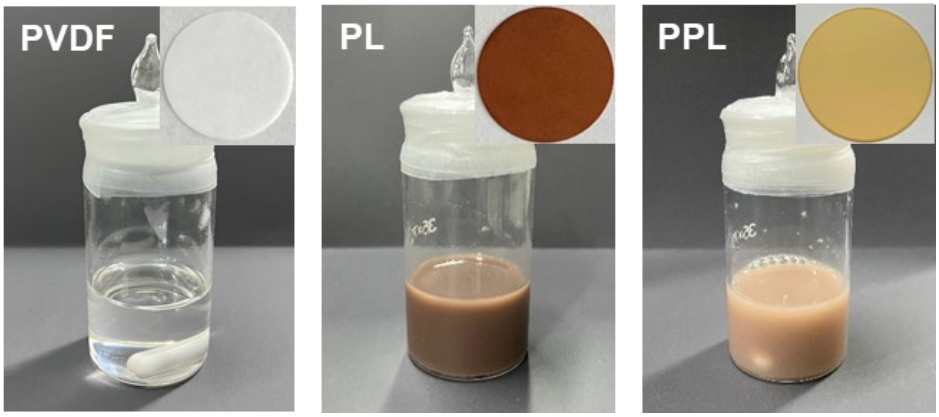


Figure 3-5 The colour difference in the precursor dispersions of PVDF, PL and PPL electrolytes.

3.5 Desolvation mechanism of solvated Li-ions in PPL electrolyte

PMHS was cross-linked with PVDF chains to facilitate the Li-ion desolvation from tightly complexed $[Li(DMF)_x]^+$ through the intermolecular interaction. This lowered the energy barrier required for creating bare Li-ions, thus paving the way for their subsequent transport across bulk LLZTO fillers. The activation of Li-ion conduction through LLZTO fillers fills a missing piece, that is the Li-ion pathways through polymer-ceramic-polymer, in the blueprint for multipath Li-ion transport in CSEs

(Figure 3-6). This would significantly improve the Li-ion transport efficiency and achieve high ionic conductivity.

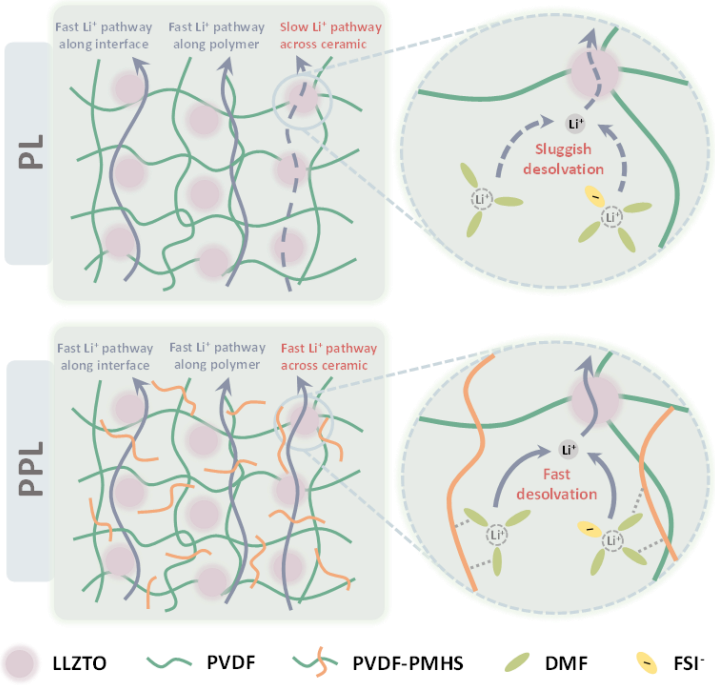


Figure 3-6 Schematic Li-ion transport pathways and Li-ion desolvation mechanism in PL and PPL electrolytes.

In PVDF electrolyte, all the residual DMF was bounded with Li-ions by forming N-C=O···Li coordination, corresponding to the FTIR peak at 674 cm^{-1} (Figure 3-3a) and the Raman peak at 667 cm^{-1} (Figure 3-4) [143]. Red shifts of the two bands were observed in the spectra of PL electrolyte, and even more remarkable for PPL electrolyte, indicating ever-decreasing N-C=O···Li coordination from PVDF to PPL electrolytes due to the partial desolvation of Li-ions. This was further verified by the magic angle spinning (MAS) ^{6}Li solid-state nuclear magnetic resonance (NMR) results (Figure 3-7). The ^{6}Li chemical shifts of PVDF, PL and PPL electrolytes were -0.08, -0.03 and 0.02 ppm. The downfield shifts of ^{6}Li resonance indicated reduced electron density around Li-ions due to the decreased N-C=O···Li coordination.

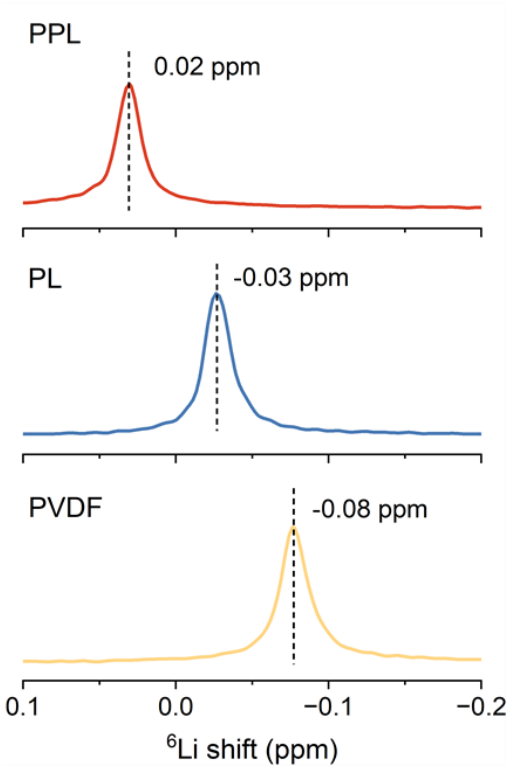
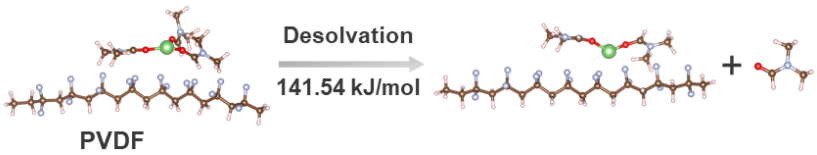
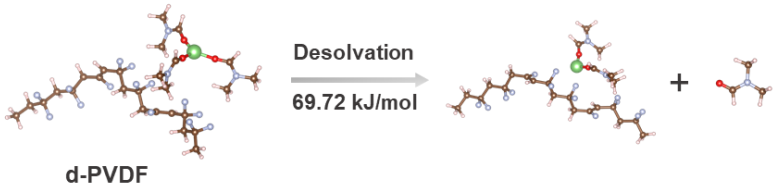


Figure 3-7 MAS ^{6}Li solid-state NMR spectra of PVDF, PL and PPL electrolytes.

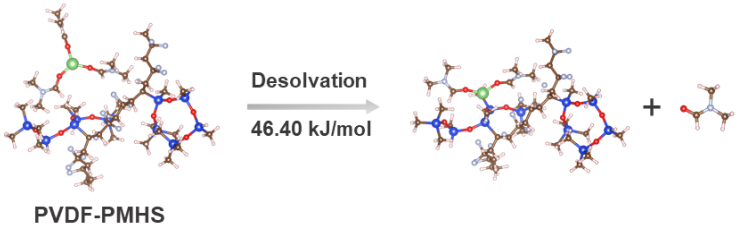
The different coordination environments in the three electrolytes were attributed to the different desolvation energies of Li-ions demonstrated by the DFT calculation results (Figure 3-8). The d-PVDF in PL electrolyte showed stronger interaction with Li-DMF complex than that of PVDF, which reduced the desolvation energy of Li-ions from 141.54 kJ mol^{-1} to 69.72 kJ mol^{-1} (Figure 3-8a and b). In contrast, the further stronger interaction between PVDF-PMHS and Li-DMF complex in the PPL electrolyte reduced the desolvation energy of Li-ions to 46.40 kJ mol^{-1} (Figure 3-8c). The low desolvation energy of Li-ions in the PPL electrolyte could promote the creation of bare Li-ions, which paved the way for Li-ions migrating through bulk LLZTO fillers, ultimately leading to the achievement of highly efficient multipath Li-ion transport within the PPL electrolyte.



(a)



(b)

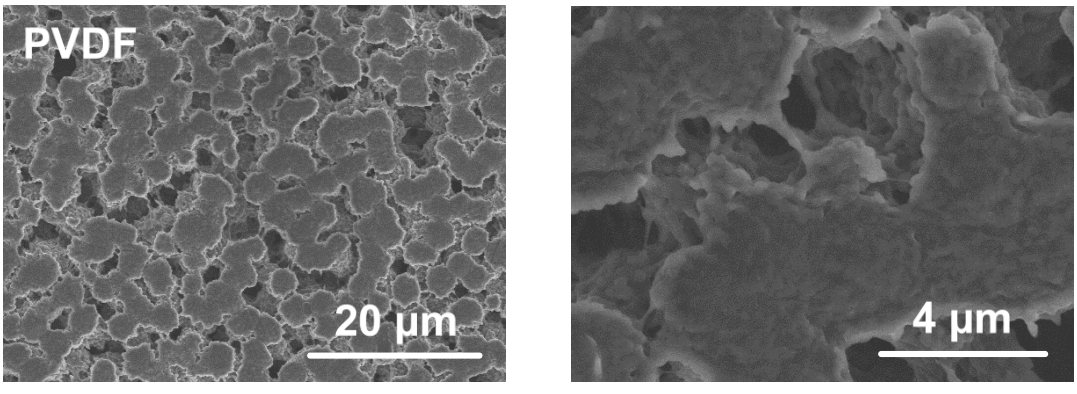


(c)

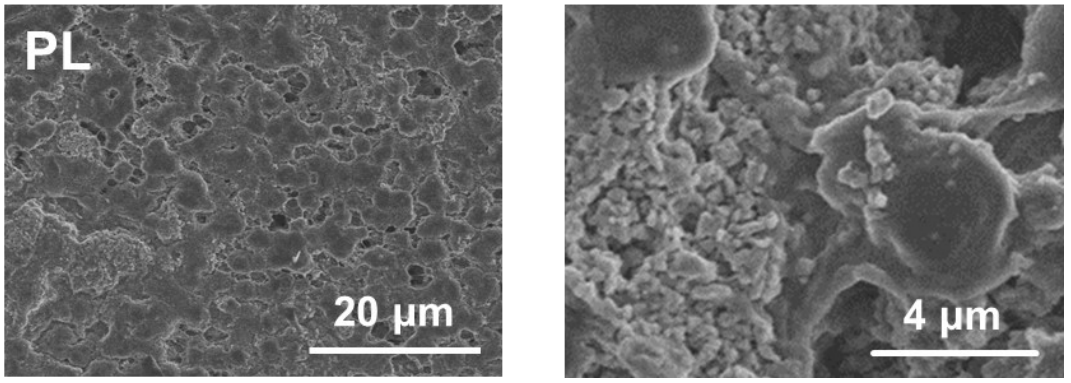
Figure 3-8 Calculated desolvation energy of Li-ions in (a) PVDF, (b) d-PVDF and (c) PVDF-PMHS by the DFT method.

3.6 Physicochemical characterisations of PVDF-based SSEs

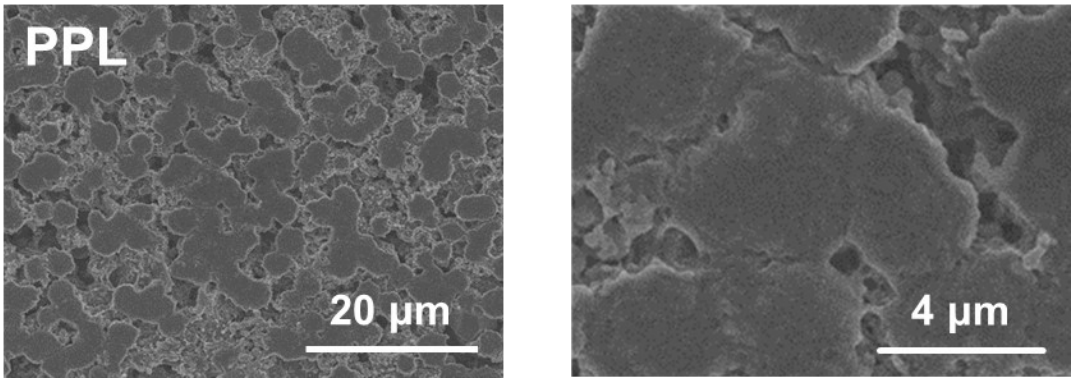
SEM was projected to characterise the micromorphology of PVDF, PL, and PPL electrolytes, shown in Figure 3-9. The PVDF membrane exhibited a porous structure with adjacent polymer spherocrystals (Figure 3-9a). After the addition of LLZTO ceramic particles, the PL membrane became more porous due to the aggregation of LLZTO particles that destroyed the polymer structure of PVDF (Figure 3-9b). In contrast, after the introduction of PMHS, the PPL electrolyte showed a relatively compact structure with uniformly distributed LLZTO particles interconnecting with the polymer spherocrystals (Figure 3-9c). This was beneficial for forming a continuous ion transportation pathway in the PPL electrolyte. Moreover, the compact and uniform PPL electrolyte film was helpful to suppress the growth of lithium dendrites which was easy to pierce the SSE and cause the short circuit of the battery.



(a)



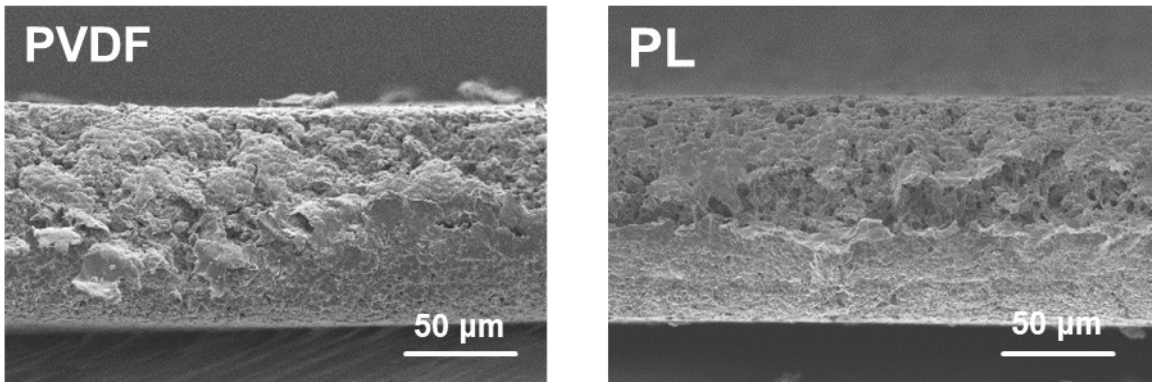
(b)



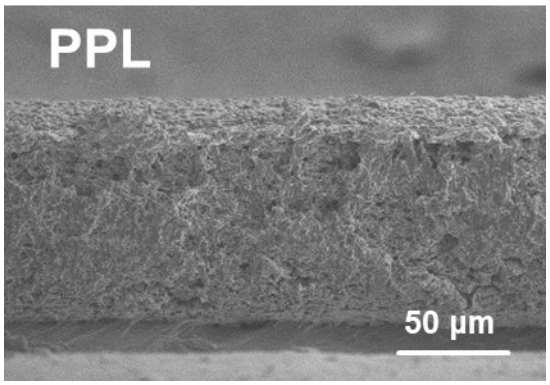
(c)

Figure 3-9 Top-view SEM images of the (a) PVDF, (b) PL and (c) PPL electrolytes.

The cross-section SEM images (Figure 3-10) of the three electrolytes also proved the uniform distribution of LLZTO and PVDF phases in the PPL electrolyte. The thickness of the PPL electrolyte was ~85 μm. By contrast, the PL electrolyte exhibited separated layers due to the phase separation of PVDF and LLZTO.



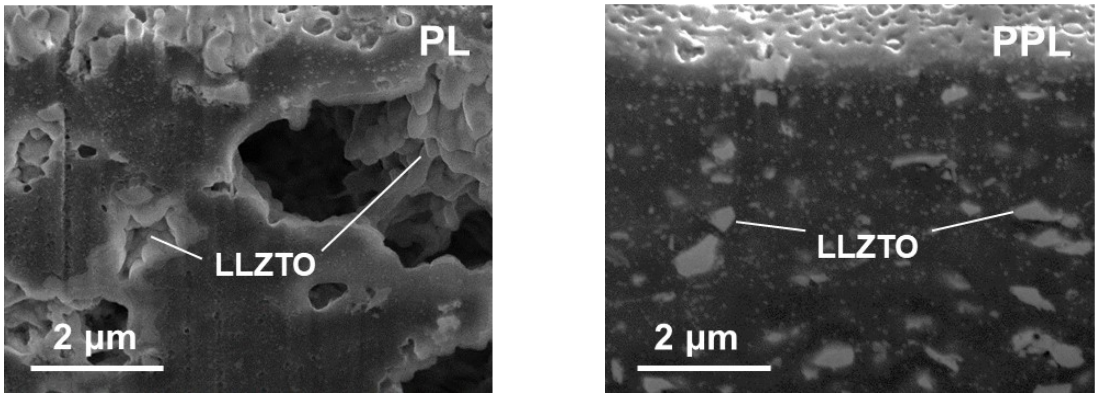
(a) (b)



(c)

Figure 3-10 Cross-sectional SEM images of the (a) PVDF, (b) PL and (c) PPL electrolytes.

The inner structures of PL and PPL electrolytes were further characterized by the focused ion beam (FIB)-SEM technique, as shown in Figure 3-11. The PPL electrolyte facilitated more uniform distribution of LLZTO fillers in its matrix compared to the PL electrolyte, attributing to the enhanced compatibility between PVDF-PMHS and LLZTO fillers.



(a) (b)

Figure 3-11 Inner structures of (a) PL and (b) PPL electrolytes characterised by the FIB-SEM technique.

The EDS mapping of F, La and Si elements in the PPL electrolyte is shown in Figure 3-12, which confirmed the uniform distribution of PMHS in the PVDF matrix. Hence, a PPL electrolyte with PMHS blocks uniformly cross-linked with PVDF backbones was obtained.

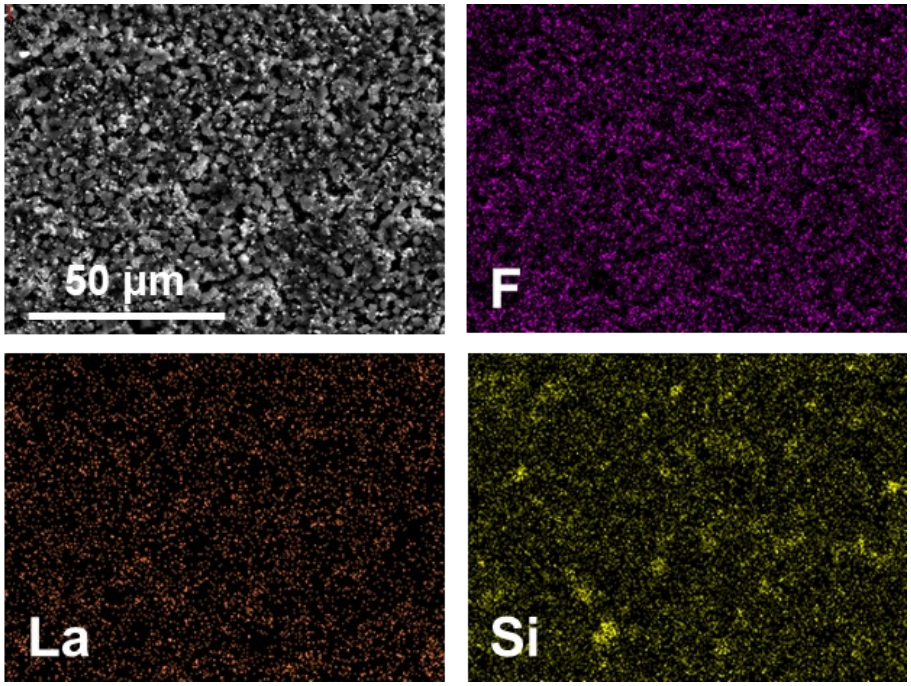
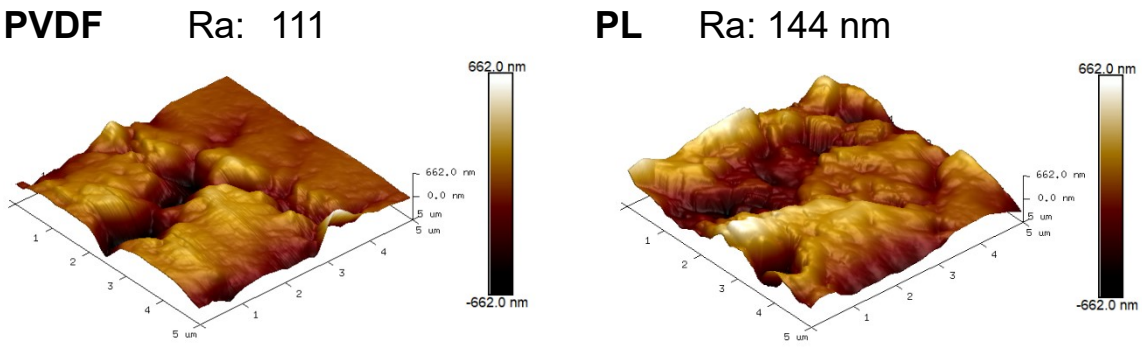
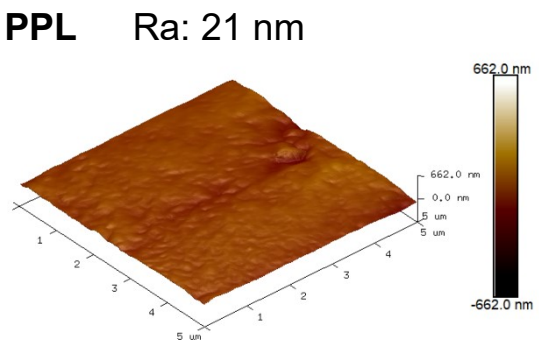


Figure 3-12 EDS mapping of F, La and Si elements in the PPL electrolyte.

The AFM images of three PVDF-based SSEs are shown in Figure 3-13. The PPL electrolyte membrane delivered an average roughness (Ra) of 21 nm, which was much lower than those of the PVDF electrolyte membrane (111 nm) and PL electrolyte membrane (144 nm). The lowest Ra of the PPL electrolyte membrane indicated its smooth and uniform surface, which could achieve better interfacial contact with the electrodes, thus facilitating the uniform transport of Li-ions.



(a) (b)

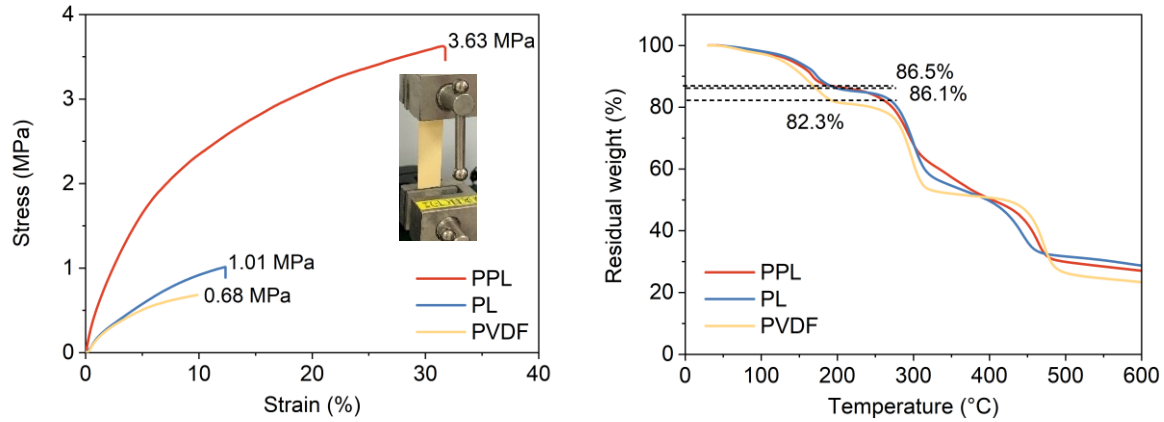


(c)

Figure 3-13 AFM images of the surface of (a) PVDF electrolyte, (b) PL electrolyte and (c) PPL electrolyte.

It is critical for SSE used in mettery to deliver excellent mechanical strength, owning to plastic deformation requirements of mettery. Moreover, the good mechanical property is also beneficial to hinder the overgrowth of lithium dendrites. Figure 3-14 (a) presents the stress-strain curves of PVDF, PL and PPL electrolytes, the tensile strengths of pure PVDF and PL were 0.68 and 1.01 MPa respectively. In comparison, the tensile stress of PPL electrolyte significantly increased to 3.63 MPa with a tensile strain of 31.7%. The tensile test of SSEs demonstrated that the solid-state PPL electrolyte used in mettery was robust enough to sustain plastic deformation, meeting the requirement of formability in the metal forming process.

To explore the thermal stability of the PVDF-based electrolyte, TGA was conducted and shown in Figure 3-14 (b). The weight loss observed below ~170 °C could be attributed to the volatilization of residual DMF solvent. This value was 17.7 wt%, 13.9 wt% and 13.5 wt% for PVDF, PL and PPL electrolytes, respectively. It was worth noting that the DMF content in the PPL electrolyte was even lower than that in both the PVDF and PL electrolytes, indicating that the improvement in the ionic conductivity of the PPL electrolyte was not attributed to the DMF. The rapid weight loss starting from 250 °C was attributed to the decomposition of lithium salt in the electrolyte. The decomposition of the PVDF component occurred only above 300 °C, which indicated that the PVDF-based electrolytes showed moderate thermal stability. The difference in the slope of the TGA curves during this period was attributed to the different decomposition behaviour of pristine PVDF, d-PVDF and PVDF-PMHS components in PVDF, PL and PPL electrolytes, respectively.

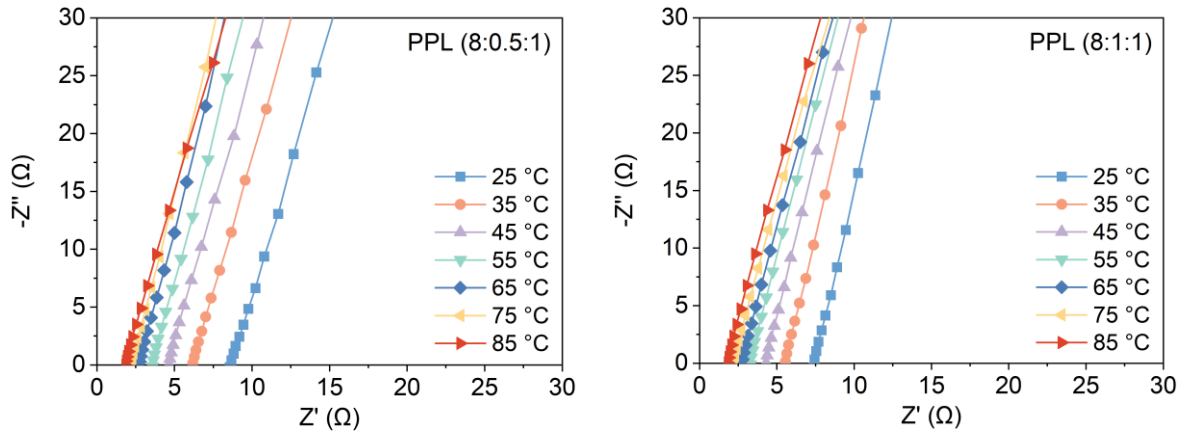


(a) (b)

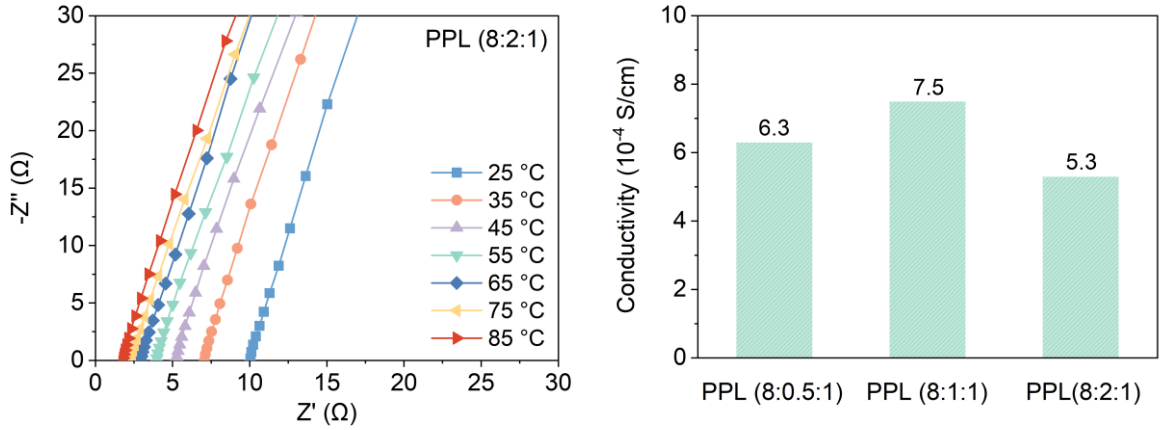
Figure 3-14 (a) Stress-strain curves of PVDF, PL and PPL electrolytes, (b) TGA curves of PVDF, PL and PPL electrolytes.

3.7 Electrochemical properties of PPL electrolytes with different PMHS weight ratios

To explore the PPL electrolyte with optimum PMHS weight ratio, PPL electrolytes with different PMHS weight ratios (PVDF: PMHS: LLZTO=8:0.5:1, 8:1:1 and 8:2:1) were fabricated, denoted as PPL (8:0.5:1), PPL (8:1:1) and PPL (8:2:1) electrolytes. Their ionic conductivity, activation energy, EIS, rate performance, and cycling performance were characterised. As shown in Figure 3-15, the ionic conductivities of PPL (8:0.5:1), PPL (8:0.5:1) and PPL (8:2:1) at the temperature of 25 °C, 35 °C, 45 °C, 55 °C, 65 °C, 75 °C and 85 °C were measured (Figure 3-15a-c). The PPL (8:1:1) exhibited the ionic conductivity of 7.5×10^{-4} S cm^{-1} at 25 °C, surpassing its counterparts of PPL (8:0.5:1) with ionic conductivity of 6.3×10^{-4} S cm^{-1} and PPL (8:2:1) with ionic conductivity of 5.3×10^{-4} S cm^{-1} (Figure 3-15d).



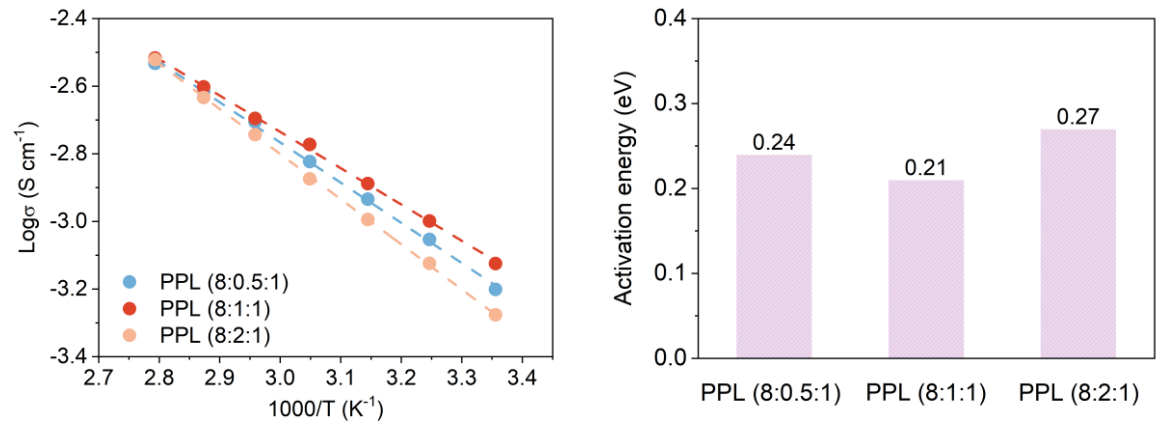
(a) (b)



(c) (d)

Figure 3-15 EIS plots of SS|SSE|SS coin cells by using (a) PPL (8:0.5:1), (b) PPL (8:1:1) and (c) PPL (8:2:1) electrolytes at different temperatures, (d) calculated ionic conductivities of PPL (8:0.5:1), PPL (8:1:1) and PPL (8:2:1) electrolytes at 25 °C.

According to the relation between temperature and ionic conductivity, the activation energy (E_a) of the PPL electrolytes with various PMHS weight ratios can be calculated by the Arrhenius formula. Figure 3-16 (a) exhibits Arrhenius plots of the ionic conductivities for PPL (8:0.5:1), PPL (8:0.5:1), and PPL (8:2:1) electrolytes. The calculated E_a of them is shown in Figure 3-16 (b). The PPL (8:1:1) electrolyte exhibited the lowest E_a of 0.21 eV, indicating the lowest migration barrier for Li-ion transport.



(a) (b)

Figure 3-16 (a) Arrhenius plots of the ionic conductivities and (b) calculated activation energy of PPL electrolytes with different PMHS weight ratios.

To further explore the optimum PMHS weight ratio in the PPL electrolyte, the solid-state NCM811|Li coin cells with PPL (8:0.5:1), PPL (8:0.5:1), and PPL (8:2:1) electrolytes were fabricated and their electrochemical performance, including EIS (Figure 3-17a), rate performance (Figure 3-17b), and cycling performance at 0.5C (Figure 3-17c) and 1C (Figure 3-17d), was measured. Compared to PPL

(8:0.5:1) and PPL (8:2:1) electrolytes, the NCM811|Li cell with PPL (8:1:1) electrolyte delivered the lowest impedance, superior rate performance and cycling performance (at both 0.5C and 1C) at 25 °C. As a result, PPL (8:1:1) was considered as the optimum ratio for PPL electrolyte, which was used in the following study.

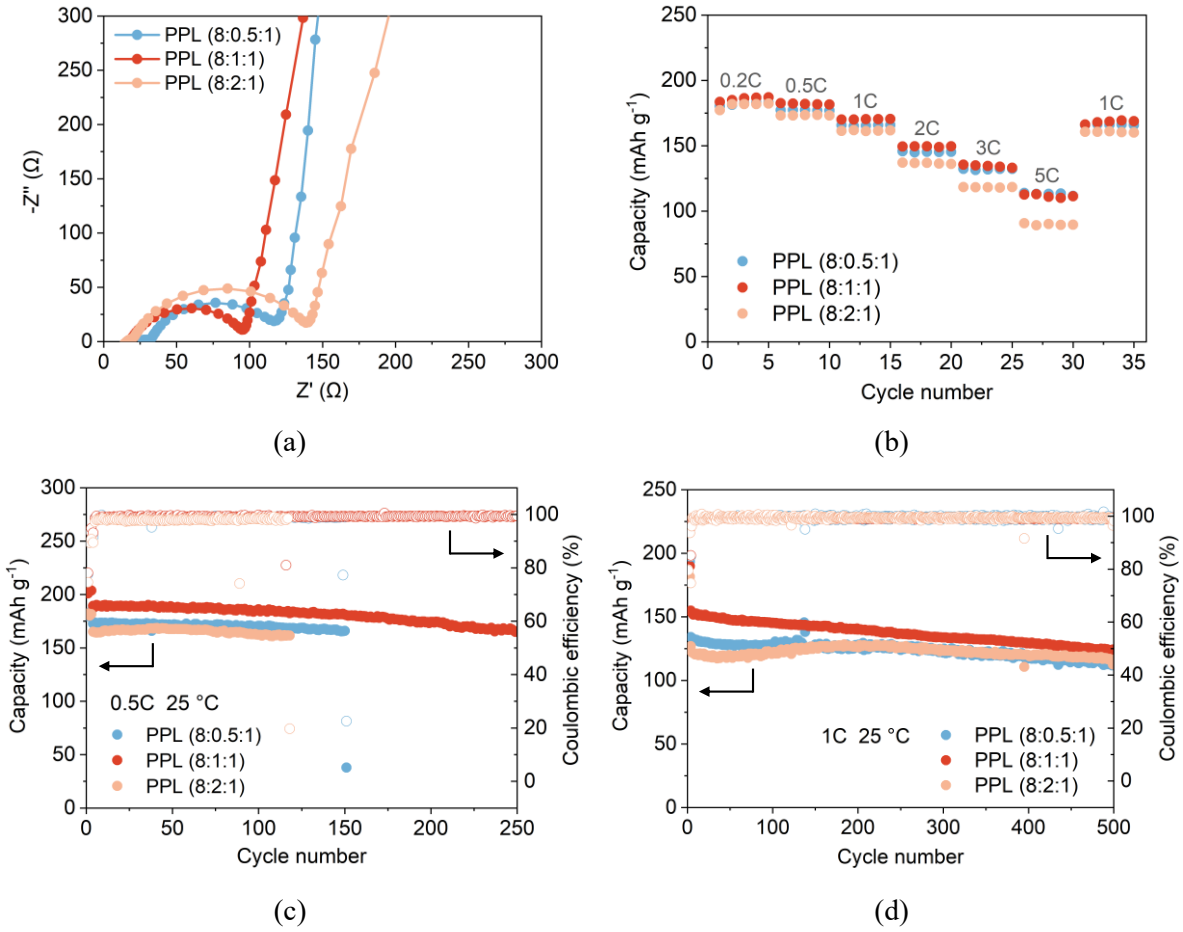


Figure 3-17 Electrochemical performance of PPL electrolytes with different PMHS weight ratios. (a) EIS plots, (b) rate performances, cycling performance and coulombic efficiency of NCM811|PPL|Li cells at (c) 0.5C and (d) 1C at 25 °C.

3.8 Electrochemical characterisations of PVDF-based SSEs

To evaluate the electrochemical properties of PVDF-based SSEs and select the optimal SSE that can be used in mettery, the coin cells with pure PVDF, PL and PPL as electrolytes were assembled and their electrochemical properties were tested. The ionic conductivity is an essential parameter to measure the ion transportability of an electrolyte used in a battery. The EIS plots of SS|SSE|SS coin cells by using PVDF and PL electrolytes at 25 °C, 35 °C, 45 °C, 55 °C, 65 °C, 75 °C and 85 °C are shown in Figure 3-18 (a) and (b). The calculated ionic conductivity of PL electrolyte was 4.5×10^{-4} S cm^{-1} at 25 °C, which was higher than 3.0×10^{-4} S cm^{-1} of PVDF electrolyte, attributing to the additional fast Li-ion pathways

along LLZTO interface and d-PVDF phase [74]. After introducing PMHS to activate another fast Li-ion pathway through bulk LLZTO fillers, the ionic conductivity was further improved to 7.5×10^{-4} S cm^{-1} at 25 °C for PPL electrolyte (Figure 3-18c).

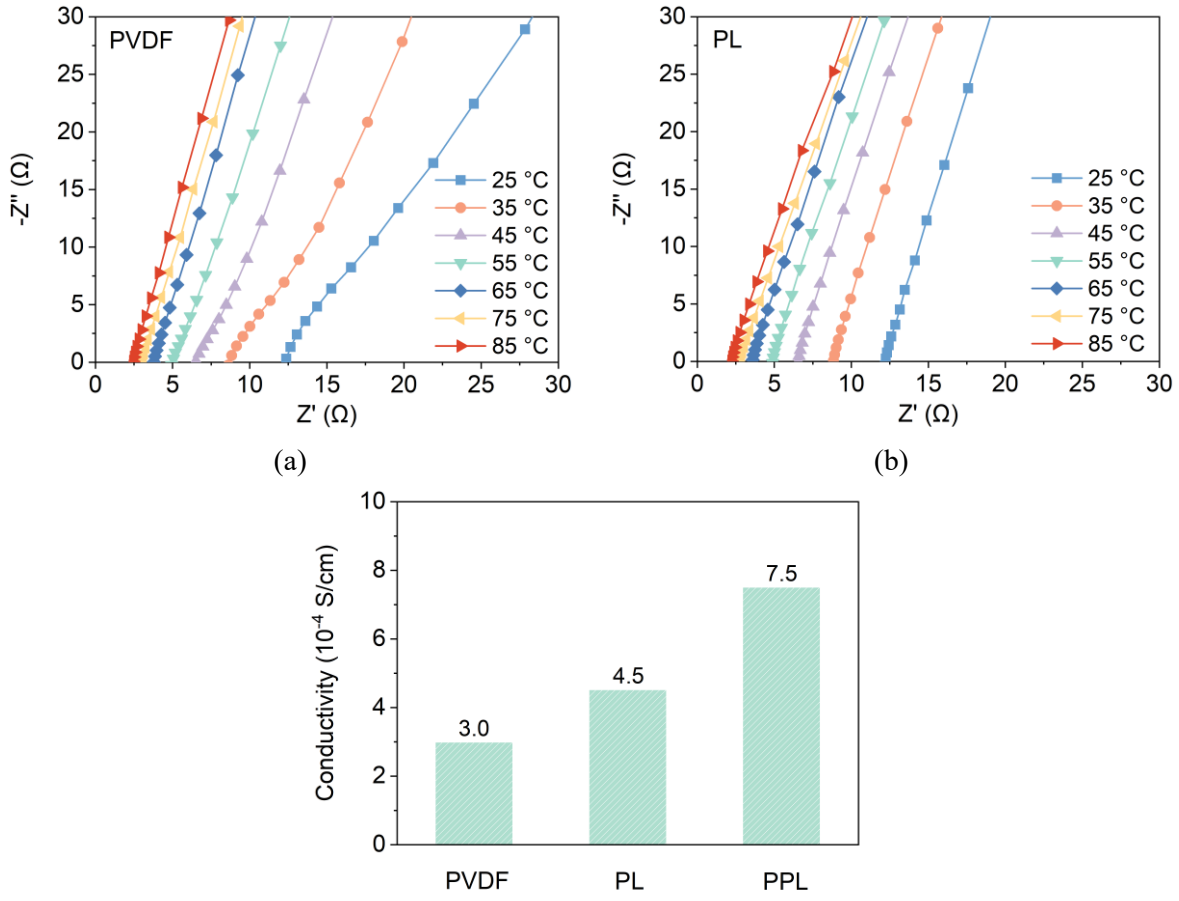
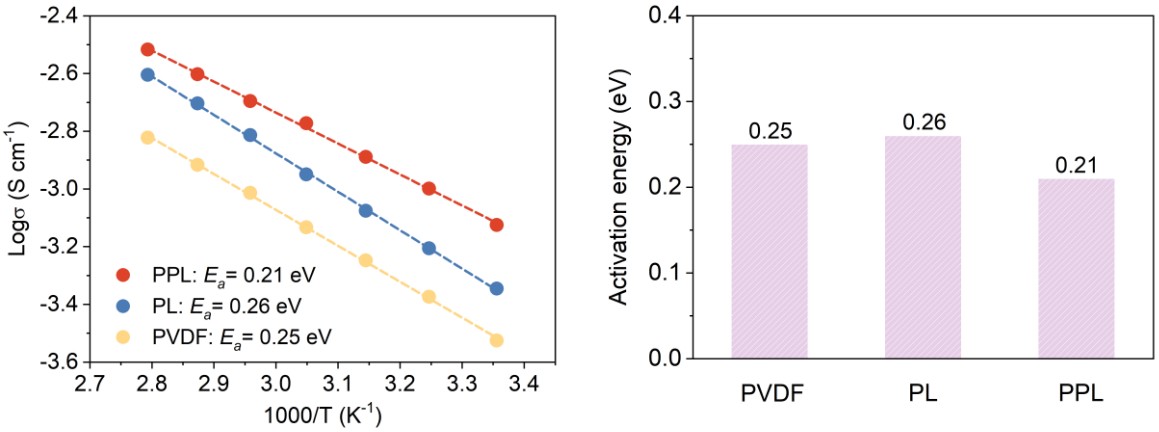


Figure 3-18 EIS plots of SS|SSE|SS coin cells by using (a) PVDF and (b) PL electrolytes at different temperatures, (c) calculated ionic conductivities of PVDF, PL and PPL electrolytes at 25 °C.

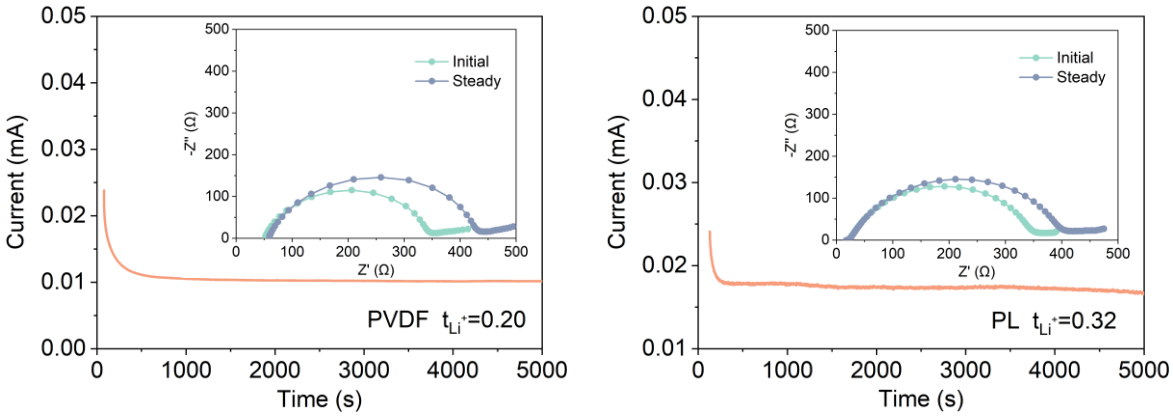
The Arrhenius plots of the ionic conductivities for PVDF, PL and PPL electrolytes is shown in Figure 3-19 (a). According to the relation between temperature and ionic conductivity, the activation energy E_a of the PVDF, PL and PPL electrolytes was calculated by the Arrhenius formula. The calculated activation energy of them is shown in Figure 3-19 (b). Compared to PVDF (0.25 eV) and PL (0.26 eV) electrolytes, the PPL electrolyte exhibited a reduced activation energy (0.21 eV), which would provide the lowest migration barrier for the Li-ion transport.



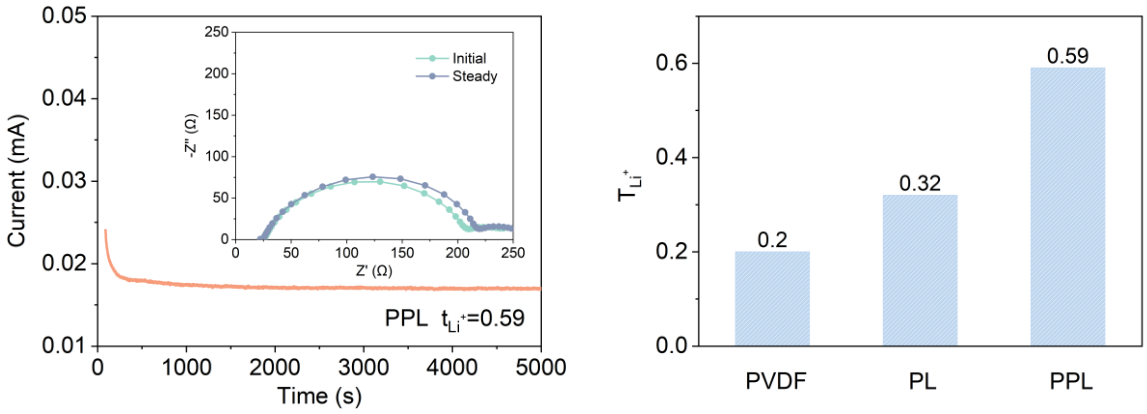
(a) (b)

Figure 3-19 (a) Arrhenius plots of the ionic conductivities and (b) calculated activation energy of PVDF, PL and PPL electrolytes.

To investigate the Li-ion migration ability, the Li-ion transference numbers of three SSEs were characterised (Figure 3-20). The PPL electrolyte exhibited a Li-ion transference number of 0.59, which was much higher than that of PVDF (0.20) and PL (0.32) electrolytes. This was because the PMHS worked as a bridge to effectively help Li-ion to migrate between PVDF and LLZTO. In addition, more single-ion conductive LLZTO fillers participated in Li-ion conduction in the PPL electrolyte. The multipath Li-ion transport mode was beneficial for uniform lithium deposition, restraining the overgrowth of lithium dendrites, particularly at high current density. Moreover, the high Li-ion transference number could reduce the concentration polarization on the cathode and anode interface in the cycling process, which improved the capacity and cycle stability.



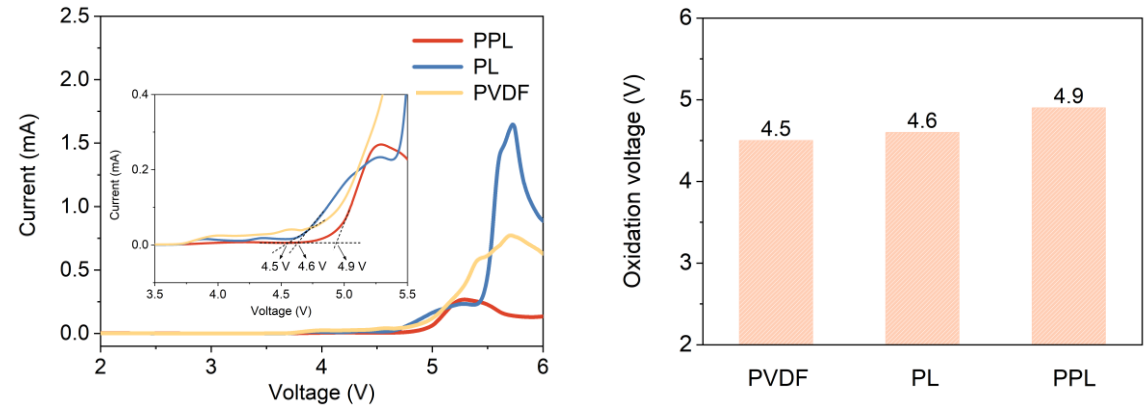
(a) (b)



(c) (d)

Figure 3-20 Li-ion transference number of PVDF, PL and PPL electrolytes. Chronoamperometry curves and corresponding EIS plots before and after the DC polarization of Li|SSE|Li symmetric cells by using (a) PVDF, (b) PL and (c) PPL electrolytes, (d) calculated Li-ion transference number of PVDF, PL and PPL electrolytes.

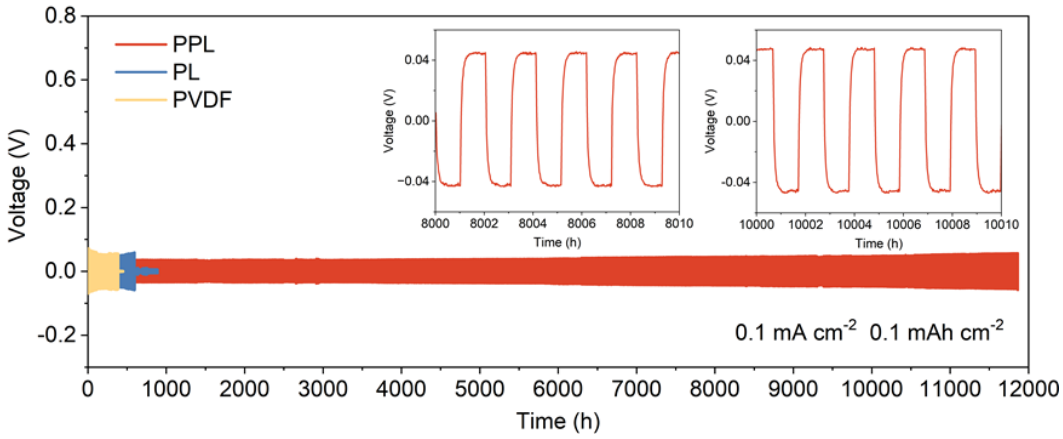
The electrochemical stability window of three SSEs was tested by the LSV method shown in Figure 3-21 (a), and the decomposition voltage of them is shown in Figure 3-21 (b). The pure PVDF electrolyte showed the lowest oxidation decomposition voltage of 4.5 V while PL exhibited a higher oxidation decomposition voltage of 4.6 V due to the addition of LLZTO particles with stronger oxidative resistance. After adding PMHS to PL electrolyte, the obtained PPL electrolyte exhibited an obviously enhanced oxidation decomposition voltage to 4.9 V due to the strong binding between PVDF and LLZTO phases, which showed great potential for high-voltage metteries. Moreover, the PPL electrolyte with a wider electrochemical window would be more stable and able to improve the coulombic efficiency.



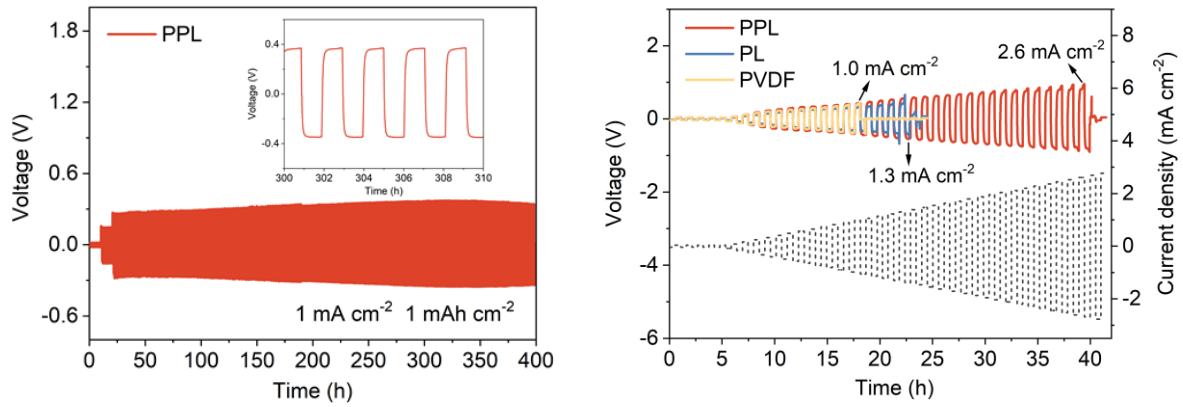
(a) (b)

Figure 3-21 (a) LSV curves and (b) oxidation voltages of PVDF, PL and PPL electrolytes.

The multipath Li-ion transport mode enabled the achievement of a uniform Li-ion flux and facilitated the homogeneous Li deposition onto the Li-metal anode, thereby decelerating the dendrite formation and reducing the risk of short circuit. The voltage profiles of Li|SSE|Li symmetric cells during Li plating/stripping could be used to display the ability of electrolyte membranes against lithium dendrites penetration which are shown in Figure 3.22. The symmetric cell using PVDF electrolyte could only plate/strip lithium for 383 h under a current density of 0.1 mA cm^{-2} before a short circuit due to the penetration of lithium dendrites through the PVDF electrolyte membrane. Compositing PVDF with LLZTO to form PL electrolyte prolonged the cycling time to 597 h due to the enhanced module of LLZTO particles which could alleviate the lithium permeation to some extent, but dendrites would still grow through the poor interphase between PVDF and LLZTO components. In sharp contrast, the symmetric cell using PPL electrolyte stably operated for more than 11800 h with a small polarisation voltage of ~40 mV (Figure 3-22a). This was attributed to the high binding strength between the LLZTO particles and the PVDF phase to form a uniform and compact film which could effectively suppress the dendrite penetration. Furthermore, the uniform lithium deposition induced by the multiple Li-ion transport pathways was another significant reason for prolonging the cycling time of the cell. Even under a high current density of 1 mA cm^{-2}, the symmetric cell using PPL electrolyte could stably cycle for nearly 400 h (Figure 3-22b). Moreover, the Li|PPL|Li symmetric cell showed a critical current density (CCD) of 2.6 mA cm^{-2}, which was much higher than that of PVDF (1.0 mA cm^{-2}) and PL (1.3 mA cm^{-2}) electrolytes (Figure 3-22c).



(a)

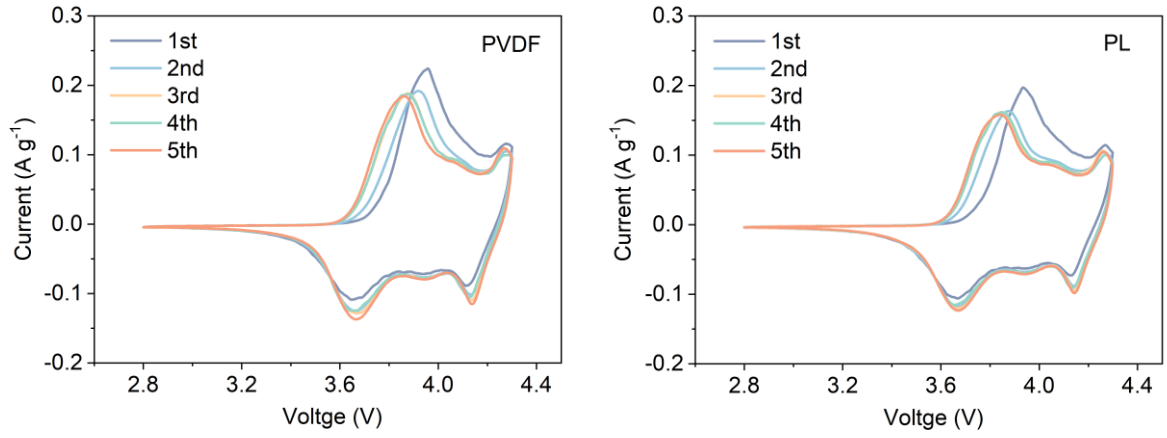


(b) (c)

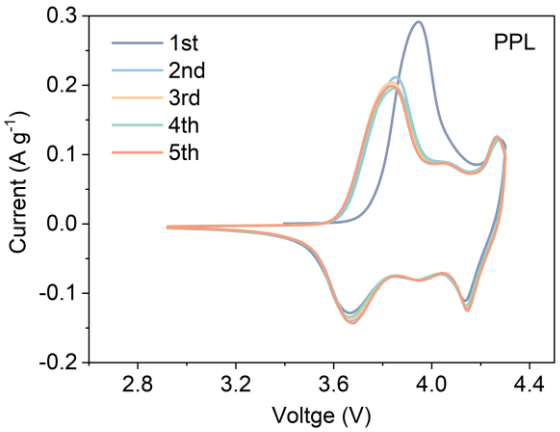
Figure 3-22 Galvanostatic voltage profiles of the Li|SSE|Li symmetric cells at a current density of (a) 0.1 mA cm^{-2} and (b) 1 mA cm^{-2}, (c) CCD test of the Li|SSE|Li symmetric cells with PVDF, PL and PPL electrolytes at 25 °C.

3.9 Electrochemical performances of NCM811|SSE|Li coin cells

To evaluate and choose the most promising PVDF-based SSE, the CR2025-type coin cells were assembled with NCM811 cathode, Li-metal anode and SSEs (NCM811|SSEs|Li coin cells). The CV measurement was performed to characterise the reversibility as well as the dynamic performance of cells with different PVDF-based SSEs (Figure 3-23). The first cathodic peak at around 3.94 V was attributed to the hexagonal-monoclinic (H1-M) phase transition of NCM811 material during the charging process, which showed an upper shift in the initial cycle compared to subsequent cycles, indicating a partially irreversible phase transition. Except for the inevitable initial irreversible phase transition, both cathodic and anodic peaks of the PPL cell were better overlapped than its counterparts, which indicated that the PPL electrolyte could suppress side reactions for high reversibility of the cathode material. Moreover, the peak current density of the PPL cell was obviously higher than those of PVDF and PL cells, indicating the superior dynamic performance of the PPL electrolyte.



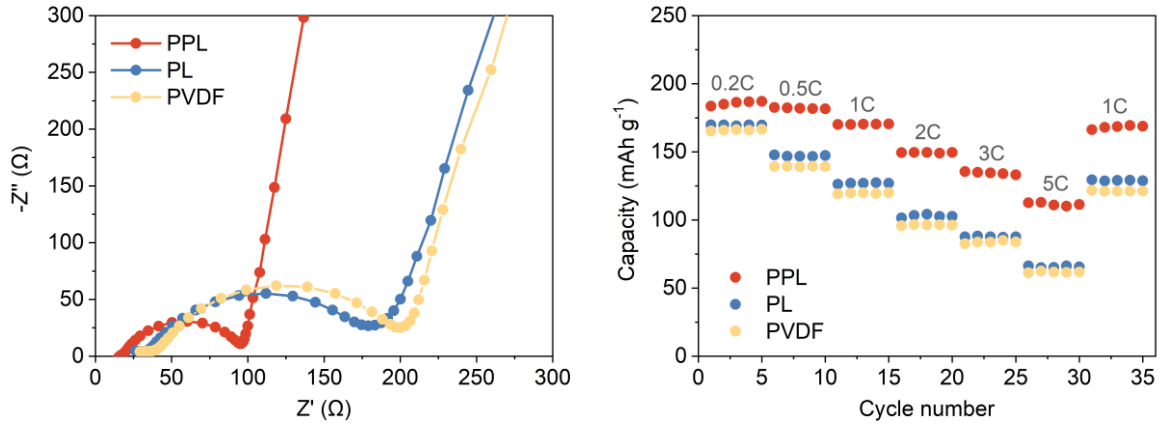
(a) (b)



(c)

Figure 3-23 CV profiles of NCM811|SSE|Li cells with (a) PVDF, (b) PL and (c) PPL as electrolytes.

The EIS profiles of NCM811|SSE|Li coin cells using the three electrolytes at room temperature are shown in Figure 3-24 (a). The cell with the PPL electrolyte exhibited an impedance of approximately 80 Ω, which was much smaller than the impedances of PL and PVDF electrolytes. The decreased impedance of PPL indicated the excellent kinetic performance of ion transport and outstanding interphase compatibility between electrolyte and electrode materials. This could be further demonstrated by rate performance results (Figure 3-24b), in which the cell with PPL electrolyte showed optimal rate performance among the three samples. NCM811|PPL|Li cell delivered specific capacities of 183.5, 182.5, 170, 149.4, 135.5 and 112.6 mAh g^{-1} at 0.2C, 0.5C, 1C, 2C, 3C and 5C, respectively, which were higher than 169.8, 147.7, 126.2, 101.5, 87.6 and 66.2 mAh g^{-1} for NCM811|PL|Li cell and 165.3, 139.2, 119, 95.7, 82.6 and 61.2 mAh g^{-1} for NCM811|PVDF|Li cell. When the current rate returned to 1C, a reversible capacity of 168.8 mAh g^{-1} for NCM811|PPL|Li cell was obtained after 35 cycles, which demonstrated the favourable electrochemical reversibility of the PPL electrolyte.



(a) (b)

Figure 3-24 (a) EIS plots and (b) rate performances of NCM811|SSE|Li cells with PVDF, PL and PPL electrolytes at 25 °C.

Figure 3-25 shows charge-discharge curves of NCM811|SSE|Li cells with PVDF (Figure 3-25a), PL (Figure 3-25b) and PPL (Figure 3-25c) electrolytes at the current densities of 0.2C, 0.5C, 1C, 2C, 3C and 5C at 25 °C. Compared to cells with PVDF and PL electrolytes, NCM811|PPL|Li cell presented lower polarisation due to the improved kinetic performance of ion mobility and the stable interface between electrolyte and electrodes.

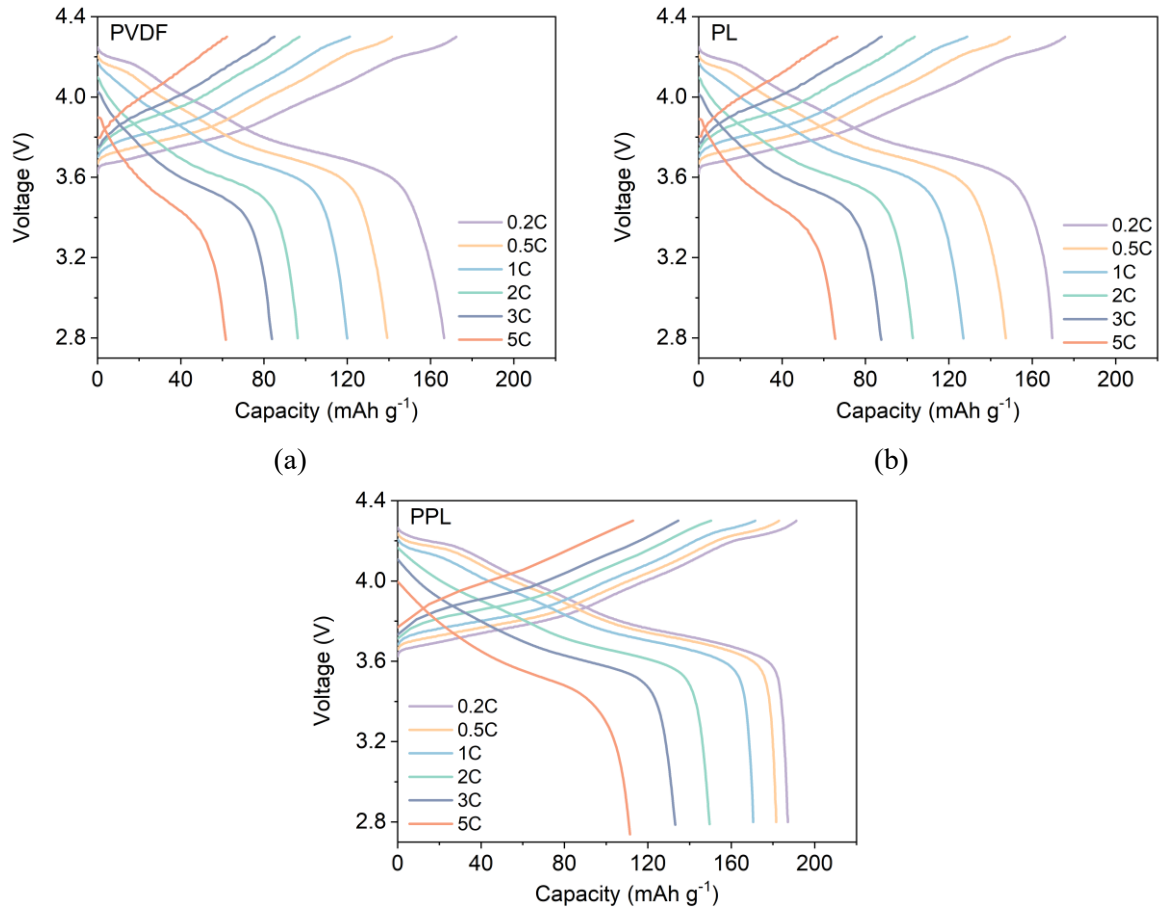


Figure 3-25 Charge-discharge profiles of NCM811|SSE|Li cells with (a) PVDF, (b) PL and (c) PPL electrolytes at different current densities at 25 °C.

The long-term cyclability and corresponding coulombic efficiency of the NCM811|SSE|Li cells with PVDF, PL and PPL electrolytes were also tested under different current densities of 0.5C (Figure 3-26a) and 2C (Figure 3-26b). At a current density of 0.5C, the NCM811|PPL|Li cell delivered the highest specific capacities of 165 mA h g^{-1} with a capacity retention of 87.1% after 250 cycles, outclassing those of its counterparts. This situation could be also reflected in the results of cycling at 2C, in which

the NCM811|PPL|Li cell stably cycled with a high specific capacity of 125.5 mAh g^{-1} and a capacity retention of 81.9% after 2200 cycles, accompanied by an average coulombic efficiency of over 99%. In comparison, the cells with pure PVDF and PL lectrolytes delivered lower capacities and were short-circuited soon after 311 and 131 cycles, respectively. The ultralong cycling stability of NCM811|PPL|Li cell was attributed to the tough and high-conductive electrolyte which could withstand lithium dendrites penetration while providing an unimpeded ion pathway.

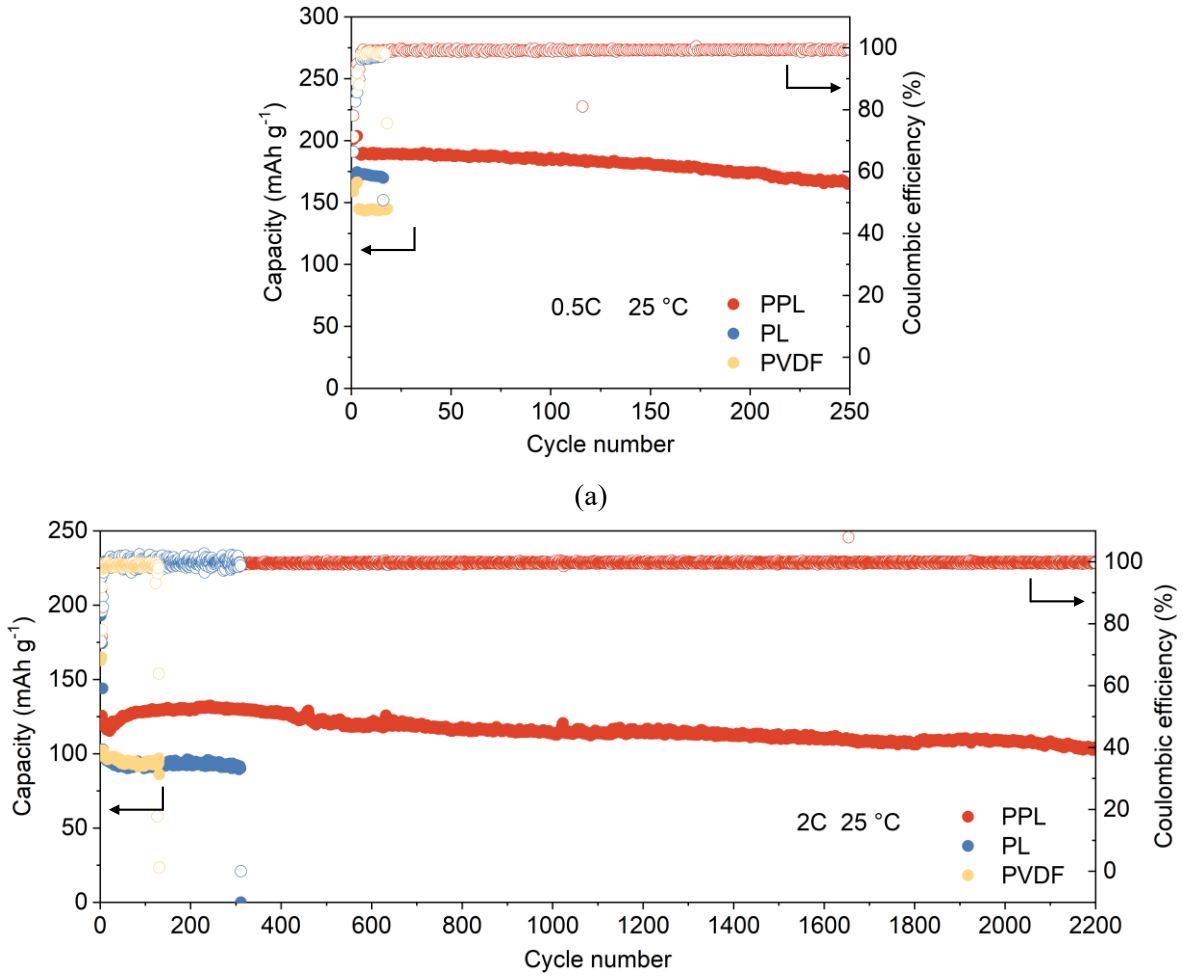


Figure 3-26 Cycling performance and coulombic efficiency of NCM811|SSE|Li cells with PVDF, PL and PPL electrolytes at (a) 0.5C and (b) 2C at 25 °C.

The galvanostatic charge-discharge profiles of NCM811|SSE|Li cells with PVDF (Figure 3-27a), PL (Figure 3-27b) and PPL (Figure 3-27c) electrolytes at 10th, 30th, 50th, 80th and 100th cycles were measured at a current density of 1C in the voltage range 2.8-4.3V at 25 °C. The discharge specific capacity of NCM811|PPL|Li cell was 154.1 mAh g^{-1} at the 10th cycle, which was much higher than NCM811|PVDF|Li cell (118.5 mAh g^{-1}) and NCM811|PL|Li cell (121 mAh g^{-1}). After 100 cycles, the NCM811|PPL|Li cell still delivered a high discharge specific capacity of 146.6 mAh g^{-1}. The superior

specific capacity retention (95.1%) and minor polarisation of PPL electrolyte after 100 cycles indicated its great potential for use in mettery.

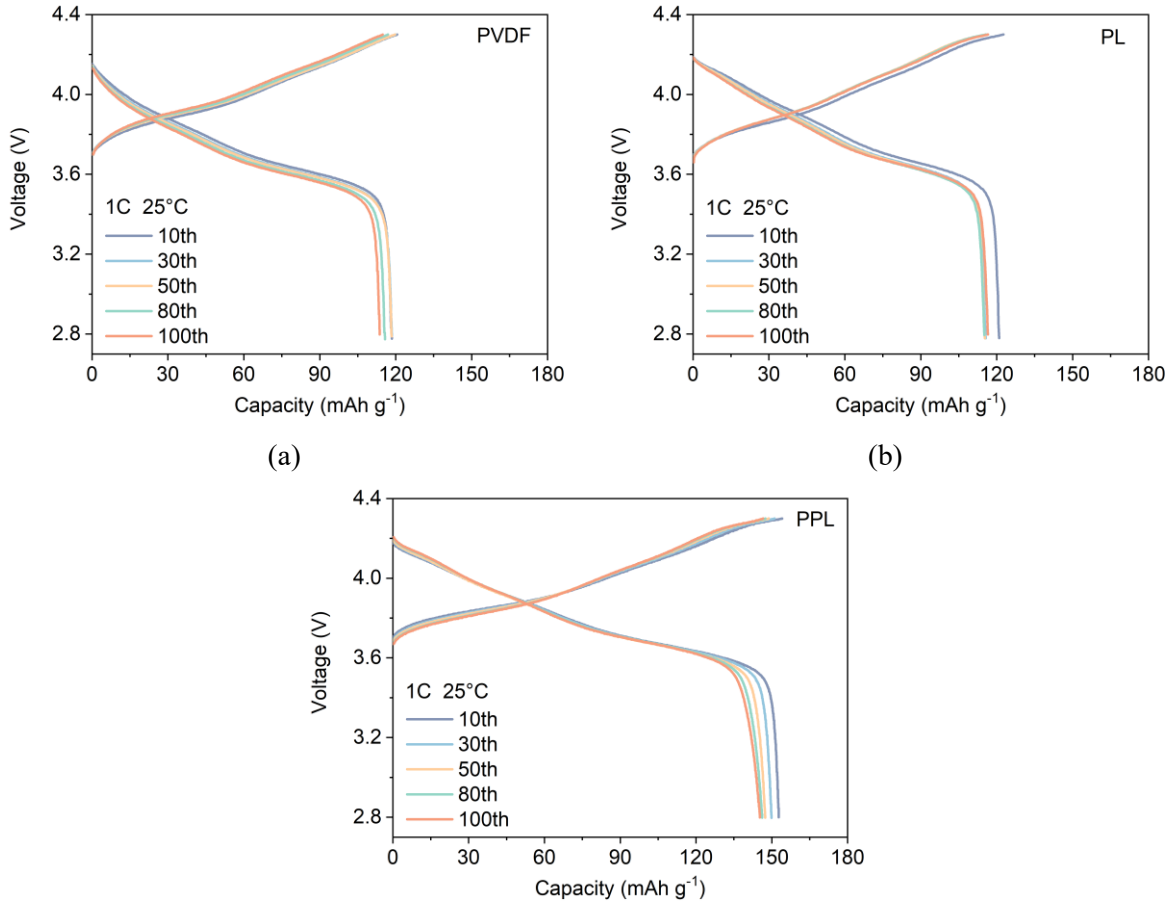


Figure 3-27 Galvanostatic charge-discharge profiles of NCM811|SSE|Li cells with (a) PVDF, (b) PL and (c) PPL electrolytes at the current density of 1C.

At a higher cathodic areal capacity of 1.6 mAh cm^{-2}, as shown in Figure 3-28, the NCM811|PPL|Li cells still exhibited superior stability, delivering a specific capacity of 155.4 mAh g^{-1} and capacity retention of 83.7% after 778 cycles at the current density of 0.2 C, while both the NCM811|PVDF|Li and NCM811|PL|Li cells showed overcharge with capacity fading rapidly.

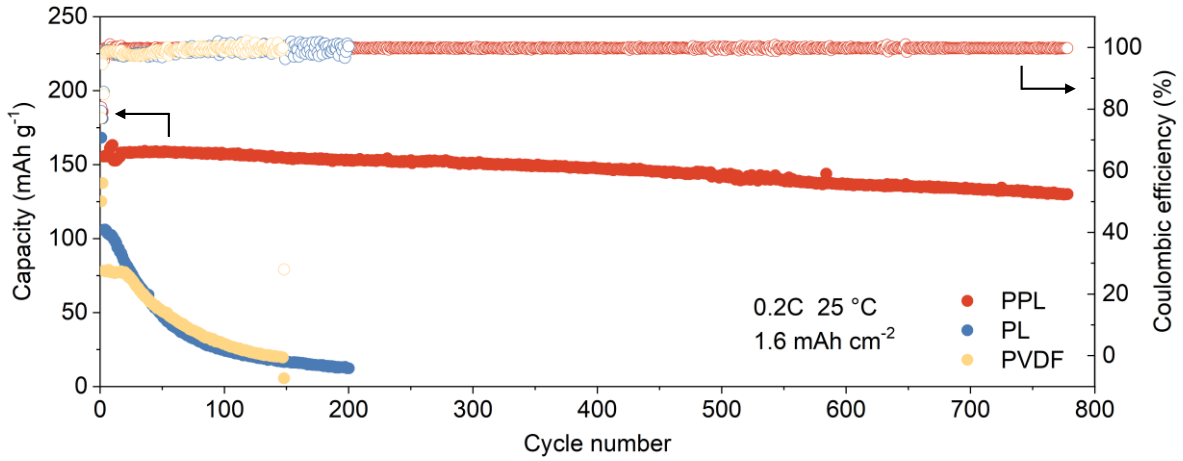


Figure 3-28 Cycling performance and coulombic efficiency of NCM811|SSE|Li cells with higher cathodic areal capacities of 1.6 mAh cm^{-2} by using PVDF, PL and PPL electrolytes at 0.2C at 25 °C.

When the cathodic areal capacity reached 3.1 mAh cm^{-2}, a value closing to commercial level, the NCM811|PPL|Li solid-state cell delivered a specific capacity of 149.3 mAh g^{-1} and stably operated for 150 cycles with 86% capacity retention, demonstrating great practical potential (Figure 3-29).

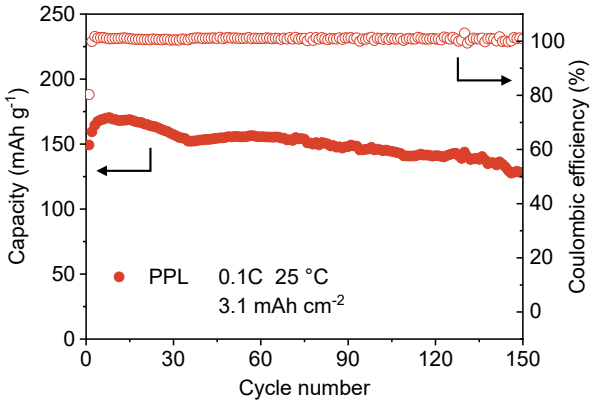


Figure 3-29 Cycling performance and coulombic efficiency of NCM811|PPL|Li cell with high cathodic areal capacities of 3.1 mAh cm^{-2} at 0.1 at 25 °C.

Furthermore, NCM811|SSE|Li solid-state pouch cells by using PVDF, PL, and PPL electrolytes were fabricated with the cycling performance shown in Figure 3-30. The NCM811|PPL|Li solid-state pouch cell delivered a specific capacity of 160.6 mAh g^{-1}, with a capacity retention of 80% after 300 cycles at 0.5 C. In contrast, the pouch cells using PVDF and PL electrolytes showed fast capacity decay.

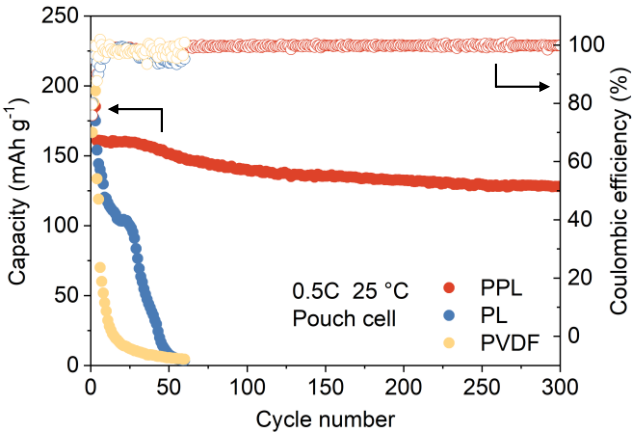
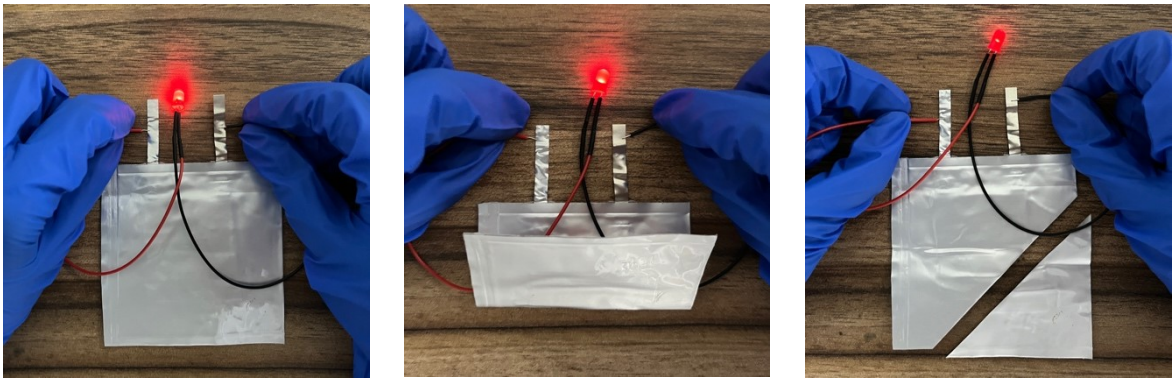


Figure 3-30 Cycling performance and coulombic efficiency of NCM811|SSE|Li pouch cells with PVDF, PL and PPL electrolytes at 0.5 C at 25 °C.

In addition, as shown in Figure 3-31, the NCM811|PPL|Li pouch cell was able to light a light-emitting diode (LED) even under folding and cutting states.



(a) (b) (c)

Figure 3-31 Optical pictures of NCM811|PPL|Li solid-state pouch cells powering an LED under (a) normal, (b) folding and (c) cutting states.

Moreover, as shown in Figure 3-32, even at the low temperature of -20 °C, NCM811|PPL|Li cell showed capacity fluctuations during cycling while still achieving a capacity of 156.1 mAh g^{-1} after 200 cycles. In contrast, the cells by using PVDF and PL electrolytes failed to work at such low temperature. Therefore, the PPL electrolyte enabled the NCM811|Li solid-state batteries with outstanding overall electrochemical performance.

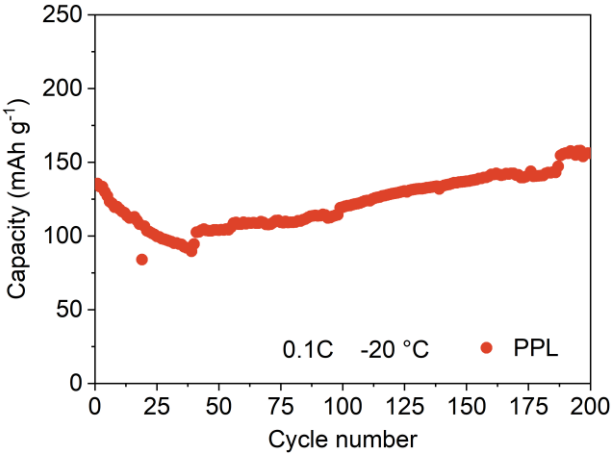
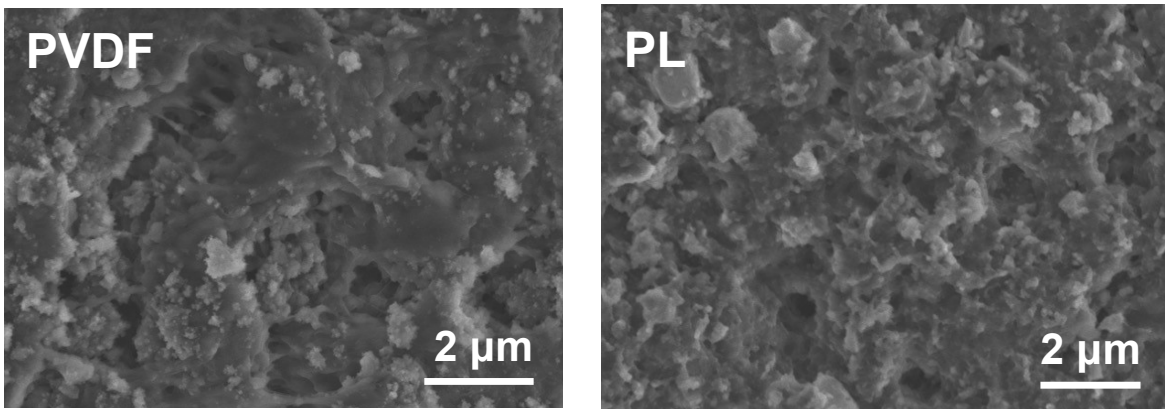


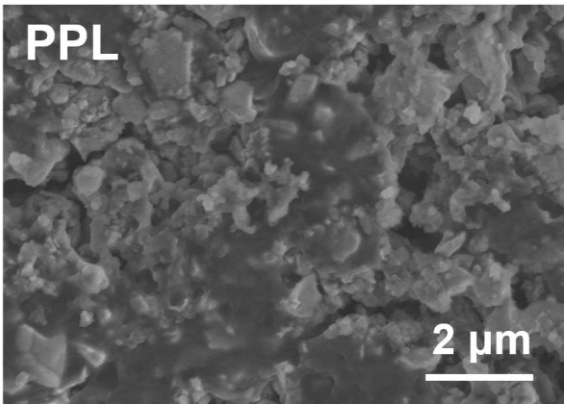
Figure 3-32 Cycling performance of NCM811|PPL|Li cell at 0.1C at -20 °C.

3.10 Structural evolution and interfacial chemistry of SSEs and electrodes

The morphologies of PVDF, PL and PPL electrolytes after 100 charge-discharge cycles at 1C are shown in Figure 3-33. The original spherulite structure of the PVDF phase in both PVDF and PL electrolytes was destroyed due to the decomposition of PVDF against Li metal. Moreover, mossy products were observed on the surface of PVDF and PL electrolytes due to the excess decomposition of Li salt. In contrast, the PPL electrolyte maintained an intact structure with no decomposition products observed on the electrolyte surface after 100 cycles. This was attributed to the protecting solid-electrolyte interphase (SEI) formed on the surface of the Li-metal anode derived from the reduction of PMHS that effectively prevented the uncontrollable decomposition of the PVDF phase and Li salt of the PPL electrolyte. Therefore, the PPL electrolyte delivered high interfacial stability with the Li-metal anode, thus improving the cycling stability.



(a) (b)



(c)

Figure 3-33 SEM images of (a) PVDF, (b) PL and (c) PPL electrolytes after 100 cycles at 1C.

Figure 3-34 (a), (c) and (e) show the TEM images of NCM cathodes by using PVDF, PL and PPL electrolytes after 100 cycles at 1C. The three cathodes all exhibited cathode electrolyte interfaces (CEI) on the surface, which originated from the decomposition of PVDF, Li salt, DMF and PMHS in the electrolytes. Thick and non-uniform CEI was observed on NCM811 cathodes paired with PVDF (NCM-PVDF) and PL (NCM-PL) surfaces, which may retard the transport of Li-ion through the cathode, thus causing large polarisation and capacity decay of batteries. By contrast, a more uniform and thinner (3.2 nm) CEI was formed on the NCM811 cathode paired with PPL (NCM-PPL) after 100 cycles, which may be ascribed to the prior decomposition of PMHS on the cathode surface that prevented the excess decomposition of other electrolyte components.

The high-resolution transmission electron microscopy (HR-TEM) images and fast Fourier transform (FFT) analysis were used to characterise the microstructures and phase-transition layer of the NCM cathodes (Figure 3-34 b, d and f). After 100 cycles, an integrated phase-transition layer composed of a rock-salt phase layer (site 1) and a mixing phase layer (site 2) combined the rock-salt and layered structures were formed on the surface of NCM particle for the three samples, which was due to the mixed arrangement of lithium sites and nickel sites during the Li-ion stripping and insertion. The NCM-PVDF and NCM-PL exhibited thick phase-transition layers of ~31 and ~20 nm, respectively due to the large impedance of lithium transport through the thick CEI layer. Comparatively, the phase-transition layer thickness of the NCM-PPL has significantly reduced to ~8 nm due to the fast lithium transmission dynamics contributed by the thin and uniform CEI layer. As a result, the thin and uniform PPL-derived CEI layer on the NCM surface significantly protected the NCM microstructures and thus highly facilitated its cyclability.

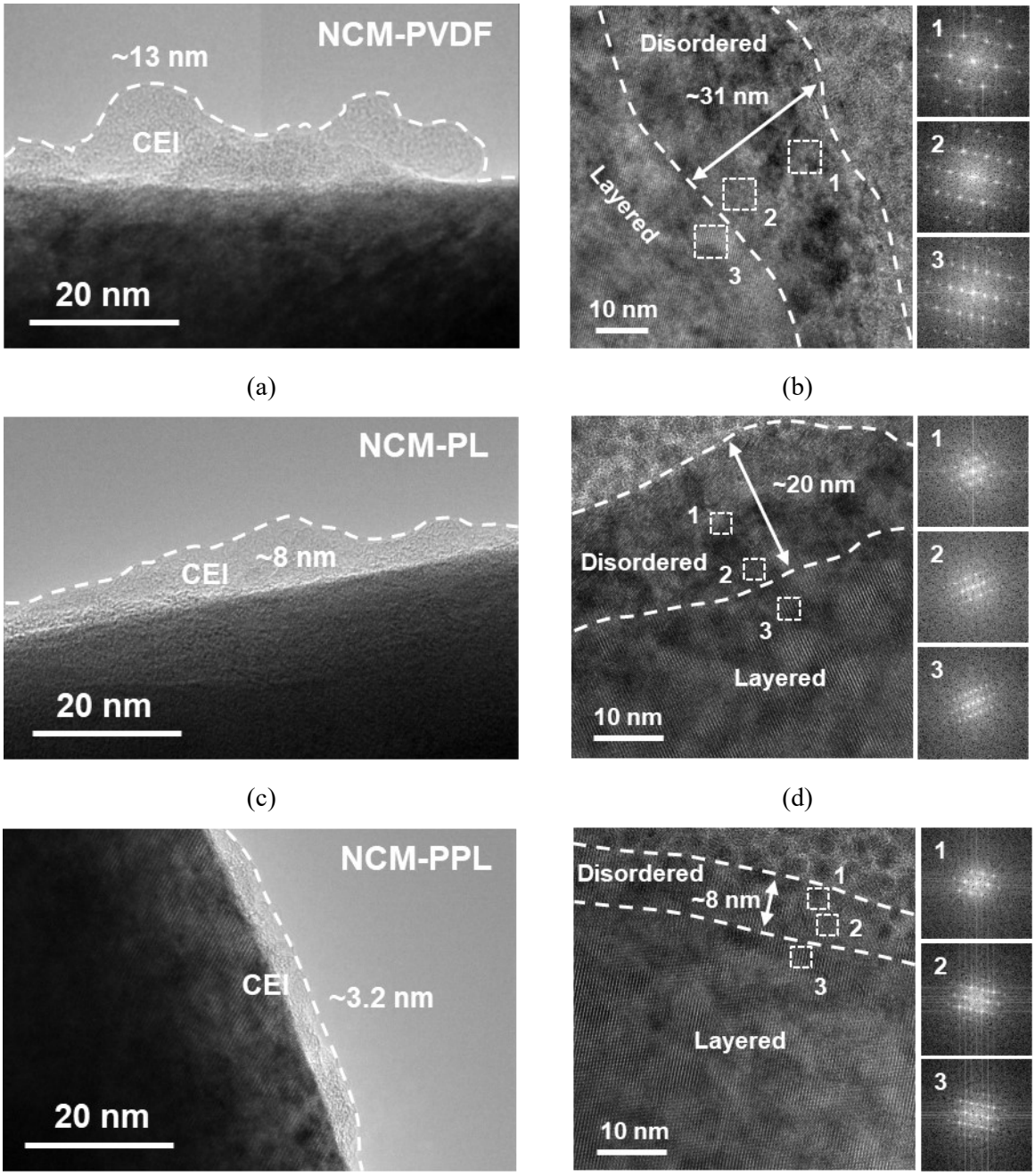


Figure 3-34 TEM images of CEI of cycled NCM cathodes by using (a) PVDF, (c) PL and (e) PPL electrolytes, TEM and FFT images of cycled NCM cathodes by using (b) PVDF, (d) PL and (f) PPL electrolytes after 100 cycles at 1C.

Figure 3-35 shows the SEM images of cycled NCM811 cathodes after 100 cycles by using PVDF, PL and PPL electrolytes, respectively. Cracks were observed on the NCM particles whose surface was covered with floccule for PVDF and PL-derived cathodes due to the side reactions of electrolytes with NCM. However, NCM particles maintained structural integrity with smooth and cleaner surface

morphology by using PPL electrolyte, indicating that the thin and stable CEI on the NCM would greatly protect the NCM structure from cracking and prevent electrolyte oxidation during charge-discharge cycling. Therefore, the NCM cathode using PPL electrolyte exhibited high reversible capacity, high capacity retention at a high rate and cyclability.

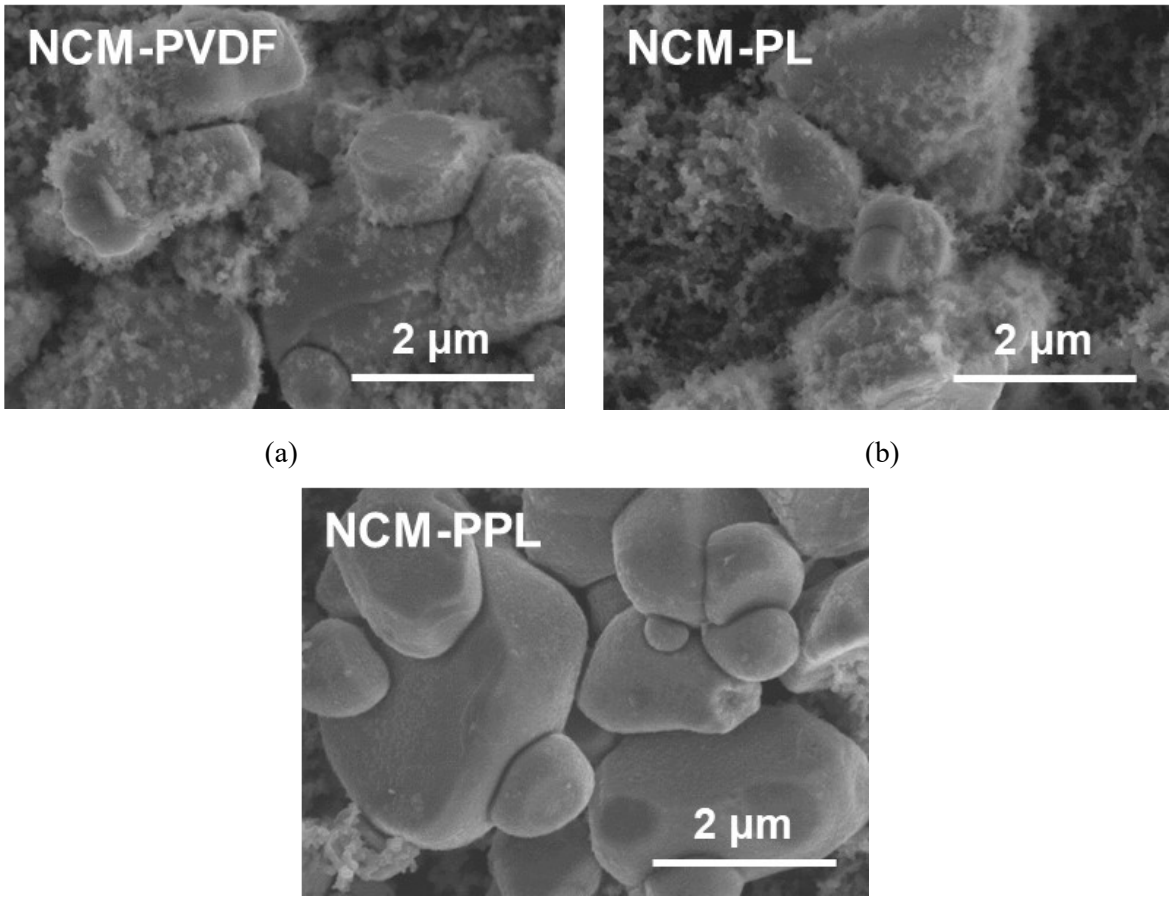
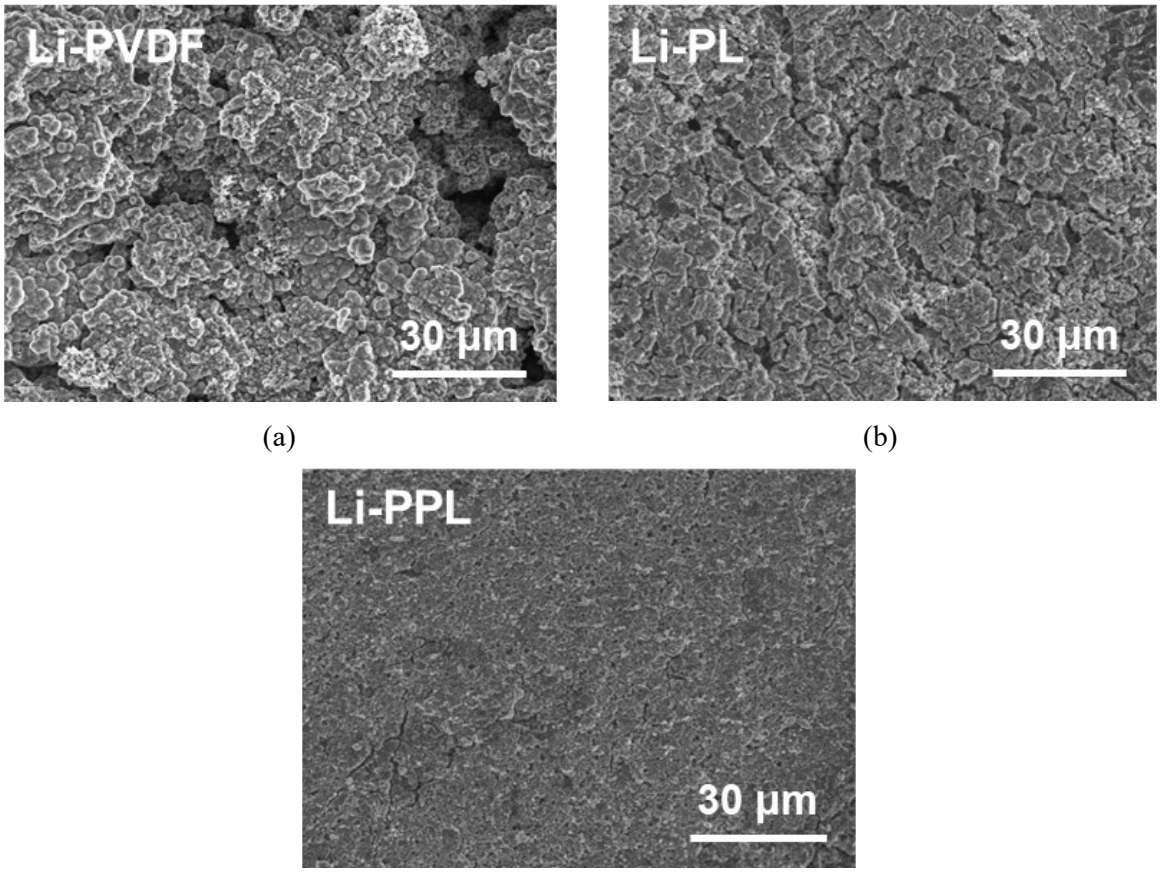


Figure 3-35 SEM images of cycled NCM811 cathodes by using (a) PVDF, (b) PL and (c) PPL electrolytes after 100 cycles at 1C.

The SEM images of the cycled Li-metal anode paired with PVDF (Li-PVDF), PL (Li-PL) and PPL (Li-PPL) electrolytes after 100 charge-discharge cycles are shown in Figure 3-36. The Li-PPL demonstrated a more uniform and denser Li plating morphology compared to Li-PVDF and Li-PL, indicating that the PMHS-derived robust SEI on Li anode along with PPL electrolyte with high-efficient Li-ion transport path was beneficial for uniform and even Li deposition. Therefore, the PPL electrolyte could effectively protect the Li anode from the overgrowth of lithium dendrites.



(a) (b)

(c)

Figure 3-36 SEM images of cycled Li anodes by using (a) PVDF, (b) PL and (c) PPL electrolytes after 100 cycles at 1C.

Figure 3-37 shows the EIS plots of NCM811|PVDF|Li, NCM811|PL|Li and NCM811|PPL|Li cells after the 1st, 10th and 50th cycles. The PVDF-derived and PL-derived cells exhibited higher impedance than PPL-derived cell during charge-discharge cycling. Also, the impedance of PVDF and PL cells increased during the cycling due to the unstable and ever-growing CEI and SEI on the surface of both NCM cathode and Li anode, leading to capacity decay in long-term cycling. Comparatively, the impedance of NCM811|PPL|Li cell decreased after 50 cycles due to the activation process that perfected the transport path of Li-ions, which also indicated the formation of stable and fast-kinetic CEI and SEI layers on electrodes, resulting in much-improved cycling stability of NCM811|PPL|Li cell.

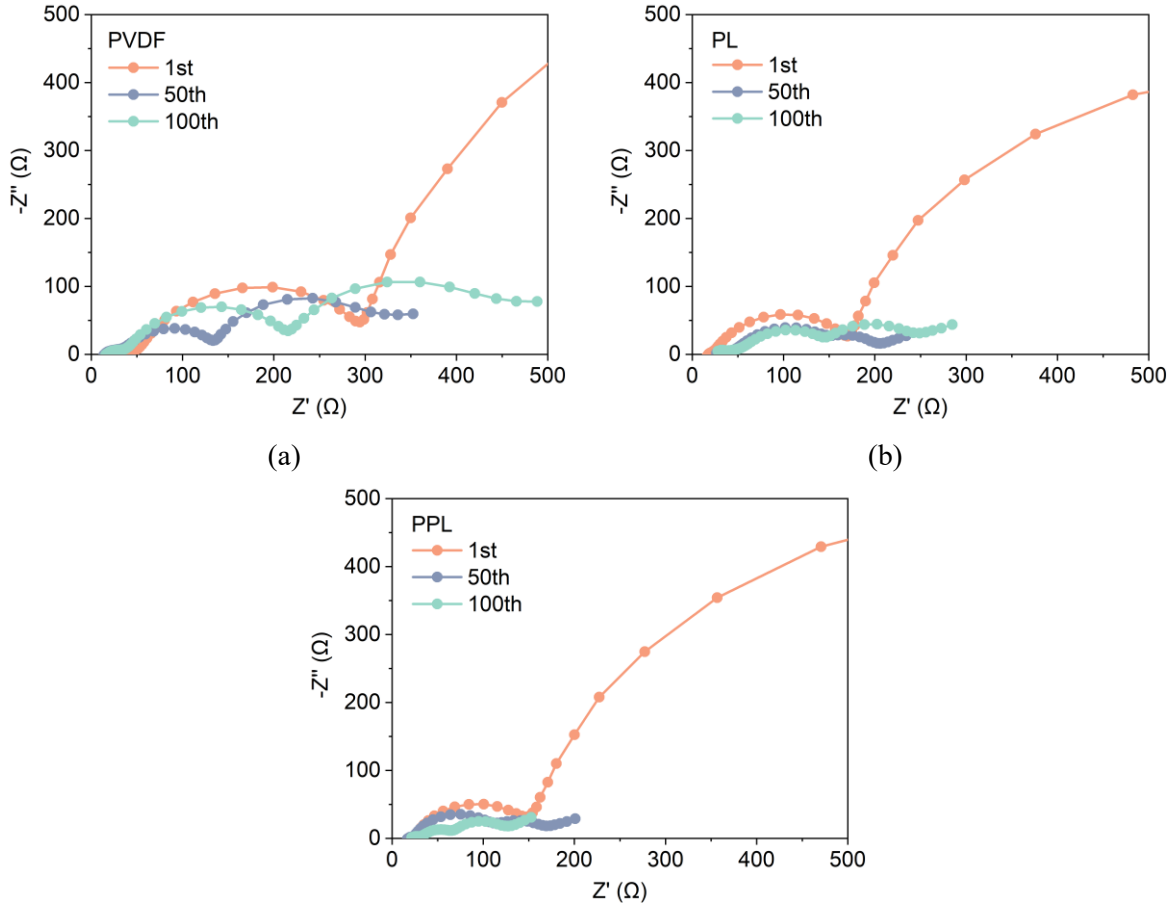
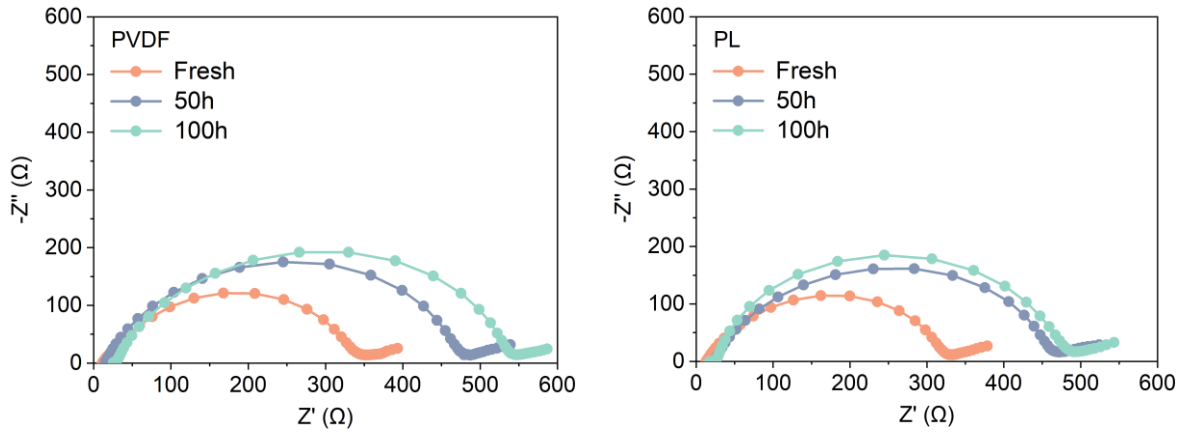
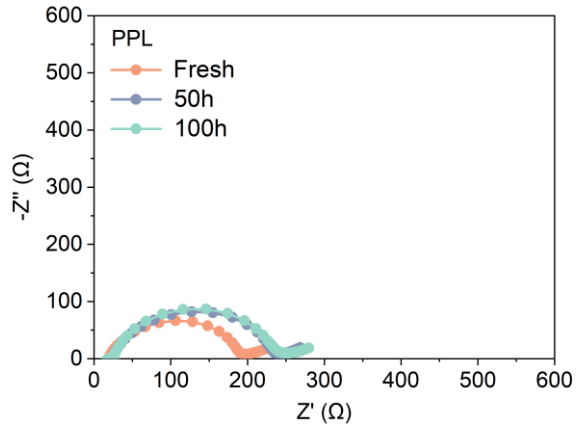


Figure 3-37 EIS plots of (a) NCM811|PVDF|Li, (b) NCM811|PL|Li and (c) NCM811|PPL|Li cells after 1st, 50th and 100th cycles.

The EIS plots of Li|PVDF|Li, Li|PL|Li and Li|PPL|Li cells before cycle and after 50 and 100 cycles were also investigated (Figure 3-38). The Li|PPL|Li cells exhibited significantly decreased impedance and impedance increment compared to Li|PVDF|Li and Li|PL|Li cells, indicating the formation of a more stable electrolyte/Li anode interface due to the reduced side reactions in Li|PPL|Li cells.



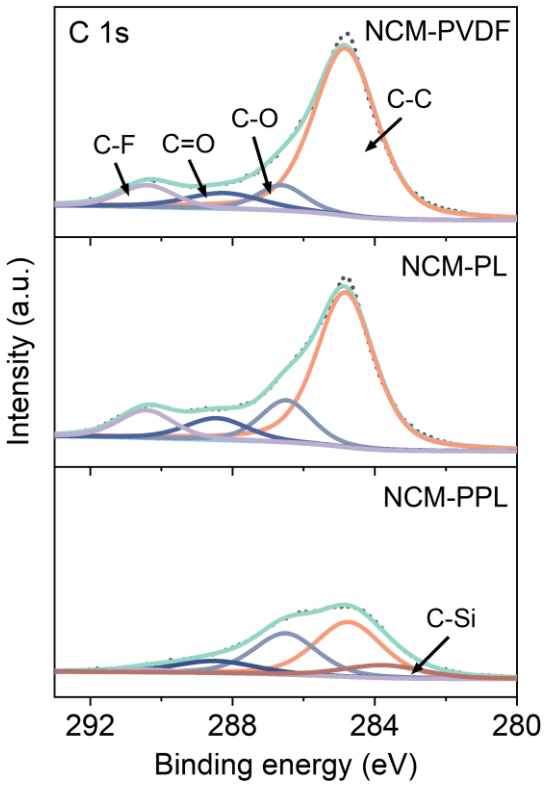
(a) (b)



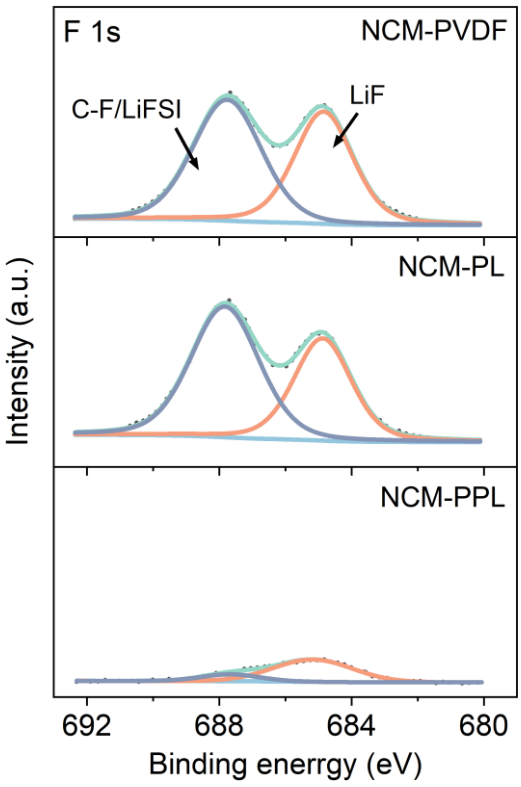
(c)

Figure 3-38 EIS plots of (a) Li|PVDF|Li, (b) Li|PL|Li and (c) Li|PPL|Li cells before cycle and after 50th and 100th cycles.

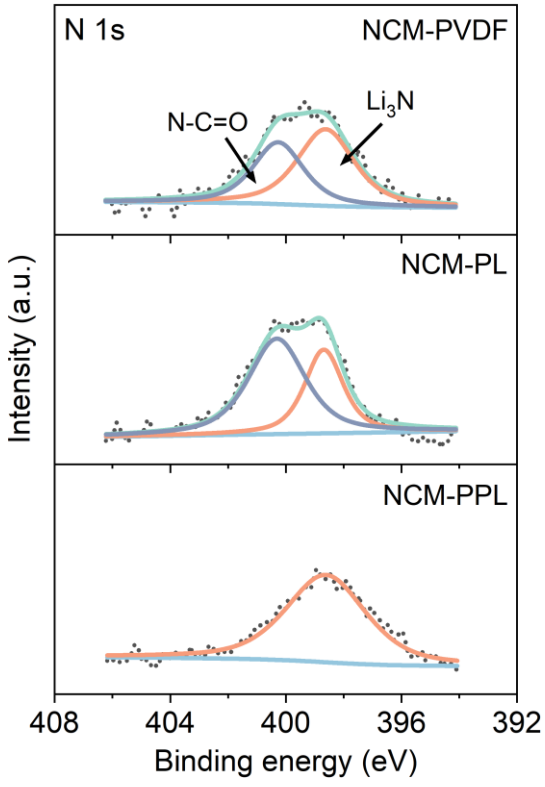
To further explore the mechanism of improved cycling stability of cathode by PPL electrolyte, the XPS spectra for C 1s, F 1s, N 1s, S 2p and Si 2p of NCM811 cathode by using PVDF electrolyte (NCM-PVDF), PL electrolyte (NCM-PL) and PPL electrolyte (NCM-PPL) after 100 cycles were conducted, as shown in Figure 3-39. In the C 1s spectra, the carbon content on the surface of NCM-PVDF and NCM-PL was higher than that in NCM-PPL, indicating thickened CEI of the former two cathodes derived from electrolyte decomposition. The presence of a C-F peak both in C 1s and F 1s spectra in NCM-PVDF and NCM-PL indicated the serious oxidation decomposition of PVDF on the NCM cathode. The markedly weaker F 1s and S 2p signals of NCM-PPL surface compared to those of NCM-PVDF and NCM-PL indicated less Li salt (LiFSI) decomposition. Moreover, the absence of the N-C=O signal in the N 1s spectrum of NCM-PPL also indicated the inhibition of DMF decomposition. The presence of a C-Si signal in C 1s and a C-Si-O signal in Si 2p spectra of the NCM-PPL proved that PMHS decomposed and participated in the formation of CEI. Therefore, it is reasonable to infer that the PMHS-derived proactive CEI containing C-Si-O components in the NCM-PPL could reduce the decomposition of PVDF, DMF, and Li salt in the electrolyte, which effectively protected the NCM particles from irreversible surface phase transition and cracking.


C 1s
NCM-PVDF
C-F
C=O
C-O
C-C
NCM-PL
NCM-PPL
C-Si
Intensity (a.u.)
292
288
284
280
Binding energy (eV)

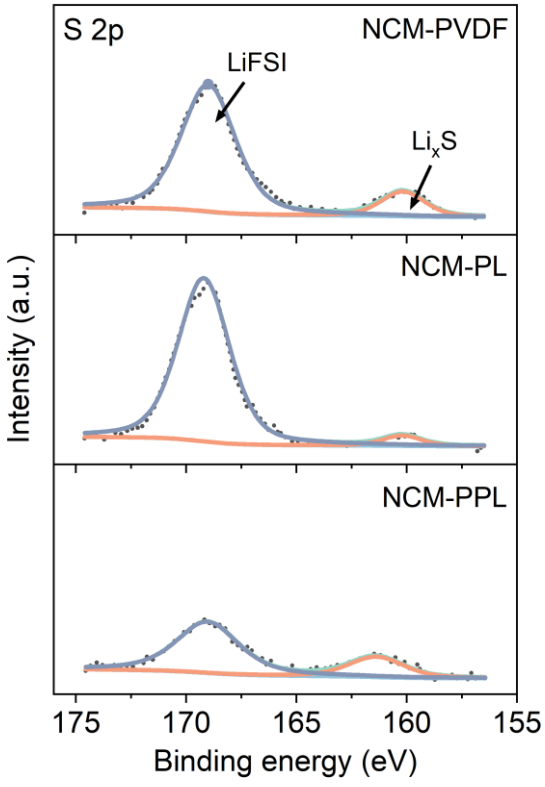
(a)


F 1s
NCM-PVDF
C-F/LiFSI
LiF
NCM-PL
NCM-PPL
Intensity (a.u.)
692
688
684
680
Binding enerrgy (eV)

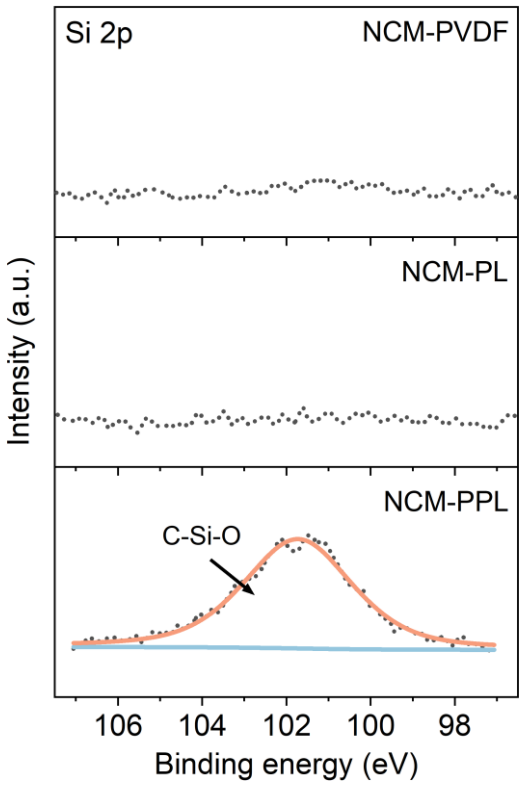
(b)


N 1s
NCM-PVDF
N-C=O
Li3N
NCM-PL
NCM-PPL
Intensity (a.u.)
408
404
400
396
392
Binding energy (eV)

(c)


S 2p
NCM-PVDF
LiFSI
LixS
NCM-PL
NCM-PPL
Intensity (a.u.)
175
170
165
160
155
Binding energy (eV)

(d)



(e)

Figure 3-39 XPS spectra for (a) C 1s, (b) F 1s, (c) N 1s, (d) S 2p and (e) Si 2p signals of NCM811 cathodes using PVDF, PL and PPL electrolytes after 100 cycles.

Figure 3-40 shows the XPS spectra for C 1s (Figure 3-40a), Si 2p (Figure 3-40b), S 2p (Figure 3-40c) and N 1s (Figure 3-40d) signals of Li-metal anodes by using PVDF electrolyte (Li-PVDF), PL electrolyte (Li-PL) and PPL electrolyte (Li-PPL). Compared to Li-PVDF and Li-PL, additional peaks of the C-Si signal in C 1s spectra and the C-Si-O signal in Si 2p spectra were observed on Li-PPL after cycling. This indicated that the PMHS participated in SEI formation. In addition, rather weak N 1s and S 2p signals were observed on the Li-PPL, indicating the distinctly reduced decomposition of DMF and Li salt. This was attributed to the PMHS-derived protective SEI that reduced the side reaction between the electrolyte and Li anode.

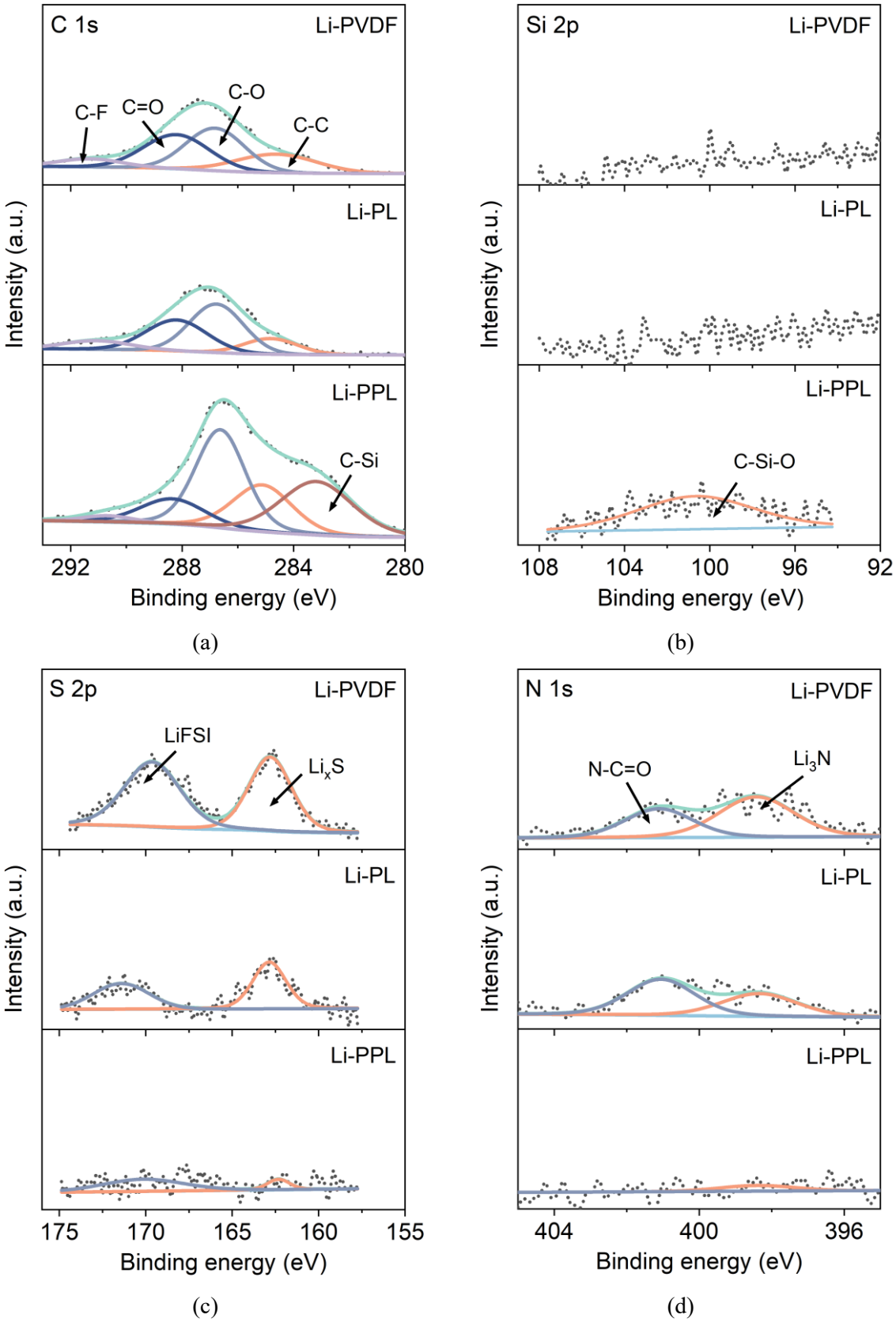
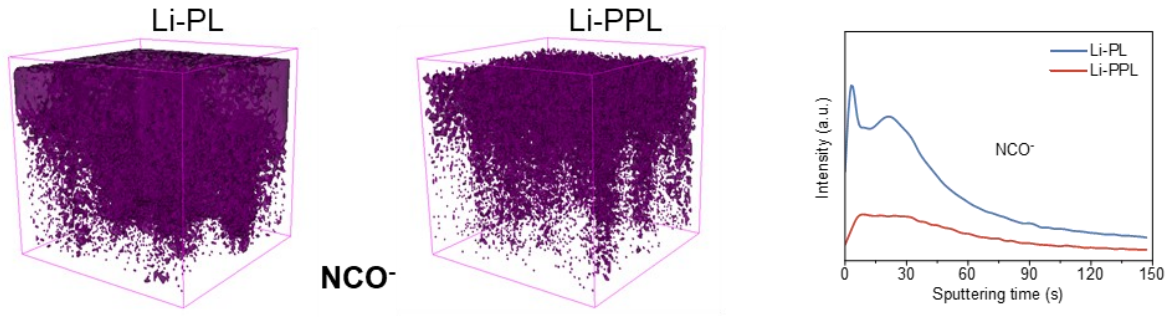
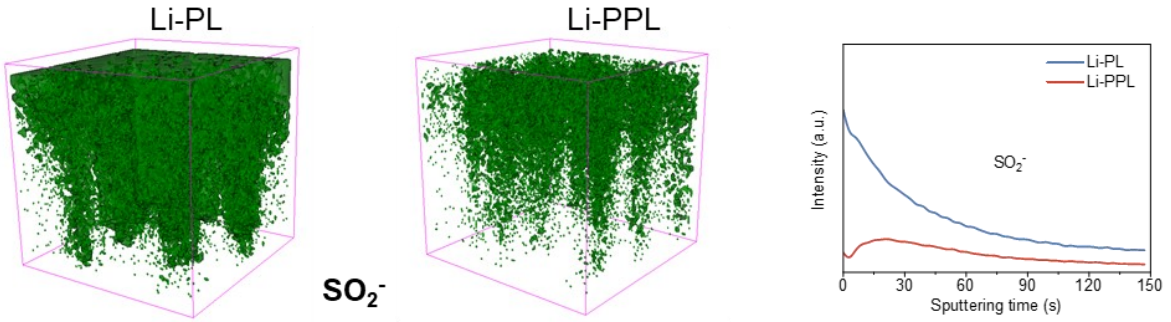


Figure 3-40 XPS spectra for (a) C 1s, (b) Si 2p, (c) S 2P and (d) N 1s signals of Li anodes using PVDF, PL and PPL electrolytes after 100 cycles.

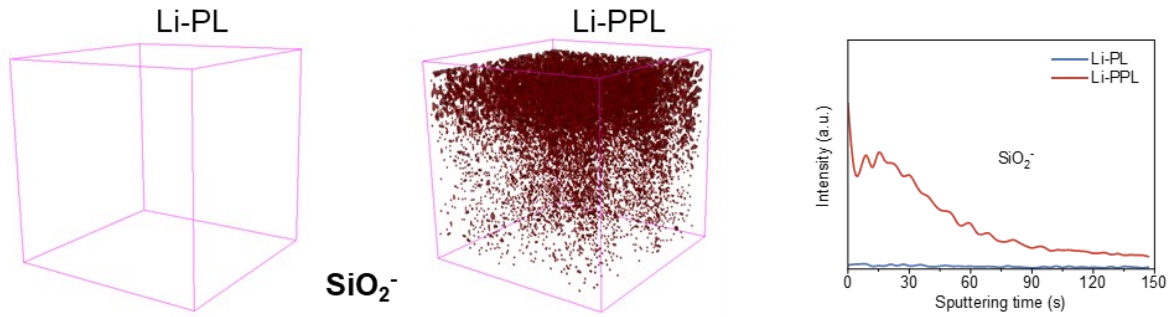
The chemical distribution of SEI at the vicinity of the Li anode surface was further characterised by ToF-SIMS. In the 3D reconstructed images and depth profiling curves of representative negative secondary ions, Li-PPL exhibited much weaker intensities of NCO^- (Figure 3-41a) and SO_2^- (Figure 3-41b) signals, indicating the reduced decomposition of both DMF solvent and Li salts on Li-PPL anode. In addition, the distribution of SiO_2^- (Figure 3-41c) and CH_3SiO^- (Figure 3-41d) signals at the near surface of Li-PPL rather than Li-PL further demonstrated the formation of PMHS-derived SEI on the Li-PPL anode. Therefore, the enhanced cycling stability of NCM811|PPL|Li solid-state batteries could be attributed to the improved structural stability of the NCM811 cathode and the Li plating behaviour of the Li-metal anode. These were achieved by the formation of protective PMHS-derived CEI and SEI as well as the improved oxidation stability of PPL electrolyte which reduced the side reaction between electrodes and electrolyte.



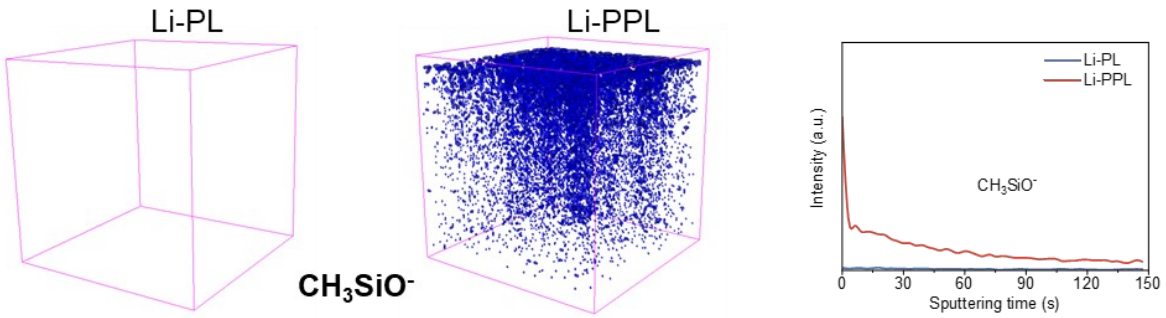
(a)



(b)



(c)



(d)

Figure 3-41 ToF-SIMS depth profiling and the 3D reconstructed images of representative negative secondary ions of (a) NCO^-, (b) SO_2^-, (c) SiO_2^- and (d) CH_3SiO^- at the vicinity of Li anode surface.

3.11 Summary

Three formable PVDF-based SSEs (pure PVDF, PL and PPL electrolytes) were developed as candidates for use in mettery. By investigating their physicochemical characteristics, electrochemical characteristics, and electrochemical performances in coin cells, the PPL electrolyte was considered the optimum SSE compared to PVDF and PL electrolytes.

In PPL electrolyte, PMHS functioning as a bridge could strongly connect the PVDF and LLZTO components, thus delivering the highest tensile strength of 3.63 MPa with a tensile strain of 31.7%. In addition, PMHS was crosslinked with PVDF to reduce the desolvation energy of Li-ions from the Li-DMF complex, which facilitated the formation of bare Li-ions and their subsequent entrance to LLZTO bulk. This activated the Li-ion pathways through LLZTO and resulted in efficient multipath Li-ion transport within the PPL electrolyte. The PPL electrolyte thereby exhibited a high ionic conductivity of 7.5×10^{-4} S cm^{-1} and a high electrochemical oxidation potential of up to 4.9 V at 25 °C.

Moreover, the PPL electrolyte showed improved compatibility with both NCM811 cathode and Li-metal anode due to the formation of PMHS-derived protective CEI and SEI that reduced side reactions. This enabled the solid-state Li|PPL|Li symmetric cells to operate an ultra-long lifespan of more than 11800 h with a small polarization voltage of ~40 mV under 0.1 mA cm^{-2}, showing a favourable Li dendrites suppression ability. The assembled solid-state NCM811|PPL|Li coin cell exhibited the least impedance, and ultrahigh long-term cycling stability with an initial specific capacity of 125.5 mAh g^{-1} and a capacity retention of 81.9% after 2200 cycles at 2C. Meanwhile, it also exhibited an excellent rate performance of 112.6 mAh g^{-1} at 5C and a reversible capacity of 168.8 mAh g^{-1} when the current density returned to 1C after 35 cycles, which was superior to the PVDF and PL electrolytes. The optimal electrochemical performance was attributed to the compact, robust, and high-conductive PPL electrolyte that suppresses the lithium dendrites penetration and facilitates ion transfer. The as-prepared

formable PPL electrolyte with high mechanical strength and ionic conductivity holds great potential to apply in mettery.

Chapter 4. Effect of plastic deformation on electrochemical performance of PPL-metteries

4.1 Introduction

In this chapter, the unique architecture for the raw material of mettery was designed in consideration of formability and structural integrity. Moreover, the effect of plastic deformations (bending and uniaxial tensile deformations) on the electrochemical performance of NCM811|PPL|Li metteries (PPL-metteries) was investigated in order to formulate a basic theoretical fundamental direction for developing mettery technology. The electrochemical-damage mechanics in plastic deformed mettery was also studied enabling further improvement.

4.2 Background

To address the impact of climate change, there has been substantial development and investment in technologies aimed at clean and renewable energy, including solar photovoltaic, geothermal, solar thermal, hydroelectric, biofuels and ocean power. Due to the negative effect on environmental and social impacts of hydroelectric generation, solar power and wind power as two major renewable energies have been considered for renewable electricity production. They have grown rapidly but still supply a small fraction of global electricity since such intermittent renewable energy challenges power systems to balance electricity demand and supply regarding their fluctuations across various geographical areas and timescales [3]. To reduce the variability and improve the reliability of such renewable energy generation, integrating low-cost and large-scale energy storage into the power system plays an important role in dispatching electricity for later use.

In this regard, electrochemical energy storage as in batteries with great potential has gradually become the main solution, enabling the reliable and cost-effective use of renewable energy. Great progress has been made in recent decades on battery energy storage technologies-specially for LIBs. In the past decades, the energy density of unit cells has been improved by exploring advanced electrode (high-nickel layered oxide cathodes and silicon-carbon anodes) and electrolyte (non-aqueous organic electrolytes with novel additives) materials. Even so, the centralised battery pack with many accessories still takes up a lot of weight and space in a system, limiting performance. Therefore, exploring lightweight and efficient energy storage systems is urgently demanded. In the most recent years, the distributed energy storage realized by embodied energy storage technology is considered a promising solution for the development of lightweight and efficient production. Although embodied energy storage technologies remain mostly in the research phase, they offer great potential to enable weight savings of up to 60% [115]. The current approaches to achieve embodied energy mainly focus on

developing structural batteries, in which the reinforcing carbon fibres were employed as electrodes, simultaneously enabling electrical energy storage up to 60 Wh/kg and mechanical function with an average strength of 300-500 MPa [107, 144].

To further explore embodied energy storage, the most used plastic deformed metal component in a device was considered an ideal energy carrier due to its high electrical conductivity and mechanical properties, which is expected to provide an energy storage solution in a wide of industries, e.g., construction, industrial equipment and transportation.

4.3 Experimental details

4.3.1 Preparation of raw material of mettery

Aluminium alloy metal sheet AA5052-H111 (80mm×32mm×1mm) was employed as the multifunctional casing material and current collector with cathode and anode materials which were coated on its surface, integrating a formable cathodic metal sheet (CMS) and an anodic metal sheet (AMS). Specifically, NCM811 slurry as cathode material and lithium metal foil with a thickness of 100 μm as anode material were coated onto the surfaces of two aluminium alloy sheets in a confined area (60mm × 8mm), leaving an insulating adhesive region at the edge for secondary operations. An insulating adhesive was applied on the aluminium sheet surrounding the anode or cathode material. The raw material of NCM811|PPL|Li mettery (PPL-mettery) was fabricated in an Ar-filled glove box (O_2 < 5 ppm, H_2O < 5 ppm) by laminating the CMS, solid-state PPL electrolyte (70mm×12mm×100μm) and AMS in order. The top and bottom aluminium sheets were bonded tightly with the superior insulating adhesive, forming hermetic integrity.

4.3.2 Preparation of bending deformed PPL-metteries

The raw materials with PPL electrolyte were formed into flat PPL-metteries by applying a normal contact pressure, which triggered the electrochemical feature of metteries. Then, these flat PPL-metteries were deformed into V-shape PPL-metteries by using a three-point bending tool with the bend radius to mettery thickness ratio (R/t) of 4.30 (bend radius: 9.2 mm), 2.33 (bend radius: 5.0 mm), 1.77 (bend radius: 3.8 mm) and 1.00 (bend radius: 2.15 mm) respectively.

4.3.3 Preparation of tensile deformed PPL-metteries

The flat PPL-metteries underwent tensile deformations with the strains of 0.5%, 5%, 10% and 15% respectively by uniaxial tensile tests. The three-point bending tests and uniaxial tensile tests were conduct at a constant speed of 1mm/min by using a Universal Testing Machine (INSTRON 5982).

4.3.4 Electrochemical characterization of plastic deformed PPL-metteries

EIS of as-prepared plastic deformed PPL-metteries was recorded in a frequency ranging from 5 MHz to 100 mHz with an electrochemical workstation at 25 °C. Galvanostatic charge and discharge tests of the plastic deformed PPL-metteries were carried out on the LAND system (Figure 4-1) with a voltage ranging from 2.8 to 4.3 V at 25 °C. The PPL-metteries were activated at a charge-discharge current density of 0.1C at the first three cycles.

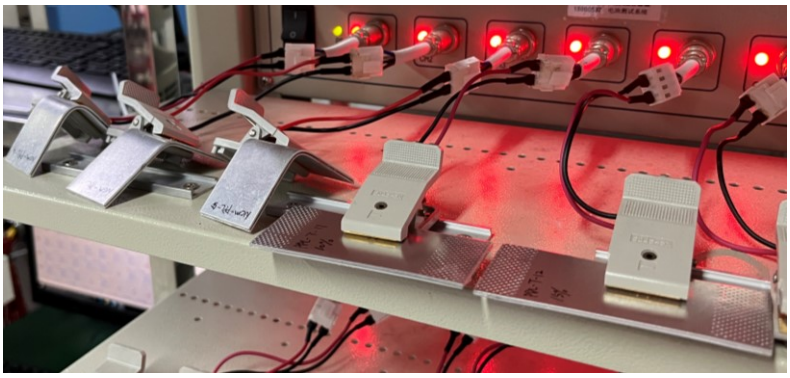


Figure 4-1 Galvanostatic charge and discharge tests of plastic deformed PPL-metteries on the LAND system.

4.4 Architecture of the raw material of mettery

To develop a mettery that incorporates electrical energy storage function into the metal component by metal forming technologies, the structural integration of metal and battery should be dramatically realized. Figure 4-2 shows a designed architecture of the raw material of mettery. It is composed of a formable cathodic metal sheet (CMS), a formable anodic metal sheet (AMS) and a formable SPE. Formable cathode, anode and electrolyte adopted in the raw material of mettery are expected to be robust enough to withstand mechanical stress in the deformation process, avoiding the disintegration of structure and the cracks of electrodes and electrolyte materials. Considering this, cathode and anode materials are directly coated onto stiff and strong aluminium alloy sheets to obtain a CMS and AMS. This is in favour of forming a highly robust and formable integrated configuration, in which the electrode material is tightly bound to the surface of the aluminium alloy sheet without relative displacement. The aluminium alloy sheet works as a current collector that efficiently transports electrical current and also a casing that hermetically encloses the electrode materials and SPE, offering protection against paretic reaction with the ambient atmosphere. The absence of conventional aluminium and copper foil as current collectors will effectively streamline the fabrication process and reduce the cost. Formable PPL electrolyte sandwiched between CMS and AMS prevents short circuit while conducting ions through the motion of polymer chains, improving the mechanical properties and

addressing safety problems caused by the liquid organic electrolyte. Moreover, due to easily packing property, it is helpful to simplify the manufacturing process and thus mass-produce the mettery. The conventional metal component in a system assembled and integrated into a raw material with a sandwich structure can be further formed into mettery with electrical energy storage through metal forming.

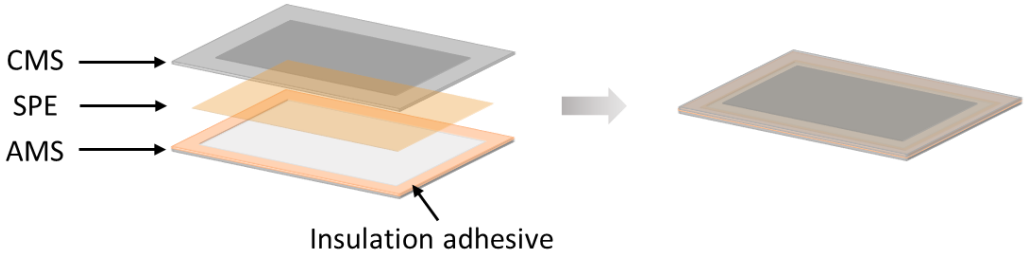
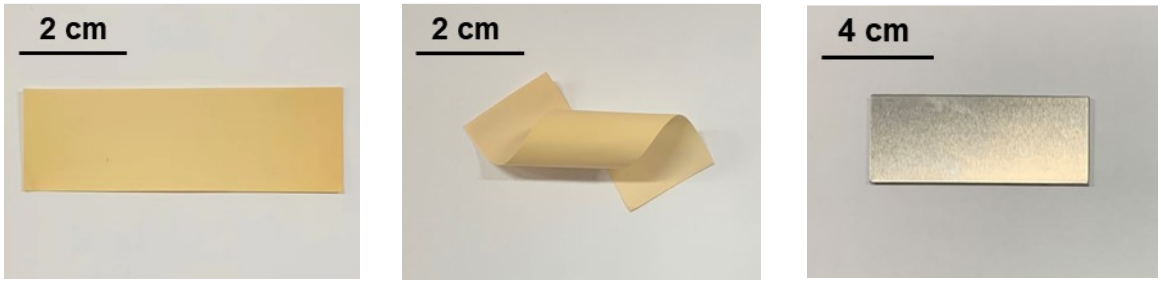


Figure 4-2 The sandwich architecture of the raw material of mettery.

4.5 PPL-metteries manufactured by metal forming technologies

Figure 4-3 shows the optical photography of the PPL electrolyte and the raw material of mettery assembled with NCM811 CMS, lithium AMS and PPL electrolyte.



(a) (b) (c)

Figure 4-3 (a, b) Optical photography of formable PPL electrolyte and (c) the raw material of PPL-mettery.

The as-assembled formable raw material with the thin, flat sandwich architecture could be efficiently deformed into the mettery with geometries as specified, by using metal forming technologies. The applied normal contact pressure during the metal forming process enables the PPL electrolyte closely bound with the cathode and anode materials, forming a tight electrode/electrolyte interface. This would further trigger the electrochemical property of mettery. Figure 4-4 exhibits the plastic deformed metteries with V-shape, M-shape and U-shapes, which can light an LED.

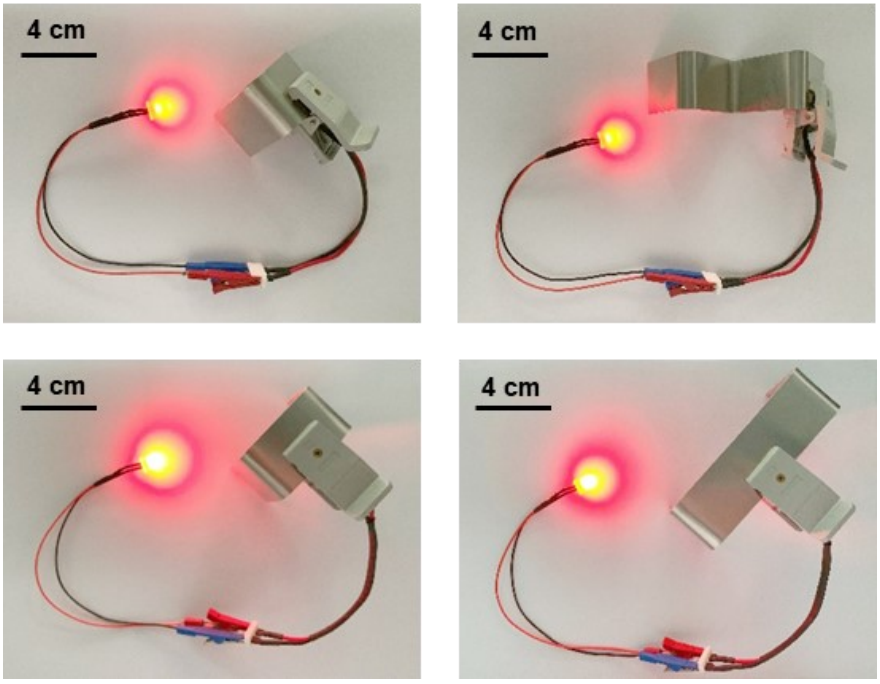
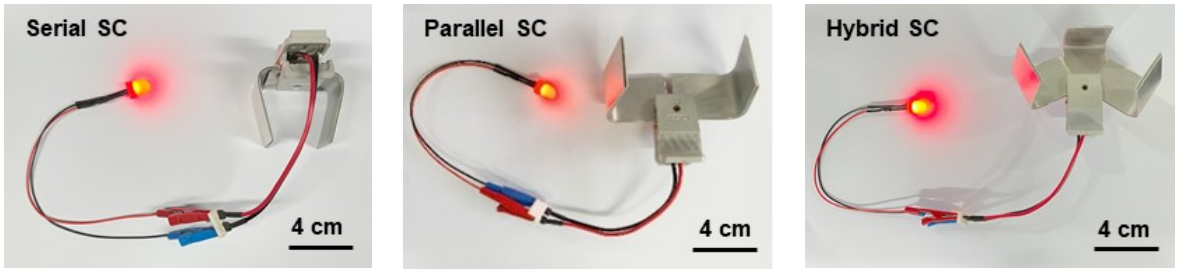


Figure 4-4 LED lighted by plastic deformed metteries.

Furthermore, multiple metteries can be integrated into a serial, parallel or hybrid structural circuit (SC), lighting an LED, as shown in Figure 4-5. The SCs enabling desired voltages and current levels can be assembled by using welding or self-rivet piercing, providing more design flexibility and high energy.



(a) (b) (c)

Figure 4-5 LED lighted by (a) serial SC, (b) parallel SC and (c) hybrid SC assembled by V-shape metteries.

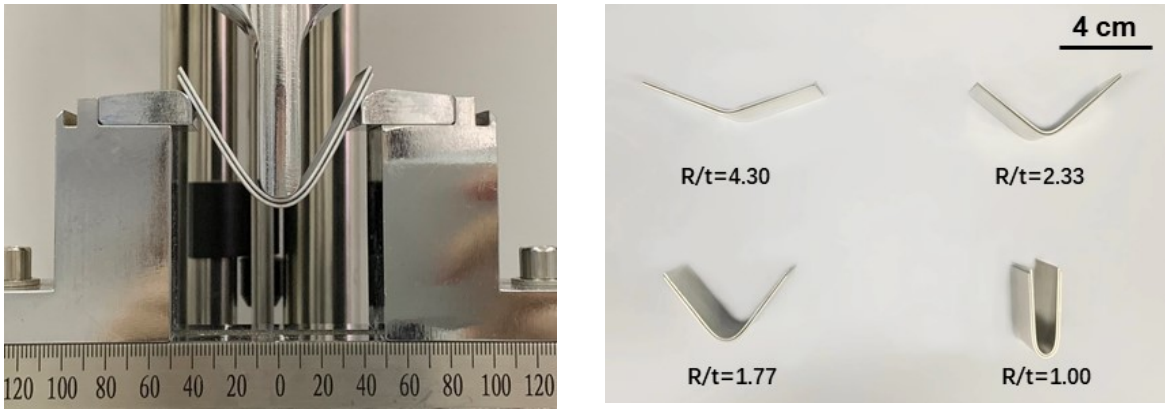
Figure 4-6 depicts the plastic deformed metteries, which can be used as metal components playing a mechanical and structural function in a system and at the same time, storing electrical energy. Metteries with various geometries are promising to cover a wide range of applications, such as consumer electronics, transportation and furniture etc.



Figure 4-6 Metteries with various geometries manufactured by metal forming technologies.

4.6 Effect of bending deformation on the electrochemical performance of PPL-mettery

Figure 4-7 shows the PPL-metteries formed by increasing plastic bending deformations with bend radius to mettery thickness ratio (R/t) of 4.30 (bend radius: 9.2 mm), 2.33 (bend radius: 5.0 mm), 1.77 (bend radius: 3.8 mm) and 1.00 (bend radius: 2.15 mm), respectively. To investigate the effect of bending deformation on the electrochemical performance of PPL-mettery, EIS and charge-discharge galvanostatic cycling of PPL-metteries with different bending radius ratios were studied.

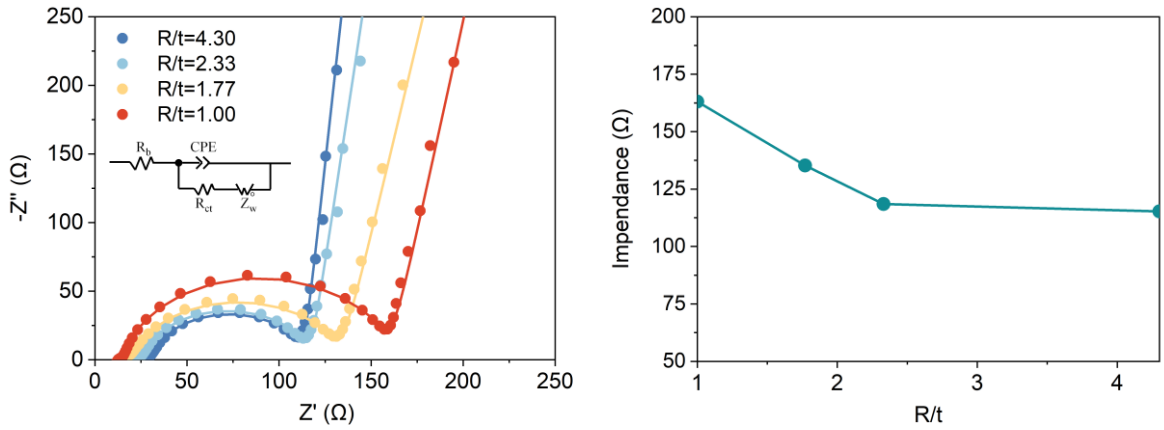


(a) (b)

Figure 4-7 (a) Bending deformed PPL-mettery formed by using three-point bending tool and (b) optical photography of bending deformed PPL-metteries with bend radius to mettery thickness ratio (R/t) of 4.30 (bend radius: 9.2 mm), 2.33 (bend radius: 5.0 mm), 1.77 (bend radius: 3.8 mm) and 1.00 (bending radius: 2.15 mm).

4.6.1 EIS of bending deformed PPL-metteries

Figure 4-8 (a) shows the Nyquist plots of as-prepared bending deformed PPL-metteries at 25 °C. The EIS fitting was conducted according to the equivalent circuit (inside in Figure 4-8a) with the results shown in Figure 4-8 (b). The impedances of PPL-mettery with R/t of 4.3, 2.33, 1.77 and 1 were 115.3, 118.46, 135.24 and 163.09 Ω respectively, showing an increasing trend with the decrease of bending radius ratios (Figure 4-8b). The effect of bending deformation on the increase of impedance was slight (less than 17.3%) when the bending radius ratio was greater than 1.77, suggesting that the localised plastic deformation caused a minor effect on the impedance of PPL-mettery. In comparison, when the bending radius ratio was less than 1, the bending deformation caused an obvious increase in impedance by at least 41.4% compared to PPL-mettery (R/t=4.30).



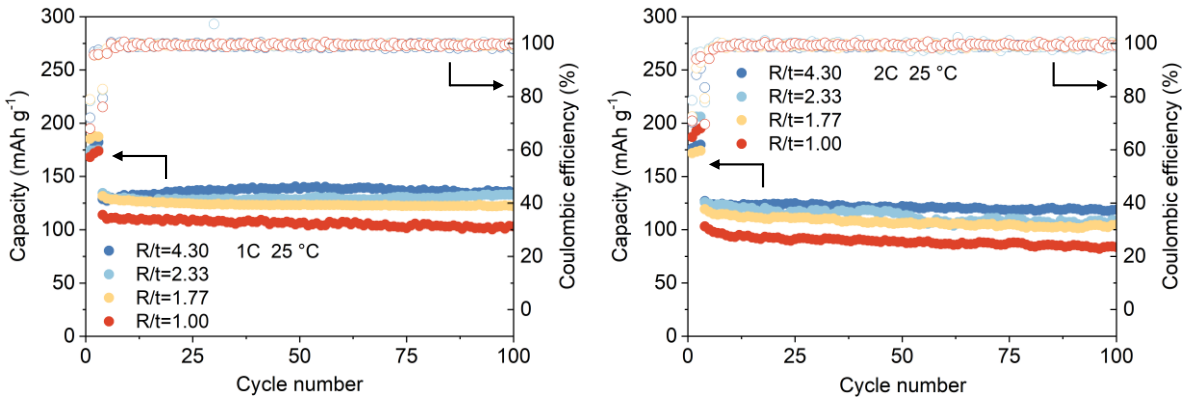
(a) (b)

Figure 4-8 (a) EIS plots of bending deformed PPL-metteries with the equivalent circuit inside and (b) the effect of bending deformation on the impedance of PPL-metteries.

4.6.2 Cycling performance of bending deformed PPL-metteries

Figure 4-9 shows cycling performance and coulombic efficiency of bending deformed PPL-metteries over 100 charge-discharge cycles under the current densities of 1C and 2C. PPL-mettery with R/t of 4.3, 2.33, 1.77 and 1 delivered initial specific capacities of 128.7, 134.4, 131.6 and 113.9 mAh g^{-1}, retaining capacities of 134, 132.9, 122.1 and 103.2 mAh g^{-1} after charge-discharge for 100 cycles at 1C (Figure 4-9a). The PPL-metteries (R/t>1.77) showed almost constant capacity and cycling stability. In contrast, the capacity of PPL-mettery (R/t=1) decreased by 23% after 100 cycles compared to mettery (R/t=4.3). At a higher current rate of 2C (Figure 4-9b), the PPL-mettery with R/t of 4.3, 2.33, 1.77 and 1 delivered the initial capacities of 126.8, 125.8, 119.2 and 103.1 mA h g^{-1} with capacity retentions of 93.7%, 86.4%, 87.8% and 81.3% respectively after 100 cycles, showing a slight decreasing cyclability with the increase of bending deformations.

These results indicated that the detrimental effect of bending deformation on the specific capacity and cycling stability of mettery (R/t>1.77) was negligible over 100 cycles. More specifically, the PPL-mettery (R/t>1.77) exhibited a minor capacity decrease of less than 8.9% at 1C and less than 12% at 2C. Although the micro-cracks within the cathode caused by bending deformation could partially destroy the integrity of the conductive path and thus limited the capacity, the reduction in capacity retention of PPL-mettery after cycling was not significant. This indicated the micro-cracks caused by bending deformation had a minor effect on the cycling stability of the PPL-mettery.



(a) (b)

Figure 4-9 Cycling performance and coulombic efficiency of bending deformed PPL-metteries at a current density of (a) 1C and (b) 2C at 25°C.

To directly display the correlation between the bending deformation and electrochemical evolution of the PPL-mettery, the bending radius ratios against specific capacity at different cycling numbers of 5, 10, 50 and 100 under the current densities of 1C and 2C were depicted (Figure 4-10). At the current density of 1C (Figure 4-10a), the specific capacity of PPL-metteries showed a negligible decrease trend with the decrease of the R/t ratios from 4.3 to 1.77. In comparison, PPL-mettery (R/t=1) displayed an evident decrease in the specific capacity. Compared to PPL-mettery (R/t=4.3), PPL-mettery (R/t=1) showed capacity degradations of approximately 13.4%, 15.3%, 23.8% and 23% at the 5th, 10th, 50th and 100th cycles, respectively.

At the current density of 2C (Figure 4-10b), a similar but more obvious overall trend can be observed, namely, specific capacity decreased with the decrease of R/t ratios. Compared to PPL-mettery (R/t=4.3), PPL-mettery (R/t=1) showed capacity degradations of approximately 19.3%, 24.3%, 27.4% and 29.5% at the 5th, 10th, 50th and 100th cycles, respectively. In addition, specific capacity also decreased with the increase in cycling numbers. PPL-mettery (R/t=1) delivered a higher capacity degradation at a higher current density of 2C than at 1C. Higher current density could accelerate the partial micro-cracks

of the cathode after the severe local plastic deformation, thus causing higher capacity fading during mettery cycling.

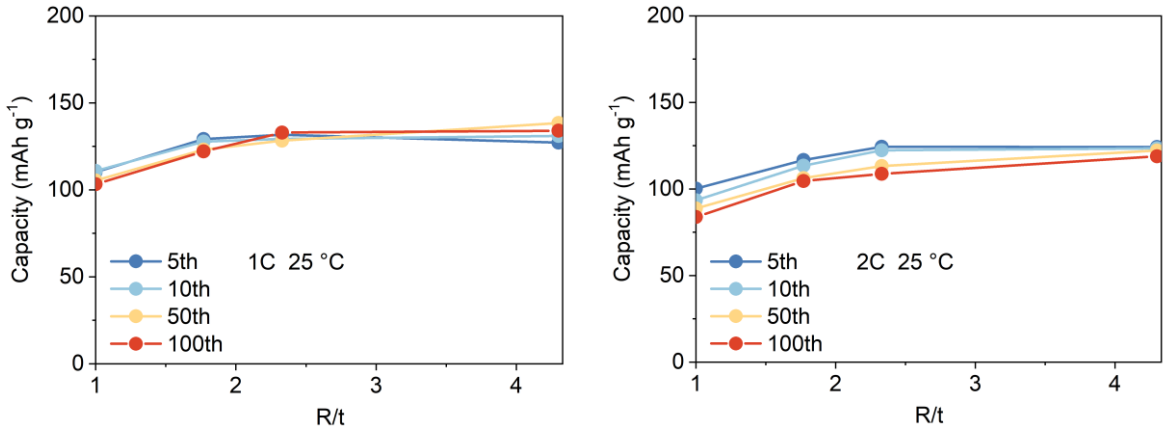
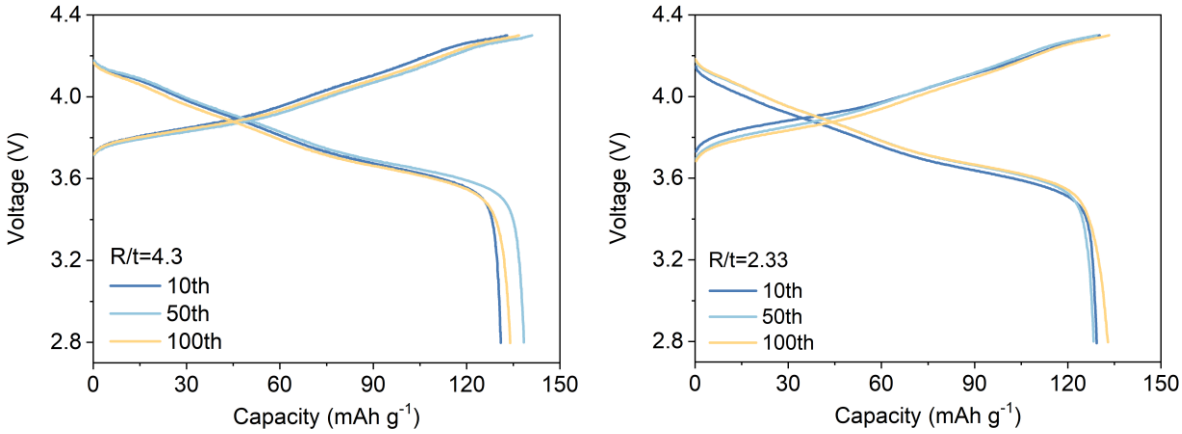
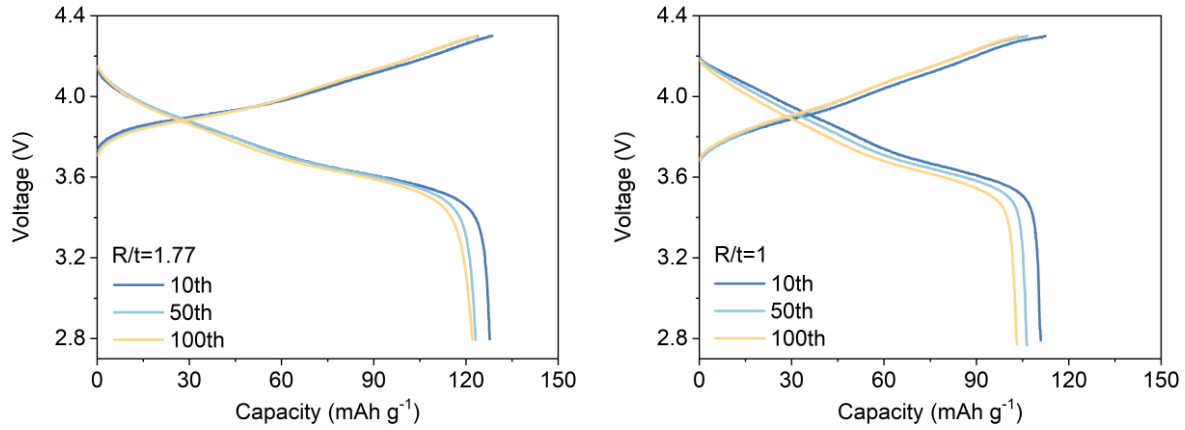


Figure 4-10 Effect of bending deformation on the specific capacity of PPL-metteries at different cycles at the current densities of (a) 1C and (b) 2C at 25 °C.

Figure 4-11 shows charge-discharge curves of bending deformed PPL-metteries (R/t ratios from 1 to 4.3) ranging from 2.8 to 4.3V at the 5th, 50th and 100th cycles at the current density of 1C. There was only a small difference in specific capacity during the cycling process, indicating that PPL-mettery could maintain a stable interface between electrodes and PPL electrolyte after bending deformation.





(c) (d)

Figure 4-11 Galvanostatic charge-discharge profiles of bending deformed PPL-metteries with R/t of (a) 4.3, (b) 2.33, (c) 1.77 and (d) 1 at the current density of 1C at 25 °C.

4.6.3 Rate performance of bending deformed PPL-metteries

The rate performance of bending deformed PPL-metteries is shown in Figure 4-12. Bending deformed PPL-mettery (R/t=4.30) delivered specific capacities of 185, 174.5, 158.4, 127.6, 110.1 and 86.5 mA h g^{-1} at the current densities of 0.2C, 0.5C, 1C, 2C, 3C and 5C, respectively. When the current density returned to 1C, a reversible capacity of 156.9 mA h g^{-1} was still achieved after 55 cycles, indicating outstanding stability of the PPL-mettery (R/t=4.30). The bending deformed PPL-mettery (R/t>1.77) showed negligible capacity degradation of less than 9.2% at 5C and less than 7% at 1C after 55 cycles compared to PPL-mettery (R/t=4.30), which demonstrated the favourable rate performance of bending deformed mettery when R/t was greater than 1.77. In comparison, the PPL-mettery (R/t=1) showed an evident capacity fading of 43% at 5C and 16% at 1C after 55 cycles compared to the PPL-mettery (R/t=4.30).

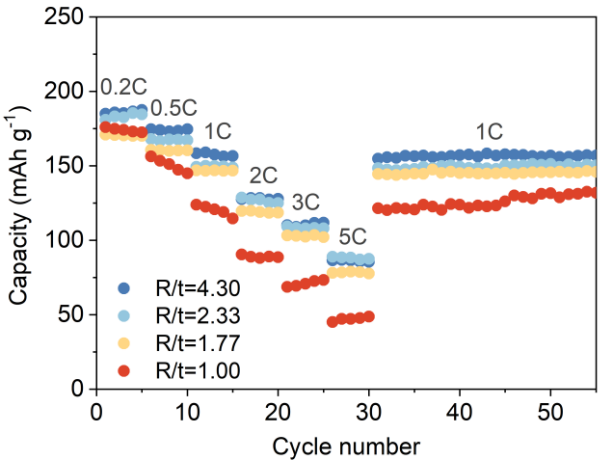


Figure 4-12 Rate performance of bending deformed PPL-metteries at 25 °C.

Figure 4-13 shows experimental and modelling results for the effect of the charge-discharge current rate and bending radius-thickness ratio on the specific capacity of bending deformed PPL-metteries, according to equation (4): an empirical model for predicting the specific capacity of a bending deformed PPL-mettery with bending radius ratios from 1 to 4.3, at the current density from 0.2C to 5C.

$$C = C_{THEO} exp(-\gamma Rate) + k\frac{R}{t} - C_{min} \quad (4)$$

Where C is the specific capacity of a bending deformed PPL-mettery; Rate is the charge-discharge current rate, ranging from 0.2C to 5C; R/t is the bend radius to mettery thickness ratio during bending deformation; C_{min} is the minimum capacity; C_{THEO} is the theoretical specific capacity of PPL-mettery; k is the impact factor for the effect of bending deformation on the specific capacity of PPL-mettery and γ is the impact factor for the effect of current rate on the specific capacity of PPL-mettery. The model constants are shown in Table 4-1.

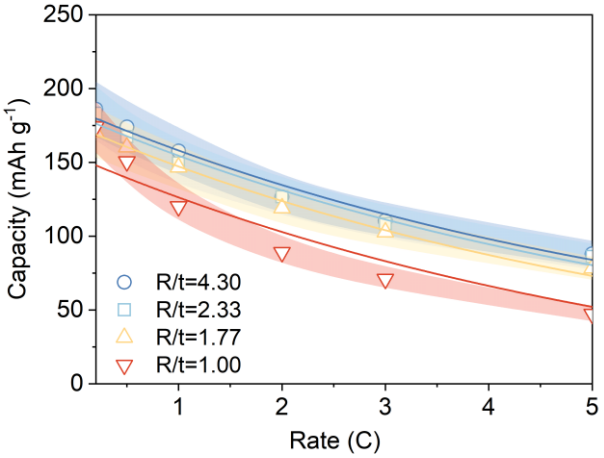


Figure 4-13 Experimental and modelling results for the effect of rate on the specific capacity of bending deformed PPL-metteries at 25 °C.

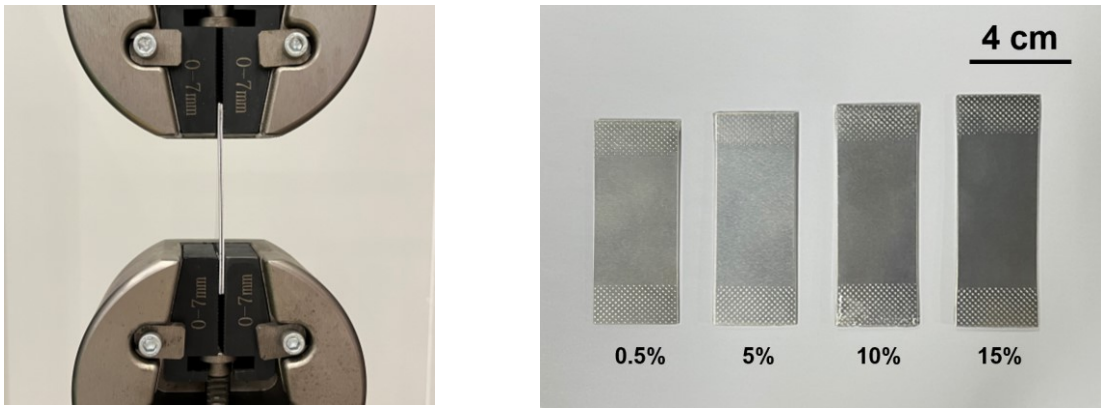
Table 4-1 Values of constants in equation (4).

Constant	C_{min} (mAh/g)	C_{THEO} (mAh/g)	k	γ
Value	25.3	180	8.3	0.17

4.7 Effect of uniaxial tensile deformation on the electrochemical performance of PPL-mettery

Figure 4-14 shows the optical pictures of the PPL-metteries with tensile strains of 0.5%, 5%, 10% and 15% formed by applying uniaxial tensile tests. Figure 4-15 shows the uniaxial tensile strain-stress curve of the PPL-mettery. The results revealed a yield strength of 132 MPa and an ultimate tensile strength

(UTS) of 204 MPa. The strain to failure was 15.6%. To investigate the effect of uniaxial tensile deformation on the electrochemical performance of PPL-mettery, EIS and charge-discharge galvanostatic cycling of PPL-metteries with different tensile strains were studied.



(a) (b)

Figure 4-14 (a) Mettery formed by applying uniaxial tensile test and (b) the tensile deformed PPL-metteries with tensile strains of 0.5%, 5%, 10% and 15%.

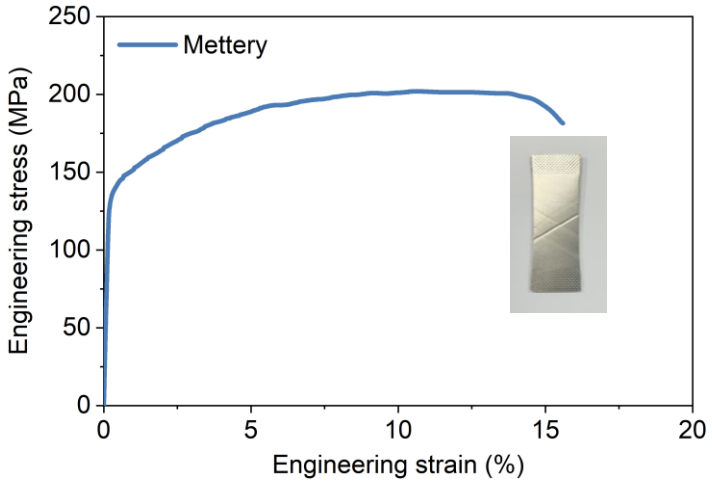
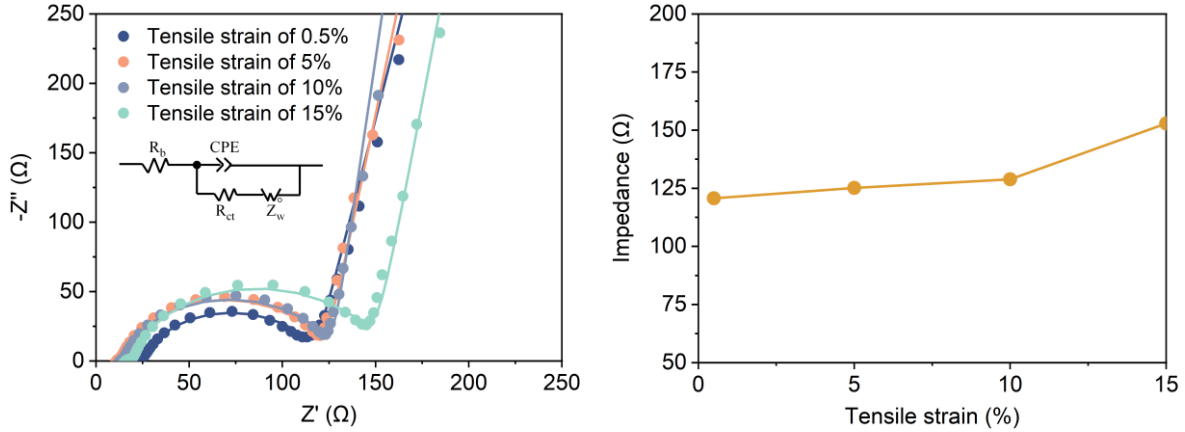


Figure 4-15 Uniaxial tensile strain-stress curve of PPL-mettery.

4.7.1 EIS of tensile deformed PPL-metteries

Figure 4-16 (a) shows the Nyquist plots of tensile deformed PPL-metteries with tensile strains of 0.5%, 5%, 10% and 15% at 25 °C respectively. To investigate the effect of tensile deformation on impedance, the EIS fitting was conducted according to the equivalent circuit (in Figure 4-16a) with the results shown in Figure 4-16 (b). The impedances of PPL-mettery with tensile strains of 0.5%, 5%, 10% and 15% were 120.64, 125.11, 128.89 and 152.9 Ω respectively, showing an increasing trend with the increase of tensile strains (Figure 1b). This was attributed to the microstructure damages of PPL electrolyte and electrode materials by higher uniaxial tensile deformation. The tensile deformation

caused the increase of impedance by 6.8% to 26.7% after suffering tensile deformation with the tensile strain from 10% to 15%, while the effect of tensile deformation on the impedance of PPL-metteries (tensile strain<10%) was negligible.



(a) (b)

Figure 4-16 (a) EIS plots of PPL-metteries formed by applying uniaxial tensile deformation with the equivalent circuit inside and (b) the effect of uniaxial tensile deformation on the impedance of PPL-metteries.

4.7.2 Cycling performance of tensile deformed PPL-metteries

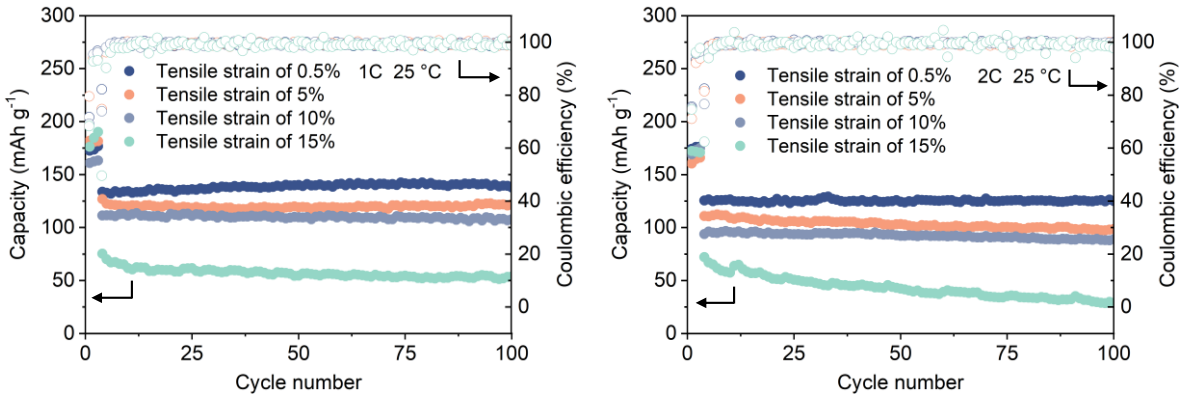
It has been found that the capacity degradation of structural battery correlate with the increase in resistance and mechanical strain [145]. In PPL-mettery, severe uniaxial tensile deformation could cause the structure destruction of the NCM811 cathode and PPL electrolyte. The microstructure of NCM811 materials might be partially destroyed after tensile deformation during charge-discharge cycling, leading to poorer contact between the conductive agent and active particles. Therefore, the utilisation of active particles in the NCM811 cathode was reduced with the loss of electrical contact partially and the decrease of conductivity. Besides, the micro-cracks of PPL electrolyte after tensile deformation would cause a decrease in the ability to conduct Li-ion and an increase in polarisation. The micro-cracks in PPL electrolyte could also partly destroy the structure of PVDF chains as well as the bridge connection between PVDF and LLZTO by PMHS. All these effects isolated the ionic conducting pathways, leading to sluggish Li-ion transport in the PPL electrolyte.

Figure 4-17 shows cycling performance and coulombic efficiency of tensile deformed PPL-metteries (tensile strains of 0.5%, 5%, 10% and 15%) over 100 charge-discharge cycles under current densities of 1C and 2C respectively. It was found that the specific capacity decreased with the increase of tensile strains. As shown in Figure 4-17 (a), the PPL-mettery with tensile strains of 0.5%, 5% and 10% delivered the initial capacities of 133.8, 126.9 and 111.3 mAh g^{-1}, and retained the capacities of 137.8,

122 and 107.9 mAh g^{-1} respectively after 100 cycles at 1C. The PPL-mettery (tensile strain>10%) formed by applying uniaxial tensile deformation showed a decreased capacity of more than 16.8% in the initial cycle and 21.7% after 100 cycles compared to the PPL-mettery (tensile strain of 0.5%). When the tensile strain reached 15%, the PPL-mettery showed an initial capacity of 75.3 mAh g^{-1} and retained capacity of 53.8 mAh g^{-1} after 100 cycles, showing a significant initial capacity degradation of 43.7% and capacity degradation of 61% after 100 cycles compared to PPL-mettery (tensile strain of 0.5%).

At a higher current density of 2C (Figure 4-17b), PPL-metteries exhibited lower specific capacity and cycling stability over 100 cycles compared to that at 1C. More specifically, PPL-metteries with tensile strains of 0.5%, 5% and 10% delivered initial capacities of 125.6, 110.9 and 93.8 mAh g^{-1}, with capacity retentions of 99.5%, 88.8% and 94.8% respectively after 100 cycles at 2C. Compared to the PPL-mettery (tensile strain of 0.5%), the PPL-mettery (tensile strain>10%) showed a capacity decrease of more than 25.3% in the initial cycle and more than 28.9% after 100 cycles. However, PPL-mettery (tensile strain of 15%) delivered an initial specific capacity of 72.1 mAh g^{-1} and capacity retention of 39.8% after 100 cycles, showing a great degradation in cycling performance

The cycling performances demonstrated the detrimental effect of uniaxial tensile deformation on the capacity of PPL-mettery was pronounced (degradation of 21.7% at 1C and 28.9% at 2C after 100 cycles) when the tensile strain was more than 10%.



(a) (b)

Figure 4-17 Cycling performance and coulombic efficiency of tensile deformed PPL-metteries at a current density of (a) 1C and (b) 2C at 25°C.

To directly display the correlation between the uniaxial tensile deformation and electrochemical evolution of the PPL-mettery, tensile strain against specific capacity at different cycling numbers of 5, 10, 50 and 100 under 1C (Figure 4-18a) and 2C (Figure 4-18b) were depicted. At both current densities of 1C and 2C, the PPL-mettery showed a significant specific capacity drop trend when then tensile strain was more than 10%. On the other hand, the specific capacity of PPL-mettery (tensile strain>10%)

decreased with the increase of cycle number during cycling, indicating that tensile deformation also exerted a negative effect on cycling stability.

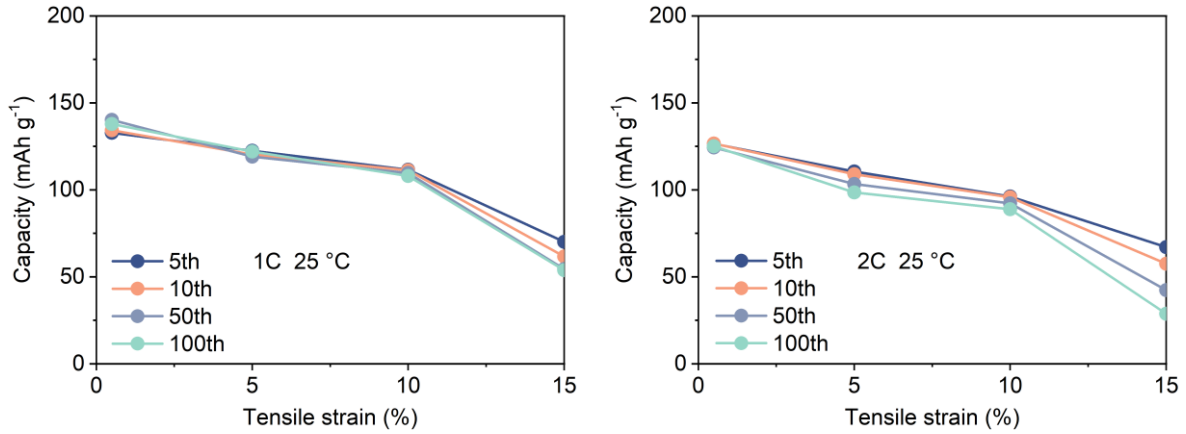
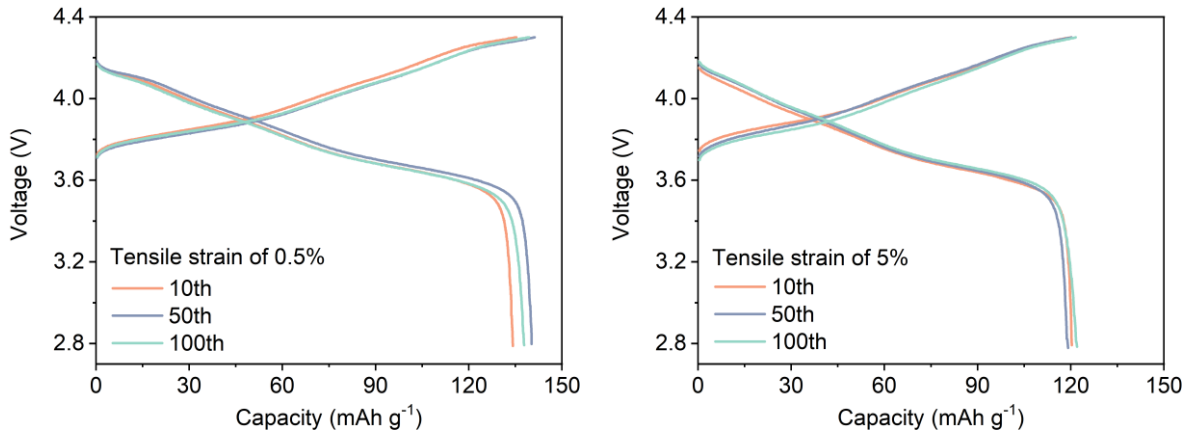
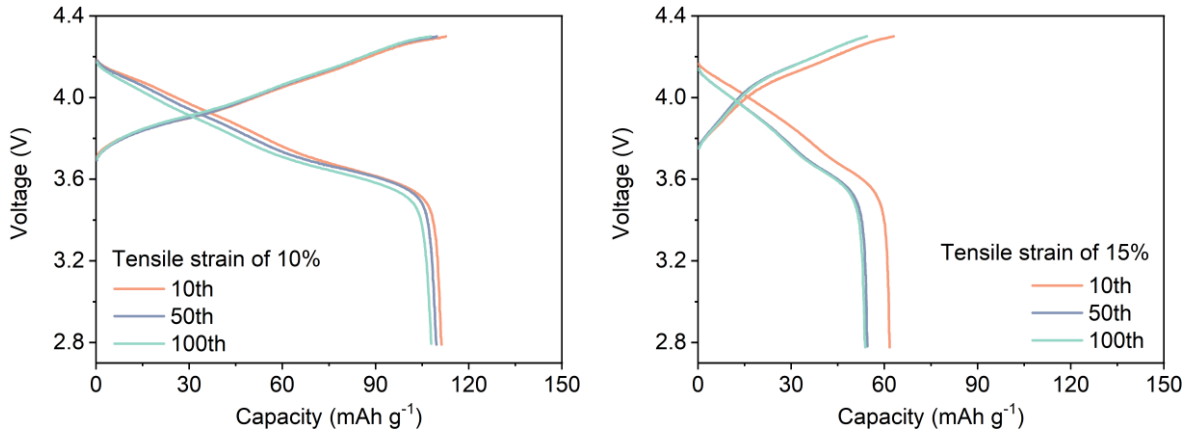


Figure 4-18 Effect of uniaxial tensile deformation on the specific capacity of PPL-metteries at 5th, 10th, 50th and 100th at a current density of (a) 1C and (b) 2C at 25 °C.

Figure 4-19 illustrates the corresponding charge-discharge curves of tensile deformed PPL-metteries with tensile strains of 0.5% (Figure 4-19a), 5% (Figure 4-19b), 10% (Figure 4-19c) and 15% (Figure 4-19d) cycled between 2.8V-4.3V at the current density of 1C. The PPL-mettery (tensile strain of 15%) not only delivered an obvious capacity decrease but also a larger difference in specific capacity after the 100th cycle, which was mainly attributed to poorer interfacial stability and higher resistance during the cycling process caused by excessive tensile deformation when the tensile strain was more than 10%.





(c) (d)

Figure 4-19 Galvanostatic charge-discharge profiles of PPL-metteries formed by applying uniaxial tensile deformation with the tensile strains of (a) 0.5%, (b) 5%, (c) 10% and (d) 15% at 1C at 25 °C.

4.7.3 Rate performance of tensile deformed PPL-metteries

Figure 4-20 shows the specific capacities of the PPL-metteries at increasing current rates from 0.2C to 5C. It was found that the specific capacity of PPL-metteries decreased with the increase in current densities, especially at the high current density of 5C. The sluggish transport of Li-ion from the cathode to the anode in tensile deformed PPL-mettery was the rate-determining step during the fast charge process, which led to concentration polarisation on the surface of the anode. This could further cause electron accumulation on the anode and made the PPL-mettery reach the cut-off voltage before fully charging at a high current density, hence leading to capacity degradation. Moreover, it was noted that the increased impedance for the tensile deformed PPL-mettery could aggravate the polarisation due to the hindrance in Li-ion transport, further decreasing the rate capability.

The PPL-mettery (tensile strain of 0.5%) achieved a capacity of 190.6, 177.7, 162, 133.3, 112.5 and 81.5 mAh g^{-1} at 0.2C, 0.5C, 1C, 2C, 3C and 5C. When the current density returned to 1C, a reversible capacity of 149.2 mAh g^{-1} was obtained after 55 cycles, indicating superior rate performance. Regarding PPL-metteries with tensile strains of 5%, 10% and 15%, there was an increasing capacity degradation compared to PPL-mettery (tensile strain of 0.5%). Particularly, the PPL-mettery (tensile strain of 15%) showed an evident capacity fading of 65.4% at 5C and 35.7% at 1C after 55 cycles compared to the mettery (tensile strain of 0.5%).

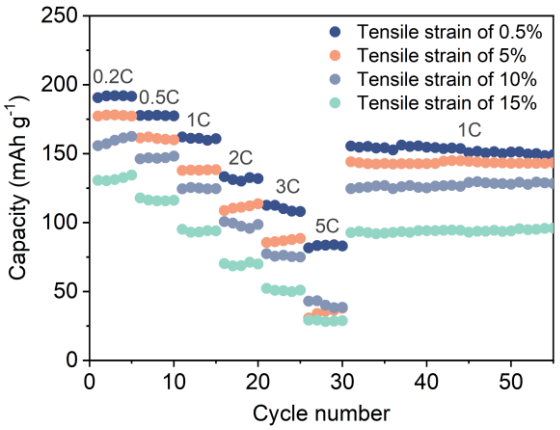


Figure 4-20 Rate performance of uniaxial tensile deformed PPL-metteries at 25 °C.

Figure 4-21 depicts experimental and modelling results for the effect of the charge-discharge current rate and tensile strain on the specific capacity of tensile deformed PPL-metteries, according to equation (5): an empirical model for predicting the specific capacity of a tensile deformed PPL-mettery with the tensile strain from 0.5% to 15%, at the current density from 0.2C to 5C.

$$C = C_{min} - k\varepsilon + C_{THEO}exp(-\gamma Rate) \quad (5)$$

Where C is the specific capacity of a tensile deformed PPL-mettery; Rate is the charge-discharge current rate, ranging from 0.2C to 5C; ε is the tensile strain of PPL-mettery during uniaxial tensile deformation, ranging from 0.5% to 15%; C_{min} is the minimum capacity; C_{THEO} is the theoretical specific capacity of PPL-mettery; k is the impact factor for the effect of uniaxial tensile deformation on the specific capacity of PPL-mettery and γ is the impact factor for the effect of current rate on the specific capacity of PPL-mettery. The model constants are shown in Table 4-2.

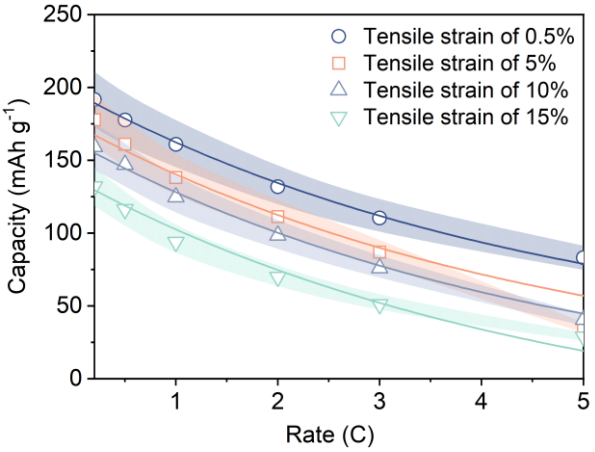


Figure 4-21 Experimental and modelling results for the effect of current rate on the specific capacity of tensile deformed PPL-metteries.

Table 4-2 Values of constants in equation (5).

Constant	C_{min} (mAh/g)	C_{THEO} (mAh/g)	k	γ
Value	16.5	180	380	0.21

4.8 Electrochemical-damage mechanics in tensile deformed PPL-metteries

4.8.1 Microstructures of tensile deformed electrodes and PPL electrolytes

To investigate the electrochemical-damage mechanics in tensile deformed PPL-mettery. The micro morphologies of tensile deformed NCM811 cathodes, Li-metal anodes and PPL solid-state electrolytes with tensile strains of 0.5%, 5%, 10% and 15% were studied by SEM. Figure 4-22 shows SEM images of MCM811 cathodes with different tensile strains. NCM811 showed smooth single-crystalline particle structures with small conductive additive particles (Super P) around them. It was found that the NCM811 structure almost maintained contact after tensile deformation with the tensile strains of 0.5%, 5%, 10% and 15%.

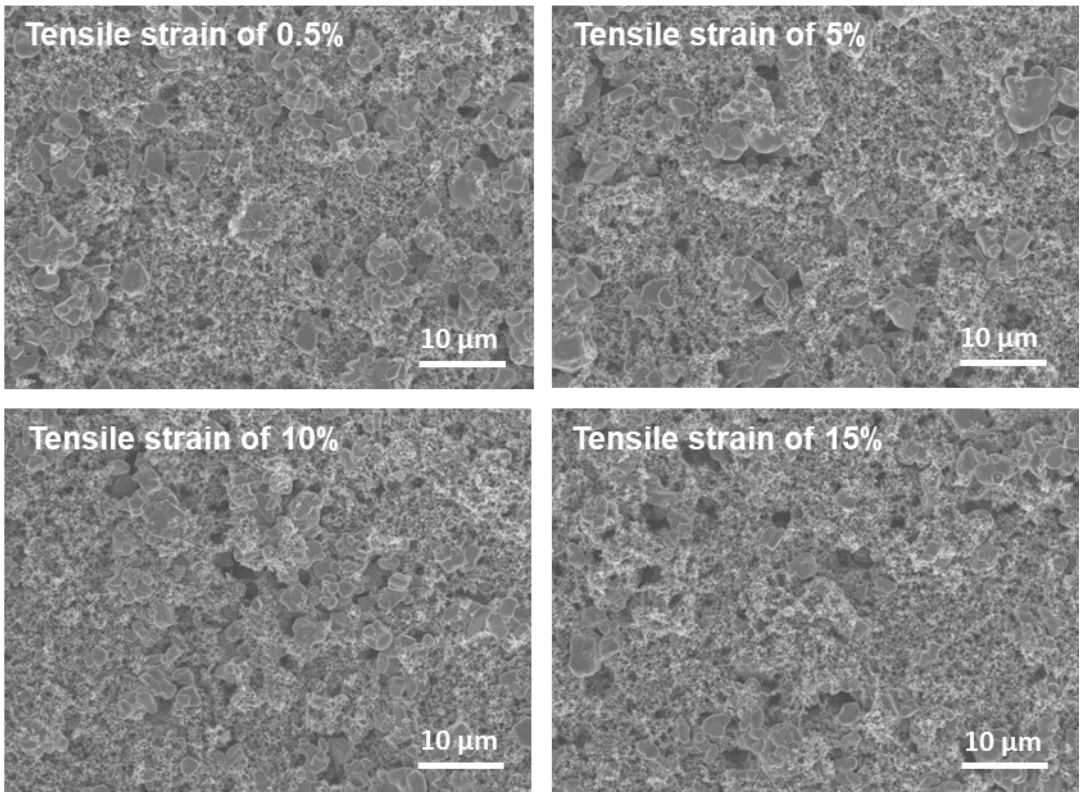


Figure 4-22 SEM images of NCM811 cathodes with the tensile strains of 0.5%, 5%, 10% and 15%.

As shown in Figure 4-23, the microstructure of fresh Li-metal anode with different tensile strains also showed no obvious difference from SEM images. There were no fractures or micro-cracks even on the surface of tensile deformed Li metal with a tensile strain of 15%. The high ductility property of Li metal that could suffer from mechanical deformations without any structural damage indicated that it would be appropriately used in mettery.

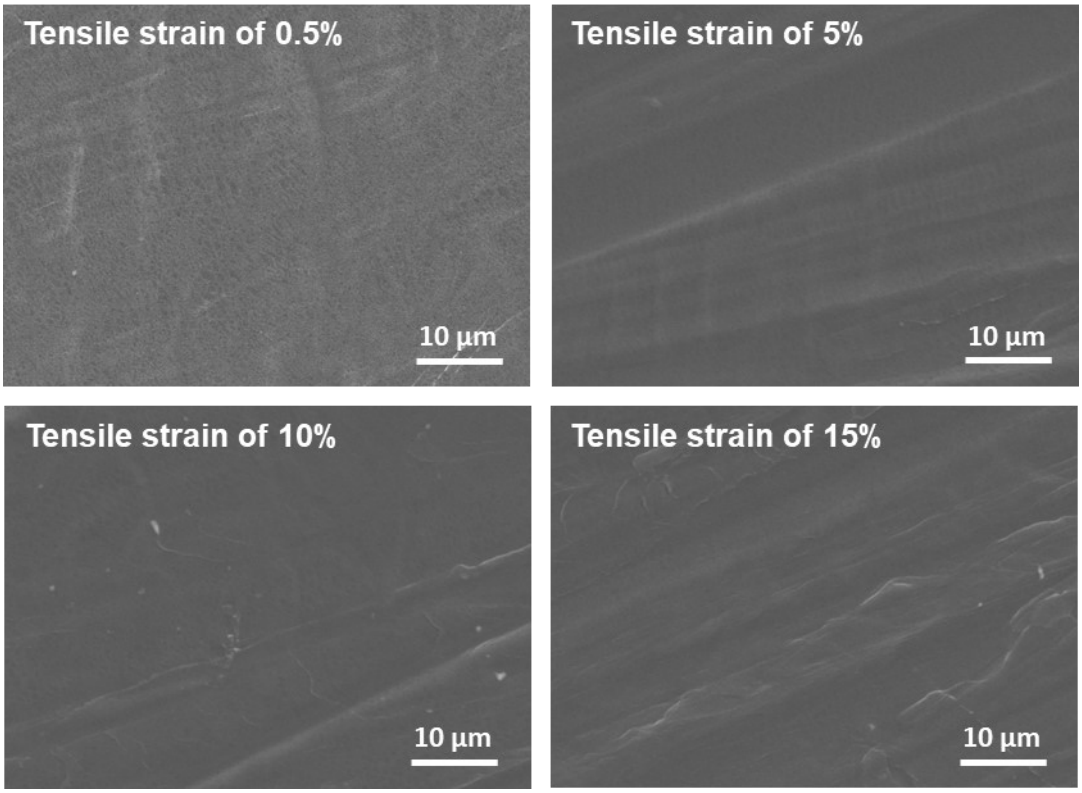


Figure 4-23 SEM images of Li-metal anodes with tensile strains of 0.5%, 5%, 10% and 15%.

The micro morphologies of solid-state PPL electrolytes with different tensile strains were investigated, as shown in Figure 4-24. The PPL electrolytes with tensile strains of 5% and 10% did not show an evident difference compared to the PPL electrolyte (tensile strain of 0.5%), indicating the effect of tensile deformation on microstructures of PPL electrolyte was negligible when tensile strain was less than 10%. However, as highlighted in Figure 4-24, distinct micro-cracks could be observed in the PPL electrolyte with a tensile strain of 15%.

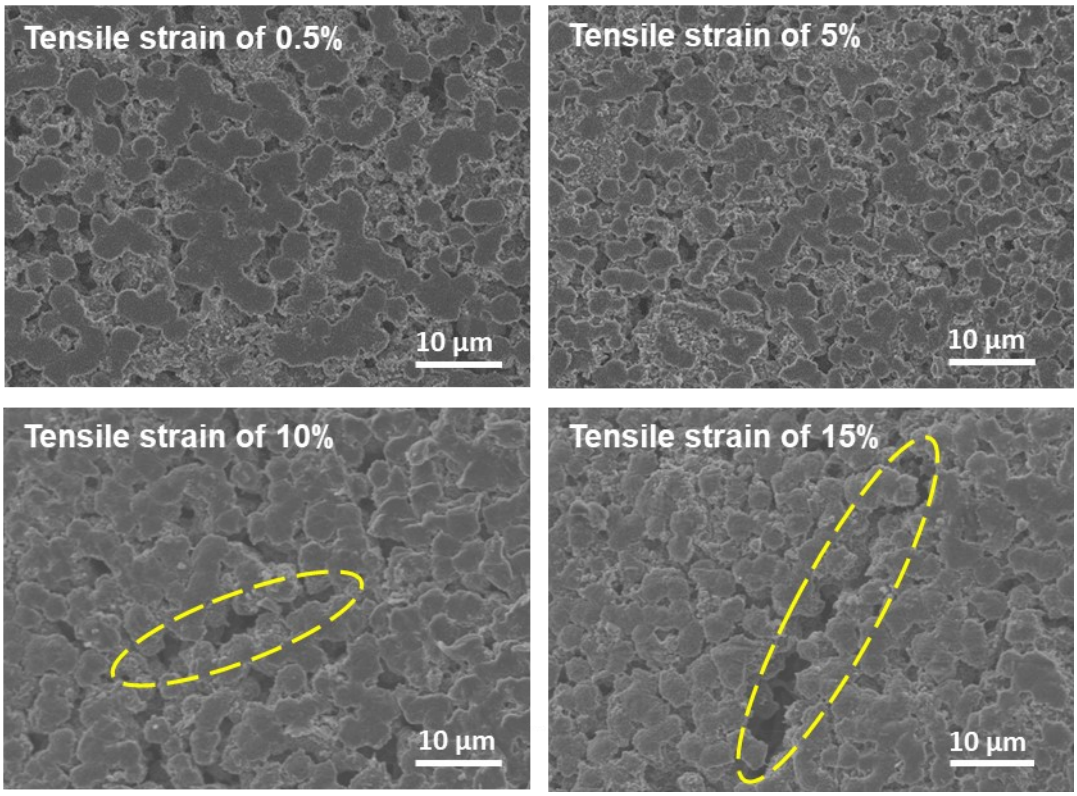


Figure 4-24 SEM images of PPL solid-state electrolytes with tensile strains of 0.5%, 5%, 10% and 15%.

Based on the SEM images of NCM cathodes, Li-metal anodes, and PPL electrolytes with different tensile strains, the microstructures of tensile deformed PPL electrolytes (tensile strain>10%) showed obvious damage, while the NCM cathodes and Li-metal anodes maintained contact microstructure after tensile deformations. This demonstrated that the electrochemical performance fading of tensile deformed PPL-mettery (tensile strain>10%) was mainly caused by micro-cracks in the PPL electrolyte, which would block the ion transport pathway and decrease the ionic conductivity.

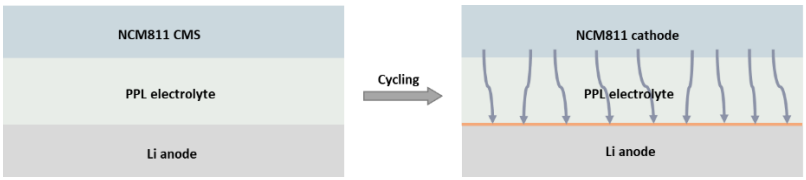
4.8.2 Mechanism of Li-ion transport in tensile deformed PPL electrolyte

Figure 4-25 shows the Li-ion transport mechanism in the intact PPL electrolyte and the PPL electrolyte with micro-cracks caused by uniaxial tensile deformation. As illustrated in Figure 4-25 (a), the uniform and compact PPL electrolyte in mettery would provide unimpeded Li-ions transport pathways, enabling Li-ions to migrate uniformly and efficiently through the continuous conducting pathway.

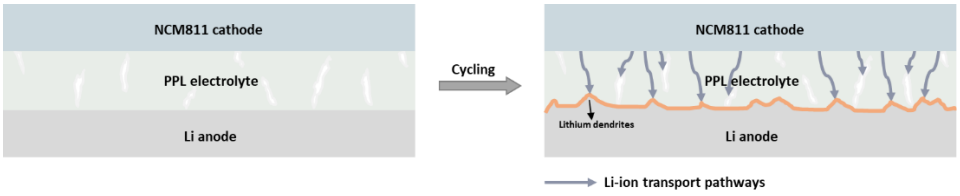
However, the micro-cracks in the PPL electrolyte caused by uniaxial tensile deformation would hinder the Li-ion transport during PPL-mettery charge-discharge cycling, leading to the lower density of Li-ions and their mobility (Figure 4-25b). Moreover, the non-uniform and discontinuous Li-ion transport pathways could cause uneven lithium deposition on the Li-metal anode, facilitating the growth of lithium dendrites, which would further result in lithium dendrites penetration easier through the

electrolyte with micro-cracks. As a result, the lower ionic conductivity of tensile deformed PPL electrolyte would decrease the electrochemical performance of mettery.

Therefore, it is necessary to enhance the ionic conductivity of the next-generation electrolyte used in mettery with tensile deformation. On the other hand, it is desired to repair the micro-cracks in the tensile deformed electrolyte, meeting the application requirements in tensile deformed metteries with a tensile strain of more than 10%.



(a)



(b)

Figure 4-25 Li-ion transport mechanism in (a) intact PPL electrolyte and (b) PPL electrolyte with micro-cracks caused by uniaxial tensile deformation.

4.9 Summary

The sandwich architecture for the raw material of mettery was designed, which was composed of a CMS, an AMS and an SPE in between. The effect of contact pressure and plastic deformations (pure bending and uniaxial tensile deformations) on the electrochemical performance of NCM811|PPL|Li metteries (PPL-metteries) was comprehensively investigated.

It was noted that the electrochemical performance of PPL-metteries decreased with the increase of plastic deformations. Compared to PPL-mettery (R/t=4.3), PPL-mettery (R/t>1.77) exhibited a minor capacity decrease of less than 8.9% at 1C and 12% at 2C over 100 cycles. The PPL-mettery (R/t=1) showed a capacity decrease of 11.5% at 1C and 23% at 2C over 100 cycles. The results indicated that the effect of bending deformation on the electrochemical performance of PPL-mettery was negligible when R/t was more than 1.77.

Compared to PPL-mettery (tensile strain of 0.5%), PPL-mettery (tensile strain>10%) showed a capacity decrease of more than 21.7% at 1C and 28.9% at 2C over 100 cycles. When plastic strain reached 15%,

PPL-mettery showed a drastic capacity decrease of 61% at 1C and 77% at 2C over 100 cycles. The micro-cracks of PPL electrolyte in tensile deformed mettery hampered the Li-ion transport and caused uneven lithium deposition, leading to lithium dendrites penetration, which was considered the main reason for performance fading and shorter cycle life in tensile deformed PPL-mettery.

Chapter 5. Development of a quasi-solid-state PPL+FEC electrolyte to enhance the electrochemical performance of tensile deformed mettery

5.1 Introduction

To improve the electrochemical performance of metteries formed by uniaxial tensile loading, a quasi-state-state PPL+FEC electrolyte with higher ionic conductivity was developed and applied in mettery. The introduction of low-flammable FEC liquid electrolyte created an efficient percolating ion transport pathway and enhanced the interfacial wettability with electrodes. The PVDF polymer worked as a mechanically-support skeleton, which confined the FEC liquid electrolyte surrounding its polymer spherocrystals to maintain a quasi-solid state. Meanwhile, the inorganic ceramic fillers (LLZTO) effectively improved the mechanical property of electrolyte. The addition of low-flammable FEC could not only improve safety but also increase the ionic conductivity of electrolyte.

5.2 Background

Conventional LIBs have critical safety concerns because of the use of liquid electrolytes, which leads to uncontrollable lithium dendrite overgrowth, causing fire accidents and explosions. Solid polymer electrolytes have been demonstrated to effectively inhibit the overgrowth of lithium dendrites when used in Li-metal batteries. However, their practical applications are still hindered by several persistent challenges, including low conductivity at room temperature, limited electrochemical window and poor mechanical strength [146]. Although introducing inorganic ceramic fillers into the polymer matrix can effectively improve the mechanical and electrochemical properties of electrolytes. The interface compatibility between polymer and ceramic fillers within electrolytes is still a challenge for achieving high ionic conductivities.

Quasi-solid-state electrolyte (QSE) that comprise a small amount of liquid electrolyte and a solid skeleton is an intermediate state between the liquid electrolyte and all-solid-state electrolyte [147]. In QSE， the liquid electrolyte improves the wettability between polymer and ceramic and enables fast ion mobility by solvating with Li-ions, while the solid skeleton contributes to the mechanical stability of the electrolyte. Compared to SSE, the QSEs exhibit enhanced ionic conductivity of more than 1 mS cm^{-1} at 25 °C [148]. They also deliver higher interfacial contact with electrodes due to the introduction of liquid electrolytes. On the other hand, the polymer-ceramic skeleton in QSE improves mechanical strength and can hinder the overgrowth of lithium dendrites. The use of QSEs in batteries can not only

improve safety but also presents higher ionic conductivity, which holds great potential in commercial applications.

5.3 Experimental details

5.3.1 Fabrication of uniaxial tensile deformed PPL+FEC-metteries

The FEC liquid electrolyte was added into the solid-state PPL electrolyte to construct a quasi-solid-state PPL+FEC electrolyte during the assembly of metteries. The tensile deformed NCM811|PPL+FEC|Li metteries (PPL+FEC-metteries) with the plastic strains of 0.5%, 5%, 10% and 15% were formed by uniaxial tensile tests with 1mm/min by the Universal Testing Machine (INSTRON 5982).

5.3.2 Material characterisation

The chemical properties of synthesized PPL+FEC electrolytes were characterized by FTIR. The morphology and microstructure of the NCM cathodes, Li-metal anodes and PPL and PPL+FEC electrolytes were characterized by SEM. TEM was used to characterise the CEI and structure of NCM811 cathodes used in tensile deformed metteries with PPL and PPL+FEC electrolytes after 100 cycles.

5.3.3 Electrochemical characterisations of tensile deformed PPL+FEC electrolytes

The electrochemical stability window of PPL+FEC electrolyte was investigated by the LSV method using a Li|PPL+FEC|SS cell with the electrochemical workstation over a voltage range of 0-6 V at a scan rate of 0.5 mV s^{-1} at 25 °C. The ionic conductivity of PPL and PPL+FEC electrolytes with tensile strains of 0.5% and 15% were characterized by SS|SS mettery and calculated according to equation (1). The activation energy was calculated according to the Arrhenius formula (2). The Li-ion transference numbers were measured in Li|Li symmetric metteries ranging from 7 MHz to 0.1 Hz with a DC voltage of 10 mV for 5000s and calculated according to equation (3).

5.3.4 Electrochemical measurements of tensile deformed PPL+FEC-metteries

Electrochemical impedance spectroscopy (EIS) of tensile deformed PPL-metteries was recorded in a frequency ranging from 5 MHz to 100 mHz with the electrochemical workstation at 25 °C. Galvanostatic charge and discharge tests of tensile deformed PPL+FEC-metteries (tensile strains of 0.5%, 5%, 10% and 15%) were carried out on the LAND system with a voltage ranging from 2.8 to 4.3 V at 25 °C. The PPL+FEC-metteries were activated at a charge-discharge current density of 0.1C at

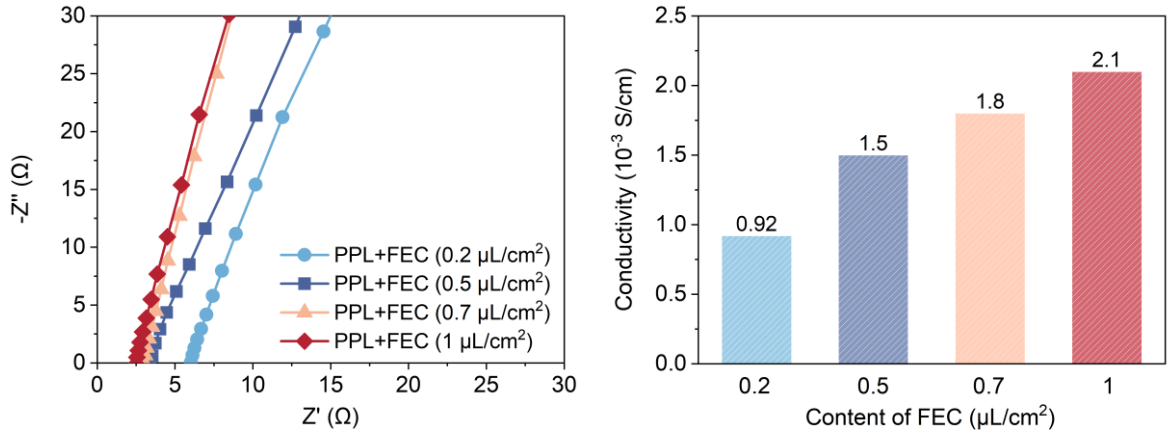
the first three cycles. Symmetric Li|PPL+FEC|Li and Li|PPL|Li metteries were performed at a current density of 0.1 mA cm^{-2} at 25 °C.

5.4 Mechanism of Li-ion transport in PPL+FEC electrolyte

QSE consisting of a liquid electrolyte and a solid skeleton is expected to apply for improving the electrochemical performance of tensile deformed mettery. Herein, a PPL+FEC electrolyte has been developed, in which the FEC liquid electrolyte would enhance the ionic conductivity of the electrolyte by enhancing the Li-ion mobility. Moreover, the FEC is expected to partially fill the micro cracks of tensile deformed electrolyte by its electrochemical decomposition products such as carbonates and lithium fluoride. Based on the above two synergistic effects, the introduction of FEC is aimed to improve the ionic conductivity and structural stability of electrolytes in tensile deformed mettery, facilitating uniform lithium metal deposition and therefore improving the electrochemical performance of tensile deformed mettery.

5.5 Electrochemical properties of PPL+FEC electrolytes with different FEC contents

To explore the optimum content of FEC in the PPL+FEC electrolyte, PPL+FEC electrolytes with four different FEC contents (0.2, 0.5, 0.7 and 1 μL/cm^2) were prepared. The ionic conductivity of them with the tensile strain of 0.5% at 25°C was implemented. Figure 5-1 (a) presents the EIS plots of SS|PPL+FEC (tensile strain of 0.5%)|SS metteries with different FEC contents at 25 °C and Figure 5-1 (b) presents the corresponding calculated ionic conductivity of them. The PPL+FEC (0.2 μL/cm^2), PPL+FEC (0.5 μL/cm^2), PPL+FEC (0.7 μL/cm^2) and PPL+FEC (1 μL/cm^2) delivered an ionic conductivity of 0.92×10^{-3}, 1.5×10^{-3}, 1.8×10^{-3} and 2.1×10^{-3} S/cm at 25°C, respectively. It was found that with the increase of FEC content in the PPL+FEC electrolyte, the ionic conductivities were measured to be gradually increased. This was attributed to the enhanced Li-ion mobility in liquid electrolytes compared to solid-state electrolytes.

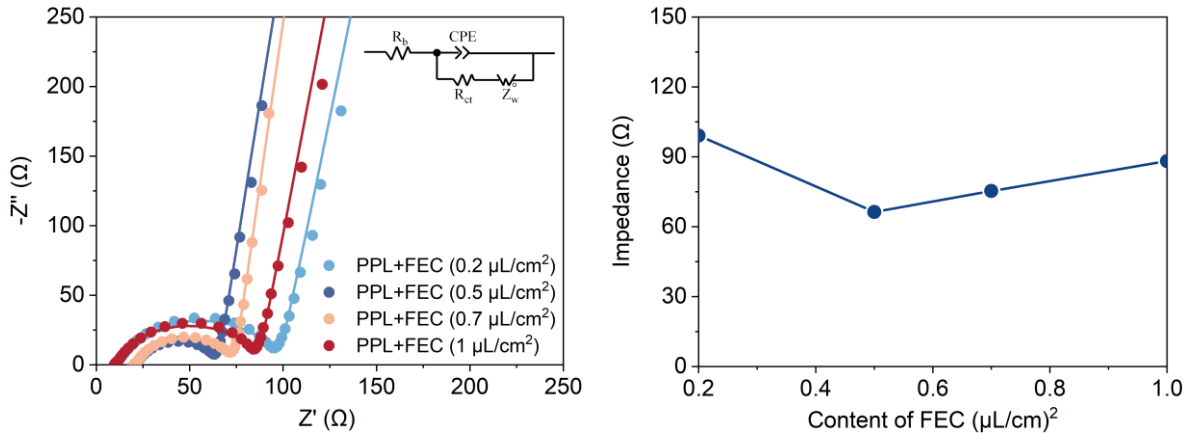


(a) (b)

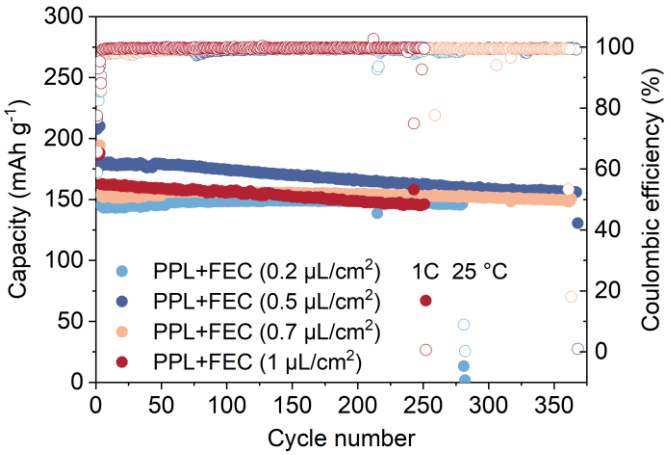
Figure 5-1 (a) EIS plots of SS|PPL+FEC(tensile strain of 0.5%)|SS metteries, (b) calculated ionic conductivities of PPL+FEC electrolytes (tensile strain of 0.5%) with FEC contents of 0.2, 0.5, 0.7 and 1 μL/cm^2 at 25°C.

The electrochemical performance of PPL+FEC electrolytes (tensile strain of 0.5%) with FEC contents of 0.2, 0.5, 0.7 and 1 μL/cm^2, including EIS and cycling performance, were conducted to further explore the optimum content of FEC in NCM811|PPL+FEC|Li mettery (PPL+FEC-mettery). Figure 5-2 (a) presents the EIS plots with the fitting result shown in Figure 5-2 (b). The PPL+FEC-metteries (tensile strain of 0.5%) with the FEC contents of 0.2, 0.5, 0.7 and 1 μL/cm^2 delivered the impedance of 99.1, 66.3, 75.3 and 88.1 Ω, respectively.

Figure 5-2 (c) depicts the cycling performance of PPL+FEC-metteries (tensile strain of 0.5%) with different FEC contents, PPL+FEC (0.5 μL/cm^2)-mettery achieved an initial specific capacity of 178.2 m Ah g^{-1} and maintained capacity retention of 89.3% after 300 cycles at 1C. In comparison, PPL+FEC-metteries with the FEC contents of 0.2, 0.7 and 1 μL/cm^2 delivered a lower initial specific capacity of 145, 154 and 162.4 mAh g^{-1} and short circuit after 281, 363 and 252 cycles, respectively.



(a) (b)



(c)

Figure 5-2 (a) EIS plots with the equivalent circuit inside and (b) impedance of PPL+FEC-metteries (tensile strain of 0.5%), (c) cycling performance of PPL+FEC-metteries (tensile strain of 0.5%) with FEC contents of 0.2, 0.5, 0.7 and 1 μL/cm^2 at 1C at 25°C.

The smaller content of FEC (0.2 μL/cm^2) caused the highest impedance and the lowest specific capacity due to lower ionic conductivity. Regarding PPL+FEC with higher content of FEC (1 μL/cm^2), although it presented the highest ionic conductivity, it would produce more decomposition products and thus increased the impedance. On the other hand, along with the more liquid FEC (1 μL/cm^2) added, the mechanical strength of the PPL+FEC electrolyte would be decreased, which more easily led to a short circuit, delivering a shorter cycle life. Therefore, the FEC with 0.5 μL/cm^2 exhibited the lowest impedance and highest cycling performance, which was considered the optimum volume of FEC in the PPL+FEC electrolyte and was focused on the following study.

5.6 Physicochemical characterization of PPL and PPL+FEC electrolytes

Figure 5-3 shows FTIR spectra of the PPL electrolyte, FEC and PPL+FEC electrolyte. After adding FEC into the PPL electrolyte, the FTIR bands of C=O stretching vibration in FEC shifted from 1823 and 1801 cm^{-1} to 1830 and 1805 cm^{-1}, and the FTIR band of C=O stretching vibration in DMF in the PPL electrolyte shifted from 1659 to 1664 cm^{-1}, indicating the strong interaction between FEC and PPL electrolyte. Moreover, the FTIR band at 1380 cm^{-1} was ascribed to the α phase of PVDF in PPL electrolyte, those at 1255 cm^{-1} and 1178 cm^{-1} are assigned to the γ phase, and that at 830 cm^{-1} was attributed to β, γ phases. The band intensity of all three phases of PVDF decreased after the addition of FEC in PPL, indicating the decreased crystallinity of PVDF, which was favourable for the Li-ion transport in the electrolyte.

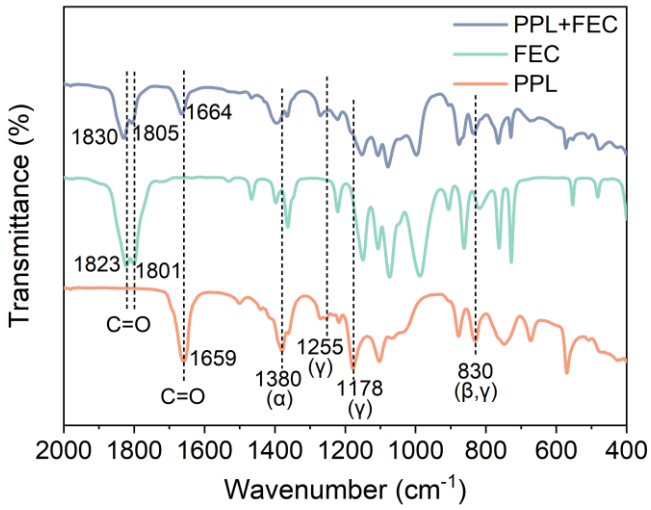


Figure 5-3 FTIR spectra of the FEC, PPL and PPL+FEC electrolytes.

The electrochemical stability windows of PPL and PPL+FEC electrolytes were tested by the LSV method. As shown in Figure 5-4, the PPL electrolyte showed an oxidation decomposition voltage of 4.9 V and the PPL+FEC electrolyte exhibited a slightly lower oxidation decomposition voltage of 4.8 V. The results indicated that the decomposition of FEC caused a negligible decrease in the electrochemical stability window.

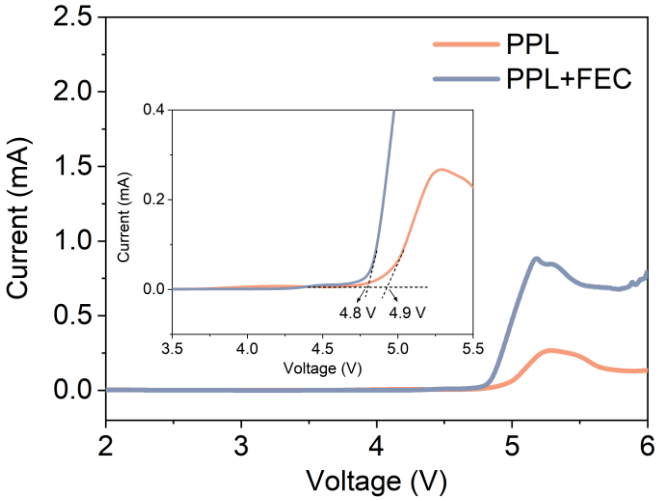


Figure 5-4 LSV curves of the PPL electrolyte and PPL+FEC electrolyte.

5.7 Electrochemical characterisations of tensile deformed PPL and PPL+FEC electrolytes

The ionic conductivity of the electrolyte would decrease after tensile deformation owing to the formation of micro-cracks, which partially destroyed the continuous Li-ion transport pathways. The ionic conductivities of PPL and PPL+FEC electrolytes with tensile strains of 0.5% and 15% at 25 °C

were measured to evaluate the ability of the addition of FEC for improving the ionic conductivity in tensile deformed electrolyte. Figure 5-5 shows the EIS plots of SS|PPL|SS metteries (Figure 5-5a) and SS|PPL+FEC|SS metteries (Figure 5-5b) at 25°C. The calculated ionic conductivity of the PPL electrolyte (tensile strain of 0.5%) was 7.2×10^{-4} S cm^{-1}, while the ionic conductivity of the PPL electrolyte (tensile strain of 15%) was 4.1×10^{-4} S cm^{-1}, showing a significant ionic conductivity reduction of 45%.

The PPL+FEC electrolyte (tensile strain of 0.5%) exhibited a high ionic conductivity of 1.5×10^{-3} S/cm, around twice higher than the PPL electrolyte (tensile strain of 0.5%). The PPL+FEC electrolyte (tensile strain of 15%) also maintained a high ionic conductivity of 1.3×10^{-3} S/cm at 25 °C. This indicated the enhanced ionic mobility after the addition of FEC could compensate for the partial loss of Li-ion pathways in tensile deformed electrolytes, preventing the significant decrease in ionic conductivity. Besides, the FEC was able to partially repair the micro-cracks of the electrolyte after tensile deformation by its decomposition products, reconstructing the ion transport pathways. This effectively helped to maintain the high ionic conductivity after tensile deformation. As a result, the tensile deformed mettery by using PPL+FEC electrolyte would deliver a superior cycling performance due to high ionic conductivity.

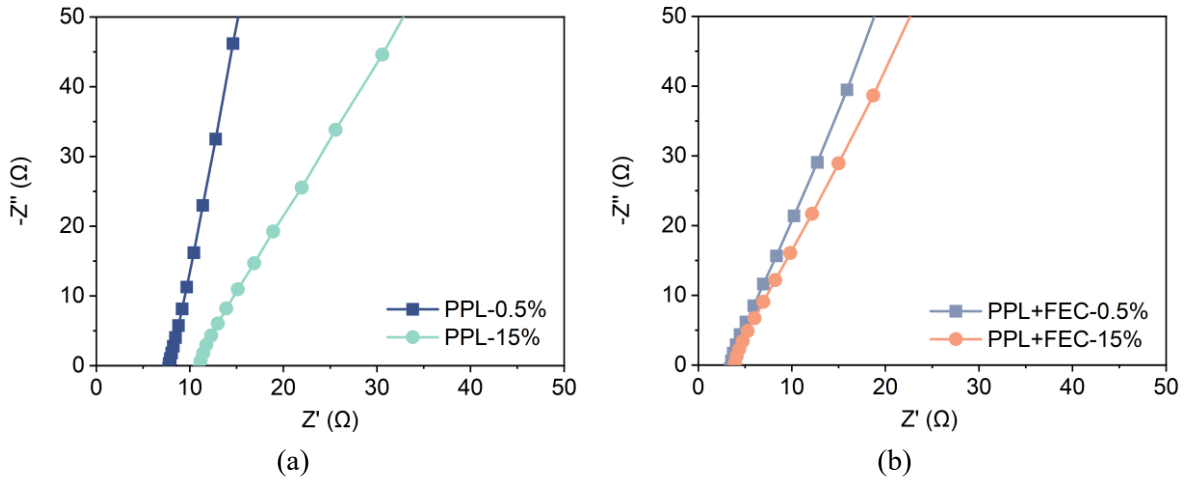


Figure 5-5 EIS plots of SS|SS metteries by using (a) PPL electrolytes and (b) PPL+FEC electrolytes with tensile strains of 0.5% and 15% at 25°C.

Figure 5-6 depicts Arrhenius plots of the ionic conductivities for PPL and PPL+FEC electrolytes (tensile strains of 0.5% and 15%). And the activation energy (E_a) for them was calculated according to their Arrhenius plots. The E_a of PPL electrolytes with tensile strains of 0.5% and 15% were 0.21 and 0.24 eV, respectively. In comparison, the E_a of PPL+FEC electrolytes with tensile strains of 0.5% and 15% were 0.13 and 0.15 eV respectively, which were much lower than the E_a of PPL electrolytes. This indicated that the PPL+FEC electrolytes showed a smaller energy barrier for Li-ion migration. As a

result, the addition of FEC facilitated Li-ion transport in the electrolyte, thereby improving the ionic conductivity.

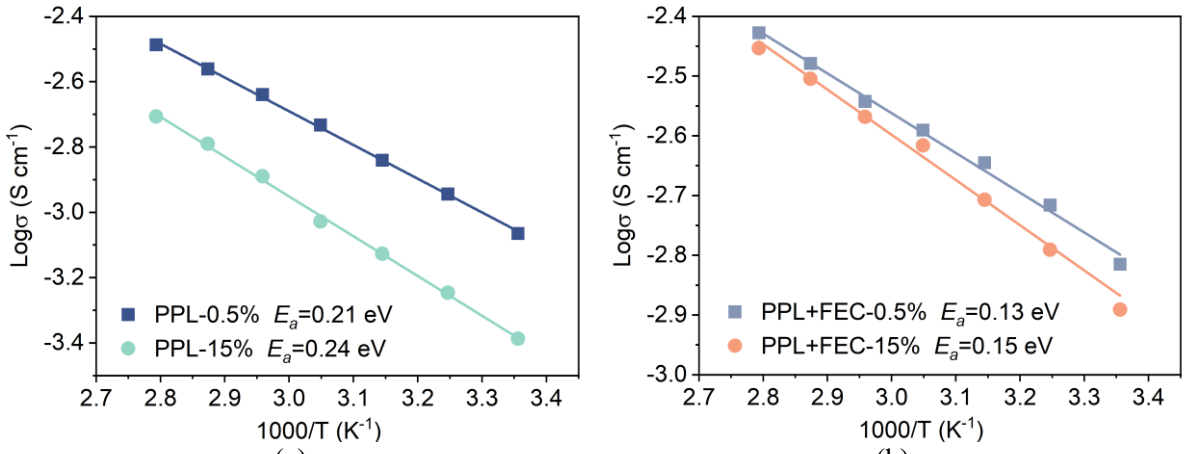
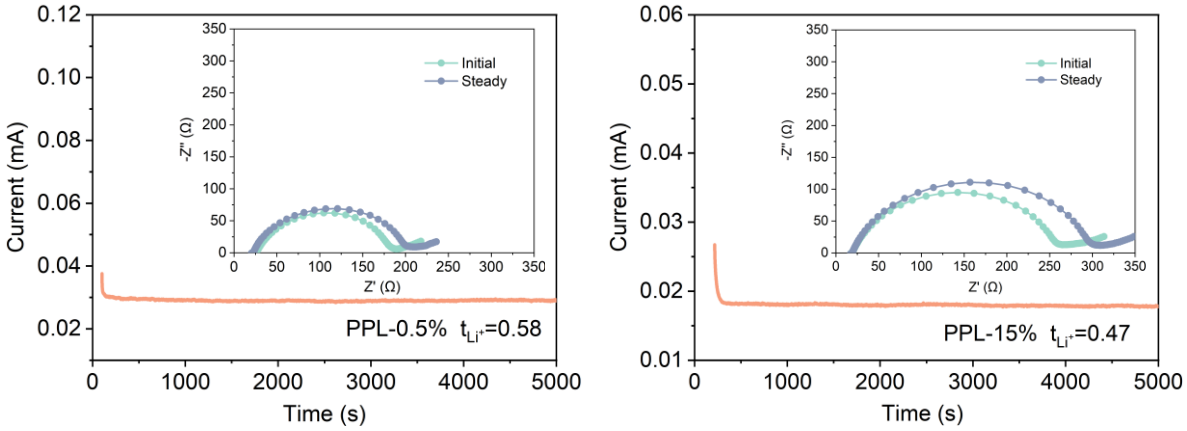
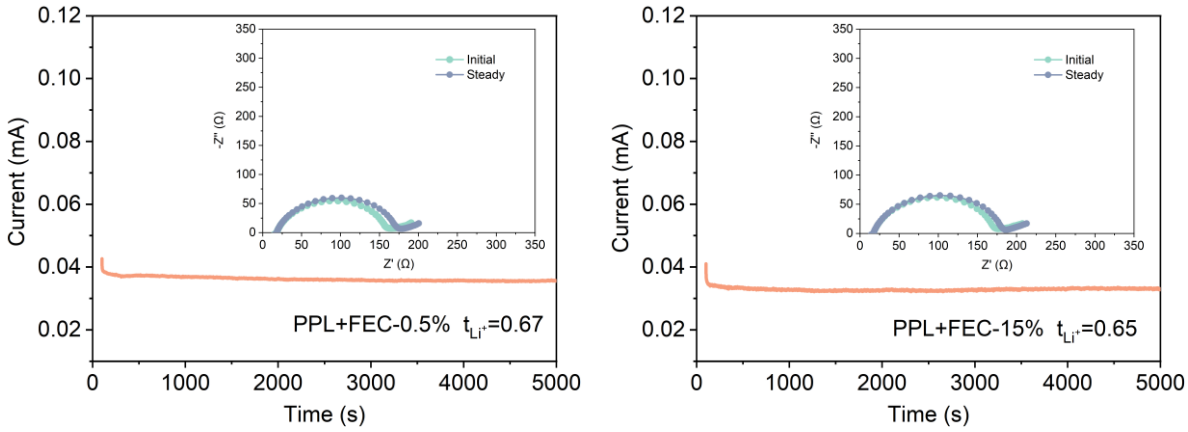


Figure 5-6 Arrhenius plots of the ionic conductivities of (a) PPL electrolytes and (b) PPL+FEC electrolytes with tensile strains of 0.5% and 15%.

As shown in Figure 5-7(a) and (c), by adding the FEC to the PPL electrolyte (tensile strain of 0.5%), the Li-ion transference number increased from 0.58 to 0.67, indicating that FEC had the ability to prevent the mobilization of the anions. Moreover, the PPL+FEC electrolyte (tensile strain of 15%) still presented a high lithium transference number of 0.65 (Figure 5-7d). By contrast, the PPL electrolyte (tensile strain of 15%) showed an obviously decreased Li-ion transference number of 0.47 (Figure 5-7b). The higher Li-ion transference number of PPL+FEC electrolyte was beneficial for reducing the polarisation of the cathode and anode, thus improving the performance of metteries.



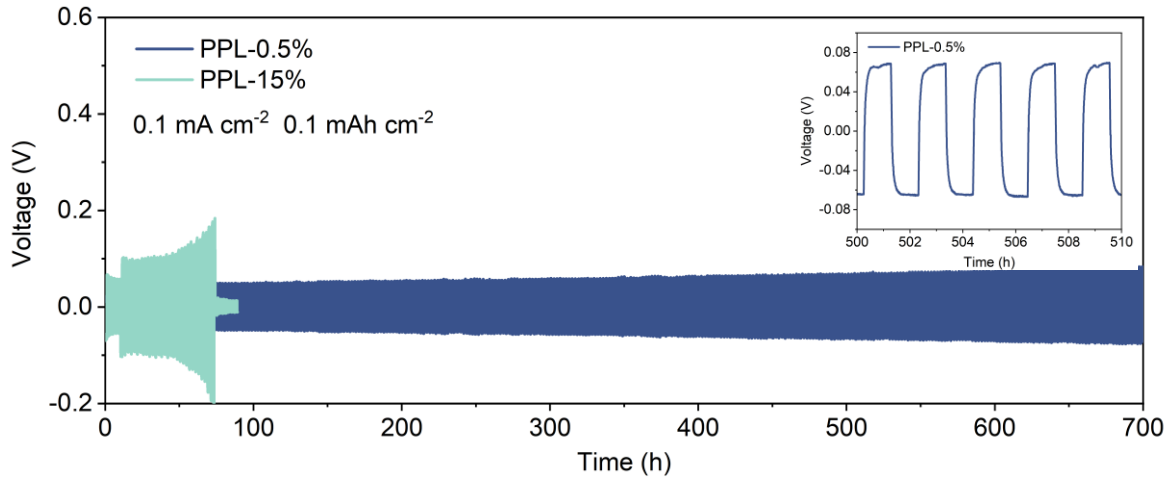


(c) (d)

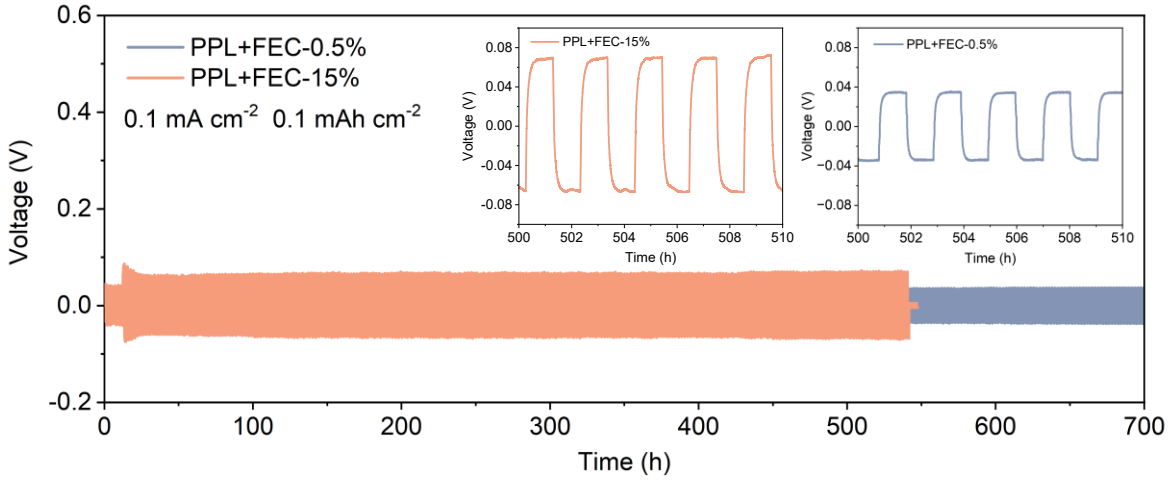
Figure 5-7 Li-ion transference number of PPL and PPL+FEC electrolytes (tensile strains of 0.5% and 15%). Chronoamperometry curves and corresponding EIS plots before and after the DC polarisation of Li|PPL|Li symmetric metteries with tensile strains of (a) 0.5% and (b) 15%, Li|PPL+FEC|Li symmetric metteries with tensile strains of (c) 0.5% and (d) 15%.

A galvanostatic cycling measurement of Li|PPL|Li and Li|PPL+FEC|Li symmetric metteries (tensile strains of 0.5% and 15%) during Li plating/stripping were conducted to investigate the dynamic interface stability of the tensile deformed electrolyte-lithium metal anode and the ability of tensile deformed electrolyte membranes against lithium dendrites penetration. As shown in Figure 5-8 (a), the voltage profile of Li|PPL|Li symmetric mettery (tensile strain of 0.5%) remained deposition stability with the overpotentials of 0.07 V during the lithium plating/stripping process under a current density of 0.1 mA cm^{-2}. In comparison, the Li|PPL|Li symmetric mettery (tensile strain of 15%) showed significantly higher and unstable overpotentials due to the micro-cracks of the PPL electrolyte. These micro-cracks in PPL electrolytes after uniaxial tensile deformation led to server lithium dendrites growth during the Li plating/stripping process. After 74 hours, the lithium dendrites penetrated through the PPL electrolyte membrane and caused a short circuit.

By contrast, as shown in Figure 5-8 (b), the Li|PPL+FEC|Li symmetric mettery (tensile strain of 0.5%) delivered a smaller overpotential of 0.04 V due to its high ionic conductivity. Moreover, the voltage profile of Li|PPL+FEC|Li symmetric mettery (tensile strain of 15%) still maintained stability during the Li plating/stripping process. It could plate/strip lithium for 542 h with an overpotential of 0.07 V before a short circuit. The results indicated that the FEC additive could construct a robust and stable SEI to prevent lithium dendrites growth.



(a)



(b)

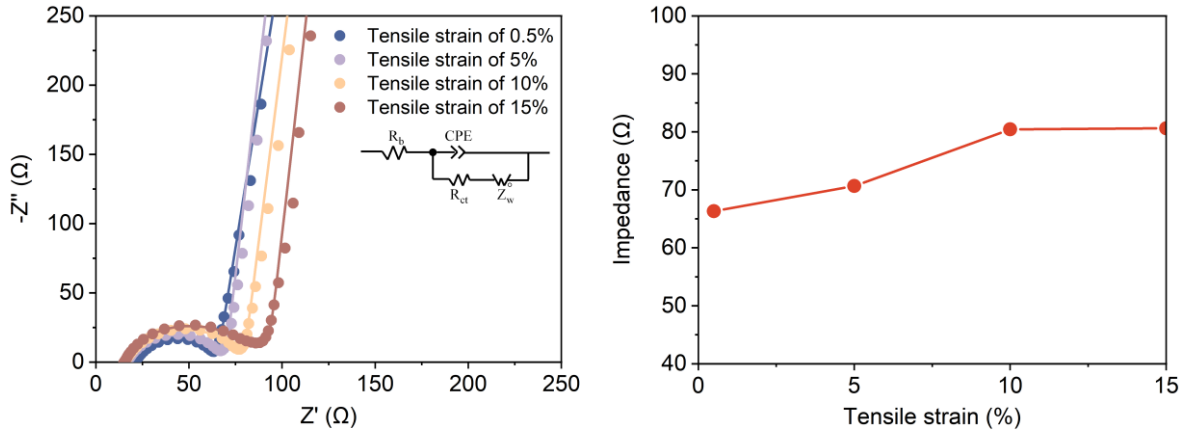
Figure 5-8 Voltage curves of (a) Li|PPL|Li and (b) Li|PPL+FEC|Li symmetric metteries with tensile strains of 0.5% and 15% at a current density of 0.1 mA cm^{-2} at 25 °C.

5.8 Effect of uniaxial tensile deformation on electrochemical performance of PPL+FEC-mettery

5.8.1 EIS of tensile deformed PPL+FEC-metteries

Figure 5-9 (a) shows the Nyquist plots of tensile deformed NCM811|PPL+FEC|Li mettery (PPL+FEC-mettery) with tensile strains of 0.5%, 5%, 10% and 15% at 25 °C. The EIS fitting was conducted according to the equivalent circuit (inside in Figure 5.9a) with the results shown in Figure 5-9 (b). The impedance of PPL+FEC-metteries with tensile strains of 0.5%, 5%, 10% and 15% were 66.31, 70.66, 80.43 and 80.62 Ω respectively, showing a slight increase. Compared to PPL-mettery, the PPL+FEC-mettery exhibited a much smaller impedance and a smaller impedance increment with increasing tensile strains. This indicated that the FEC in PPL+FEC electrolyte helped to decrease the impedance of

mettery, and more importantly, reduced the negative effect of uniaxial tensile deformation on impedance.



(a) (b)

Figure 5-9 (a) EIS plots with the equivalent circuit inside and (b) the effect of tensile deformation on the impedance of PPL+FEC-metteries with tensile strains of 0.5%, 5%, 10% and 15% formed by uniaxial tensile deformation.

5.8.2 Cycling performance of tensile deformed PPL+FEC-metteries

Figure 5-10 shows the specific discharge capacity and coulombic efficiency of tensile deformed PPL+FEC-metteries (tensile strains of 0.5%, 5%, 10% and 15%) formed by uniaxial tensile deformations at the current densities of 1C and 2C respectively. With the increase of tensile strains, the specific capacity showed a minor decrease within 16% at both 1C and 2C, suggesting that the uniaxial tensile deformation exhibited a slight detrimental impact on the cycling performance of PPL+FEC-mettery. Specifically, at the current density of 1C (Figure 5-10a), PPL+FEC-mettery with tensile strains of 0.5%, 5%, 10% and 15% delivered the initial specific capacity of 178.2, 168.1, 163 and 141.3 mAh g^{-1} and capacity retention of 91.5%, 89.1%, 92.4% and 99.7% respectively after 250 cycles.

At the current density of 2C, as shown in Figure 5-10 (b), PPL+FEC-mettery with tensile strains of 0.5%, 5%, 10% and 15% delivered the initial specific capacities of 155.2, 142.5, 140.2 and 136.3 mAh g^{-1} and capacity retentions of 81.3%, 87.7%, 80.3% and 78.1% respectively after 400 cycles. Compared to the PPL+FEC-mettery (tensile strain of 0.5%), the PPL+FEC-mettery (tensile strain of 15%) only exhibited a capacity reduction of 13.6% after 250 cycles at 1C and a capacity reduction of 15.6% after 400 cycles at 2C.

On the other hand, compared to PPL-mettery, the PPL+FEC-mettery exhibited a higher specific capacity of more than 33.2% at 1C and more than 23.6% at 2C. The high cycling and rate performance

of tensile deformed PPL+FEC-mettery could be ascribed to the high ionic conductivity of PPL+FEC electrolytes and the formation of FEC-derived CEI and SEI, which facilitated Li-ion transport and protected the NCM811 cathode and Li-metal anode from serious degradation.

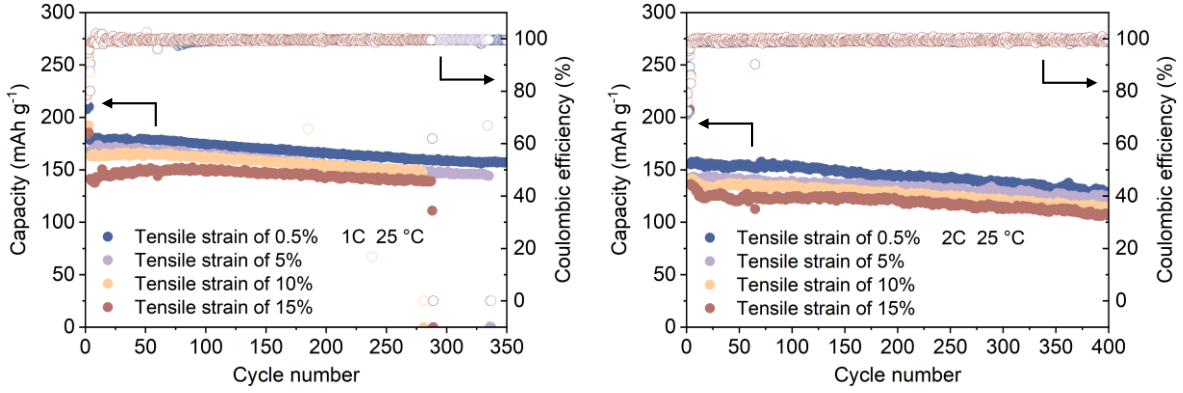


Figure 5-10 Cycling performance and coulombic efficiency of tensile deformed PPL+FEC-metteries at a current density of (a) 1C and (b) 2C at 25°C.

To directly present the correlation between the uniaxial tensile deformation and electrochemical evolution of the PPL+FEC-mettery, tensile strain against specific capacity at different cycling numbers of 50, 100, 150 and 200 under 1C (Figure 5-11a) and 2C (Figure 5-11b) was depicted. At the current density of 1C, the PPL+FEC-metteries with tensile strains of 5%, 10% and 15% showed a capacity decrease of 7.7%, 7.5% and 13.8% respectively compared to PPL+FEC-mettery (tensile strain of 0.5%) after 200 cycles. At the current density of 2C, the PPL+FEC-metteries with tensile strains of 5%, 10% and 15% showed a capacity decrease of 8.3%, 11.8% and 16.6% respectively compared to PPL+FEC-mettery (tensile strain of 0.5%) after 200 cycles.

Moreover, both at 1C and 2C, the tensile deformed PPL+FEC-metteries delivered high cycling stability, showing minor capacity fading during 200 cycles. These results demonstrated that the increase in uniaxial tensile deformation caused a slight decrease in the specific capacity and cyclability of PPL+FEC-mettery.

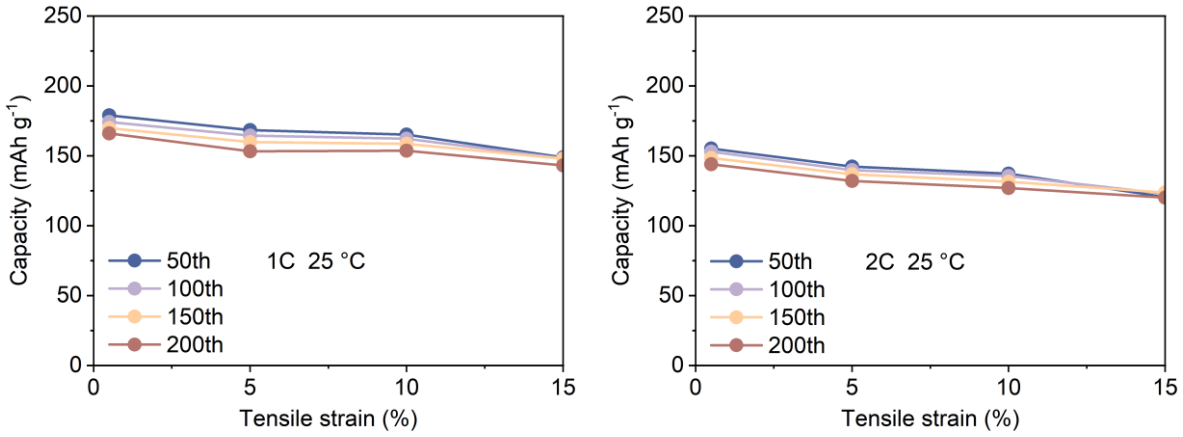
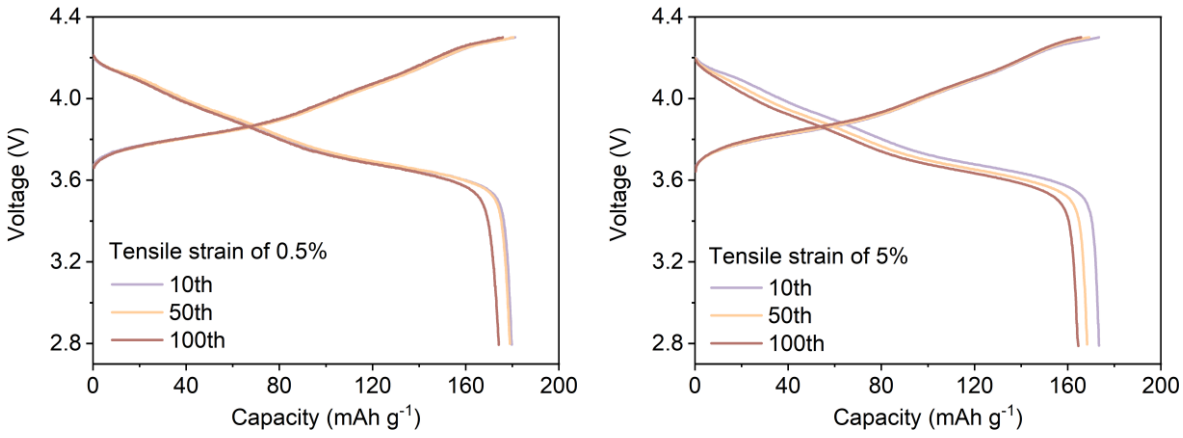


Figure 5-11 Effect of uniaxial tensile deformation on the specific capacity of PPL+FEC-metteries at different cycles at a current density of (a) 1C and (b) 2C at 25°C.

The galvanostatic charge-discharge curves of tensile deformed PPL+FEC-metteries with tensile strains of 0.5%, 5%, 10%, and 15% after the 10th, 50th, and 100th cycles were measured at of 1C at 25 °C in the voltage ranging from 2.8 to 4.3 V (Figure 5-12). The PPL+FEC-mettery (tensile strain of 0.5%) delivered a specific capacity of 174.1 mAh g^{-1} (96.7% of the theoretical value of NCM811) after 100 charge-discharge cycles. Although the specific capacity reduced slightly with increasing uniaxial tensile strains, the PPL+FEC-metteries with tensile strains of 5%, 10% and 15% still delivered a high specific capacity of 164.5, 162.2 and 148.1 mAh g^{-1} respectively after 100 cycles. Moreover, the electrochemically stable interface and enhanced ion mobility in PPL+FEC electrolytes resulted in a lower polarisation of tensile deformed PPL+FEC-metteries with tensile strains from 0.5% to 15%.



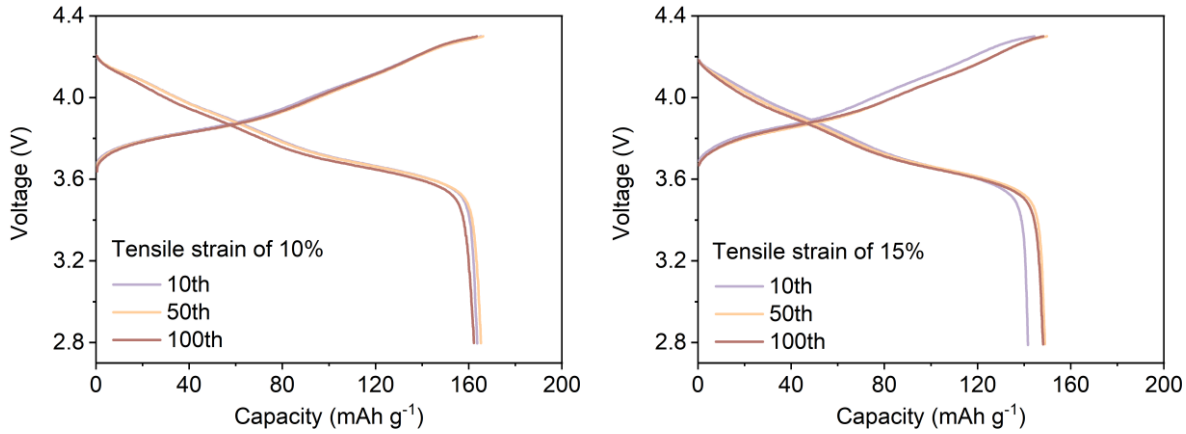


Figure 5-12 Galvanostatic charge-discharge profiles of tensile deformed PPL+FEC-metteries with tensile strains of (a) 0.5%, (b) 5%, (c) 10% and (d) 15% at 1C at 25°C.

5.8.3 Rate performance of tensile deformed PPL+FEC-metteries

To investigate the capacity and stability of tensile deformed PPL+FEC-metteries at various current densities (from 0.2C to 5C), the rate performance tests were conducted. As shown in Figure 5-13, PPL+FEC-mettery (tensile strain of 0.5%) delivered specific capacities of 191.1, 186.5, 175.8, 152.9, 138.7 and 118 mAh g^{-1} at current densities of 0.2C, 0.5C, 1C, 2C, 3C and 5C, respectively. A reversible capacity of 174.5 mAh g^{-1} was obtained when the current density returned to 1C after 55 cycles. It was notable that the tensile deformed PPL+FEC-metteries with tensile strains of 5%, 10% and 15% showed capacity reductions of approximately 3.8%, 15.7% and 26.7% at 5C and capacity reductions of approximately 3.2%, 5.2% and 9.3% at 1C after 55 cycles compared to PPL+FEC-mettery (tensile strain of 0.5%).

On the other hand, there was a great capacity improvement with the addition of FEC in PPL electrolytes for tensile deformed metteries. Particularly at the high current density of 5C, PPL+FEC-mettery exhibited a capacity increase of more than 44.8% compared to PPL-mettery.

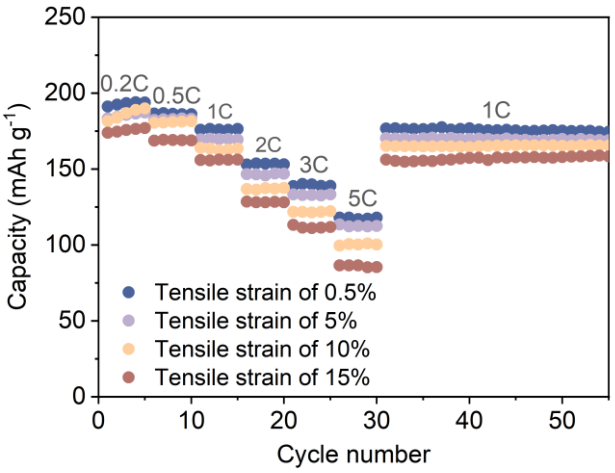


Figure 5-13 Rate performance of tensile deformed PPL+FEC-metteries at 25°C.

Figure 5-14 shows experimental and modelling results for the effect of the charge-discharge current rate on the specific capacity of tensile deformed PPL+FEC-metteries, according to equation (6): an empirical model for predicting the specific capacity of a tensile deformed PPL+FEC-mettery with tensile strain from 0.5% to 15%, at the current density from 0.2C to 5C.

$$C = C_{min} - k\varepsilon + C_{THEO} exp(-\gamma Rate) \quad (6)$$

Where C is the specific capacity of a tensile deformed PPL+FEC-mettery; Rate is the charge-discharge current rate, ranging from 0.2C to 5C; ε is the tensile strain of PPL+FEC-mettery during tensile deformation, ranging from 0.5% to 15%; C_{min} is the minimum capacity; C_{THEO} is the theoretical specific capacity of PPL+FEC-mettery; k is the impact factor for the effect of uniaxial tensile deformation on specific capacity and γ is the impact factor for the effect of current rate on specific capacity.

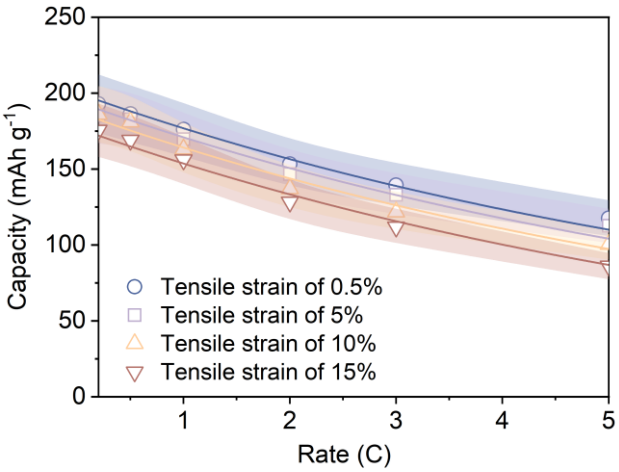


Figure 5-14 Experimental and modelling results for the effect of rate on the specific capacity of tensile deformed PPL+FEC-metteries at 25°C.

The model constants are shown in Table 5-1. Both the values of k and γ for PPL+FEC-mettery were lower than that of PPL-mettery (Table 4-2), indicating that the tensile deformation and current density showed a lower detrimental impact on the capacity for PPL+FEC-mettery.

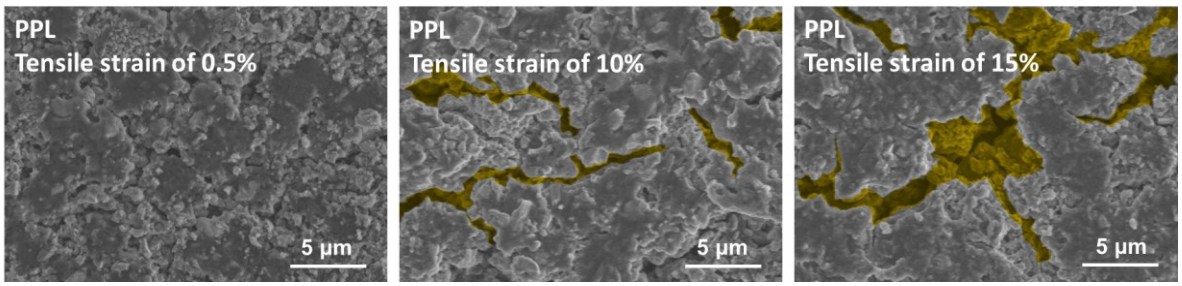
Table 5-1 Values of constants in equation (6).

Constant	C_{min}	C_{THEO} (mAh/g)	k	γ
Value	21.2	180	150	0.14

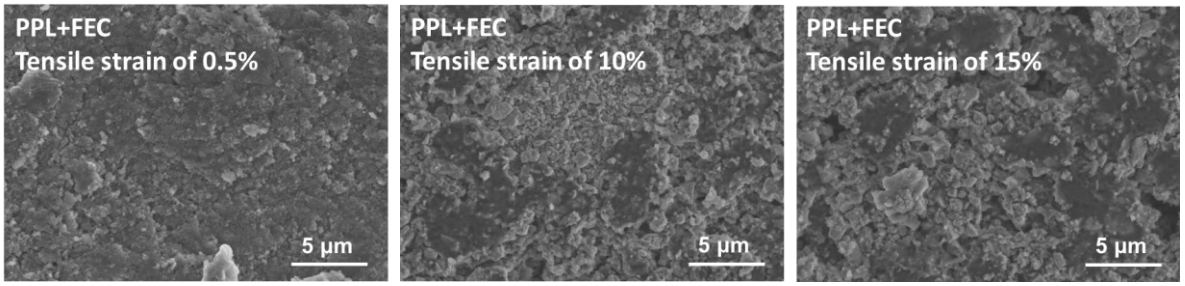
5.9 Structural evolution of tensile deformed electrolytes and electrodes

The SEM of electrolytes, NCM cathodes and Li-metal anodes in tensile deformed PPL-metteries and PPL+FEC-metteries after 100 charge-discharge cycles were conducted to investigate the effect of the addition of FEC in the electrolyte. The SEM images of PPL and PPL+FEC electrolytes in the tensile deformed metteries after 100 cycles are shown in Figure 5-15. As shown in Figure 5-15 (a), PPL electrolytes with tensile strains of 10% and 15% exhibited structural micro-cracks after 100 cycles compared to the intact morphology of the PPL electrolyte (tensile strain of 0.5%). The tensile deformed PPL electrolyte with a partially destroyed structure would impair the continuity of ionic conductive pathways, leading to a decrease in electrochemical performance.

Figure 5-15 (b) shows PPL+FEC electrolytes in tensile deformed metteries after 100 cycles. Compared to PPL electrolytes (tensile strains of 10% and 15%), the PPL+FEC electrolytes (tensile strains of 10% and 15%) exhibited much smaller cracks, which indicated the addition of FEC in the electrolyte was capable of repairing the micro-cracks during the charge-discharge cycling process. This was because the decomposition products of FEC such as carbonates and lithium fluoride could partially fill the micro-cracks to reconstruct the Li-ion pathways.



(a)



(b)

Figure 5-15 SEM images of cycled (a) PPL electrolytes and (b) PPL+FEC electrolytes in tensile deformed metteries with tensile strains of 0.5%, 10% and 15% after 100 cycles at 1C.

Figure 5-16 shows the TEM images of NCM cathodes in tensile deformed PPL-metteries and PPL+FEC-metteries with tensile strains of 0.5%, 10%, and 15% after 100 cycles at 1C. As shown in Figure 5-16 (a), the CEI on the surface of the NCM cathodes by using PPL electrolytes were approximately 4, 6 and 11 nm for tensile strains of 0.5%, 10% and 15%, respectively. The micro-cracks in the PPL electrolyte caused by uniaxial tensile deformation could induce more DMF transfer and decomposition on the NCM cathode and further form a thicker CEI film with high resistance on the NCM particle surface. This thick CEI would prevent the transport of Li-ion through the cathode, thus causing large polarisation and capacity degradation of tensile deformed PPL-metteries.

The thinner CEI could be observed on the surface of the NCM cathodes in tensile deformed PPL+FEC-metteries after 100 cycles (Figure 5-16b). It was generated by the decomposition of constituents, including PVDF, Li salt, DMF, PMHS, and FEC, in the PPL+FEC electrolytes. The thickness of CEI covered on the surface of NCM cathodes was approximately 3.3, 3.6 and 3.7 nm for tensile strains of 0.5%, 10% and 15% respectively, showing a minor increase in thickness. Compared to NCM in tensile deformed PPL-metteries, NCM in PPL+FEC-metteries presented a thinner and uniform protective CEI. Particularly tensile strains of 10% and 15%, showed a thickness reduction of 40% and 66%, which might be attributed to the prior decomposition of FEC on the NCM cathode surface that hindered excess decomposition of other electrolyte constituents. The thinner and protective CEI could facilitate the Li-ion transfer and suppress the side reactions on the interface, thus causing higher specific capacity and cycling stability of PPL+FEC-mettery.

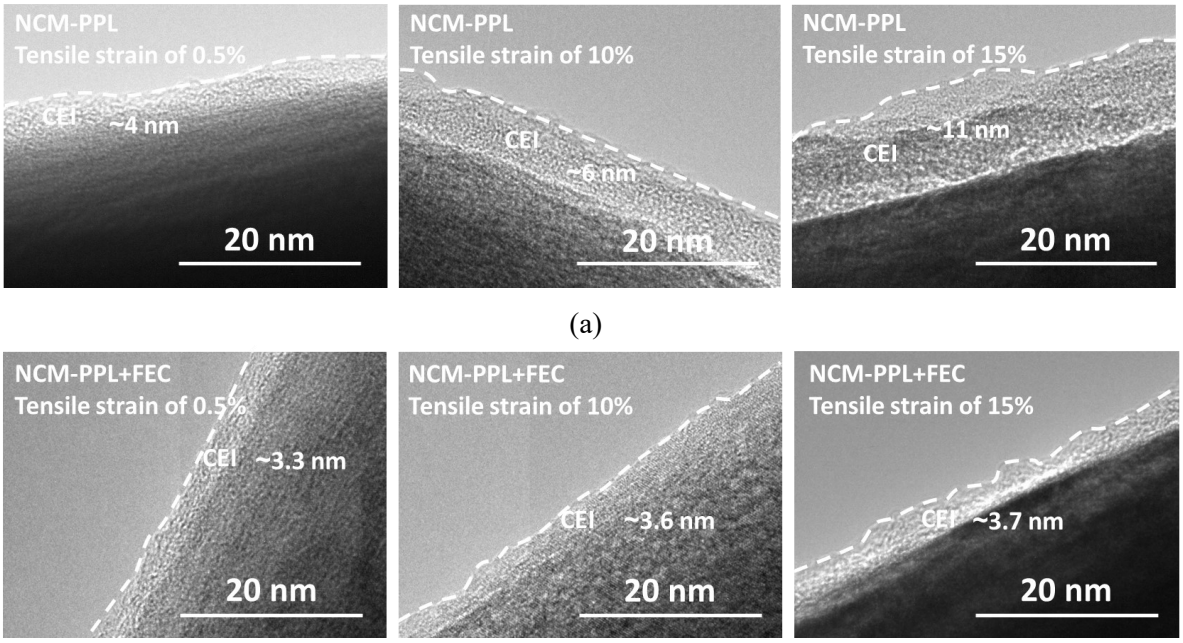
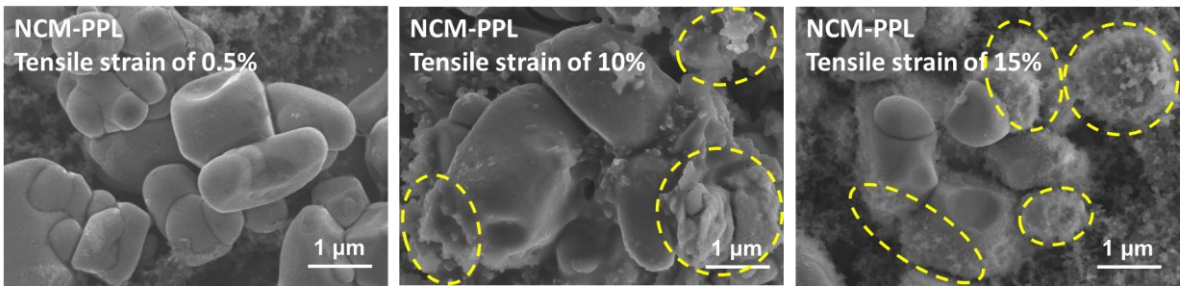


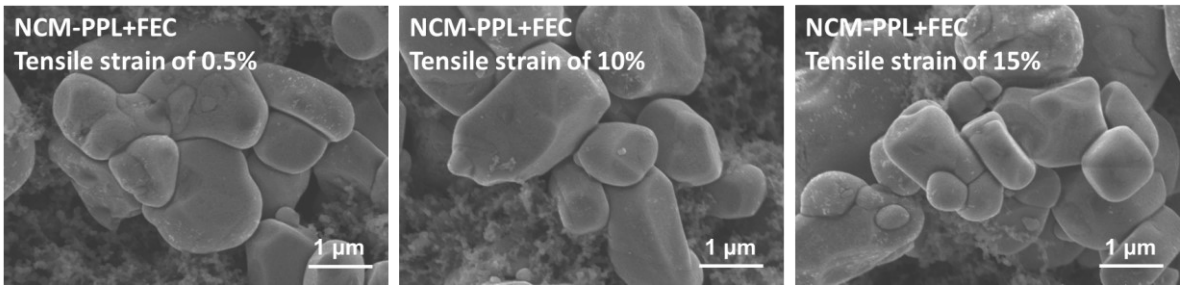
Figure 5-16 TEM images of CEI of cycled NCM cathodes in tensile deformed (a) PPL-metteries and (b) PPL+FEC-metteries with tensile strains of 0.5%, 10% and 15% after 100 cycles at 1C.

Figure 5-17 shows SEM images of cycled NCM cathodes in tensile deformed PPL-metteries and PPL+FEC-metteries with tensile strains of 0.5%, 10% and 15% after 100 cycles. The NCM particles maintained an intact microstructure with a smooth surface in both PPL-metteries and PPL+FEC-metteries with a tensile strain of 0.5%, indicating that the thin and stable CEI on the NCM could effectively protect the NCM structure. Nevertheless, as highlighted in Figure 5-17 (a), by using PPL electrolytes, the micro-cracks caused by uniaxial tensile deformation with tensile strains of 10% and 15% led to DMF decomposition which adhered to the NCM particles during the charge-discharge process, destroying the interface and microstructure of NCM particles.

In comparison, after the introduction of FEC in electrolytes (Figure 5-17b), the NCM structures still maintained contact with tensile strains of 10% and 15% after 100 cycles. This indicated that the FEC in PPL+FEC electrolyte could protect the NCM microstructure during the cycling process, thus exhibiting a high cycling performance.



(a)

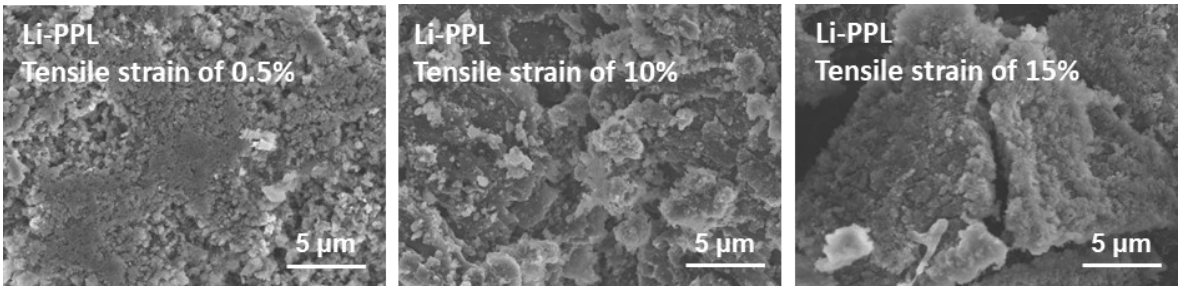


(b)

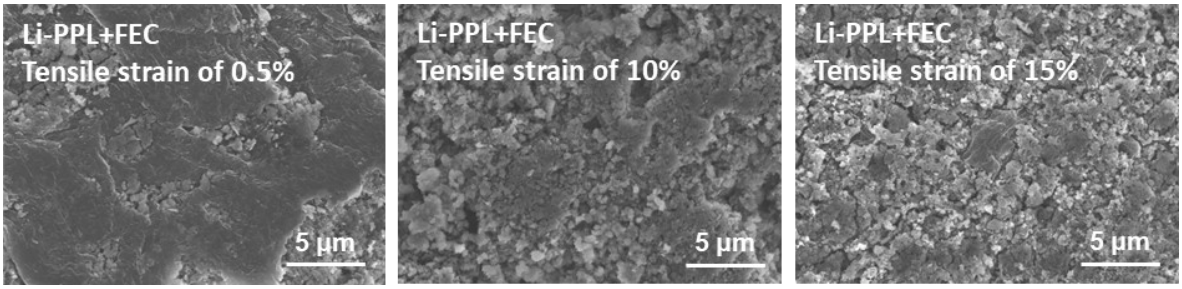
Figure 5-17 SEM images of cycled NCM cathodes in tensile deformed (a) PPL-metteries and (b) PPL+FEC-metteries with tensile strains of 0.5%, 10% and 15% after 100 cycles at 1C.

Figure 5-18 shows SEM images of cycled Li-metal anodes in tensile deformed PPL-metteries and PPL+FEC-metteries with tensile strains of 0.5%, 10% and 15% after charge-discharge 100 cycles. As shown in Figure 5-18 (a), the uneven Li metal plating could be observed in tensile deformed PPL-metteries (tensile strains of 10% and 15%) compared to the relatively uniform and flat Li plating morphology in PPL-mettery (tensile strain of 0.5%). This was attributed to the excessive decomposition of DMF in tensile deformed PPL-metteries, forming an unstable and inhomogeneous SEI that caused the uneven distribution and deposition of Li-ions.

In comparison, Li-metal anodes in tensile deformed PPL+FEC-metteries exhibited a more uniform morphology after 100 cycles (Figure 5-18b). This was because of the high surface energy of LiF generated by FEC decomposition, which was beneficial for the uniform and evenly lateral deposition of Li, hindering the Li dendrites generation.



(a)



(b)

Figure 5-18 SEM images of cycled Li-metal anodes in tensile deformed (a) PPL-metteries and (b) PPL+FEC-metteries with tensile strains of 0.5%, 10% and 15% after 100 cycles at 1C.

5.10 Summary

A quasi-solid-state PPL+FEC electrolyte was developed in order to improve the electrochemical performance of tensile deformed mettery, particularly for the tensile strain of more than 10%. The PPL+FEC electrolyte presented high ionic conductivity of 1.5×10^{-3} S/cm and the tensile deformed PPL+FEC electrolyte (tensile strain of 15%) still maintained a high ionic conductivity of 1.3×10^{-3} S/cm, a low activation energy of 0.15 eV and a high Li-ion transference number of 0.65 at 25°C. It was found that PPL+FEC electrolyte helped to construct a stable interface between the electrolyte and Li-metal anode, which improved the electrochemical performance and prevented the overgrowth of lithium dendrites in tensile deformed PPL+FEC-metteries, significantly enhancing the capacity and the cycle life.

As a result, the Li|PPL+FEC|Li symmetric mettery (tensile strain of 15%) could plate/strip lithium for 542 h and with overpotentials of 0.07 V before a short circuit. The PPL+FEC-mettery (tensile strain of 15%) achieved a specific capacity of 140.9 mAh g^{-1} after 250 cycles at 1C and a specific capacity of 106.5 mAh g^{-1} after 400 cycles at 2C. Compared to tensile deformed PPL-mettery, the tensile deformed PPL+FEC-mettery exhibited a significantly enhanced cycling performance and rate performance, delivering an increased specific capacity of more than 33.2% at 1C, more than 23.6% at 2C and more than 44.8% at 5C.

Chapter 6. Conclusion and future works

6.1 Thesis review and conclusions

In the present research, a polymer-based composite solid electrolyte PPL with enhanced Li-ion conductivity and mechanical strength was developed, which enables Li|PPL|NCM811 cell with superior

electrochemical performance. By using PPL as formable electrolyte, a novel metal battery, mettery, was developed. Based on the comprehensive study for the effect of plastic deformation on the electrochemical performance of mettery and the electrochemical-damage mechanics, the mettery was further improved by modifying the electrolyte, demonstrating enhanced energy storage capability after plastic deformation. Building on this work, the conventional sheet metal component can be manufactured into a mettery by metal forming technologies whilst enabling high electrical energy storage, facilitating zero-pollution society. The conclusions of this research are summarised as follows:

1. Three formable PVDF-based (pure PVDF, PL and PPL) SSEs were developed as candidates to be used in mettery. Among these SSEs, the PPL electrolyte with a proper composition showed a compact microstructure and the highest tensile strength of 3.63 MPa with a tensile strain of over 30% due to the strong binding between polymer and ceramic components by PMHS additive.
2. Electrochemical properties of the PVDF-based SSEs were characterised and analysed in coin cells for assisting the selection of high-performance SSE employed in mettery. In the PPL electrolyte, PMHS crosslinking with PVDF reduced the desolvation energy of $[Li(DMF)_x]^+$ to bare Li-ions through intermolecular interaction. This decoupled the Li-ion conduction from $[Li(DMF)_x]^+$ migration and facilitated high-efficiency multipath Li-ion transport in the PPL electrolyte, achieving the high ionic conductivity of 7.5×10^{-4} S cm^{-1} at 25 °C. The symmetric Li|PPL|Li cell could stably operate for more than 11800 h with a small polarization voltage of ~40 mV under a current density of 0.1 mA cm^{-2}, showing a favourable Li dendrites suppression ability.
3. The assembled solid-state NCM811|PPL|Li coin cell delivered low impedance, and ultrahigh long-term cycling stability with an initial specific capacity of 125.5 mAh g^{-1} and a capacity retention of 81.9% after 2200 cycles at 2C. Meanwhile, it exhibited an excellent rate performance of 112.6 mAh g^{-1} at 5C and a reversible capacity of 168.8 mAh g^{-1} when the current density returned to 1C after 35 cycles, which was superior to the PVDF and PL electrolytes. The optimal electrochemical performance was attributed to the compact, robust, and high-conductive PPL electrolyte that suppressed the lithium dendrites penetration and facilitated ion transfer. These results demonstrated that PPL electrolyte is the most appropriate formable SSE to be applied in mettery.
4. The PPL-metteries were manufactured and the effects of plastic deformations (bending and uniaxial tensile deformations) on electrochemical performance (including EIS, reversible specific capacity, cycling stability and rate performance) of them were studied. The detrimental effect of bending deformation on the electrochemical performance of PPL-mettery was slight when R/t was more than 1.77 owing to the utilisation of mechanically robust and high-

conductive PPL electrolyte. More specifically, compared with mettery (R/t=4.3), mettery (R/t>1.77) exhibited a minor capacity decrease of less than 8.9% over 100 cycles at 1C.

5. The uniaxial tensile deformation also caused an electrochemical performance decrease of PPL-mettery. Compared to PPL-mettery (tensile strain of 0.5%), PPL-mettery (tensile strain>10%) showed a capacity degradation of more than 21.7% over 100 cycles at 1C.
6. The electrochemical-damage mechanics in tensile deformed mettery was studied. It was found that the micro-cracks of tensile deformed PPL electrolyte hampered the Li-ion transport and led to uneven lithium deposition, prompting lithium dendrites penetration, which was considered the main reason for performance fading and short cycle life.
7. To improve the electrochemical performance of tensile deformed mettery, a quasi-solid state PPL+FEC electrolyte was developed, in which the FEC could not only greatly increase the ionic conductivity but also repair the micro-cracks caused by uniaxial tensile deformation, forming integrated Li-ion transport pathways and also creating a stable and robust electrolyte/electrode interface. Therefore, PPL+FEC-mettery (tensile strain of 15%) delivered a specific capacity of 140.9 mAh g^{-1} after 250 cycles at 1C and a specific capacity of 106.5 mAh g^{-1} after 400 cycles at 2C. The tensile deformed PPL+FEC-mettery exhibited a higher specific capacity of more than 23% and over twice longer cycle life compared to tensile deformed PPL-mettery.

6.2 Future work

Future work for improvement or further study on this research inculdes:

- Develop novel mechano-electrical analysis and design methodology for mettery. The data collected from experiments will be analysed by advanced physics-informed machine learning techniques to provide a fundamental understanding on the mechano-electrical properties of mettery. Advanced mechano-electrical analysis and design methodology will then be developed by using COMSOL Multiphysics software with advanced scientific plug-ins to enable the prediction of voltage and current flow in a mettery and structural circuits.
- Develop advanced Computer-aided engineering (CAE) tools for manufacturing mettery. Advanced finite element analysis (FEA) by using AutoForm will be carried out for design, analysis and optimisation of the mettery manufacturing process, e.g., roll forming, of mettery. Based on the findings, the CAE tools for mettery forming will be developed and experimentally validated.
- Develop a lab scale ‘pilot production line’ and forming process (and tooling) to enable the roll forming and hemming operations to produce mettery with a constant cross-sectional shape with a length of over 1m. The mettery formed by the new forming technology will be tested according

to the design specifications. The mechano-electrical characteristics and degradation mechanisms of mettery will be thoroughly studied enabling optimised design to be developed with the aid of advanced CAE tools.

- Explore the intelligence features (e.g. responsive interaction, logic gates and machine learning) of mettery.

Appendix A: Developing mettery structural circuits enabling the interaction intelligence in conventional metal formed products

Benefiting from the intrinsically high electrical conductivity and geometric diversity of metteries, multiple metteries can be assembled into a structural circuit (SC), i.e., a structural component (assembly) featuring intrinsic intelligence, such as interaction intelligence (Appendix A); logic intelligence (Appendix B), and learning intelligence (Appendix C)

As shown in Figure A-1, a single mettery displayed an open circuit voltage (OCV) of approximately 3.1V. The serial SC assembled by two metteries delivered an OCV of 6.2 V while the parallel SC assembled by two metteries delivered an OCV of 3.1 V, as shown in Figure A-1 (b). With the sensible design, various kinds of SCs can be triggered by tension and compression activities, which could be voltage-sensitive switches.

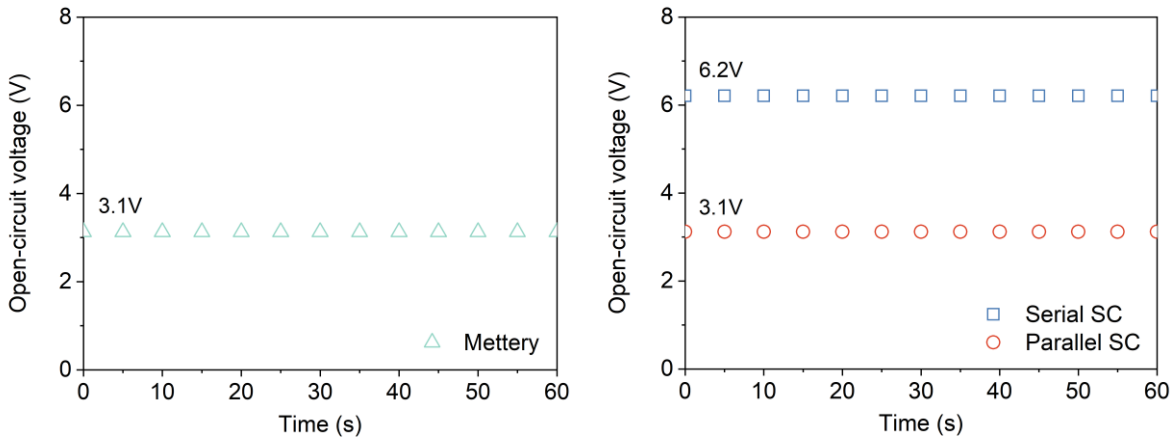


Figure A-1 Open-circuit voltage of (a) A single mettery and (b) Serial SC and parallel SC.

As shown in Figure A-2, two U-shaped metteries were assembled into a SC with intrinsic interaction intelligence. The convex of one mettery was fabricated into a cathode while the convex of another mettery was fabricated as an anode. The OCV of each mettery was approximately 3.1V. It was found from the testing results that, by applying a tensile load of 0.5N, the configuration of the SC was converted into a series circuit, leading to a total voltage output of 6.2V. Conversely, applying a compressive load of -0.5N, the configuration of the SC was converted into a parallel circuit, leading to a total voltage output of 3.1V. The interactions of this SC with the environment represented by a compressive or a tensile load can be detected, responded and indicated by voltage outputs (3.1 or 6.2V).

The interaction intelligence characteristics of the mettery structural circuits will enable a SC to interact with the environment in a responsive mode, leading to significant energy savings compared to the state-

of-art sensor technologies [149], which require a continuous power supply and thus significant energy consumption.

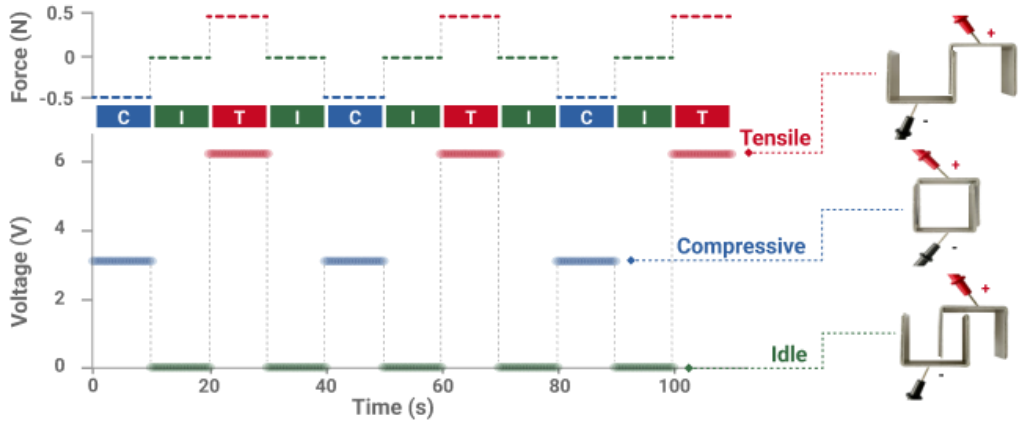


Figure A-2 Interaction intelligence realsed by built by a SC composed of two U-shape metteries.

Appendix B: Developing mettery structural circuits enabling the logic intelligence in conventional metal formed products

The logic gates are the basic building blocks of all digital electronic circuits and microprocessor-based systems. As shown in Figure B-1, by assembling three U-shape metteries in an SC, various mechano-electrical logic gates were constructed, which could perform Boolean operations effectively and efficiently.

Each mettery acts as the force control switch to construct the desired circuits and therefore deliver the corresponding voltage signal. Following conventional logic operations, the voltage binary output will be different according to the type of logic gate being applied and the combination of force inputs being carried out. Four of the most commonly used logic gates were developed using three U-shape metteries and one insulation layer, including the AND gate, OR gate, NAND gate and NOR gate.

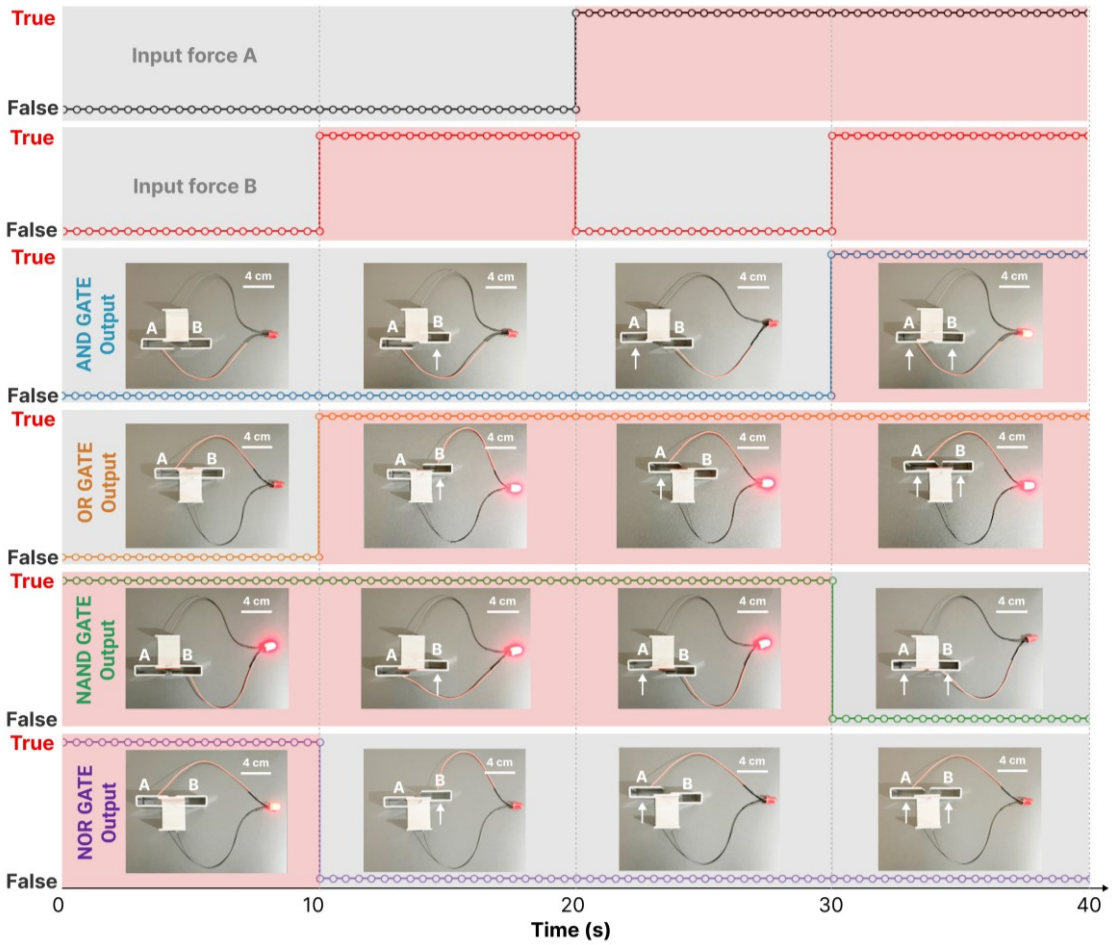


Figure B-1 Logic gates characteristics enabled by three U-shape metteries..

Moreover, as integrated circuits are composed of multiple conventional logic gates, mettery logic gates can also form an advanced control system in a similar way. Figure B-2 presents an illustration of two OR gates and one AND gate assembly, where the input force is noted as [0,0,0,0] with a binary output voltage of False at the initial state. When an input force [1,0,0,0] is applied, the action at the primary layer can be transferred to the secondary layer through force propagation, leading to a binary output voltage of True. In this case, there are 16 different combinations of input states. An infinite number of more advanced control systems could be developed with various basic logic gates and more input states according to the desired voltage outputs.

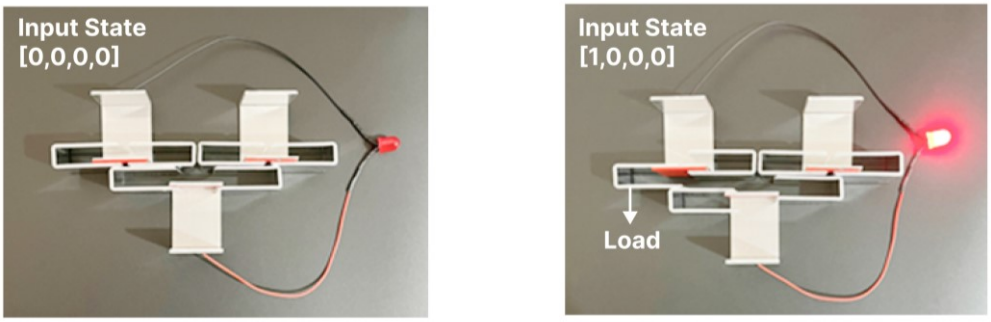


Figure B-2 Combination of multiple mettery logic gates (two OR Gates and one AND Gate).

Appendix C: Developing mettery structural circuits enabling the learning intelligence in conventional metal formed products

In this study, human-like meta-learning machinery is presented consisting of four U-shape metteries, with cognitive learning, decision-making, and self-reconfigurability attributes. Namely, this learning machinery adapts behaviour by learning from interactions with the environment, such as force or displacement input signals (signal A/B/C in Figure C-1); and autonomously determines the appropriate re-configuration of its behaviour according to learning outcomes, expressed as output voltage signals.

(1) Cognitive learning: Weak forces applied to A and B induce ‘elastic’ displacement signals, allowing A and B to revert to their original states. The meta-learning machinery learns from four different A and B input (binary displacement) states: [0,0], [0,1], [1,0], [1,1], each of them for 10 seconds, and introduces corresponding voltage outputs. As illustrated by the initial 40 seconds in Figure C-1, these outputs are positive for the first three states while remaining zero for the final state, thus exhibiting Boolean characteristics as NAND gate behaviour.

(2) Decision-making: The meta-learning machinery autonomously makes decisions subject to a large external input impulse of C, resulting in a new structure through 'plastic' deformation.

(3) Self-reconfigurability: As depicted in 40 to 80 seconds in Figure C-1, the meta-learning machinery autonomously reconfigures into a different behaviour for the four input states experienced prior to ‘plastic’ deformation. This results in a zero output for the initial state and positive outputs for the remaining three states, indicative of an OR gate behaviour. The self-reconfigurability attribute of this meta-learning machinery replicates the ‘neuroplasticity’ of the human brain cells. Consequently, the output signals and signal pathways can be autonomously reconfigured from exposure to environmental interactions, such as classifying a strong external load as a danger or memorising a novel experience.

The phenomenon where a homogeneous stimulus can induce varied cellular responses depending on the synapse's structure pre- and post-plastic deformation highlights an intrinsic biological capacity for memory and learning processes [150]. In a similar way to meta-learning machinery, the proposed transformation of Boolean characteristics in response to stimulus enables the possibility of learning and memorising by conventional metal components, integrating intelligence features into mechanical systems.

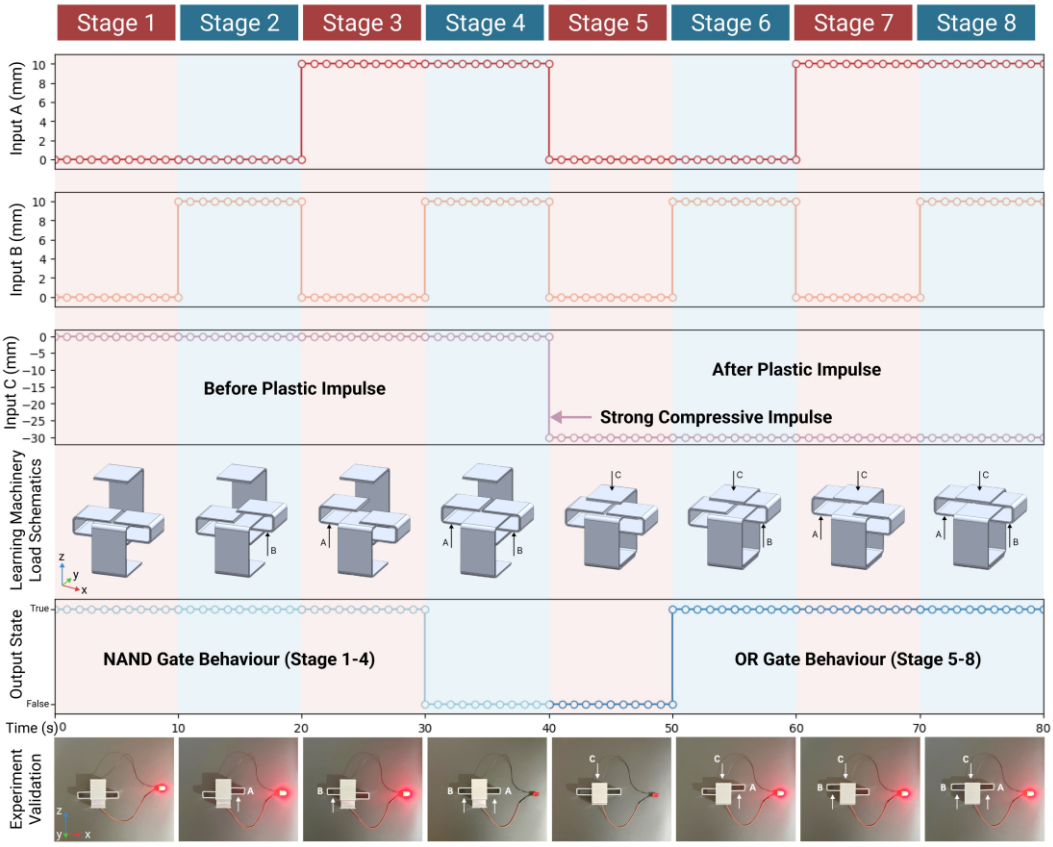


Figure C-1 Meta-learning machinery assembled by four U-shape metteries.

Reference

1. Secretariat, R., *Renewables 2020 global status report.* Rep. Paris: REN12, 2020.

2. Murdock, H.E., et al., *Renewables 2021-global status report.* 2021.

3. Braff, W.A., J.M. Mueller, and J.E. Trancik, *Value of storage technologies for wind and solar energy.* Nature Climate Change, 2016. **6**(10): p. 964-969.

4. Roper, W. *High Demand for Lithium-Ion Batteries*. 2020; Available from: https://www.statista.com/chart/23808/lithium-ion-battery-demand/.

5. *Hydroelectricity*. 2022; Available from: https://www.iea.org/energy-system/renewables/hydroelectricity.

6. *Electricity Data Explorer*. 2022; Available from: https://ember-climate.org/data/data-tools/data-explorer/.

7. Jones, D. *Global Electricity Review 2022*. 2022; Available from: https://ember-climate.org/insights/research/global-electricity-review-2022/.

8. Muhammad Kamran, M.R.F., *Renewable Energy Conversion Systems*. 2021: Academic Press.

9. *Hydro*. 2023; Available from: https://www.omexom.com/expertises/power/hydro/.

10. *Facts about hydropower*. 2023; Available from: https://www.hydropower.org/iha/discover-facts-about-hydropower.

11. Saarinen, L., P. Norrlund, and U. Lundin, *Field measurements and system identification of three frequency controlling hydropower plants.* IEEE Transactions on Energy Conversion, 2015. **30**(3): p. 1061-1068.

12. Bartle, A., *Hydropower potential and development activities.* Energy Policy, 2002. **30**(14): p. 1231-1239.

13. Mussa, M., H. Teka, and H. Ayicho, *Environmental impacts of hydropower and alternative mitigation measures.* current investigations in agriculture and current research, 2018. **2**(2).

14. Somani, A., et al., *Hydropower value study: Current status and future opportunities*. 2021, Technical Report PNNL-29226. Hydrowires. Richland, WA: Pacific Northwest ….

15. Irena, *Majority of New Renewables Undercut Cheapest Fossil Fuel on Cost*. 2021, Press Release.

16. Council, G.W.E., *Global wind report 2021.* Global Wind Energy Council: Brussels, Belgium, 2021: p. 6-7.

17. Ritchie, H., M. Roser, and P. Rosado, *Energy. Our world in data.* OurWorldInData. org, 2020.

18. Komusanac, I., et al., *Wind energy in Europe*, in *2020 Statistics and the outlook for 2021–2025*. 2021.

19. *Wind Energy Factsheet*. 2022; Available from: https://css.umich.edu/publications/factsheets/energy/wind-energy-factsheet.

20. *Betz limit*. 2023; Available from: https://energyeducation.ca/encyclopedia/Betz_limit.

21. Rodriguez, P., et al., *Reactive power control for improving wind turbine system behavior under grid faults.* IEEE Transactions on Power Electronics, 2009. **24**(7): p. 1798-1801.

22. Molina, M.G. and P.E. Mercado, *Modelling and control design of pitch-controlled variable speed wind turbines*, in *Wind turbines*. 2011, IntechOpen.

23. Buljan, A. *162 Offshore Wind Farms Up and Running Worldwide, 26 More Under Construction*. 2021; Available from: https://www.offshorewind.biz/2021/02/09/162-offshore-wind-farms-up-and-running-worldwide-26-more-under-construction/.

24. Stehly, T., P. Beiter, and P. Duffy, *2019 cost of wind energy review*. 2020, National Renewable Energy Lab.(NREL), Golden, CO (United States).

25. *Offshore Wind Outlook 2019*. 2019, International Energy Agency.

26. Wiser, R., et al., *Expert elicitation survey predicts 37% to 49% declines in wind energy costs by 2050.* Nature Energy, 2021. **6**(5): p. 555-565.

27. Possner, A. and K. Caldeira, *Geophysical potential for wind energy over the open oceans.* Proceedings of the National Academy of Sciences, 2017. **114**(43): p. 11338-11343.

28. Council, G.W.E., *Floating offshore wind—a global opportunity.* The Global Wind Energy Council, 2022.

29. Johnson, B. *Wind farms could power every home by 2030*. 2020; Available from: https://www.bbc.co.uk/news/uk-politics-54421489.

30. Scott, K., *Introduction to Electrolysis, Electrolysers and Hydrogen Production*, in *Electrochemical Methods for Hydrogen Production*. 2019, Royal Society of Chemistry. p. 1-27.

31. Chapman, A., et al., *A review of four case studies assessing the potential for hydrogen penetration of the future energy system.* International journal of hydrogen energy, 2019. **44**(13): p. 6371-6382.

32. *Solar explained Photovoltaics and electricity*. 2023; Available from: https://www.eia.gov/energyexplained/solar/photovoltaics-and-electricity.php.

33. Greening, B. and A. Azapagic, *Domestic solar thermal water heating: A sustainable option for the UK?* Renewable Energy, 2014. **63**: p. 23-36.

34. Asmelash, E. and G. Prakash, *Future of Solar Photovoltaic: Deployment, investment, technology, grid integration and socio-economic aspects.* International Renewable Energy Agency, Abu Dhabi, 2019.

35. *Renewable Power Generation Costs in 2020*. 2021.

36. *Renewables 2021*. 2021, International Energy Agency.

37. *Renewables 2022 Global Status*. 2022, REN21.

38. Brun, K., T.C. Allison, and R. Dennis, *Thermal, mechanical, and hybrid chemical energy storage systems*. 2020: Academic Press.

39. Paoli, L. and T. Gül, *Electric cars fend off supply challenges to more than double global sales.* 2022.

40. Michael Renner, B.P., Rabea Ferroukhi, Padmashree Gehl Sampath, Xavier Garcia Casals, Arslan Khalid, Diala Hawila, Jinlei Feng, Celia Garcia-Banos, *Analysis built on Renewable energy benefits: Measuring the economics (IRENA, 2016) MEASURING THE SOCIO-ECONOMIC FOOTPRINT OF THE ENERGY TRANSITION: THE ROLE OF SUPPLY CHAINS*. 2019, International Renewable Energy Agency.

41. Irle, R. *Global EV Sales for 2022*. 2023; Available from: https://www.ev-volumes.com/.

42. Bullock, K.R., *Lead/acid batteries.* Journal of Power Sources, 1994. **51**(1): p. 1-17.

43. Weinert, J.X., A.F. Burke, and X. Wei, *Lead-acid and lithium-ion batteries for the Chinese electric bike market and implications on future technology advancement.* Journal of Power Sources, 2007. **172**(2): p. 938-945.

44. Xia, W., et al., *Metal–organic frameworks and their derived nanostructures for electrochemical energy storage and conversion.* Energy & Environmental Science, 2015. **8**(7): p. 1837-1866.

45. Jung, J., L. Zhang, and J. Zhang, *Lead-acid battery technologies: fundamentals, materials, and applications*. Vol. 8. 2015: Crc Press.

46. Huggins, R.A. and R.A. Huggins, *Energy storage: fundamentals, materials and applications*. 2016: Springer.

47. Liu, Y., et al., *Advanced hydrogen storage alloys for Ni/MH rechargeable batteries.* Journal of Materials Chemistry, 2011. **21**(13): p. 4743-4755.

48. Cano, Z.P., et al., *Batteries and fuel cells for emerging electric vehicle markets.* Nature energy, 2018. **3**(4): p. 279-289.

49. Fetcenko, M.A., et al., *Recent advances in NiMH battery technology.* Journal of Power Sources, 2007. **165**(2): p. 544-551.

50. Ouyang, L., et al., *Progress of hydrogen storage alloys for Ni-MH rechargeable power batteries in electric vehicles: A review.* Materials Chemistry and Physics, 2017. **200**: p. 164-178.

51. Zhan, F., et al., *Characteristics of Ni/MH power batteries and its application to electric vehicles.* Journal of Alloys and Compounds, 1999. **293-295**: p. 804-808.

52. Armand, M. and J.-M. Tarascon, *Building better batteries.* nature, 2008. **451**(7179): p. 652-657.

53. Larcher, D. and J.-M. Tarascon, *Towards greener and more sustainable batteries for electrical energy storage.* Nature chemistry, 2015. **7**(1): p. 19-29.

54. Chen, Z., et al., *Advanced cathode materials for lithium-ion batteries.* MRS Bulletin, 2011. **36**(7): p. 498-505.

55. Whittingham, M.S., *Lithium batteries and cathode materials.* Chemical reviews, 2004. **104**(10): p. 4271-4302.

56. Cyril, A.A., A.D. Singh, and S. Sengupta, *Structural Battery.*

57. Pejman, R., E.C. Kumbur, and A.R. Najafi, *Multi-physics design optimization of structural battery.* Multifunctional Materials, 2021. **4**(2): p. 024001.

58. Schmuch, R., et al., *Performance and cost of materials for lithium-based rechargeable automotive batteries.* Nature energy, 2018. **3**(4): p. 267-278.

59. Saw, L.H., Y. Ye, and A.A.O. Tay, *Integration issues of lithium-ion battery into electric vehicles battery pack.* Journal of Cleaner Production, 2016. **113**: p. 1032-1045.

60. Kwade, A., et al., *Current status and challenges for automotive battery production technologies.* Nature Energy, 2018. **3**(4): p. 290-300.

61. Sakti, A., et al., *A techno-economic analysis and optimization of Li-ion batteries for light-duty passenger vehicle electrification.* Journal of Power Sources, 2015. **273**: p. 966-980.

62. Maiser, E. *Battery packaging-Technology review*. in *AIP Conference Proceedings*. 2014. American Institute of Physics.

63. Xu, W., et al., *Lithium metal anodes for rechargeable batteries.* Energy & Environmental Science, 2014. **7**(2): p. 513-537.

64. Li, W., J.R. Dahn, and D.S. Wainwright, *Rechargeable lithium batteries with aqueous electrolytes.* Science, 1994. **264**(5162): p. 1115-1118.

65. Tarascon, J.-M. and M. Armand, *Issues and challenges facing rechargeable lithium batteries.* nature, 2001. **414**(6861): p. 359-367.

66. Li, J., et al., *Solid electrolyte: the key for high-voltage lithium batteries.* Advanced Energy Materials, 2015. **5**(4): p. 1401408.

67. Ishii, K., et al., *Reactivity evaluation of NASICON-type solid electrolyte LATP, LAGP and Olivine-type cathode LCP.* Materials Letters, 2022. **324**: p. 132736.

68. Jackman, S.D. and R.A. Cutler, *Stability of NaSICON-type Li1.3Al0.3Ti1.7P3O12 in aqueous solutions.* Journal of Power Sources, 2013. **230**: p. 251-260.

69. Li, Y., et al., *Optimizing Li+ conductivity in a garnet framework.* Journal of Materials Chemistry, 2012. **22**(30): p. 15357-15361.

70. Zhu, J., et al., *A Multilayer Ceramic Electrolyte for All-Solid-State Li Batteries.* Angewandte Chemie International Edition, 2021. **60**(7): p. 3781-3790.

71. Lu, J. and Y. Li, *Perovskite-type Li-ion solid electrolytes: a review.* Journal of Materials Science: Materials in Electronics, 2021. **32**: p. 9736-9754.

72. Yu, R., et al., *Synthesis and characterization of perovskite-type (Li, Sr)(Zr, Nb) O3 quaternary solid electrolyte for all-solid-state batteries.* Journal of Power Sources, 2016. **306**: p. 623-629.

73. Shi, Z., et al., *A 3D fiber skeleton reinforced PEO-based polymer electrolyte for high rate and ultra-long cycle all-solid-state batteries.* Journal of Materials Chemistry A, 2021. **9**(37): p. 21057-21070.

74. Zhang, X., et al., *Synergistic Coupling between Li6.75La3Zr1.75Ta0.25O12 and Poly(vinylidene fluoride) Induces High Ionic Conductivity, Mechanical Strength, and Thermal Stability of Solid Composite Electrolytes.* Journal of the American Chemical Society, 2017. **139**(39): p. 13779-13785.

75. Fang, R., et al., *Li2S6-Integrated PEO-based polymer electrolytes for all-solid-state lithium-metal batteries.* Angewandte Chemie, 2021. **133**(32): p. 17842-17847.

76. Yang, K., et al., *Stable Interface Chemistry and Multiple Ion Transport of Composite Electrolyte Contribute to Ultra-long Cycling Solid-State LiNi0. 8Co0. 1Mn0. 1O2/Lithium Metal Batteries.* Angewandte Chemie International Edition, 2021. **60**(46): p. 24668-24675.

77. Fu, F., et al., *Regulating lithium deposition via bifunctional regular-random cross-linking network solid polymer electrolyte for Li metal batteries.* Journal of Power Sources, 2021. **484**: p. 229186.

78. Widstrom, M.D., et al., *Enabling high performance all-solid-state lithium metal batteries using solid polymer electrolytes plasticized with ionic liquid.* Electrochimica Acta, 2020. **345**: p. 136156.

79. Du, Z., et al., *Effects of plasticizer content and ceramic addition on electrochemical properties of cross-linked polymer electrolyte.* Journal of The Electrochemical Society, 2021. **168**(5): p. 050549.

80. Wang, J., et al., *Synergistic effects of plasticizer and 3D framework toward high-performance solid polymer electrolyte for room-temperature solid-state lithium batteries.* ACS Applied Energy Materials, 2021. **4**(4): p. 4129-4137.

81. Yuan, B., et al., *Self-assembly synthesis of solid polymer electrolyte with carbonate terminated poly(ethylene glycol) matrix and its application for solid state lithium battery.* Journal of Energy Chemistry, 2019. **38**: p. 55-59.

82. He, Y., N. Liu, and P.A. Kohl, *Difunctional block copolymer with ion solvating and crosslinking sites as solid polymer electrolyte for lithium batteries.* Journal of Power Sources, 2021. **481**: p. 228832.

83. Jie, J., et al., *High-performance PVDF-HFP based gel polymer electrolyte with a safe solvent in Li metal polymer battery.* Journal of Energy Chemistry, 2020. **49**: p. 80-88.

84. Chen, X.C., et al., *Gel composite electrolyte–an effective way to utilize ceramic fillers in lithium batteries.* Journal of Materials Chemistry A, 2021. **9**(10): p. 6555-6566.

85. Aono, H., et al., *Ionic conductivity and sinterability of lithium titanium phosphate system.* Solid State Ionics, 1990. **40-41**: p. 38-42.

86. Yu, X. and A. Manthiram, *Enhanced Interfacial Stability of Hybrid-Electrolyte Lithium-Sulfur Batteries with a Layer of Multifunctional Polymer with Intrinsic Nanoporosity.* Advanced Functional Materials, 2019. **29**(3): p. 1805996.

87. Hu, J., et al., *Porous film host-derived 3D composite polymer electrolyte for high-voltage solid state lithium batteries.* Energy Storage Materials, 2020. **26**: p. 283-289.

88. Jiang, T., et al., *Solvent-free synthesis of thin, flexible, nonflammable garnet-based composite solid electrolyte for all-solid-state lithium batteries.* Advanced Energy Materials, 2020. **10**(12): p. 1903376.

89. Bae, J., et al., *A 3D nanostructured hydrogel-framework-derived high-performance composite polymer lithium-ion electrolyte.* Angewandte Chemie International Edition, 2018. **57**(8): p. 2096-2100.

90. Wang, C., et al., *Solid-state plastic crystal electrolytes: effective protection interlayers for sulfide-based all-solid-state lithium metal batteries.* Advanced Functional Materials, 2019. **29**(26): p. 1900392.

91. Blake, A.J., et al., *3D printable ceramic–polymer electrolytes for flexible high-performance li-ion batteries with enhanced thermal stability.* Advanced energy materials, 2017. **7**(14): p. 1602920.

92. Lin, D., et al., *High ionic conductivity of composite solid polymer electrolyte via in situ synthesis of monodispersed SiO2 nanospheres in poly (ethylene oxide).* Nano letters, 2016. **16**(1): p. 459-465.

93. Sathyanathan, T. and C. Pugazhendhi Sugumaran, *Enhancement of Ionic Conductivity and Dielectric Permittivity for PMMA-Based Polymer Electrolyte with BaTiO3 NanoFiller.* International Journal of Nanoscience, 2020. **19**(05): p. 1950035.

94. Alexander, K., *Technology roadmap: hydrogen and fuel cells*. 2015, Technical report, International Energy Agency.

95. Zhao, G., et al., *Life cycle cost analysis: A case study of hydrogen energy application on the Orkney Islands.* International Journal of Hydrogen Energy, 2019. **44**(19): p. 9517-9528.

96. Wei, M., S.J. Smith, and M.D. Sohn, *Experience curve development and cost reduction disaggregation for fuel cell markets in Japan and the US.* Applied Energy, 2017. **191**: p. 346-357.

97. Miotti, M., J. Hofer, and C. Bauer, *Integrated environmental and economic assessment of current and future fuel cell vehicles.* The International Journal of Life Cycle Assessment, 2017. **22**: p. 94-110.

98. Alazemi, J. and J. Andrews, *Automotive hydrogen fuelling stations: An international review.* Renewable and Sustainable Energy Reviews, 2015. **48**: p. 483-499.

99. Aubin, C.A., et al., *Towards enduring autonomous robots via embodied energy.* Nature, 2022. **602**(7897): p. 393-402.

100. Asp, L.E., et al., *Structural battery composites: a review.* Functional Composites and Structures, 2019. **1**(4): p. 042001.

101. Pereira, T., et al., *Embedding thin-film lithium energy cells in structural composites.* Composites Science and Technology, 2008. **68**(7): p. 1935-1941.

102. Roberts, S.C. and G.S. Aglietti, *Structural performance of a multifunctional spacecraft structure based on plastic lithium-ion batteries.* Acta Astronautica, 2010. **67**(3): p. 424-439.

103. Wang, Y., C. Peng, and W. Zhang, *Mechanical and electrical behavior of a novel satellite multifunctional structural battery.* 2014.

104. Ladpli, P., et al., *Multifunctional energy storage composite structures with embedded lithium-ion batteries.* Journal of Power Sources, 2019. **414**: p. 517-529.

105. Thomas, J.P. and M.A. Qidwai, *The design and application of multifunctional structure-battery materials systems.* Jom, 2005. **57**(3): p. 18.

106. Zhang, Y., et al., *Multifunctional structural lithium-ion battery for electric vehicles.* Journal of Intelligent Material Systems and Structures, 2017. **28**(12): p. 1603-1613.

107. Asp, L.E., et al., *A structural battery and its multifunctional performance.* Advanced Energy and Sustainability Research, 2021. **2**(3): p. 2000093.

108. Asp, L.E. and E.S. Greenhalgh, *Structural power composites.* Composites Science and Technology, 2014. **101**: p. 41-61.

109. Lendlein, A. and R.S. Trask, *Multifunctional materials: concepts, function-structure relationships, knowledge-based design, translational materials research.* Multifunctional Materials, 2018. **1**(1): p. 010201.

110. Liu, P., E. Sherman, and A. Jacobsen, *Design and fabrication of multifunctional structural batteries.* Journal of Power Sources, 2009. **189**(1): p. 646-650.

111. Wong, E., et al., *Design and processing of structural composite batteries.* Proceedings of SAMPE, 2007: p. 3-7.

112. Ekstedt, S., M. Wysocki, and L. Asp, *Structural batteries made from fibre reinforced composites.* Plastics, rubber and composites, 2010. **39**(3-5): p. 148-150.

113. Moyer, K., et al., *Polymer reinforced carbon fiber interfaces for high energy density structural lithium-ion batteries.* Sustainable Energy & Fuels, 2020. **4**(6): p. 2661-2668.

114. Shirshova, N., et al., *Multifunctional structural energy storage composite supercapacitors.* Faraday discussions, 2014. **172**: p. 81-103.

115. Johannisson, W., D. Zenkert, and G. Lindbergh, *Model of a structural battery and its potential for system level mass savings.* Multifunctional Materials, 2019. **2**(3): p. 035002.

116. Carlstedt, D. and L.E. Asp, *Performance analysis framework for structural battery composites in electric vehicles.* Composites Part B: Engineering, 2020. **186**: p. 107822.

117. Manthiram, A., X. Yu, and S. Wang, *Lithium battery chemistries enabled by solid-state electrolytes.* Nature Reviews Materials, 2017. **2**(4): p. 16103.

118. Murugan, R., V. Thangadurai, and W. Weppner, *Fast Lithium Ion Conduction in Garnet-Type Li7La3Zr2O12.* Angewandte Chemie International Edition, 2007. **46**(41): p. 7778-7781.

119. Bohnke, O., *The fast lithium-ion conducting oxides Li3xLa2/3−xTiO3 from fundamentals to application.* Solid State Ionics, 2008. **179**(1): p. 9-15.

120. Tan, D.H.S., et al., *Elucidating Reversible Electrochemical Redox of Li6PS5Cl Solid Electrolyte.* ACS Energy Letters, 2019. **4**(10): p. 2418-2427.

121. MacGlashan, G.S., Y.G. Andreev, and P.G. Bruce, *Structure of the polymer electrolyte poly(ethylene oxide)6:LiAsF6.* Nature, 1999. **398**(6730): p. 792-794.

122. Abraham, K.M., H.S. Choe, and D.M. Pasquariello, *Polyacrylonitrile electrolyte-based Li ion batteries.* Electrochimica Acta, 1998. **43**(16): p. 2399-2412.

123. Zou, Z., et al., *Mobile Ions in Composite Solids.* Chemical Reviews, 2020. **120**(9): p. 4169-4221.

124. Li, S., et al., *Progress and Perspective of Ceramic/Polymer Composite Solid Electrolytes for Lithium Batteries.* Advanced Science, 2020. **7**(5): p. 1903088.

125. Zheng, J. and Y.-Y. Hu, *New Insights into the Compositional Dependence of Li-Ion Transport in Polymer–Ceramic Composite Electrolytes.* ACS Applied Materials & Interfaces, 2018. **10**(4): p. 4113-4120.

126. Zheng, J., et al., *Interface-Enabled Ion Conduction in Li10GeP2S12–Poly(ethylene Oxide) Hybrid Electrolytes.* ACS Applied Energy Materials, 2019. **2**(2): p. 1452-1459.

127. Zheng, J., et al., *Li-ion transport in a representative ceramic–polymer–plasticizer composite electrolyte: Li7La3Zr2O12–polyethylene oxide–tetraethylene glycol dimethyl ether.* Journal of Materials Chemistry A, 2017. **5**(35): p. 18457-18463.

128. Zheng, J., M. Tang, and Y.-Y. Hu, *Lithium Ion Pathway within Li7La3Zr2O12-Polyethylene Oxide Composite Electrolytes.* Angewandte Chemie International Edition, 2016. **55**(40): p. 12538-12542.

129. Yang, T., et al., *Composite Polymer Electrolytes with Li7La3Zr2O12 Garnet-Type Nanowires as Ceramic Fillers: Mechanism of Conductivity Enhancement and Role of Doping and Morphology.* ACS Applied Materials & Interfaces, 2017. **9**(26): p. 21773-21780.

130. Liu, M., et al., *Tandem Interface and Bulk Li-Ion Transport in a Hybrid Solid Electrolyte with Microsized Active Filler.* ACS Energy Letters, 2019. **4**(9): p. 2336-2342.

131. Liu, M., et al., *Improving Li-ion interfacial transport in hybrid solid electrolytes.* Nature Nanotechnology, 2022. **17**(9): p. 959-967.

132. Li, Z., et al., *Ionic Conduction in Composite Polymer Electrolytes: Case of PEO:Ga-LLZO Composites.* ACS Applied Materials & Interfaces, 2019. **11**(1): p. 784-791.

133. Pan, K., et al., *A Flexible Ceramic/Polymer Hybrid Solid Electrolyte for Solid-State Lithium Metal Batteries.* Advanced Materials, 2020. **32**(17): p. 2000399.

134. Zhang, Z., et al., *Agglomeration-free composite solid electrolyte and enhanced cathode-electrolyte interphase kinetics for all-solid-state lithium metal batteries.* Energy Storage Materials, 2022. **51**: p. 19-28.

135. Zhao, L., et al., *Building cross-phase ion transport channels between ceramic and polymer for highly conductive composite solid-state electrolyte.* Cell Reports Physical Science.

136. Zhang, X., et al., *Self-Suppression of Lithium Dendrite in All-Solid-State Lithium Metal Batteries with Poly(vinylidene difluoride)-Based Solid Electrolytes.* Advanced Materials, 2019. **31**(11): p. 1806082.

137. Yang, K., et al., *Stable Interface Chemistry and Multiple Ion Transport of Composite Electrolyte Contribute to Ultra-long Cycling Solid-State LiNi0.8Co0.1Mn0.1O2/Lithium Metal Batteries.* Angewandte Chemie International Edition, 2021. **60**(46): p. 24668-24675.

138. Shi, P., et al., *A dielectric electrolyte composite with high lithium-ion conductivity for high-voltage solid-state lithium metal batteries.* Nature Nanotechnology, 2023.

139. Mi, J., et al., *Topology crafting of polyvinylidene difluoride electrolyte creates ultra-long cycling high-voltage lithium metal solid-state batteries.* Energy Storage Materials, 2022. **48**: p. 375-383.

140. Zhang, X., et al., *High Cycling Stability for Solid-State Li Metal Batteries via Regulating Solvation Effect in Poly(Vinylidene Fluoride)-Based Electrolytes.* Batteries & Supercaps, 2020. **3**(9): p. 876-883.

141. Liu, Q., et al., *Polymer electrolytes based on interactions between [solvent-Li+] complex and solvent-modified polymer.* Energy Storage Materials, 2022. **51**: p. 443-452.

142. Wójcik-Bania, M., *Influence of the addition of organo-montmorillonite nanofiller on cross-linking of polysiloxanes – FTIR studies.* Spectrochimica Acta Part A: Molecular and Biomolecular Spectroscopy, 2021. **252**: p. 119491.

143. Zhang, X., et al., *Response to Comment on "Self-Suppression of Lithium Dendrite in All-Solid-State Lithium Metal Batteries with Poly(vinylidene difluoride)-Based Solid Electrolytes".* Advanced Materials, 2020. **32**(14): p. 2000026.

144. Galos, J., et al., *Energy storage structural composites with integrated lithium‐ion batteries: a review.* Advanced Materials Technologies, 2021. **6**(8): p. 2001059.

145. Shalouf, S.M., J. Zhang, and C. Wang, *Effects of mechanical deformation on electric performance of rechargeable batteries embedded in load carrying composite structures.* Plastics, Rubber and Composites, 2014. **43**(3): p. 98-104.

146. Zhou, M., et al., *Ultrathin yet robust single lithium‐ion conducting quasi‐solid‐state polymer‐brush electrolytes enable ultralong‐life and dendrite‐free lithium‐metal batteries.* Advanced Materials, 2021. **33**(29): p. 2100943.

147. Jaumaux, P., et al., *Non‐flammable liquid and quasi‐solid electrolytes toward highly‐safe alkali metal‐based batteries.* Advanced Functional Materials, 2021. **31**(10): p. 2008644.

148. Yang, K., et al., *Determining the Role of Ion Transport Throughput in Solid‐State Lithium Batteries.* Angewandte Chemie International Edition, 2023. **62**(24): p. e202302586.

149. Rezvanitabar, A., et al., *A power-efficient bridge readout circuit for implantable, wearable, and IoT applications.* IEEE sensors journal, 2020. **20**(17): p. 9955-9962.

150. Kandel, E.R., *The molecular biology of memory storage: a dialogue between genes and synapses.* Science, 2001. **294**(5544): p. 1030-1038.